JPTM

Journal of Pathology and Translational Medicine

Journal of Pathology and Translational Medicine

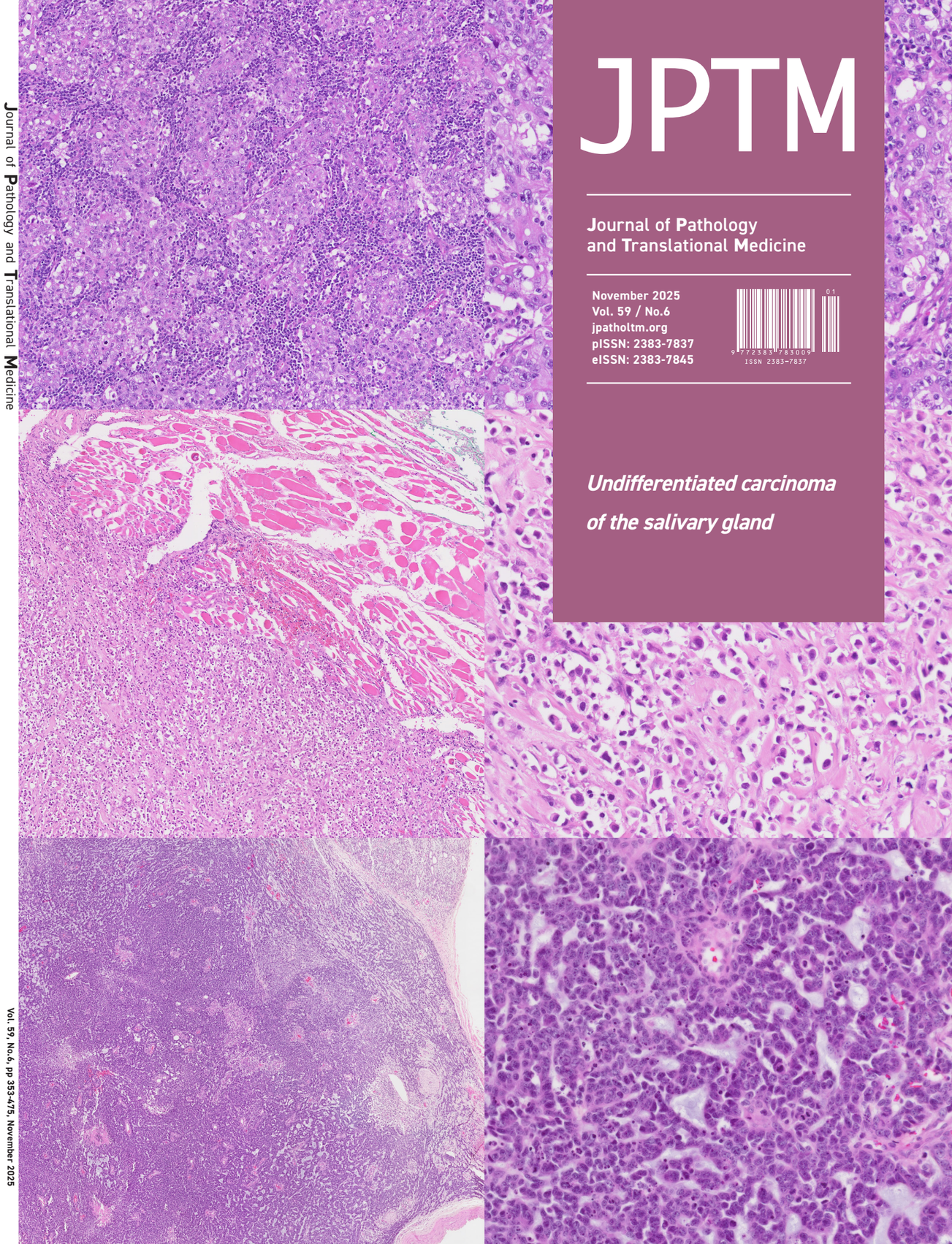

JPTM

Journal of Pathology and Translational Medicine

November 2025
Vol. 59 / No.6
jpatholtm.org
pISSN: 2383-7837
eISSN: 2383-7845

Undifferentiated carcinoma of the salivary gland

Vol. 59, No.6, pp 353-475, November 2025

JPTM

jpatholtm.org
pISSN 2383-7837 · eISSN 2383-7845

Vol. 59, No.6, November 2025

Published on 15 November 2025

Aims & Scope

The Journal of Pathology and Translational Medicine is an open venue for the rapid publication of major achievements in various fields of pathology, cytopathology, and biomedical and translational research. The Journal aims to share new insights into the molecular and cellular mechanisms of human diseases and to report major advances in both experimental and clinical medicine, with a particular emphasis on translational research. The investigations of human cells and tissues using high-dimensional biology techniques such as genomics and proteomics will be given a high priority. Articles on stem cell biology are also welcome. The categories of manuscript include original articles, review and perspective articles, case studies, brief case reports, and letters to the editor.

Subscription Information

To subscribe to this journal, please contact the Korean Society of Pathologists/the Korean Society for Cytopathology. Full text PDF files are also available at the official website (https://jpatholtm.org). *Journal of Pathology and Translational Medicine* is indexed by Emerging Sources Citation Index (ESCI), PubMed, PubMed Central, Scopus, KoreaMed, KoMCI, WPRIM, Directory of Open Access Journals (DOAJ), and CrossRef. Circulation number per issue is 50.

Contact the Korean Society of Pathologists/the Korean Society for Cytopathology

Publishers: Kang, Gyeong Hoon, MD; Choi, Yoon Jung, MD
Editors-in-Chief: Jung, Chan Kwon, MD; Park, So Yeon, MD
Published by the Korean Society of Pathologists/the Korean Society for Cytopathology

Editorial Office
Suite 706, 217 Saechang-ro, Yongsan-gu, Seoul 04376, Korea
Tel: +82-2-795-3094 Fax: +82-2-790-6635 E-mail: office@jpatholtm.org
#1508 Renaissancetower, 14 Mallijae-ro, Mapo-gu, Seoul 04195, Korea
Tel: +82-2-593-6943 Fax: +82-2-593-6944 E-mail: office@jpatholtm.org

Printed by M2PI
#805, 26 Sangwon 1-gil, Seongdong-gu, Seoul 04779, Korea
Tel: +82-2-6966-4930 Fax: +82-2-6966-4945 E-mail: support@m2-pi.com

Manuscript Editing by InfoLumi Co.
210-202, 421 Pangyo-ro, Bundang-gu, Seongnam 13522, Korea
Tel: +82-70-8839-8800 E-mail: infolumi.chang@gmail.com

Front cover image: Various histopathological features of undifferentiated salivary carcinomas (p. 365)

Editorial Board

JPTM

jpatholtm.org
pISSN 2383-7837 · eISSN 2383-7845

Contents

Vol. 59, No.6, November 2025

REVIEW ARTICLE

ORIGINAL ARTICLES

JPTM

jpatholtm.org
pISSN 2383-7837 · eISSN 2383-7845

Contents

Vol. 59, No.6, November 2025

CASE STUDIES

NEWSLETTER

JPTM

REVIEW ARTICLE

pISSN 2383-7837 · eISSN 2383-7845

Journal of Pathology and Translational Medicine 2025; 59: 353-360
https://doi.org/10.4132/jptm.2025.08.12

Breast schwannoma: review of entity and differential diagnosis

Sandra Ixchel Sanchez, Ashley Cimino-Mathews

Department of Pathology, The Johns Hopkins University School of Medicine and The Johns Hopkins Hospital, Baltimore, MD, USA

Schwannomas are benign peripheral nerve sheath tumors composed of Schwann cells, which uncommonly involve the breast. Most breast schwannomas are clinically present as a superficial palpable breast mass but may also be detected on screening mammography. Excision is the preferred treatment if symptomatic, and these are not known to recur. Histomorphology is similar to other anatomic sites: bland spindle cells with wavy nuclei, nuclear palisading (Verocay bodies), variably hypercellular (Antoni A) and hypocellular (Antoni B) areas, myxoid stroma, hyalinized vessels and variable cystic degeneration. Classic immunohistochemistry is diffuse and strong labeling for S100 and Sox10. Notable diagnostic pitfalls specific to the breast include myofibroblastoma, particularly the palisaded variant, and fascicular pseudoangiomatous stromal hyperplasia.

Keywords: Schwannoma; Breast; Peripheral nerve sheath tumor

INTRODUCTION

Schwannomas are a well-described entity in soft tissue. These are benign peripheral nerve sheath tumors, composed of Schwann cells, most commonly occur in the head, trunk, and flexor surfaces of upper and lower extremities. Less described due to their rare nature are schwannomas that occur in breast parenchyma (2.6%) or axilla (5%) [1,2]. Although they resemble those of other anatomic sites, they pose a diagnostic pitfall with other spindle cell tumors in the breast [3]. The accurate diagnosis of this neoplasm, especially on small core biopsy specimens, plays a critical role for appropriate patient management and therapeutic options.

EPIDEMIOLOGY AND PATHOGENESIS

Schwannomas most often occur in adults in the third to fifth decade of life, with equal occurrences in males and females [1]. The pathogenesis of schwannomas is not well understood, although there are several hypotheses. One hypothesis is a genetic mutation or sporadic change leads to loss of merlin, which then causes overexpression of growth factors. This leads to tumorigenesis with decreased cell cycle arrest [4]. Another hypothesis involves genetic mutation(s) causing peripheral nerves to be vulnerable to stress and injury, which leads to unregulated Schwann cell proliferation and tumorigenesis [5].

MOLECULAR FINDINGS

Most schwannomas in the breast and other anatomic sites occur sporadically (90%). The remainder of schwannomas are attributed to various genetic alterations, and multiple occurrences may also be syndromic. A well described syndrome is Carney's complex, which harbors *PRKAR1a* mutations [6], psammomatous melanotic schwannomas predominantly in the upper gastrointestinal tract and sympathetic chain, myxomas

Received: July 8, 2025 **Revised:** July 26, 2025 **Accepted:** August 11, 2025
Corresponding Author: Ashley Cimino-Mathews, MD
Departments of Pathology and Oncology, The Johns Hopkins Medical Institutions, 401 N. Broadway, Room 2242, Baltimore, MD 21231, USA
Tel: +1-410-614-6753, Fax: +1-410-614-9663, E-mail: acimino1@jhmi.edu

and Sertoli cell tumors [4]. Neurofibromin 2 (NF2)–related schwannomatosis due to alterations in *NF2* [7] presents with numerous peripheral nerve sheath tumors, unilateral vestibular schwannoma, and meningioma [6]. Other types of schwannomatosis are due to loss of heterozygosity of chromosome 22q [7], and missense and truncating mutations of *DGCR8* [6], *LZTR1* [6], and *SMARCB1* [6].

CLINICAL FEATURES AND RADIOLOGY FINDINGS

Majority of breast schwannomas present as a palpable, mobile, and nontender mass [8], although pain has been reported in some cases [9]. Breast schwannomas may also be incidentally detected on screening mammography. Using the Breast Imaging Reporting and Data System (BI-RADS), a system for standardizing mammogram reporting, these are often reported as 4A [8]. This category is considered suspicious for malignancy and is followed by an ultrasound and core biopsy [10].

On mammography, schwannomas present as a well-circumscribed, oval shaped, hyperdense nodule without microcalcifications (Fig. 1A). Ultrasound demonstrates a round/oval, well-circumscribed, homogenous, hypoechoic nodule with parallel orientation (Fig. 1B) [11,12]. Although not routinely performed, magnetic resonance imaging (MRI) is another modality to examine breast schwannomas. MRI T1 demonstrates a low signal and isointense nodule, while MRI T2 demonstrates a heterogeneous hyperintense signal with strong homogeneous contrast enhancement [13].

PROGNOSIS AND TREATMENT

Breast schwannomas are benign tumors with a favorable prognosis. Expectant management is appropriate if the lesion is stable and patient is asymptomatic. Surgical excision is recommended in cases where the lesion is growing or patient is symptomatic. There is no evidence of recurrence after excision [14].

PATHOLOGIC FINDINGS

Gross description

Schwannomas have a similar gross appearance across anatomic locations, and none are unique to the breast. These often have a tan or yellow cut surface and are well demarcated from adjacent breast stroma. Degrees of hemorrhage and cystic changes are variable [4,15]. The plexiform variant of schwannoma has a distinct multinodular architecture [4].

Frozen sections

Features on frozen section for schwannomas include a bland spindle cell proliferation with various degrees of cellularity (Fig. 2) [16,17]. Individual cells demonstrate anisonucleosis, and have wavy, elongated nuclei with tapering ends. These are arranged in parallel along the fibrillary and variably collagenous stroma. Hemosiderin deposition may also be present [17]. It is important to note that frozen artifact is often prominent, which includes cytoplasmic vacuolization and gaps between collagen. Nuclear freezing artifact may also lead to an incorrect impression of malignancy [18].

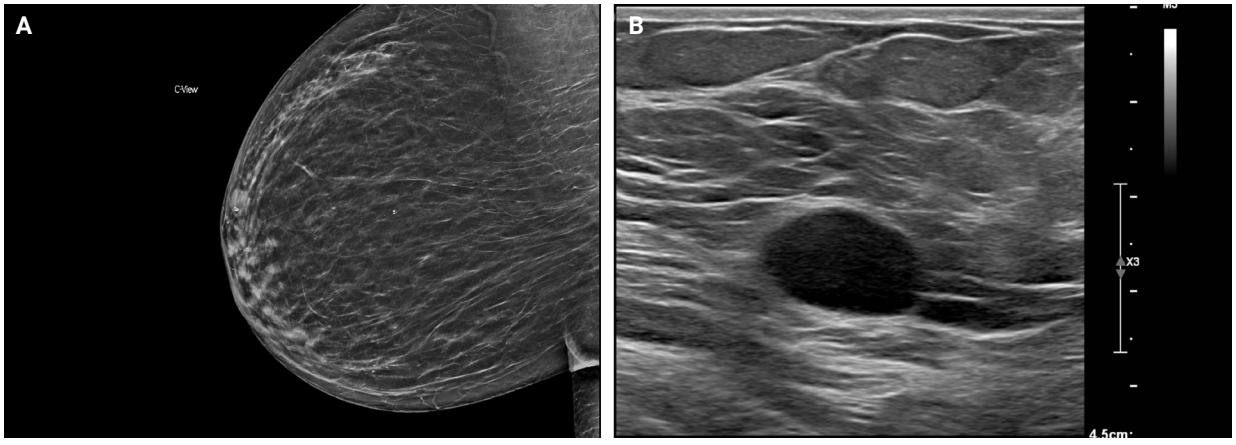

Fig. 1. Mammogram with a well-circumscribed oval mass with equal density. The arrow indicates the lesion (A). Ultrasound with an oval hypoechoic mass with well-circumscribed margins (B).

https://doi.org/10.4132/jptm.2025.08.12

Histomorphology

Microscopically, breast schwannomas are well-circumscribed or encapsulated and can have prominent nodularity (Fig. 3A). Classic schwannomas have a bland spindle cell proliferation with various degrees of anisonucleosis, and wavy, elongated nuclei with tapering ends. These are arranged in parallel rows (nuclear palisading), also known as Verocay bodies (Fig. 3B). There is an abrupt transition between hypercellular (Antoni A) and hypocellular areas (Antoni B) (Fig. 3C). Antoni B areas have loose and myxoid stroma (Fig. 4A). Other key features to schwannomas include numerous small to medium sized vessels with prominent hyalinization and thrombi inside the lumen (Fig. 4B) and may also contain areas of hemorrhage or hemosiderin deposition [3,19].

It is worthwhile to be aware of the schwannoma variants, which can cause diagnostic confusion due to the histologic variations. To briefly describe, ancient schwannomas often show degenerative atypia, calcifications, cystic degeneration and various degrees of hemorrhage [20]. Cellular schwannomas have

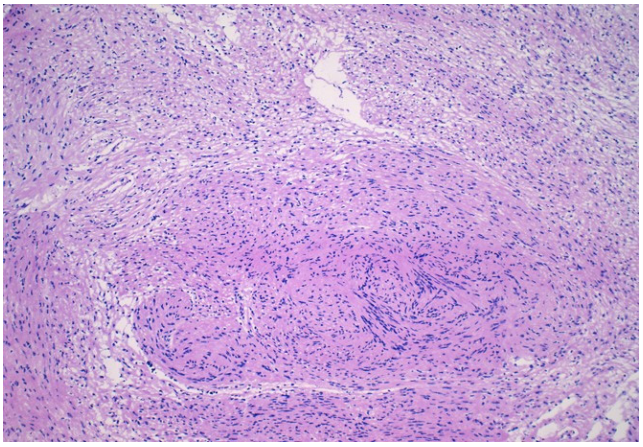

Fig. 2. Intraoperative frozen section of schwannoma demonstrating a spindle cell proliferation with Verocay bodies, and variable cellularity (Antoni A and B). Clear cell change and white gaps in tissue are due to frozen section artifact.

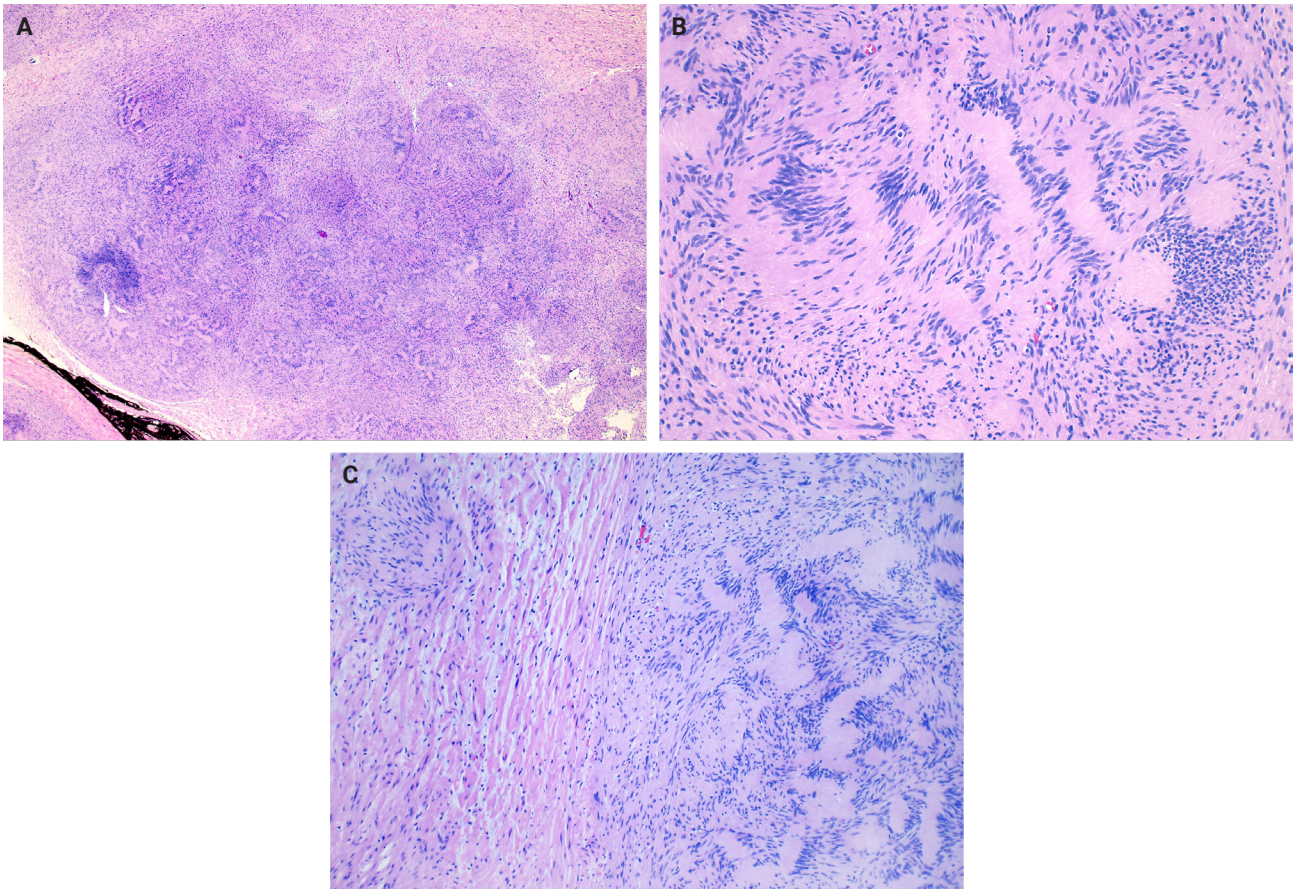

Fig. 3. Excision of breast schwannoma with nodularity (A), Verocay bodies (B), and Antoni A and B regions (C).

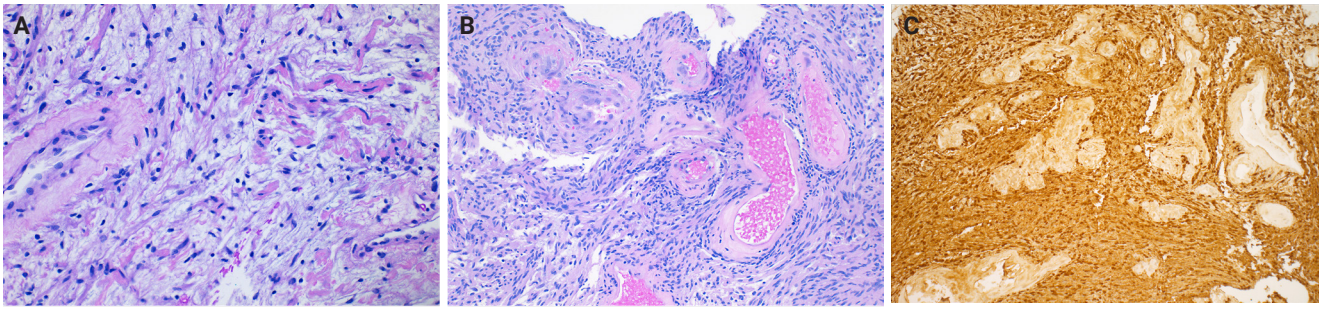

Fig. 4. Core biopsy of breast schwannoma with myxoid loose stroma (A), variably sized hyalinized vessels with intraluminal fibrin thrombi (B) and diffuse nuclear and cytoplasmic S100 reactivity in lesional Schwann cells (S100 immunohistochemistry) (C).

areas with a predominant Antoni A pattern, fascicular growth, lymphoid aggregates, increased mitotic activity and infiltrate margins [20]. Plexiform schwannomas have intraneural-nodular pattern, rare mitosis, and are less well-circumscribed [20]. Epithelioid cell schwannomas are characterized with epithelioid cells displaying abundant eosinophilic cytoplasm, nuclear pseudoinclusions and prominent nucleoli [19]. Reticular schwannoma is a rare variant that displays abundant myxoid change and microcysts [20]. The full profile of each variant is described in Table 1.

Immunohistochemistry

Immunohistochemistry is often needed to diagnose schwannomas, especially with small core tissue samples in the breast. The two most important positive stains are S100 (Fig. 4C) and SOX10, which are strong and diffuse in Schwann cells [3]. Schwannomas can also be positive for CD34 (weak, variable), calretinin, CD56, CD68 [21], podoplanin and Type IV collagen [22]. Classically, these are negative for estrogen receptor (ER), progesterone receptor, human epidermal growth factor receptor 2, smooth muscle markers (smooth muscle actin, desmin) and epithelial membrane antigen (capsule/perineurium only) [3]. Cytokeratins are generally negative, but may have rare labeling [23].

Cytomorphology

Fine needle aspiration (FNA) of breast masses is performed worldwide, but less often in the United States, where core needle biopsy (CNB) is most utilized. Cytomorphologic features of schwannoma are similar to those of other anatomic sites. These include Antoni A areas with cohesive fascicles with variable cellularity, dense fibrillary matrix, and Verocay bodies. Antoni B areas have short spindle/wavy cells, myxoid background and

Table 1. Schwannoma variants and key morphologic differences [19]

Schwannoma variant	Morphologic features
Ancient schwannoma	Degenerative atypia
	Cystic degeneration
	Hemorrhage
	Calcifications
	Stromal hyalinization
	Frequent histiocytes and macrophages
Cellular schwannoma	Predominantly Antoni A pattern
	<10% of total tumor Antoni B area
	Fascicular growth pattern
	Foamy histiocyte aggregates
	Lymphoid aggregates
	Increased mitotic activity (usually <4–5 mitoses/10 HPFs)
	Coagulative necrosis (up to 10% of cases)
	Infiltrative margins
Plexiform schwannoma	Intraneural-nodular pattern
	Predominantly Antoni A pattern
	Absent to rare mitosis
	Less well-circumscribed
	Capsule may be absent
	Associated with NF2-related schwannomatosis
Epithelioid cell schwannoma	Epithelioid cells: abundant eosinophilic cytoplasm, nuclear pseudoinclusions, prominent nucleoli
	Fibro-myxoid stroma
	Can have nuclear atypia
Reticular schwannoma	Abundant myxoid change
	Microcysts
	Rare variant
Other rare features	Neuroblastoma-like schwannoma
	Pseudoglandular structures
	Lipoblastic differentiation

HPF, high power field; NF2, neurofibromin 2.

https://doi.org/10.4132/jptm.2025.08.12

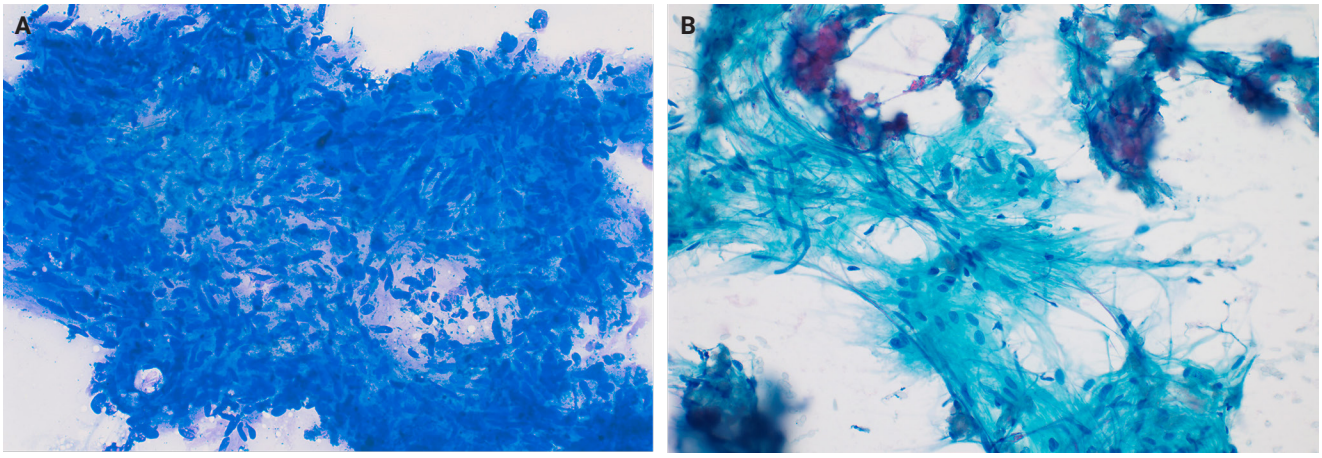

Fig. 5. Fine needle aspiration of schwannoma with hypercellular, cohesive fragments of bland spindled cells (Diff-Quik) (A) and delicate fibrillary cytoplasm in fibrous stroma (Pap stain) (B).

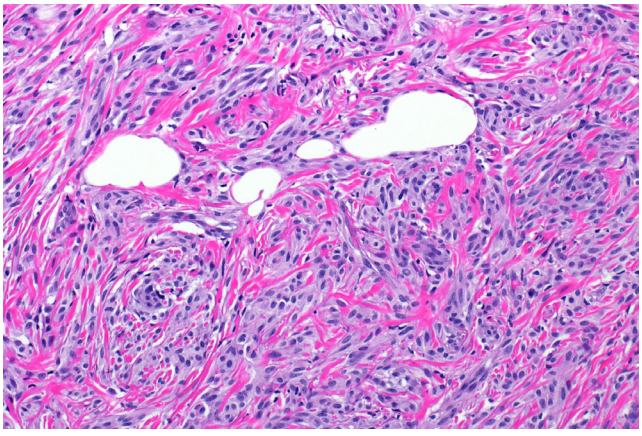

Fig. 6. Resection of myofibroblastoma with classic features, including bland spindled cells with an amphophilic cytoplasm, dense eosinophilic collagen bundles and admixed adipocytes.

microcysts (Fig. 5A, B). It is important to note the limitations for utilizing FNA to diagnose schwannomas. These specimens often have low diagnostic sensitivity (0%–40%), and are often unsatisfactory due to prominent cystic change, dense stroma, and hypocellular areas. CNB has now gained acceptance as a complementary method to FNA, which provides tissue for immunohistochemical studies [24].

Differential diagnosis

The differential for schwannomas is similar to other anatomic sites, including neurofibroma, neuroma, leiomyoma, nodular fasciitis, desmoid-type fibromatosis, malignant peripheral nerve sheath tumor, melanoma and dermatofibrosarcoma protuberans. However, it is important to note additional differential diagnoses particularly relevant in the breast.

Myofibroblastoma with classic features has bland spindle cells with amphophilic cytoplasm and bright eosinophilic collagen bundles and admixed adipocytes (Fig. 6). However, the palisaded variant has spindle cells with nuclear palisading and alternating cellularity, which resembles Verocay bodies and Antoni A and B regions, respectively (Fig. 7A). These may also contain gaping, hyalinized blood vessels (Fig. 7B), cystic degeneration, and myxoid stroma. On the contrary with schwannomas, myofibroblasts have strong nuclear immunoreactivity for ER (Fig. 7C) and membranous CD34 (Fig. 7D) [25,26]. Fibroepithelial neoplasms (fibroadenoma and phyllodes tumor) may contain stromal fascicular pseudoangiomatous stromal hyperplasia (PASH)–like pattern with nuclear palisading (Fig. 8A). The lesional myofibroblasts may display elongated nuclei with palisading, resembling Verocay bodies of schwannoma (Fig. 8B) [3]. Fibromatosis-like metaplastic carcinoma is infiltrative, with fascicles of spindled cells displaying only mild to moderate cytologic atypia, including hyperchromasia and increased mitotic activity [3]. This entity is positive for a broad spectrum of cytokeratins, while schwannomas only have rare labeling [23]. PASH is hormone-dependent, which leads to an increase in stromal myofibroblasts which dissect through dense stroma. The myofibroblasts are spindled in morphology with tapering ends and occasionally wavy nuclei. Fascicular PASH has increased stromal cellularity with nuclear palisading, which overlaps in morphology with schwannoma [3]. A summary of key differentiating features of these entities is described in Table 2.

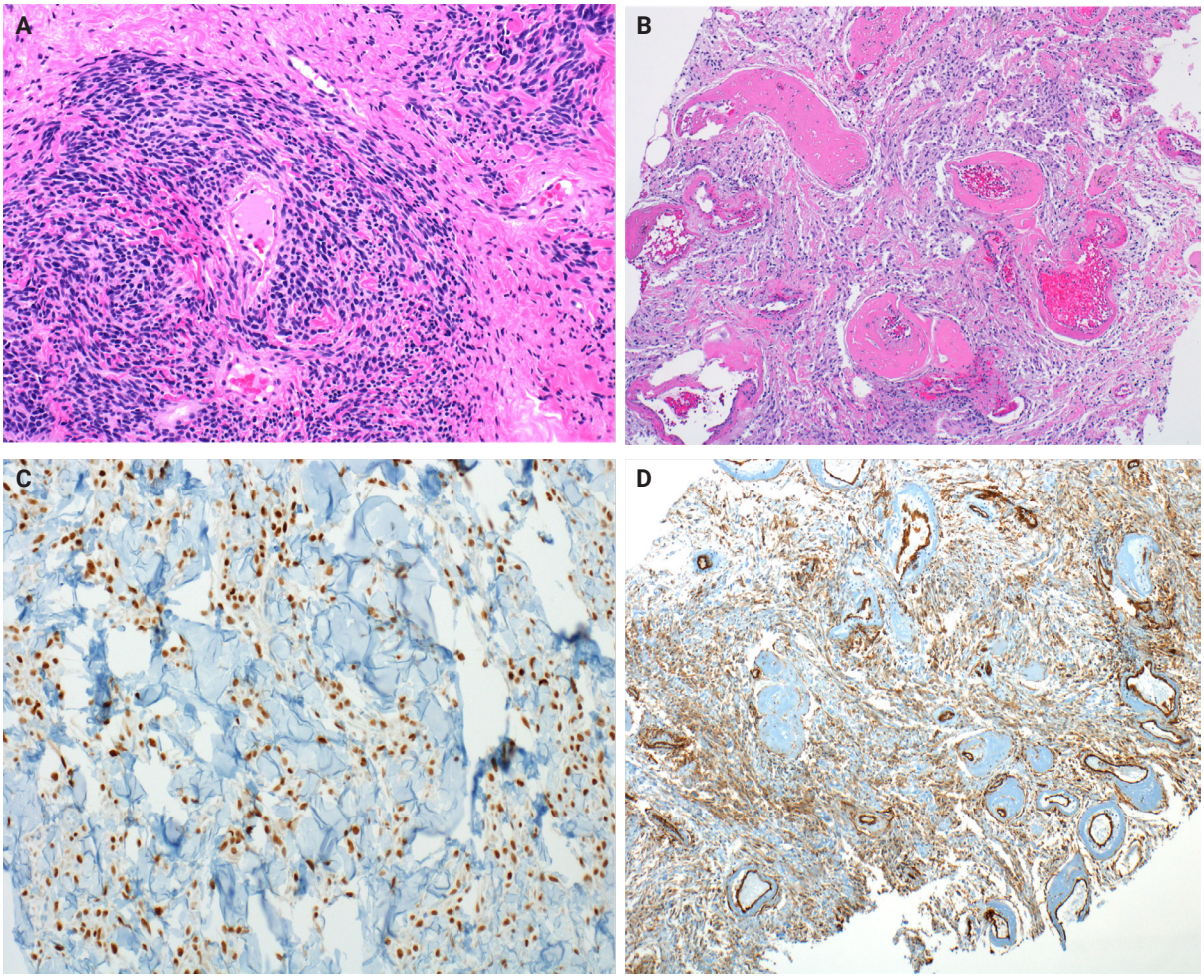

Fig. 7. Resection of myofibroblastoma, palisading variant, with hyper- and hypocellular areas (A), hyalinized and variably dilated vessels (B), myofibroblasts with diffuse estrogen receptor (ER) nuclear positivity (ER immunohistochemistry) (C) and myofibroblasts with diffuse membranous CD34 positivity (CD34 immunohistochemistry) (D).

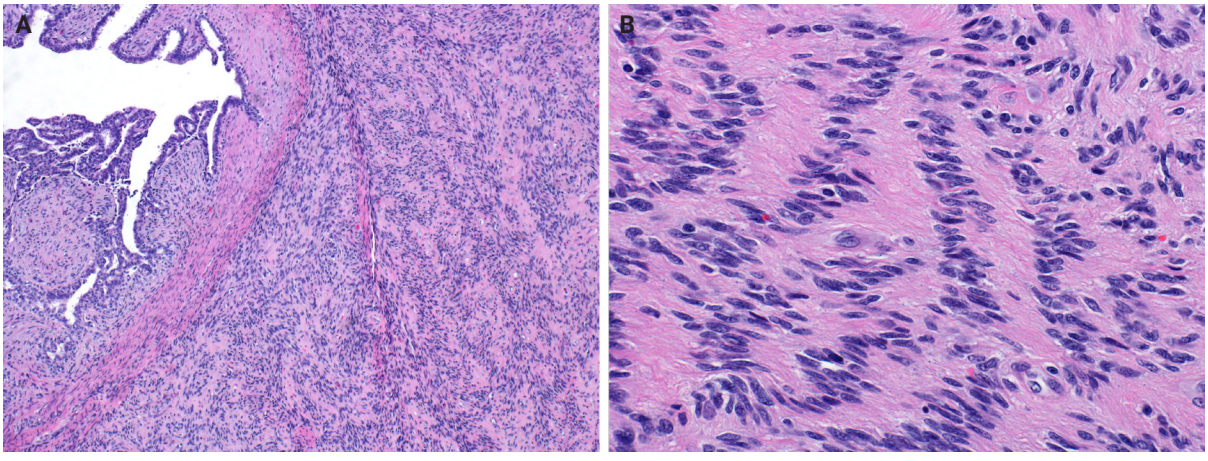

Fig. 8. Resection of breast borderline phyllodes tumor with benign epithelial leaf-like architecture and abrupt transition to cellular stroma (A) and myofibroblasts with elongated nuclei with palisading and ribbon-like architecture, resembling Verocay bodies (B).

https://doi.org/10.4132/jptm.2025.08.12

Table 2. Mimicker neoplasms of breast schwannoma and differentiating features

Differential diagnosis	Histologic features	Immunohistochemistry
Myofibroblastoma, palisaded variant	Admixed adipocytes Brightly eosinophilic, keloidal-like collagen bundles	Positive: CD34, ER; smooth muscle markers (SMA, desmin, calponin; variable) Negative: S100, SOX10
Pseudoangiomatous stromal hyperplasia (PASH)	Forms slit-like spaces mimicking vascular spaces Appears infiltrative due to involvement of intralobular and extralobular stroma	Positive: CD34, ER, PR, smooth muscle markers (SMA, desmin, calponin; variable) Negative: S100, SOX10
Fibroepithelial neoplasm (fibroadenoma and phyllodes tumor)	Benign epithelial component with intracanalicular, peri-canalicular, or leaf-like architecture Infiltrative growth	Positive: CD34 (variable), smooth muscle markers (SMA, desmin, calponin; variable) Negative: S100, SOX10
Fibromatosis-like metaplastic carcinoma	Widely infiltrative Brightly eosinophilic keloidal-like collagen Associated low-grade adenosquamous carcinoma	Positive: cytokeratins (AE1/AE3, 34betaE12, OSCAR; variable), p63 Negative: S100, SOX10

ER, estrogen receptor; SMA, smooth muscle actin; PR, progesterone receptor.

CONCLUSION

Breast schwannomas have similar histologic features and immunophenotype as other anatomic sites. However, as with other breast spindle cell neoplasms, these can be particularly challenging on limited core biopsy material. Understanding histologic distinctions between the differential diagnoses and utilizing a selective immunohistochemical panel is key for classification of breast schwannomas.

Ethics Statement
Not applicable.

Availability of Data and Material
All data generated or analyzed during the study are included in this published article (and its supplementary information files).

Code Availability
Not applicable.

ORCID
Sandra Ixchel Sanchez https://orcid.org/0000-0003-1866-1619
Ashley Cimino-Mathews https://orcid.org/0000-0002-0638-7969

Author Contributions
Writing—original draft preparation: SIS, ACM. Writing—review & editing: SIS, ACM. Approval of final manuscript: all authors.

Conflicts of Interest
The authors declare that they have no potential conflicts of interest.

Funding Statement
No funding to declare.

REFERENCES

1. Aref H, Abizeid GA. Axillary schwannoma, preoperative diagnosis on a tru-cut biopsy: case report and literature review. Int J Surg Case Rep 2018; 52: 49-53.
2. Dialani V, Hines N, Wang Y, Slanetz P. Breast schwannoma. Case Rep Med 2011; 2011: 930841.
3. White MJ, Cimino-Mathews A. Diagnostic approach to mesenchymal and spindle cell tumors of the breast. Adv Anat Pathol 2024; 31: 411-28.
4. Hilton DA, Hanemann CO. Schwannomas and their pathogenesis. Brain Pathol 2014; 24: 205-20.
5. Helbing DL, Schulz A, Morrison H. Pathomechanisms in schwannoma development and progression. Oncogene 2020; 39: 5421-9.
6. Dhamija R, Plotkin S, Gomes A, Babovic-Vuksanovic D. LZTR1- and SMARCB1-related schwannomatosis. In: Adam MP, Feldman J, Mirzaa GM, et al., eds. GeneReviews [Internet]. Seattle: University of Washington, 2024 [cited 2025 Mar 10]. Available from: https://www.ncbi.nlm.nih.gov/books/NBK487394/.
7. Goetsch Weisman A, Weiss McQuaid S, Radtke HB, Stoll J, Brown B, Gomes A. Neurofibromatosis- and schwannomato-

sis-associated tumors: approaches to genetic testing and counseling considerations. Am J Med Genet A 2023; 191: 2467-81.
8. Parikh Y, Sharma KJ, Parikh SJ, Hall D. Intramammary schwannoma: a palpable breast mass. Radiol Case Rep 2016; 11: 129-33.
9. Kang YJ, Woo OH, Kim A. Nipple schwannoma: a case report and literature review on nipple mass. J Breast Cancer 2024; 27: 72-7.
10. Barazi H, Gunduru M. Mammography BI RADS grading. StatPearls [Internet]. Treasure Island: StatPearls Publishing, 2023 [cited 2025 Mar 10]. Available from: https://www.ncbi.nlm.nih.gov/books/NBK539816/.
11. Uchida N, Yokoo H, Kuwano H. Schwannoma of the breast: report of a case. Surg Today 2005; 35: 238-42.
12. Bellezza G, Lombardi T, Panzarola P, Sidoni A, Cavaliere A, Giansanti M. Schwannoma of the breast: a case report and review of the literature. Tumori 2007; 93: 308-11.
13. Duehrkoop M, Frericks B, Ankel C, Boettcher C, Hartmann W, Pfitzner BM. Two case reports: breast schwannoma and a rare case of an axillary schwannoma imitating an axillary lymph node metastasis. Radiol Case Rep 2021; 16: 2154-7.
14. Lee HS, Jung EJ, Kim JM, et al. Schwannoma of the breast presenting as a painful lump: a case report. Medicine (Baltimore) 2021; 100: e27903.
15. Ashoor A, Lissidini G, Girardi A, Mirza M, Baig MS. Breast Shwannoma: time to explore alternative management strategy? Ann Diagn Pathol 2021; 54: 151773.
16. Kim C, Chung YG, Jung CK. Diagnostic conundrums of schwannomas: two cases highlighting morphological extremes and diagnostic challenges in biopsy specimens of soft tissue tumors. J Pathol Transl Med 2023; 57: 278-83.
17. Fujita H, Tajiri T, Machida T, et al. Scoring system for intraoperative diagnosis of intracranial schwannoma by squash cytology. Cytopathology 2022; 33: 196-205.
18. Tihan T. Schwannoma. In: Adesina A, Tihan T, Fuller C, Poussaint T, eds. Atlas of pediatric brain tumors. New York: Springer, 2010; 145-52.
19. Magro G, Broggi G, Angelico G, et al. Practical approach to histological diagnosis of peripheral nerve sheath tumors: an update. Diagnostics (Basel) 2022; 12: 1463.
20. Rodriguez FJ, Folpe AL, Giannini C, Perry A. Pathology of peripheral nerve sheath tumors: diagnostic overview and update on selected diagnostic problems. Acta Neuropathol 2012; 123: 295-319.
21. Park JY, Park H, Park NJ, Park JS, Sung HJ, Lee SS. Use of calretinin, CD56, and CD34 for differential diagnosis of schwannoma and neurofibroma. Korean J Pathol 2011; 45: 30-5.
22. Vijai R, Kumar JR, Arihanth R, Prabu M, Bharath N, Rahman K, et al. Schwannomas: atypical presentation and challenges. Case Rep Clin Med 2019; 8: 93-8.
23. Fanburg-Smith JC, Majidi M, Miettinen M. Keratin expression in schwannoma; a study of 115 retroperitoneal and 22 peripheral schwannomas. Mod Pathol 2006; 19: 115-21.
24. Ahn D, Lee GJ, Sohn JH, Jeong JY. Fine-needle aspiration cytology versus core-needle biopsy for the diagnosis of extracranial head and neck schwannoma. Head Neck 2018; 40: 2695-700.
25. Laforga JB, Escandon J. Schwannoma-Like (Palisaded) myofibroblastoma: a challenging diagnosis on core biopsy. Breast J 2017; 23: 354-6.
26. Magro G, Foschini MP, Eusebi V. Palisaded myofibroblastoma of the breast: a tumor closely mimicking schwannoma: report of 2 cases. Hum Pathol 2013; 44: 1941-6.

https://doi.org/10.4132/jptm.2025.08.12

JPTM

ORIGINAL ARTICLE

pISSN 2383-7837 · eISSN 2383-7845

Journal of Pathology and Translational Medicine 2025; 59: 361-370
https://doi.org/10.4132/jptm.2025.07.07

Characterization of undifferentiated carcinoma of the salivary gland: clinicopathological and immunohistochemical analyses in comparison with lymphoepithelial carcinoma

Sangjoon Choi[1], Gyuheon Choi[2], Hee Jin Lee[3], Joon Seon Song[3], Yoon Se Lee[4], Seung-Ho Choi[4], Kyung-Ja Cho[3]

[1]Pathology Center, Shinwon Medical Foundation, Gwangmyeong, Korea
[2]Department of Pathology, Samkwang Medical Laboratories, Seoul, Korea
[3]Department of Pathology, Asan Medical Center, University of Ulsan College of Medicine, Seoul, Korea
[4]Department of Otolaryngology, Asan Medical Center, University of Ulsan College of Medicine, Seoul, Korea

Graphical abstract

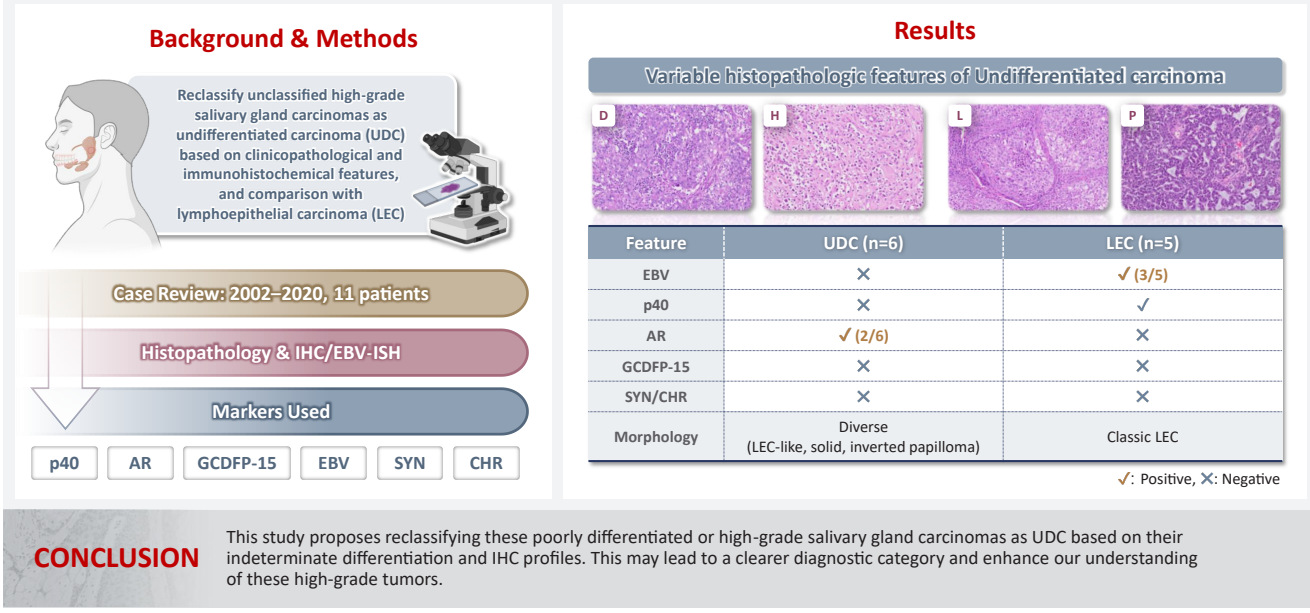

JPTM

ORIGINAL ARTICLE

pISSN 2383-7837 · eISSN 2383-7845

Journal of Pathology and Translational Medicine 2025; 59: 361-370
https://doi.org/10.4132/jptm.2025.07.07

Characterization of undifferentiated carcinoma of the salivary gland: clinicopathological and immunohistochemical analyses in comparison with lymphoepithelial carcinoma

Sangjoon Choi[1], Gyuheon Choi[2], Hee Jin Lee[3], Joon Seon Song[3], Yoon Se Lee[4], Seung-Ho Choi[4], Kyung-Ja Cho[3]

[1]Pathology Center, Shinwon Medical Foundation, Gwangmyeong, Korea
[2]Department of Pathology, Samkwang Medical Laboratories, Seoul, Korea
[3]Department of Pathology, Asan Medical Center, University of Ulsan College of Medicine, Seoul, Korea
[4]Department of Otolaryngology, Asan Medical Center, University of Ulsan College of Medicine, Seoul, Korea

Background: This study aimed to reclassify a subset of poorly differentiated salivary gland carcinoma that do not conform to any entities of the current World Health Organization (WHO) classification into the category of undifferentiated carcinoma (UDC) because they lack specific histologic differentiation or immunophenotype. **Methods:** Cases of salivary gland carcinomas from Asan Medical Center (2002–2020) that did not fit any existing WHO classification criteria and were diagnosed as poorly differentiated carcinoma, high-grade carcinoma, or UDC, were retrospectively reviewed. Immunohistochemical (IHC) staining for p40, neuroendocrine markers, androgen receptor (AR), and gross cystic disease fluid protein 15 (GCDFP-15) and Epstein-Barr virus (EBV) in situ hybridization (ISH) were performed. Clinical data were collected from the electronic medical records. **Results:** Six salivary gland carcinomas did not align with any specific entities and lacked distinct differentiation. Two of six cases displayed lymphoepithelial carcinoma (LEC)-like morphology but were negative or showed negligible immunoreactivity for p40 and EBV ISH, distinguishing them from LEC of the salivary gland. Two cases showed strong AR positivity, suggesting a potential overlap with salivary duct carcinoma (SDC) but lacked classic SDC morphologies and GCDFP-15 expression. No cases expressed neuroendocrine markers. **Conclusions:** This study proposes reclassifying these poorly differentiated or high-grade salivary gland carcinomas as UDC based on their indeterminate differentiation and IHC profiles. This may lead to a clearer diagnostic category and enhance our understanding of these high-grade tumors.

Keywords: Salivary glands; Carcinoma, undifferentiated; Carcinoma, poorly differentiated; Carcinoma, lymphoepithelial

INTRODUCTION

Malignant salivary gland neoplasms are rare, constituting approximately 6% of head and neck tumors [1]. They are categorized into unique subgroups based on their distinct histomorphology, immunoprofiles, and molecular alterations [2]. However, a subset of poorly differentiated tumors does not meet the current diagnostic criteria established by the World Health Organization (WHO) classification of head and neck tumors.

Poorly differentiated carcinomas (PDCs) of the salivary glands, which was defined as primary carcinomas showing large and small cell types with or without neuroendocrine differentiation in the 4th edition of the WHO classification of head and neck tumors, were removed in the 5th edition [2,3]. This disease entity included undifferentiated carcinoma (UDC),

Received: May 3, 2025 **Revised:** June 19, 2025 **Accepted:** July 7, 2025
Corresponding Author: Kyung-Ja Cho, MD
Department of Pathology, Asan Medical Center, University of Ulsan College of Medicine, 88 Olympic-ro 43-gil, Songpa-gu, Seoul 05505, Korea
Tel: +82-2-3010-4560, Fax: +82-2-472-7898, E-mail: kjc@amc.seoul.kr

large-cell neuroendocrine carcinoma, and small-cell neuroendocrine carcinoma.

In recent years, we have encountered several malignant salivary gland tumors that cannot be classified into specific entities based on the WHO classification, prompting a thorough review of our archival cases. The tumor cells of these cases displayed variable histological features; however, some cases were similar to UDC of other head and neck sites and accompanied by abundant lymphoplasmacytic infiltration around the tumor, resembling lymphoepithelial carcinoma (LEC) of the salivary gland. These cases were initially diagnosed as PDC, high-grade carcinoma (HGC), or UDC. This study aimed to redefine these unclassified tumors through a comprehensive investigation of their clinicopathological and immunohistochemical (IHC) features, particularly in comparison with LEC.

MATERIALS AND METHODS

Patient selection

The cases were reviewed and selected from the computerized database of the Asan Medical Center from January 2002 to December 2020, using the search terms "poorly differentiated carcinoma," "high-grade carcinoma," "undifferentiated carcinoma," and "lymphoepithelial carcinoma." We collected the clinical information of the patients using electronic medical records, including age at diagnosis, sex, tumor location, surgical and adjuvant treatments, postoperative recurrence and metastasis, progression-free survival, and overall survival (OS).

Histopathological analysis

All available hematoxylin and eosin-stained slides were thoroughly reviewed by two board-certified pathologists (S.C. and K.-J.C.). Histopathological data including tumor morphology and architectural patterns, largest dimension of the tumor, extension to extraparenchymal soft tissues, lymphovascular and perineural invasion, metastasis to the lymph nodes, and extranodal extension status were collected. The most representative slides were selected for IHC and in situ hybridization (ISH) studies.

IHC staining

Tissue microarrays were constructed from the formalin-fixed paraffin-embedded blocks for IHC and ISH analysis. Three 2-mm cores of tumor-rich areas were selected from each block. IHC staining was performed using an OptiView DAB IHC Detection Kit on a BenchMark XT automatic immunostaining device (Ventana Medical Systems, Inc., Tucson, AZ, USA) according to the manufacturer's instructions. After antigen retrieval, the slides were incubated with three antibodies: p40 (1:4, mouse monoclonal, clone BC28, catalog No., Ventana Medical Systems, Inc.), androgen receptor (AR; prediluent, rabbit monocloncal, clone SP107, catalog No. 760-4605, Ventana Medical Systems, Inc.), gross cystic disease fluid protein 15 (GCDFP-15; 1:50, clone 23A3, Neomarkers Inc., Fremont, CA, USA), synaptophysin (1:100, rabbit monoclonal, clone MRQ-40, catalog No. 336R-96, Cell Marque, Rocklin, CA, USA), chromogranin (1:1,600, mouse monoclonal, clone DAK-A3, catalog No. M0869, Dako, Glostrup, Denmark), cytokeratin 7 (CK-7; 1:400, Dako), and p63 (1:200, Dako).

Epstein-Barr virus ISH

Epstein-Barr virus (EBV) detection was performed on paraffin sections using the BenchMark XT automatic immunostaining device (Ventana Medical Systems, Inc.) according to the manufacturer's instructions, as previously described [4]. Sections were visualized by Ventana EBV ISH iView Blue Detection Kit (catalog No. 800-092, Ventana Medical Systems, Inc.) and INFORM EBV probe (catalog No. 800-2842, Ventana Medical Systems, Inc.). The sections that exhibited strong nuclear signals of the tumor cells were considered positive.

RESULTS

Identification and classification

For over 19 years, a total of six patients were diagnosed with PDC, HGC, or UDC of the salivary gland, and five patients were diagnosed with LEC of the salivary gland. The clinicopathological characteristics and IHC and ISH results of the six PDC, HGC, and UDCs and five LEC cases are summarized in Fig. 1. PDC, HGC, and UDCs were distinguished from LEC by negative p40 IHC and EBV ISH.

Clinical characteristics

Table 1 summarizes the clinical characteristics of 11 patients. The patients with PDC, HGC, and UDC were between 45 and 74 years old (median, 67 years). Four patients were male, and two were female. Four tumors were located in the submandibular gland, and two were identified in the parotid gland. All patients underwent resection (parotidectomy or wide excision) with neck lymph node dissection. After surgery, three of five

https://doi.org/10.4132/jptm.2025.07.07

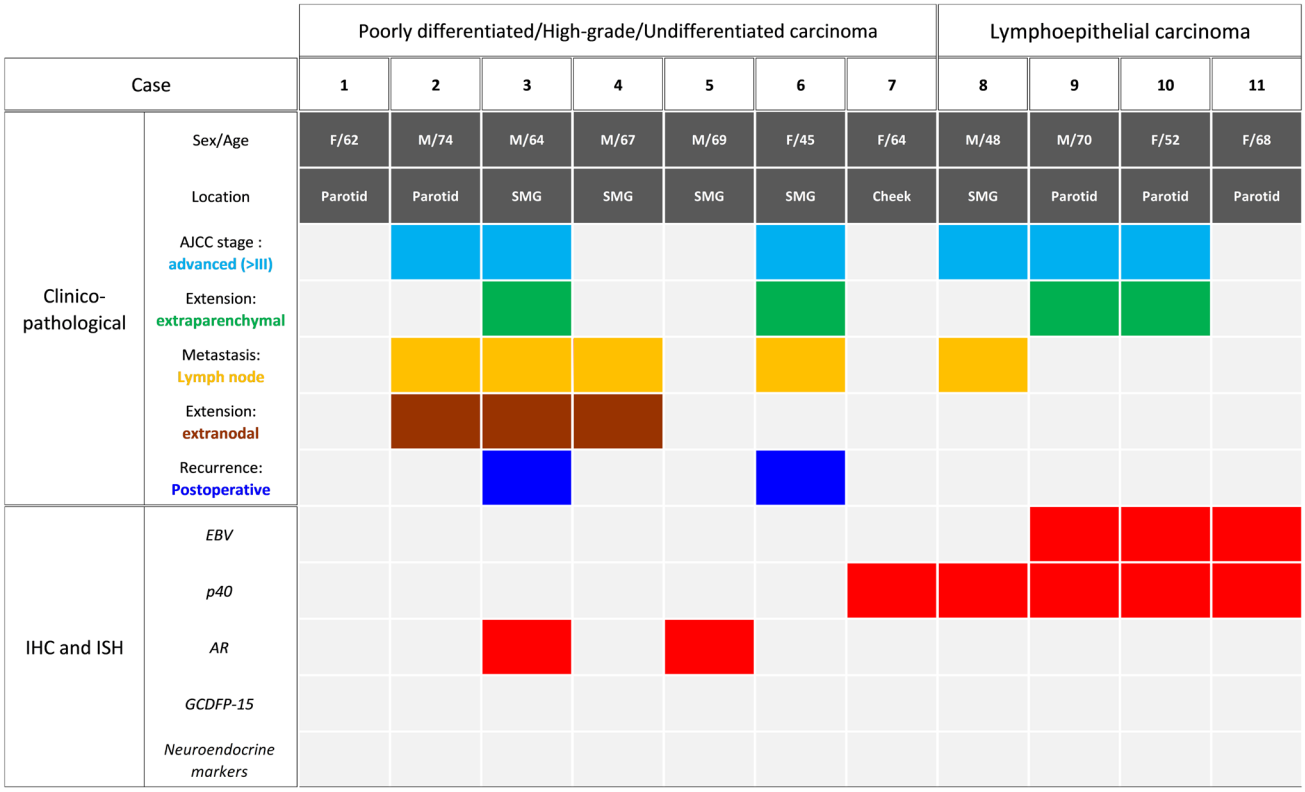

Fig. 1. Summary of the clinicopathological and immunohistochemical characteristics of poorly differentiated carcinoma and lymphoepithelial carcinoma of the salivary gland. The gray boxes represent the absence of clinicopathological findings or negative immunostaining, whereas colored boxes (sky blue, green, yellow, brown, blue, and red) represent the presence of clinicopathological findings or positive immunostaining. SMG, submandibular gland; AJCC, American Joint Committee on Cancer; IHC, immunohistochemistry; ISH, in situ hybridization; EBV, Epstein-Barr virus; AR, androgen receptor; GCDFP-15, gross cystic disease fluid protein 15.

Table 1. Clinical characteristics

Case No.	Initial diagnosis	Sex	Age (yr)	Tumor location	Surgical treatment	Adjuvant treatment	Postoperative recurrence	DFS (mo)	Current status	OS (mo)
1	PDC	F	62	Parotid	Parotidectomy with neck dissection	RT	None	139	FU loss	139
2	HGC	M	74	Parotid	Parotidectomy with neck dissection	RT	None	42	Dead	42
3	UC	M	64	Submandibular	Excision with modified neck dissection	CCRT	Present	5	Dead	15
4	UC	M	67	Submandibular	Excision with neck dissection	Not done	NA	6	FU loss	6
5	PDC	M	69	Submandibular	Wide excision with modified radical neck dissection	RT	None	107	Alive	107
6	PDC	F	45	Submandibular	Resection	CCRT	Present	12	Dead	19
7	LEC	F	64	Cheek	Wide excision with neck dissection	RT	None	61	FU loss	61
8	LEC	M	48	Submandibular	Excision	Not done	None	258	Alive	258
9	LEC	M	70	Parotid	Parotidectomy with left neck dissection	RT	None	93	Alive	93
10	LEC	F	52	Parotid	Parotidectomy	Not done	None	110	Alive	110
11	LEC	F	68	Parotid	parotidectomy and selective neck dissection	Not done	None	34	Alive	34

DFS, disease-free survival; OS, overall survival; PDC, poorly differentiated carcinoma; RT, radiation therapy; FU, follow-up; HGC, high-grade carcinoma; UC, undifferentiated carcinoma; CCRT, concurrent chemoradiation therapy; NA, not available; LEC, lymphoepithelial carcinoma.

patients received adjuvant concurrent chemoradiation therapy and two received radiation therapy. Local or metastatic recurrence developed in the surgical bed or lymph nodes of two patients. The disease-free survival (DFS) ranged from 5 to 139 (mean, 51.8) months, and the OS ranged from 6 to 139 (mean, 54.7) months. Three patients are currently alive, with a mean follow-up period of 84 months.

Patients with LEC were between 48 and 70 years old (median, 64 years), and two were male and three were female. Tumors were located in the parotid gland (3/5), submandibular gland (1/5), and minor salivary gland of cheek (1/5). All patients underwent surgery with or without lymph node dissection. Two patients received postoperative radiation therapy. No patient experienced local tumor recurrence or distant metastasis postoperatively. The DFS and OS ranged from 34 to 258 (mean, 111.2) months. Currently, four patients are alive, and one patient was lost to follow-up.

Pathological characteristics

Table 2 shows pathological characteristics of PDC, HGC, UDC, and LECs. Gross observation of PDC, HGC, and UDCs revealed relatively well-defined, round-to-ovoid, nodular masses. One tumor (case 5) revealed ill-defined, irregular-shaped mass. The cut surfaces of the tumors appeared white or gray-tan and were firm. The greatest dimension of the tumors ranged from 21 to 50 mm (mean, 36.2 mm). Two tumors invaded the extraparenchymal soft tissue. Four cases had neck lymph node metastases with extranodal extension.

In LEC, tumors were grossly well-circumscribed, ovoid, and lobulated, with firm, tan-white cut surfaces. The greatest dimension of the tumors ranged from 17 to 35 (mean, 23.4 mm). Two tumors exhibited extraparenchymal extension. Regional lymph node metastases were found in one patient, with extranodal extension.

PDC, HGC, and UDC cases had diverse histological features

Table 2. Pathological characteristics with IHC and ISH results

Case No.	Pathological characteristic					IHC and ISH										
	Initial Dx	Final Dx	Histology	Gross	Tumor size (mm)	EPE	LVI	PNI	LN mets (mm)	ENE	p40	AR	GCD-FP-15	SYN, CHR	EBV	Others
1	PDC	UC	LEC-like	Well-defined ovoid	21	–	–	–	–	NA	–	–	–	–	–	CK7 +
2	HGC	UC	LEC-like	Well-defined ovoid	21	–	–	–	+ (3 mm)	+	–	–	–	–	–	CK7 +
3	UC	UC	Poorly cohesive	Well-defined irregular	30	+	+	–	+ (10 mm)	+	–	+	–	–	–	CK7 –
4	UC	UC	Solid with geographic necrosis	Well-defined lobulated	50	–	+	–	+ (31 mm)	+	–	–	–	–	–	NA
5	PDC	UC	Inverted papilloma-like	Ill-defined irregular	50	–	–	–	–	NA	–	+	–	–	–	CK7 + p63 –
6	PDC	UC	Multiphenotypic	Well-defined ovoid	45	+	+	+	+ (30 mm)	NA[a]	NA	NA	NA	–	–	p63 –
7	LEC	LEC	LEC	Well-defined ovoid	35	–	–	–	–	NA	+	–	–	–	–	NA
8	LEC	LEC	LEC with SQ differentiation	Ill-defined irregular	25	–	–	–	+ (47 mm)	–	+, focal	–	–	–	–	NA
9	LEC	LEC	LEC	Well-defined ovoid	25	+	–	–	–	NA	+, focal	–	–	–	+	NA
10	LEC	LEC	LEC	Well-defined irregular	15	+	–	–	–	NA	+	–	–	–	+	NA
11	LEC	LEC	LEC	Ill-defined lobulated	17	–	–	–	–	NA	+	–	–	–	+	NA

IHC, immunohistochemistry; ISH, in situ hybridization; Dx, diagnosis; EPE, extraparenchymal extension; LVI, lymphovascular invasion; PNI, perineural invasion; LN, lymph node; ENE, exranodal extension; AR, androgen receptor; GCDFP-15, gross cystic disease fluid protein 15; SYN, synaptophysin; CHR, chromogranin; EBV, Epstein-Barr virus; PDC, poorly differentiated carcinoma; UC, undifferentiated carcinoma; LEC, lymphoepithelial carcinoma; NA, not available; CK7, cytokeratin 7; HGC; high-grade carcinoma; SQ, squamous.

[a]Extranodal extension status could not be determined due to lack of documentation in the outside surgical pathology report.

https://doi.org/10.4132/jptm.2025.07.07

(Fig. 2). In cases 1 and 2, tumors displayed LEC-like features, in which variable-sized clusters and sheets of the tumor cells were irregularly infiltrating into the adjacent stroma and arranged in a syncytial pattern without distinct cell borders. The tumor cells were predominantly comprised polygonal or ovoid epithelial cells and possessed abundant clear to eosinophilic cytoplasm and large nuclei with conspicuous nucleoli. Variable amounts of inflammatory cells, particularly lymphoplasmacytic infiltrates present in intratumoral and peritumoral stromal areas. The mitotic activity was increased and easily identified on low-power examination. Keratinization or intercellular bridges of tumor cells indicating squamous differentiation was not observed.

In case 3, the tumor was predominantly composed of poorly cohesive cells without any remarkable differentiation. The tumor cells exhibited moderate nuclear pleomorphism with irregular nuclear membrane and hyperchromatic chromatin. Atypical mitosis and tumor necrosis were frequently detected. The degree of stromal lymphoplasmacytic infiltration was lower than those in other PDCs.

Case 4 was characterized by solid sheets of tumor cells with geographic necrosis. The tumor exclusively showed a solid arrangement without other organoid patterns. Large tumor cell

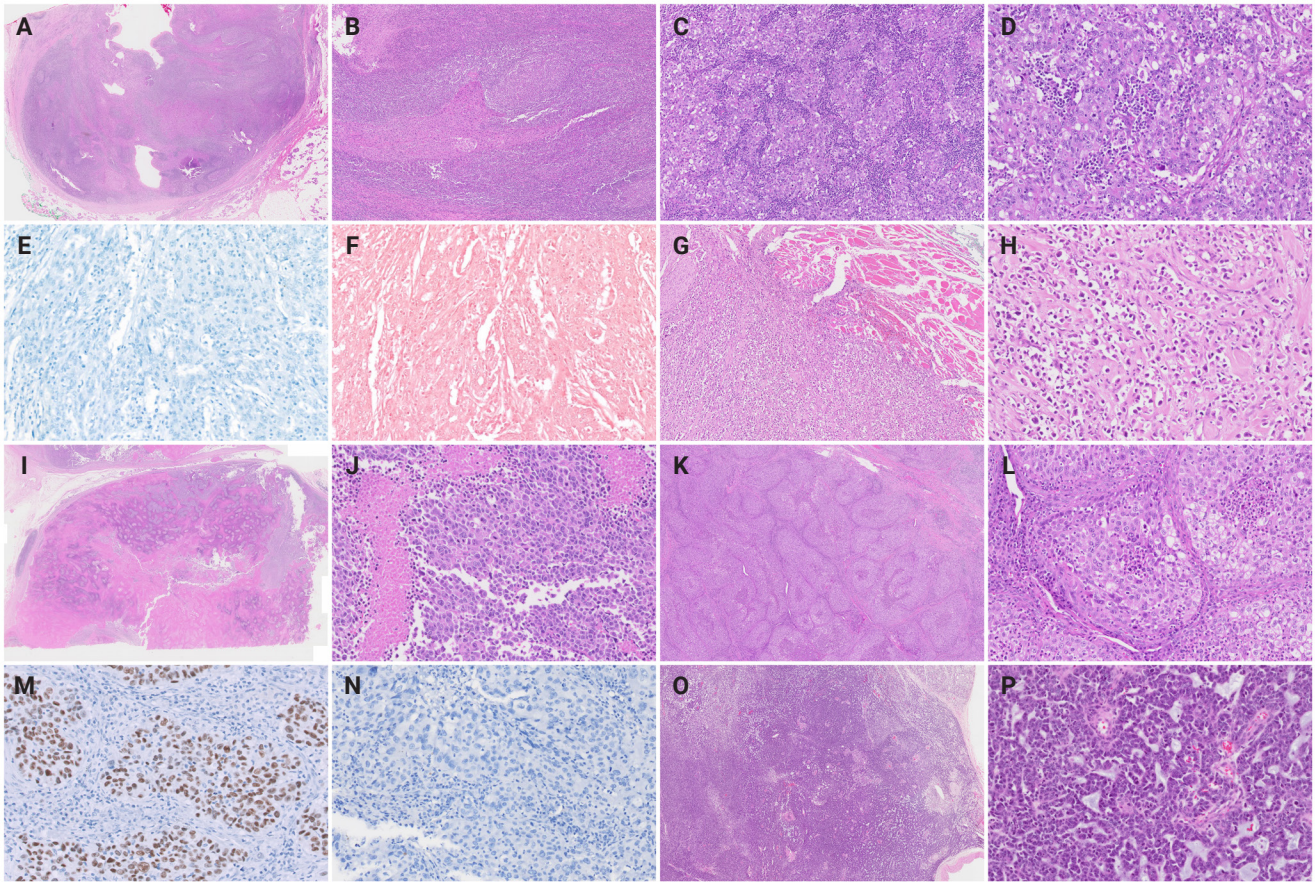

Fig. 2. Histopathological findings of poorly differentiated carcinomas with lymphoepithelial carcinoma-like pattern (cases 1 and 2) (A–F), poorly cohesive carcinoma pattern (case 3) (G, H), solid pattern with geographic necrosis (case 4) (I, J), inverted papilloma-like pattern (case 5) (K–N), and multiphenotypic pattern (case 6) (O, P). (A–D) Well encapsulated tumor with abundant lymphoid stroma displays irregular nests and with poorly defined cell borders. (E, F) p40 and Epstein-Barr virus in situ hybridization are negative in undifferentiated carcinoma with lymphoepithelial carcinoma-like feature. (G, H) Poorly cohesive carcinoma cells with no organized pattern shows destructive skeletal muscle invasion. (I, J) Solid sheets of tumor cells with high-grade nuclear atypia are accompanied by distinct massive geographic necrosis. (K, L) Variable-sized nests and sheets of stratified epithelial cells are interanastomosing and possess numerous intraepithelial neutrophils and microabscesses. Tumor cell nuclei are strongly positive for androgen receptor (M) but negative for gross cystic disease fluid protein 15 (N). (O, P) The tumor exhibits mixed architectural patterns including solid, cords, ribbons, and trabecular arrangement. Perivascular rosette-like configurations with myxoid material are easily identified.

necrosis was present with floating islands of tumor nests in variable sizes. The tumor cells possessed abundant eosinophilic cytoplasm with pleomorphic nuclei and showed brisk mitotic activity.

In case 5, inverted papilloma-like histomorphology was observed. Tumor cells consisted of stratified transitional-type epithelium with frequent transmigrating neutrophils and microabscesses, which was reminiscent of sinonasal papilloma of the nasal cavity. The tumor cells displayed vesicular chromatin, prominent cherry-red nucleoli, abundant eosinophilic cytoplasm, and distinct cell borders. The peritumoral intervening stroma was small or narrow and had mild-to-moderate lymphocytic infiltration.

Case 6 was a multiphenotypic HGC with somewhat myoepithelial-cell like histological features. Tumor cells exhibited solid sheets, ill-formed cords, and trabecular or perivascular pseudorosette-like patterns and possessed round nuclei with scanty cytoplasm. Apoptotic bodies and mitotic figures were frequently observed throughout the tumor. The degree of tumor-infiltrating lymphocytes was lower than that of other PDCs or LECs. All cases lacked glandular or squamous differentiation.

The histological features of LEC in the salivary gland were similar to LECs found in other locations (Fig. 3). The tumor cells were arranged in cords, sheets, or nests and harbored moderate amounts of eosinophilic cytoplasm and large vesicular nuclei with prominent nucleoli. Tumor cells had indistinct cell borders, resulting in syncytial growth patterns. Distinct peri- or intratumoral lymphoplasmacytic infiltration and scattered lymphoid follicles were observed. In one case (case 8), tumor cells with occasional keratin pearl formation and dyskeratosis within squamous eddies were identified.

Immunostaining and EBV-ISH results

The immunophenotypical characteristics and ISH results are shown in Table 2. PDC, HGC, and UDCs were distinguished from LECs by no or negligible immunoreactivity for p40 and negative EBV ISH. Neuroendocrine differentiation was denied by negative expression for synaptophysin and chromogranin. Cases 3 and 5 displayed diffuse and strong positivity for AR in the tumor nuclei but were negative for GCDFP-15. In case 6, p40, AR, and GCDFP-15 IHCs were unavailable because of insufficient tissue on a paraffin block. Additionally, CK7 and p63 immunostaining results were available in a subset of cases. CK7 was positive in cases 1, 2, and 5, and negative in case 3. Notably, p63 was negative in cases 5 and 6, which may support the absence of squamous or basal/myoepithelial differentiation in these tumors. In contrast, all LECs displayed moderate-to-strong p40 positivity in the tumor nuclei with a variable proportion of staining. Three of the LECs (50%) were diffusely and strongly positive for EBV ISH. Neuroendocrine markers, AR, and GCDFP-15 were all negative in LECs.

DISCUSSION

In the 4th edition of the WHO classification of head and neck tumors, PDC included a subcategory for UDC, which can only be diagnosed in the absence of metastasis from other sites [2,5]. However, clinical features, macroscopic and microscopic findings, or immunohistophenotypes for PDC or UDC have not been described in detail. Moreover, PDC including UDC has been removed in the 5th edition of the WHO classification of head and neck tumors [3].

Nevertheless, certain poorly differentiated (PD) tumors of the salivary gland do not fit into any of the current diagnostic criteria. Thus, classifying these tumors as UDC is more appropriate than simply salivary gland carcinoma not otherwise specified (NOS). Moreover, salivary gland carcinoma NOS in the current WHO classification is described as displaying a wide range of ductal or glandular proliferation patterns, similar to adenocarcinoma NOS, in the previous classification. In this study, UDC was defined as high-grade carcinomas showing no ductal, glandular, squamous, or neuroendocrine differentiation. The six tumors, which were initially diagnosed as PDC, HGC, or UDCs exhibited diverse histologic growth patterns but were devoid of specific differentiation, were classified as UDC. To the best of our knowledge, this is the first study to propose a definition of UDC of the salivary gland, providing a comprehensive analysis of clinicopathological and IHC features of PD tumors of the salivary gland. A diagnostic flowchart summarizing our proposed approach to salivary gland UDC classification is provided in Fig. 4.

Few studies have documented the clinicopathological and IHC characteristics of UDC of the salivary gland. However, limited IHC and ISH analysis in these studies could not completely exclude other high-grade salivary gland carcinomas and led to an inconclusive classification of the tumors as UDC. Our comprehensive analysis including p40, neuroendocrine markers, AR, and GCDFP-15 IHC and EBV-ISH results, provides a clearer distinction of these PD tumors than other high-grade salivary gland carcinomas including LEC and salivary duct car-

https://doi.org/10.4132/jptm.2025.07.07

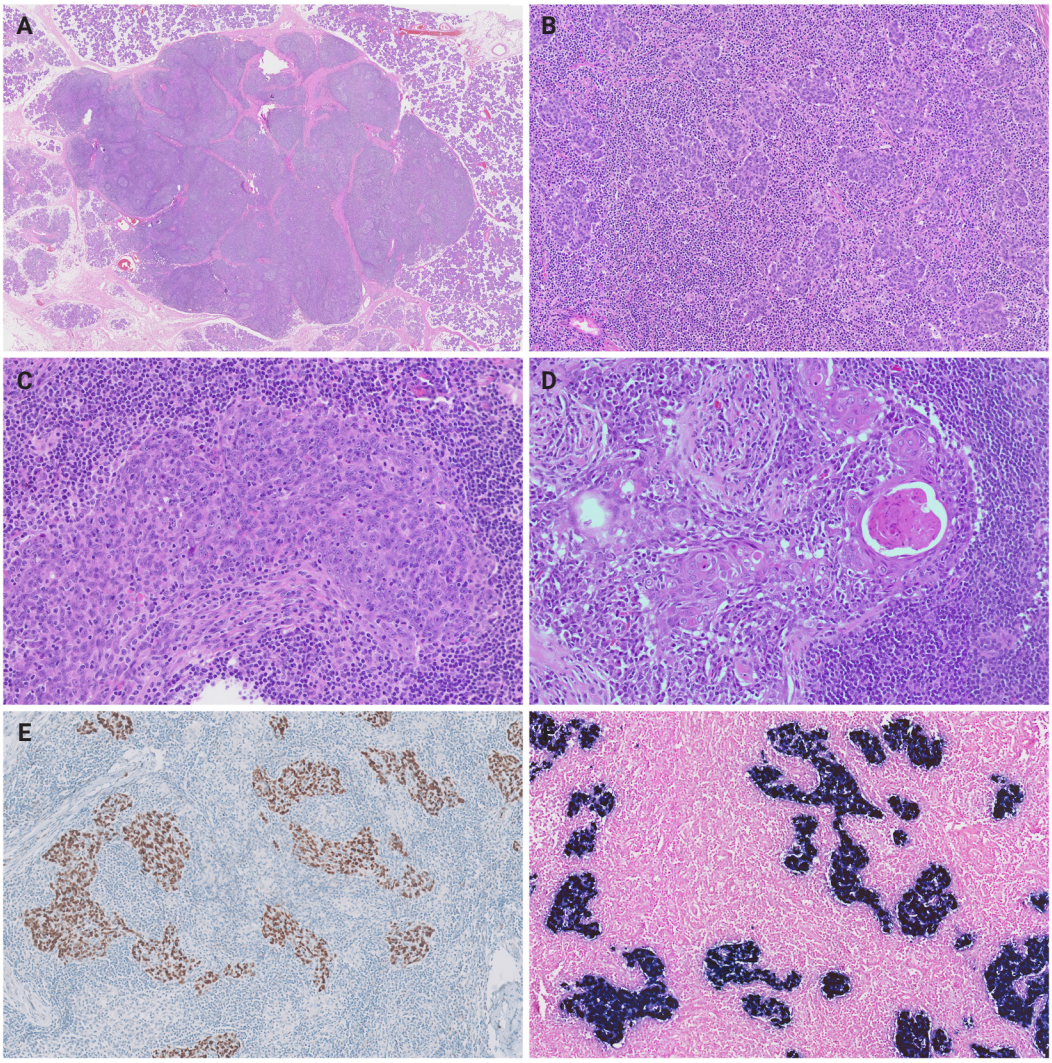

Fig. 3. Histopathological findings, immunohistochemical results, and Epstein-Barr virus-encoded RNA in situ hybridization results of lymphoepithelial carcinoma of the salivary gland (cases 7–11). (A) On scanning view, a well-circumscribed nodular mass with fibrous septa is surrounded by the non-neoplastic parotid gland. (B) Low-power magnification shows variable-sized tumor cell clusters infiltrating the stromal tissue with abundant lymphoplasmacytic infiltrates and lymphoid follicles. (C) High-power magnification exhibits an admixture of tumor cells with syncytial appearance and intratumoal inflammatory cells. The tumor cells possessed moderate eosinophilic cytoplasm, large round-to-ovoid nuclei with vesicular chromatin, and single conspicuous eosinophilic nuclei. (D) Squamous differentiation of tumor cells is occasionally present. (E) Tumor cells display strong nuclear p40 expression. (F) Epstein-Barr virus in situ hybridization shows positive signals in tumor nuclei.

cinoma (SDC).

Sheen et al. [6] reported the clinicopathological characteristics of 12 patients with salivary gland tumors with undifferentiated morphology. They defined UDC as a malignant epithelial tumor lacking any phenotypic characteristics observable by light microscopy and classified LEC as a distinct UDC subtype. Based on the histology and EBV-ISH results, they classified nine cases as LEC (abundant lymphoid stroma+/EBV+) and three as UDC (lymphoid stroma–/ EBV–). Detailed histological features of UDC cases were not described, and tumor cells only showed positive immunostaining for cytokeratin but were negative for S-100, human melanoma black-45 (HMB-45), leukocyte common antigen, and mucin. Among patients with UDC, one experienced lymph node (LN) metastasis and died within 3 months, whereas another patient without LN metastasis survived for 19 years without recurrence or metastasis.

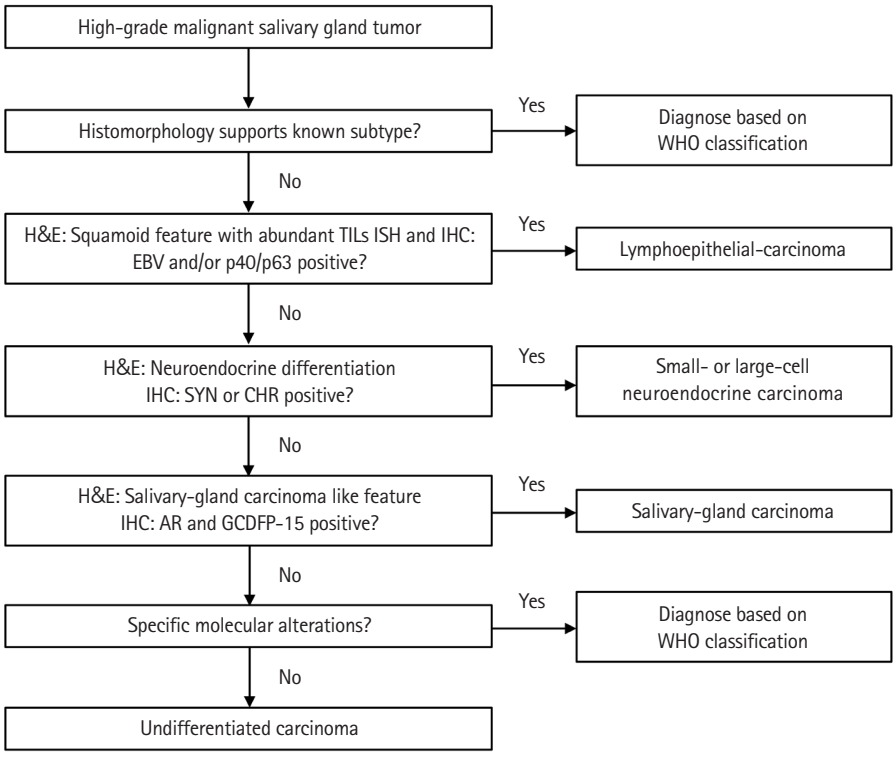

Fig. 4. Proposed diagnostic algorithm for undifferentiated carcinoma (UDC) of the salivary gland. The flowchart illustrates a sequential diagnostic approach using histomorphology and immunohistochemistry (IHC) to distinguish UDC from other high-grade salivary gland carcinomas. TIL, tumor-infiltrating lymphocytes; ISH, in situ hybridization; EBV, Epstein-Barr virus; SYN, synaptophysin; CHR, chromogranin; AR, androgen receptor; GCDFP-15, gross cystic disease fluid protein 15; WHO, World Health Organization.

Hatta et al. [7] reported five cases of UDC of the parotid gland, as well as their clinicopathological features and immunostaining results. They also defined UDC as a malignant epithelial tumor, which is too poorly differentiated to be classified in any other group of carcinoma, and introduced heterogeneous morphologies of tumor cells. The tumors had various histological appearances, including features resembling LEC, epidermoid/mucoepidermoid carcinoma, small cell carcinoma, and malignant hemangiopericytoma. All five cases resulted in death caused by distant metastasis within 2.5 years. IHC analysis for vimentin, smooth muscle actin, desmin, HMB-45, and S-100 was performed to exclude malignant mesenchymal tumors and melanoma, which were negative; however, the analysis did not include squamous or neuroendocrine markers, AR, GCDFP-15, or EBV ISH; thus, classifying the cases as LEC, neuroendocrine carcinoma, SDC, or UDC was inconclusive.

Interestingly, LEC-like features were present in two UDCs (cases 1 and 2) in this study. These tumors require differentiation from true LEC via p40 IHC and EBV-ISH analysis. LECs of the salivary glands exhibit undifferentiated morphology of tumor cells with syncytial sheet-like growth patterns and occasionally have squamous differentiation. Most LECs show diffuse moderate-to-strong p40 or p63 expression on IHCs and are frequently positive for EBV ISH [8,9]. Although the two LEC-like UDC cases in this study were not associated with EBV infection, they lacked histologic and immunophenotypic evidence of squamous differentiation; thus, it could be different from conventional LEC.

In this study, two of the six UDC cases displayed diffuse and strong AR expression, which was frequently reported in SDC [10]. SDC is a primary salivary gland carcinoma showing aggressive biological behavior and has male predilection with old age [11]. Histologically, SDCs demonstrate a complex architecture, including solid, cribriform, and papillary-cystic patterns, often accompanied by comedotype necrosis [12]. The tumor cells are characterized by their large pleomorphic nuclei with coarse chromatin and distinct nucleoli and abundant eosinophilic cytoplasm. Several subtypes including sarcomatioid,

https://doi.org/10.4132/jptm.2025.07.07

mucin-rich, micropapillary, basal-like, oncocytic, and rhabdoid morphology have been reported [13-16]. Cases 3 and 5 had different histological features (poorly cohesive and inverted papilloma-like) but exhibited diffuse and strong AR immunoreactivity, which are possible in high-grade SDCs. However, the lack of the classic morphology of SDC, and the GCDFP-15 expression was not diagnostic for SDC. Moreover, AR expression has been reported in various malignant salivary gland tumors, including primary squamous cell carcinoma, adenoid cystic carcinoma, mucoepidermoid carcinoma, myoepithelial carcinoma, and polymorphous adenocarcinoma [17,18]. Although AR expression is frequently observed in SDC and often supports its diagnosis, it should always be interpreted in conjunction with the tumor's histomorphologic characteristics and other immunophenotypic features, rather than being used as a standalone diagnostic criterion for SDC.

This study has limitations. First, the clinicopathological results were derived from a relatively small size cohort conducted at a single institution. Given the rarity of UDC of the salivary gland, single-center studies are inherently limited to refine the full clinicopahological spectrum of the disease. Collaborative multicenter studies with larger case numbers, standardized diagnostic protocols, and long-term clinical follow-up are required to enhance the generalizability of findings. Second, one case initially diagnosed as PDC (case 6) was not available for p40, AR, and GCDFP-15 studies, thereby limiting a definitive exclusion of LEC or SDC. Although the tumor demonstrated negative immunoreactivity for p63 and the histological features did not support both entities, the absence of a complete immunophenotypic profile remains a diagnostic limitation. Third, our study did not include a full panel of IHC studies for the differentiation of various salivary gland neoplasms. Given the well-documented morphological overlap among various salivary gland carcinomas, the use of a broader range of immunostainings—including SOX10, DOG1, S100, mammaglobin, and GATA3—is considered essential for accurate classification. In our study, due to the retrospective design and limited availability of archived tissue, we prioritized immunostains based on the predominant histomorphologic features of each tumor. Fourth, molecular testing, such as next-generation sequencing or fluorescence ISH was not performed in this study. Recent literatures highlight the utility of molecular diagnostics in uncovering disease-specific genomic alterations in histologically ambiguous salivary gland tumors. The absence of such ancillary molecular studies in our cohort may have limited our ability to fully exclude specific tumor entities or identify rare genetic subtypes. Future studies should incorporate a more comprehensive IHC panel, along with molecular profiling, to better delineate undifferentiated salivary gland carcinomas.

In summary, this study proposes to elucidate the definition of UDC by comprehensive analysis of histological features through IHC and ISH analyses. We observed several cases of primary high-grade or PDCs of the salivary gland, which are negative for p40, GCDFP-15, neuroendocrine markers, and EBV ISH, so we suggest classifying these tumors as UDC, a category that has been removed in the 5th edition of the WHO classification. Our detailed clinicopathological and IHC analyses of these cases will clarify the categorization of tumors with undifferentiated morphology and enhance our understanding of UDCs in the salivary gland.

Ethics Statement

All procedures performed in studies involving human participants were in accordance with the ethical standards of the institutional and/or national research committee and with the 1964 Helsinki declaration and its later amendments or comparable ethical standards. The Institutional Review Board of Asan Medical Center approved this study (IRB No. 2023-1538) and waived informed consent for this study.

Availability of Data and Material

No datasets were generated or analysed during the current study.

Code Availability

Not applicable.

ORCID

Sangjoon Choi https://orcid.org/0000-0003-2108-0575
Gyuheon Choi https://orcid.org/0000-0002-2825-987X
Hee Jin Lee https://orcid.org/0000-0002-4963-6603
Joon Seon Song https://orcid.org/0000-0002-7429-4254
Yoon Se Lee https://orcid.org/0000-0001-6534-5753
Seung-Ho Choi https://orcid.org/0000-0001-9109-9621
Kyung-Ja Cho https://orcid.org/0000-0002-4911-7774

Author Contributions

Conceptualization: KJC. Data curation: SC, GC. Formal analysis: SC. Investigation: SC. Methodology: KJC. Project administration: SC, KJC. Resources: GC, HJL, JSS, YSL, SHC, KJC.

Supervision: KJC. Validation: HJL, JSS, KJC. Visualization: SC. Writing—original draft: SC. Writing—review & editing: KJC. Approval of final manuscript: all authors.

Conflicts of Interest

J.S.S., a contributing editor of the *Journal of Pathology and Translational Medicine*, was not involved in the editorial evaluation or decision to publish this article. All remaining authors have declared no conflicts of interest.

Funding Statement

No funding to declare.

REFERENCES

1. Lin HH, Limesand KH, Ann DK. Current state of knowledge on salivary gland cancers. Crit Rev Oncog 2018; 23: 139-51.
2. El-Naggar AK, Chan JK, Grandis JR, Takata T, Slootweg PJ. WHO classification of head and neck tumours. 4th ed. Lyon: IARC Press, 2017.
3. WHO Classification of Tumours Editorial Board (2022). Head and neck tumours [Internet]. Lyon: International Agency for Research on Cancer, 2022 [cited 2025 Mar 3]. Available from: https://tumourclassification.iarc.who.int/chapters/52.
4. Lee M, Jo U, Song JS, et al. Clinicopathologic characterization of cervical metastasis from an unknown primary tumor: a multicenter study in Korea. J Pathol Transl Med 2023; 57: 166-77.
5. Franchi A, Skalova A. Undifferentiated and dedifferentiated head and neck carcinomas. Semin Diagn Pathol 2021; 38: 127-36.
6. Sheen TS, Tsai CC, Ko JY, Chang YL, Hsu MM. Undifferentiated carcinoma of the major salivary glands. Cancer 1997; 80: 357-63.
7. Hatta C, Terada T, Okita J, Kakibuchi M, Kubota A, Sakagami M. Clinicopathological study of undifferentiated carcinoma of the parotid gland. Auris Nasus Larynx 2003; 30: 273-7.
8. Thompson LD, Whaley RD. Lymphoepithelial carcinoma of salivary glands. Surg Pathol Clin 2021; 14: 75-96.
9. Zhang C, Gu T, Tian Z, et al. Lymphoepithelial carcinoma of the parotid gland: clinicopathological analysis of 146 cases from a single institute. Head Neck 2022; 44: 2055-62.
10. Can NT, Lingen MW, Mashek H, et al. Expression of hormone receptors and HER-2 in benign and malignant salivary gland tumors. Head Neck Pathol 2018; 12: 95-104.
11. Nakaguro M, Sato Y, Tada Y, et al. Prognostic implication of histopathologic indicators in salivary duct carcinoma: proposal of a novel histologic risk stratification model. Am J Surg Pathol 2020; 44: 526-35.
12. Williams L, Thompson LD, Seethala RR, et al. Salivary duct carcinoma: the predominance of apocrine morphology, prevalence of histologic variants, and androgen receptor expression. Am J Surg Pathol 2015; 39: 705-13.
13. Padberg BC, Sasse B, Huber A, Pfaltz M. Sarcomatoid salivary duct carcinoma. Ann Diagn Pathol 2005; 9: 86-92.
14. Kusafuka K, Maeda M, Honda M, Nakajima T. Mucin-rich salivary duct carcinoma with signet-ring cell feature ex pleomorphic adenoma of the submandibular gland: a case report of an unusual histology with immunohistochemical analysis and review of the literature. Med Mol Morphol 2012; 45: 45-52.
15. Simpson RH. Salivary duct carcinoma: new developments–morphological variants including pure in situ high grade lesions; proposed molecular classification. Head Neck Pathol 2013; 7 Suppl 1: S48-58.
16. Kusafuka K, Yamada H, Ishino K, et al. Salivary duct carcinoma eith rhabdoid features: no or aberrant expression of E-cadherin and genetic changes in CDH1: immunohistochemical and genetic analyses of 17 cases. Am J Surg Pathol 2021; 45: 439-49.
17. Jo U, Song JS, Choi SH, Nam SY, Kim SY, Cho KJ. Primary squamous cell carcinoma of the salivary gland: immunohistochemical analysis and comparison with metastatic squamous cell carcinoma. J Pathol Transl Med 2020; 54: 489-96.
18. Matiku S, Murenzi G, Rugengamanzi E, et al. Androgen receptor overexpression by immunohistochemistry in malignant salivary gland tumors in Tanzania. BMC Cancer 2025; 25: 29.

https://doi.org/10.4132/jptm.2025.07.07

JPTM

ORIGINAL ARTICLE

pISSN 2383-7837 · eISSN 2383-7845

Journal of Pathology and Translational Medicine 2025; 59: 371-381
https://doi.org/10.4132/jptm.2025.07.08

Clinicopathological implications of miR-3127 in melanoma

Truong Phan-Xuan Nguyen[1], Minh-Khang Le[2], Chau M. Bui[3], Vuong Gia Huy[4]

[1]Department of Pathology, School of Medicine, University of Medicine & Pharmacy at Ho Chi Minh City, Ho Chi Minh, Vietnam
[2]Department of Pathology, University of Yamanashi, Yamanashi, Japan
[3]Department of Pathology, University of Rochester Medical Center, Rochester, NY, USA
[4]Department of Pathology, University of Iowa Hospitals and Clinics, Iowa City, IA, USA

Graphical abstract

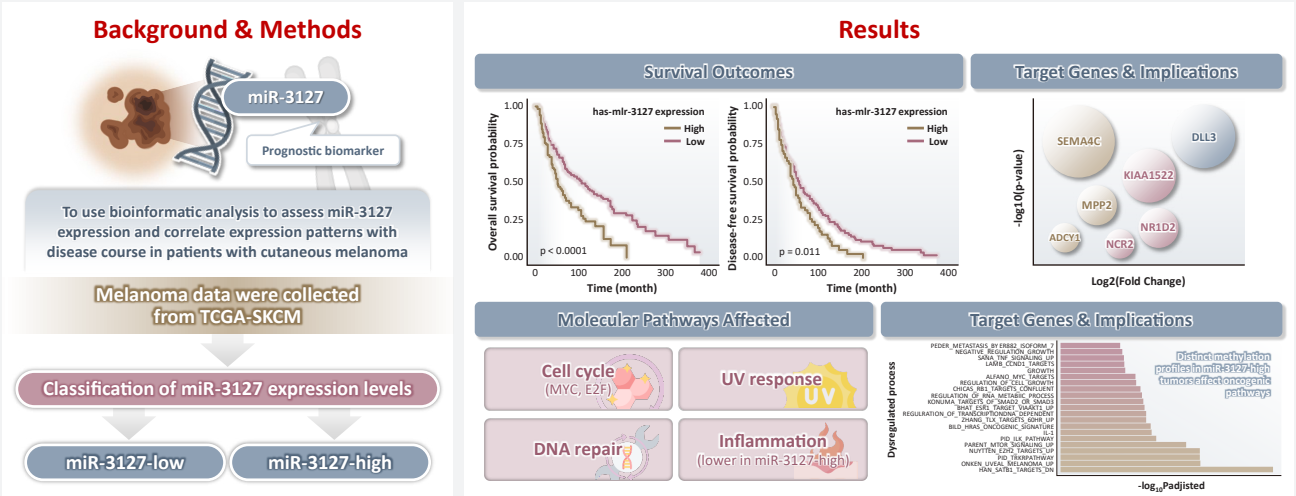

CONCLUSION

Our findings demonstrate that miR-3127 is a useful biomarker to predict prognosis of melanoma, with increased expression of miR-3127 being associated with an unfavorable prognosis. These results suggest that miR-3127 may play an important role in the complex mechanisms underlying the multi-step process of melanoma progression. The expression profile of miR-3127 could function as a prognostic indicator, aiding in the management and treatment of patients with melanoma.

Nguyen TPX et al. Journal of Pathology and Translational Medicine

JPTM

ORIGINAL ARTICLE

pISSN 2383-7837 · eISSN 2383-7845

Journal of Pathology and Translational Medicine 2025; 59: 371-381
https://doi.org/10.4132/jptm.2025.07.08

Clinicopathological implications of miR-3127 in melanoma

Truong Phan-Xuan Nguyen[1], Minh-Khang Le[2], Chau M. Bui[3], Vuong Gia Huy[4]

[1]Department of Pathology, School of Medicine, University of Medicine & Pharmacy at Ho Chi Minh City, Ho Chi Minh, Vietnam
[2]Department of Pathology, University of Yamanashi, Yamanashi, Japan
[3]Department of Pathology, University of Rochester Medical Center, Rochester, NY, USA
[4]Department of Pathology, University of Iowa Hospitals and Clinics, Iowa City, IA, USA

Background: Cutaneous melanoma is the most lethal of all skin cancers. Recent studies suggested that miR-3127 is dysregulated in multiple tumor types and has important roles in tumorigenesis and cancer progression, giving it potential as a prognostic biomarker. The aim of this study was to use bioinformatic analysis to assess miR-3127 expression and correlate expression patterns with disease course in patients with cutaneous melanoma. **Methods:** miRNA, mRNA sequencing, DNA methylation data, and clinical information of cutaneous melanoma cases were downloaded from the Human Cancer Atlas – Skin Cutaneous Melanoma (TCGA-SKCM). miR-3127 expression was classified into miR-3127–low and miR-3127–high clusters using maximally selected rank statistics. **Results:** Clustering analysis showed that high expression of miR-3127 (≥20.3 reads per million) was associated with worse progression-free ($p < .001$) and overall ($p = .011$) survival compared to low miR-3127 expression. More than five thousand differentially expressed genes between the two miR-3127 sample groups encoded cell differentiation markers, cytokines, growth factors, translocated cancer genes, and oncogenes. Pathway analysis revealed that miR-3127–high samples related to activity of proliferation, DNA repair, and ultraviolet response. **Conclusions:** The expression level of miR-3127 could act as a prognostic indicator for patients with melanoma.

Keywords: Survival; Cancer survival; Melanoma; miRNA; Prognosis

INTRODUCTION

Cutaneous melanoma, which frequently develops from the epidermal-dermal junction where melanocytes undergo malignant transformation, is known for its rapid progression, high invasiveness, metastatic potential, and limited responsiveness to treatment [1]. There were an estimated 324,000 new cases and approximately 57,000 deaths worldwide in 2020 of this primary skin cancer [2]. Surgical removal of the primary melanoma typically yields favorable outcomes, resulting in a relatively high survival rate. However, the 3-year survival rate drops to only 5%–32% when melanoma spreads to lymph nodes or distant sites [3]. Therefore, it is crucial to identify effective biomarkers for melanoma to improve prognostic accuracy and guide targeted treatments.

MicroRNAs (miRNAs) are a class of small non-coding RNAs that regulate gene expression post-transcription by binding to the 3′-untranslated regions (UTRs) of target mRNAs. miRNAs are crucial in the regulation of tumor growth and metastasis [4]. Recent studies suggested that miR-3127 functions in a variety of malignancies as either a tumor suppressor or an oncogene [5]. For instance, there is evidence to suggest that downregulation of miR-3127-5p could facilitate the transition from epithelial to mesenchymal by activating the WNT/FZD4/β-catenin signaling pathway, thereby promoting tumor progression and metastasis [6]. Furthermore, miR-3127 represses the growth and invasion of bladder cancer cells by directly targeting the 3′-UTR of *RAP2A*, whereas in hepatocellular carcinoma (HCC), it stimulates proliferation and tumorigenesis via the AKT/FOXO1 signaling pathway [5-7]. At present, the precise function of

Received: March 31, 2025 **Revised:** June 29, 2025 **Accepted:** July 8, 2025
Corresponding Author: Vuong Gia Huy, MD, PhD
Department of Pathology, University of Iowa Hospitals and Clinics, Iowa City, IA 52242, USA
Tel: +1-4057193776, E-mail: huyvuong@hotmail.com

miR-3127 in melanoma and its role in disease progression are not well understood.

In this study, we aimed to investigate the association between expression levels of miR-3127, clinicopathological characteristics, and overall survival (OS) in cases of melanoma. We also worked on establishing miR-3127 as a prognostic biomarker to help guide the management and treatment of patients with melanoma.

MATERIALS AND METHODS

Data preprocessing

We accessed The Human Cancer Atlas – Skin Cutaneous Melanoma (TCGA-SKCM) (https://portal.gdc.cancer.gov/projects/TCGA-SKCM) and retrieved data regarding miRNA expression (n = 450 samples), mRNA expression (n = 472 samples), and DNA methylation (n = 472 samples) of melanoma patients. We first filtered out normal samples and included primary (n=237) and metastatic (n=209) tumor samples. We categorized samples from stages I and II, as well as tumors from stages III and IV with code "01," as primary samples. Meanwhile, samples from stages III and IV with code "06" were classified as metastatic samples. Metastatic melanomas included tumors from regional sites (such as regional lymph nodes and regional skin/soft tissue) as well as distant sites. We then eliminated duplicated samples (same sample type in a patient). Finally, the numbers of samples available for miRNA, mRNA, and DNA methylation were 446, 468, and 467, respectively. Included clinical characteristics were age, sex, race, Breslow's depth, TNM stages, radiation, chemotherapy, OS, and disease-free survival (DFS).

Clustering of miR-3127 expression

Maximally selected rank statistics (MSRS) is a method that selects the cut-off point, whose rank metric is maximum [8]. Since our purpose was to investigate the clinicopathological significance of miR-3127, we employed standardized log-rank statistics as the ranking metric. This metric usually evaluates the association between genes and/or miRNAs and survival outcomes [9]. We used the expression of miR-3127 and OS to compute the rank metric. We then divided the studied samples into tumors with low (miR-3127–low) and high (miR-3127–high) expressions of miR-3127.

mRNA and miRNA expression analyses

We employed the DESeq2 pipeline to perform differential expression analysis (DEA) [10]. DEA was conducted to compare each miRNA and mRNA expression between miR-3127–high and miR-3127–low samples. In pathway analysis, we used the gene set enrichment analysis (GSEA) method to examine the difference in the pathway activity between these two sample groups [11]. The Benjamini-Hochberg multiple corrections were applied to reduce false-positive results.

DNA methylation analysis

We followed the ChAMP pipeline to perform differential methylation position (DMP), differential methylation region (DMR), and methylation GSEA [12]. We focused on the difference in methylation statuses between miR-3127–low and miR-3127–high tumors.

Analysis platform

We used R software programming language ver. 4.2.2 (R Foundation for Statistical Computing, Vienna, Austria) for all the analyses. For clinicopathological analyses, we performed Wilcoxon and chi-squared tests for continuous and categorical variables, respectively. For survival analyses, Kaplan-Meier, univariate, and multivariate Cox analyses were conducted. All the hypothesis tests were considered significant when $p < .05$ or adjusted $p < .5$.

RESULTS

Clustering analysis showed high expression of miR-3127 conferred worse outcomes

Using MSRS, the optimal miR-3127 expression threshold was 20.3 read per million (RPM) (Fig. 1A, D). Therefore, samples were classified as miR-3127–low (n = 317) and miR-3127–high (n = 129) based on miR-3127 expression of <20.3 and ≥20.3 RPM, respectively. Table 1 presented a summary of the study cohort's characteristics, divided into miR-3127–high and miR-3127–low groups. Among the samples, 48.8% of metastatic and 51.2% of non-metastatic patients exhibited high miR-3127 expression, with no statistically significant difference observed. This indicates that miR-3127 expression was not associated with metastatic status.

Overall, patients with miR-3127–high samples showed significantly poorer DFS ($p < .001$) and OS ($p = .011$) (Table 2, Fig. 1B, C). When stratified into primary and metastatic groups, those with miR-3127–high metastatic melanoma exhibited the poorest prognosis. Notably, patients with miR-3127–high non-metastatic melanoma had both worse OS and DFS

https://doi.org/10.4132/jptm.2025.07.08

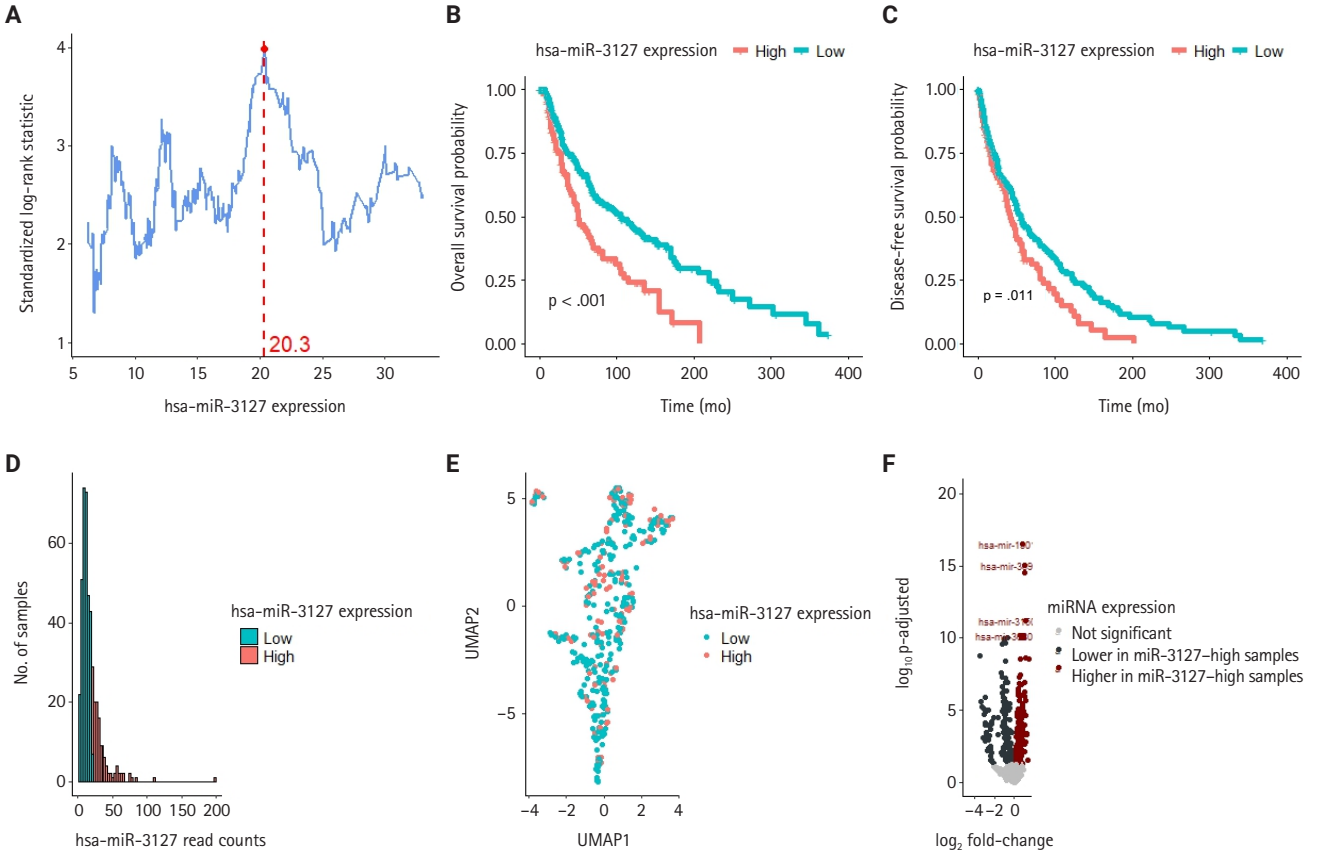

Fig. 1. miR-3127 expression and its association with melanoma patient outcomes. (A) Maximally selected rank statistics method using standardized log-rank statistic as the metric. (B) Kaplan-Meier curves showing the overall survival between miR-3127–low and miR-3127–high melanoma patients. (C) Kaplan-Meier curves showing the disease-free survival between miR-3127–low and miR-3127–high melanoma patients. (D) Histogram showing the distribution of miR-3127 read counts. (E) Uniform manifold approximation and projection dimension reduction plot illustrating the miRNA space color-coded by miR-3127 expression status. (F) Volcano plot demonstrating the results of DESeq2 analysis of miRNA expression. The top 5 most significant genes are labeled.

compared to those with miR-3127–low metastatic melanoma (Supplementary Fig. S1).

Fig. 1E illustrated the even distributions of miR-3127–low and miR-3127–high in miRNA "space," suggesting limited relationships between miR-3127 and other miRNAs. DEA of miRNA expression found that 165 (8.8%) and 150 (8.0%) miRNAs of 1,881 miRNA probes were respectively upregulated and downregulated in miR-3127–high samples (Supplementary Table S1). DEA revealed that the top 5 differentially expressed miRNAs (excluding miR-3127) were miR-1301, miR-3691, miR-6509, miR-3150b, and miR-3680-1 (Fig. 1F).

Large portions of genes in cell differentiation markers, cytokines, growth factors, translocated cancer genes, and oncogenes are differentially expressed by miR-3127 groups

The DEA of mRNA expression indicated 5,484 differentially expressed genes (DEGs), accounting for 9.1% of genes analyzed (Supplementary Table S2). Fig. 2A shows the dimension reduction of only DEGs, where miR-3127–high samples are more densely distributed in the lower area of the graph. To investigate the expression pattern of miR-3127 targets, we first collected the target genes of miR-3127 by accessing collection "C3" of the MSigDB database and retrieving genes in MIR3127-3P and MIR3127-5P (Supplementary Table S3). We then examined the DEGs within these genes (Fig. 2B). Among the predicted tar-

Table 1. Clinicopathological characteristics of miR-3127–low and miR-3127–high melanoma patients

Variable	miR-3127–low (n = 317)	miR-3127–high (n = 129)	p-value
Age (yr)	58 (15–90)	60 (23–87)	.547
Sex			.062
Female	130 (41.0)	40 (31.0)	
Male	187 (59.0)	89 (69.0)	
Race			.503
Asian	7 (2.3)	5 (4.0)	
Black	1 (0.3)	0 (0.0)	
White	309 (97.4)	124 (96.0)	
Breslow depth (mm)	2.9 (0.0–75.0)	3.2 (0.0–74.0)	.391
Sample			.668
Primary	171 (53.9)	66 (51.2)	
Metastatic	146 (46.1)	63 (48.8)	
T category[a]			.765
T0	19 (7.2)	4 (3.7)	
Tis	5 (1.9)	3 (2.8)	
T1	28 (10.6)	9 (8.3)	
T2	56 (21.1)	22 (20.4)	
T3	58 (21.9)	26 (24.1)	
T4	99 (37.4)	44 (40.7)	
N category[a]			.974
N0	160 (56.7)	65 (57.0)	
N1	48 (17.0)	21 (18.4)	
N2	36 (12.8)	13 (11.4)	
N3	38 (13.5)	15 (13.2)	
M category[a]			>.99
M0	282 (94.3)	114 (94.2)	
M1	17 (5.7)	7 (5.8)	
AJCC stage[a]			.865
I	51 (18.6)	23 (20.2)	
II	94 (34.3)	34 (29.8)	
III	113 (41.2)	50 (43.9)	
IV	16 (5.8)	7 (6.1)	
Radiation[a]			.491
No	297 (95.8)	119 (93.7)	
Yes	13 (4.2)	8 (6.3)	
Chemotherapy[a]			.600
No	225 (78.7)	87 (75.7)	
Yes	61 (21.3)	28 (24.3)	
Overall survival (mo)	42 (0–374)	33 (1–208)	.056
Disease-free survival (mo)	28 (0–368)	27 (0–201)	.056

AJCC, American Joint Committee on Cancer.
[a]Variable could not be fully obtained because certain data were unavailable.

get genes, the expressions of *PAFAH1B2*, *FAM172A*, *GOLM2*, *NKAPD1*, and *DDX6* were lower in miR-3127–high samples while *SEMA4C*, *KIAA1522*, *DLL3*, *SEMA4F*, and *MPP2* were highly expressed by miR-3127–high tumors. In the analysis of the overall mRNA dataset, the top 10 most significant DEGs (Fig. 2C) included two downregulated genes (*IGFBP3* and *KIAA0040*) and eight upregulated genes (*RTN4R*, *PAK4*, *SNTA1*, *CNNM3*, *NAXE*, *SMYD5*, *PPARD*, and *EPHX1*).

We then asked which gene functions were largely different between the two miR-3127 sample groups. We collected the genes belonging to eight important function families, including cell differentiation markers (CDM), cytokine and growth factor (CGF), homeodomain proteins (HP), oncogenes (O), protein kinase (PK), translocated cancer gene (TCG), transcription factor (TF), and tumor suppressor (TS). The detail information can be found in the website of the MSigDB databse (https://www.gsea-msigdb.org/gsea/msigdb/human/gene_families.jsp). We used genes that only belong to CDM (n = 367), CGF (n = 452), HP (n = 291), O (n = 328), PK (n = 513), TCG (n = 290), TF (n = 1536), and TS (n = 82). Genes with mutual functions were excluded. Fig. 2D shows the number of genes in each function family, color-coded by DEGs. We found that large proportions of CDM (48.3%), CGF (47.1%), TCG (42.1%), and oncogenes (41.8%) were DEGs.

Pathway analysis revealed that miR-3127–high samples related to activity of proliferation, DNA repair, and ultraviolet response and lower inflammation-related processes

We employed collection H (hallmark gene sets) of the MSigDB database, including 50 hallmark pathways. Next, we performed the classic GSEA to compare the pathway activity between miR-3127–low and miR-3127–high samples (Fig. 2E). The full results are shown in Supplementary Table S4. Overall, there were 15 upregulated and 16 downregulated pathways while 19 pathways showed no significant difference. We found that cell cycle-related (MYC targets, E2F targets, and G2M checkpoint), DNA repair, upregulated genes of ultraviolet (UV) response, and metabolism-related (glycolysis and reactive oxygen species) pathways were enriched in miR-3127–high melanomas. On the other hand, miR-3127–low samples showed the enrichment of inflammation-related (interferon-γ and α response, and inflammatory responses) processes.

https://doi.org/10.4132/jptm.2025.07.08

Table 2. Univariate and multivariate Cox analyses of overall survival in the studied cohort

Variable	Univariate			Multivariate		
	HR	95% CI	p-value	HR	95% CI	p-value
miR-3127						
Low	1			1		
High	1.8	1.4–2.5	<.001	1.5	1.0–2.1	.033
Age (10 yr)	1.3	1.1–1.4	<.001	1.2	1.0–1.3	.015
Race						
Asian	1			1		
Black	0.2	0.0–1.5	.106	n/a	n/a	n/a
White	0.2	0.1–0.5	<.001	0.2	0.1–0.6	.004
Breslow's depth (cm)	1.3	1.1–1.5	<.001	1	0.8–1.3	.889
T category						
T1	1			1		
T2	1.6	0.8–3.0	.171	1.7	0.8–3.4	.151
T3	2.2	1.1–4.1	.017	2.4	1.0–6.0	.059
T4	3.8	2.1–7.2	<.001	4.7	1.8–12.2	.001
N category						
N0	1			1		
N1	1.6	1.1–2.3	.025	2.7	0.9–8.0	.080
N2	1.6	1.0–2.4	.051	3.6	1.1–11.4	.028
N3	2.6	1.7–4.1	<.001	7.4	2.4–23.2	<.001
M category						
M0	1					
M1	1.7	0.9–3.3	.094			
Radiation						
No	1					
Yes	1	0.5–1.9	.994			
Chemotherapy						
No	1					
Yes	0.9	0.7–1.3	.658			

HR, hazard ratio; CI, confidence interval; n/a, not available.

Methylation analysis

Investigation of the 1,000 most variable methylation positions (Fig. 3A, left) showed no clear difference in the distribution between miR-3127–low and miR-3127–high samples. Fig. 3A illustrates the proportion of hypomethylated and hypermethylated CpG probes (in miR-3127–high samples) by CpG island (Fig. 3A, middle) and features (Fig. 3A, right). In DMP, there were 57 hypomethylated, 10 hypermethylated, and three mixed CpG positions that exhibited both hypermethylation and hypomethylation in miR-3127–high melanomas (Fig. 3B) while six and two DNA regions of these tumors were hypermethylated and hypomethylated, respectively, in DMR (Fig. 3C) when compare to miR-3127–low melanomas. In summary, *ABCC2*, *ABLIM1*, *CXXC5*, *GAS7*, *HLA-DMA*, *IFITIM1*, *LOC400794*, *PRKD2*, *S100A4*, *SPTBN1*, and *TAPBP* were found to be hypermethylated in miR-3127–high melanomas compared to miR-3127–low melanomas. In methylation GSEA, there were a total of 122 biological processes that were significantly altered. Epigenetic dysregulation took place in several cancer-related processes, including SATB1 targets (adjusted $p < .001$), uveal melanoma signal (adjusted $p < .001$), tropomyosin receptor kinase receptor (TRKR) pathway (adjusted $p < .001$), EZH2 targets (adjusted $p < .001$), and mammalian target of rapamycin (mTOR) pathway (adjusted $p < .001$) (Fig. 3D). The full result is shown in Supplementary Table S5.

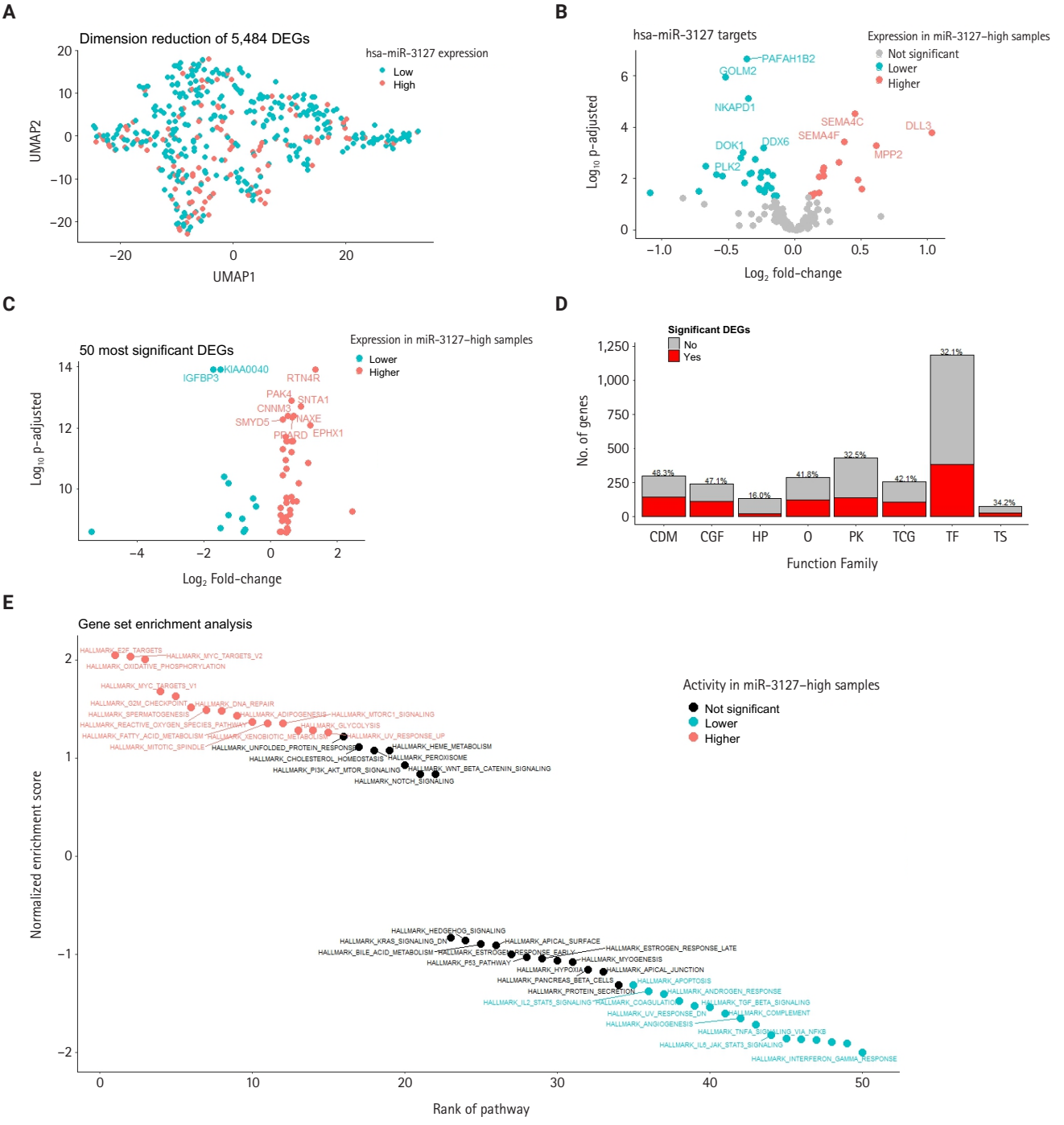

Fig. 2. Gene expression and pathway analysis by miR-3127 groups. (A) Uniform manifold approximation and projection dimension reduction plot showing mRNA space color-coded by miR-3127 expression status. (B) Volcano plot displaying DESeq2 results for mRNA expression limited to miR-3127 target genes. (C) Volcano plot displaying DESeq2 results for overall mRNA expression considering the 50 most significant genes out of 60,660 genes, with the top 10 most significant genes labeled. (D) Bar plot illustrating the proportion of differentially expressed genes (DEGs) across functional families, including cell differentiation markers (CDM), cytokines and growth factors (CGF), homeodomain proteins (HP), oncogenes (O), protein kinases (PK), translocated cancer genes (TCG), transcription factors (TF), and tumor suppressors (TS). (E) Correlogram presenting normalized enrichment scores in descending order from left to right.

https://doi.org/10.4132/jptm.2025.07.08

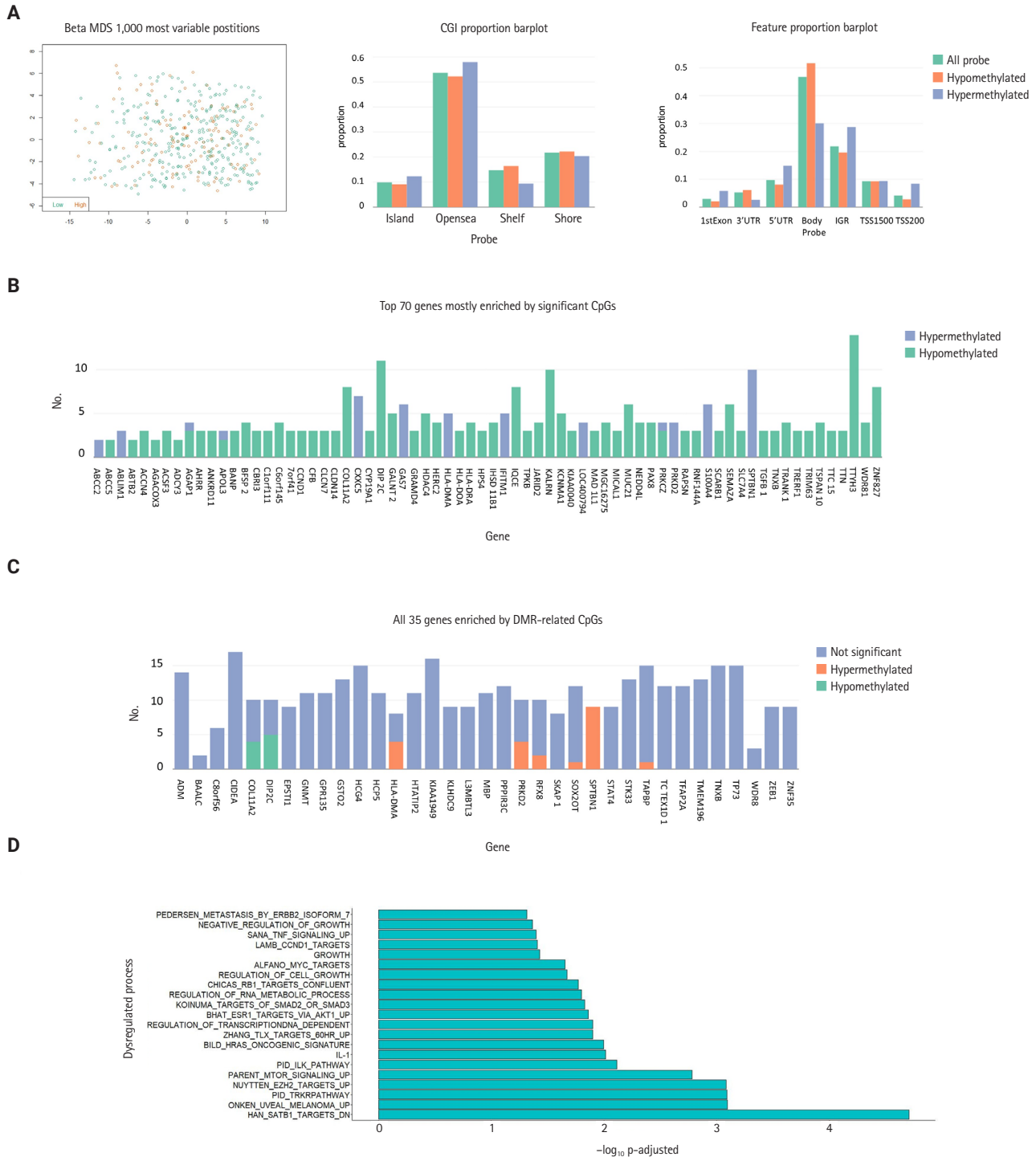

Fig. 3. Methylation analysis in relation to miR-3127 expression. (A) Multidimensional scaling (MDS) plot of methylation patterns in miR-3127–low and miR-3127–high samples (left). Bar plots summarizing hypomethylated and hypermethylated probes in miR-3127–high samples by CpG island category (middle) and feature type (right). (B) Bar plot showing the top 70 significant genes based on differentially methylated probes in miR-3127–high versus miR-3127–low melanomas. (C) Bar plot showing the top 35 significant genes based on differentially methylated regions (DMRs) in miR-3127–high versus miR-3127–low melanomas. (D) Horizontal bar plot summarizing methylation gene set enrichment analysis results.

DISCUSSION

Melanoma, the most prevalent malignant skin cancer, is marked by rising incidence, mortality rates, and significant disease burden [1,2]. Despite advancements in diagnosis and treatment, the three-year survival rate is still poor, particularly for metastatic melanoma [3]. The identification of appropriate biomarkers is needed to enhance prognostication and overall outcomes for patients with melanoma.

Accumulating evidence suggests that miRNAs play crucial roles in various stages of cancer development, including melanoma [4,13]. Some studies have highlighted miRNAs as potential biomarkers for cancer diagnosis, targeted therapy, and prognosis [14,15]. Whether miR-3127 functions as an oncogene or TS depends on its target genes. For instance, miR-3127-5p has been shown to be a TS in non–small-cell lung cancer (NSCLC), wherein a decrease in miR-3127-5p levels encourages epithelial-mesenchymal transition by activating the WNT/FZD4/β-catenin signaling pathway, thereby promoting tumor progression and metastasis. [6]. Another study revealed that miR-3127 suppresses NSCLC cell proliferation and invasion by regulating the oncogene *ABL1*, leading to the inhibition of the RAS/ERK pathway [16]. Interestingly, in HCC, miR-3127 acts as an oncogene by activating AKT/FOXO1 signaling through direct targeting of the 3'-UTR of *PHLPP1/2* [7]. However, the mechanisms and target genes of miR-3127 in melanoma remain unclear. To our knowledge, this study is the first to explore the expression patterns of miR-3127 and its association with patient survival in a melanoma patient cohort.

In this study, we investigated the expression of miR-3127 in melanoma samples by utilizing The Cancer Genome Atlas (TCGA) miRNAs, mRNA-sequencing, and DNA methylation data for subsequent analysis. Our findings revealed that patients with elevated miR-3127 levels (≥20.3 RPM) exhibited significantly poorer PFS and OS compared to those with lower miR-3127 levels. miR-3127 expression was found to be independent of metastatic status. In metastatic melanoma, elevated miR-3127 levels were linked to the worst clinical outcomes. Interestingly, non-metastatic patients with high miR-3127 expression demonstrated even lower OS and DFS than those with low miR-3127 expression in metastatic cases. These findings indicate that elevated miR-3127 expression may be a useful prognostic marker in melanoma, both in early-stage disease and in metastatic settings.

Moreover, we uncovered evidence implicating miR-3127 in several biological pathways pertinent to the pathogenesis of melanoma. In miR-3127–high melanoma, five other upregulated miRNAs were identified: miR-1301, miR-3691, miR-6509, miR-3150b, and miR-3680-1. Most of these miRNAs have established roles in tumor cell proliferation, invasion, or metastasis. miR-1301 is a recently discovered miRNA that exhibits abnormal expression across various tumors types, and dysregulated expression of miR-1301 is often linked to a poor prognosis. Studies have shown its involvement in promoting invasion, migration, and epithelial-mesenchymal transition progression by downregulating *NBL1* expression in esophageal cancer and facilitating cell proliferation via targeting *SIRT1* in gastric cancer [17-19]. Similarly, miR-3691-5p promotes HCC cell migration and invasion by activating phosphoinositide 3-kinase (PI3K)/Akt signaling through targeting PTEN [20]. miR-6509 has been associated with the progression of HCC in SNHG6/miR-6509-5p/HIF1A axis function and gastric cancer by binding to the long non-coding RNA *HOXA10-AS* to upregulate Y-box binding protein 1 [21,22]. Meanwhile, miR-3150b-3p is thought to act as a TS in colorectal cancer and HCC by inhibiting cancer cell proliferation, migration, and invasion through targeting *GOLPH3* via the GOLPH3-mediated JAK2/STAT3 pathway [23,24]. Prior research on miR-3680-1 is limited. Although there are no prior studies investigating the association between these miRNAs and melanoma, their active expression in other cancer types suggests that they may be worth exploring as new therapeutic targets.

To further elucidate the active mechanisms of miR-3127, we conducted target gene predictions and observed elevated expression of *SEMA4C*, *KIAA1522*, *DLL3*, *SEMA4F*, and *MPP2* in miR-3127–high tumors. *SEMA4C* was an important regulator of axonal guidance linked to tumor development. High *SEMA4C* expression is associated with the promotion of epithelial-mesenchymal transition and predicts a poor prognosis in colorectal carcinoma [25]. *KIAA1522* is involved in oncogenic KRAS pathways, and its high expression serves as an independent biomarker predicting unfavorable survival and platinum resistance in NSCLC patients [26]. *KIAA1522* also promotes the in vitro proliferation, invasion, and migration of tumor cells, as well as distant metastasis of colorectal cancer in vivo. Additionally, *KIAA1522* upregulates the Notch signaling pathway in colorectal cancer cell lines in vitro and lung metastatic nodes in vivo [27]. *DLL3* plays a pivotal role in Notch signaling, influencing various cellular processes such as differentiation, proliferation, survival, and apoptosis [28]. *SEMA4F* acts as a

https://doi.org/10.4132/jptm.2025.07.08

key regulator of tumorigenesis and is associated with the activity-dependent progression of glioblastoma [29]. The elevated expression of these genes supports the notion of a poor prognosis in the miR-3127–high tumors group.

We identified numerous DEGs between miR-3127–high and miR-3127–low melanoma samples. Among the upregulated genes in the miR-3127–high group were *RTN4R*, *PAK4*, *SNTA1*, *CNNM3*, *NAXE*, *SMYD5*, *PPARD*, and *EPHX1*, while *IGFBP3* and *KIAA0040* were downregulated. These genes are associated with various functions including as CDM, cytokines, growth factors, TCG, and oncogenes. For instance, *PAK4* is a member of the PAK family and plays a crucial role in regulating cell adhesion, migration, proliferation, and survival. Its expression is frequently dysregulated in cancer [30,31]. *SNTA1*/*P66shc*-mediated Rac1 activation has been linked to increased reactive oxygen species production and migratory potential in breast cancer cells [32]. The protein tyrosine phosphatase PRL-2 forms a complex with the magnesium transporter CNNM3 to promote tumorigenesis [33]. Conversely, *IGFBP-3*, which was downregulated in tumors with elevated miR-3127 levels, binds to insulin-like growth factors to inhibit cell proliferation [34].

Pathway analysis demonstrated that genes predominantly associated with cell cycle functions, DNA repair, response to UV exposure, and metabolic were enriched in melanomas with high miR-3127 levels. Conversely, miR-3127–low samples exhibited enrichment in inflammation-related genes, such as elevated expression of *PAFAH1B2*, a key player in inflammation and anaphylaxis [35]. The impact of inflammation on cancer is double-edged: it can either promote or suppress tumor progression. Chronic inflammation tends to facilitate tumor development and resistance to treatment, while acute inflammatory reactions can stimulate dendritic cell maturation, antigen presentation, and anti-tumor immune responses [36,37], which could account for the favorable prognosis seen in patients with low miR-3127 levels. Additionally, in methylation GSEA, a total of 122 biological processes were significantly altered, indicating epigenetic dysregulation in various cancer-related processes such as those mediated by SATB1 targets, uveal melanoma signal, the TRKR pathway, EZH2 targets, and the mTOR pathway.

While miRNA signatures have shown promise as prognostic markers for melanoma, there are challenges associated with their application. A key limitation of this research is inherent to performing bioinformatic analysis from the TCGA database. There is a need to establish standardized methodologies to conduct larger studies with independent validation sets to ensure the reliability of miRNA signatures detected in these analyses. Addressing these challenges will contribute to the effective utilization of miR-3127 signatures in clinical settings.

Our findings demonstrate that miR-3127 is a useful biomarker to predict prognosis of melanoma, with increased expression of miR-3127 being associated with an unfavorable prognosis. These results suggest that miR-3127 may play an important role in the complex mechanisms underlying the multi-step process of melanoma progression. The expression profile of miR-3127 could function as a prognostic indicator, aiding in the management and treatment of patients with melanoma.

Supplementary Information

The Data Supplement is available with this article at https://doi.org/10.4132/jptm.2025.07.08.

Ethics Statement

Not applicable.

Availability of Data and Material

The datasets used and analyzed during the current study are available from the corresponding author on reasonable request.

Code Availability

Not applicable.

ORCID

Truong Phan-Xuan Nguyen https://orcid.org/0000-0001-6965-5863
Minh-Khang Le https://orcid.org/0000-0002-4571-0888
Chau M. Bui https://orcid.org/0000-0002-5371-6251
Vuong Gia Huy https://orcid.org/0000-0001-6213-765X

Author Contributions

Conceptualization: TPXN, MKL, CMB, VGH. Data curation: TPXN, MKL. Formal analysis: TPXN, MKL. Investigation: TPXN, MKL. Methodology: TPXN, MKL, CMB, VGH. Project administration: TPXN, VGH. Resources: TPXN, MKL. Software: MKL. Supervision: VGH. Validation: TPXN, MKL. Visualization: MKL. Writing—original draft: TPXN. Writing—review & editing: MKL, CMB, VGH. Approval of final manuscript: all authors.

Conflicts of Interest
The authors declare that they have no potential conflicts of interest.

Funding Statement
No funding to declare.

REFERENCES

1. Karimi K, Lindgren TH, Koch CA, Brodell RT. Obesity as a risk factor for malignant melanoma and non-melanoma skin cancer. Rev Endocr Metab Disord 2016; 17: 389-403.
2. Sung H, Ferlay J, Siegel RL, et al. Global cancer statistics 2020: GLOBOCAN estimates of incidence and mortality worldwide for 36 cancers in 185 countries. CA Cancer J Clin 2021; 71: 209-49.
3. Song X, Zhao Z, Barber B, Farr AM, Ivanov B, Novich M. Overall survival in patients with metastatic melanoma. Curr Med Res Opin 2015; 31: 987-91.
4. Lin S, Gregory RI. MicroRNA biogenesis pathways in cancer. Nat Rev Cancer 2015; 15: 321-33.
5. Wang X, Meng R, Hu QM. LINC00319-mediated miR-3127 repression enhances bladder cancer progression through upregulation of RAP2A. Front Genet 2020; 11: 180.
6. Yang Y, Sun Y, Wu Y, et al. Downregulation of miR-3127-5p promotes epithelial-mesenchymal transition via FZD4 regulation of Wnt/beta-catenin signaling in non-small-cell lung cancer. Mol Carcinog 2018; 57: 842-53.
7. Jiang J, Zhang Y, Guo Y, et al. MicroRNA-3127 promotes cell proliferation and tumorigenicity in hepatocellular carcinoma by disrupting of PI3K/AKT negative regulation. Oncotarget 2015; 6: 6359-72.
8. Hothorn T, Lausen B. On the exact distribution of maximally selected rank statistics. Comput Stat Data Anal 2003; 43: 121-37.
9. Peace KE. Design and analysis of clinical trials with time-to-event endpoints. Boca Raton: CRC Press, 2018.
10. Love MI, Huber W, Anders S. Moderated estimation of fold change and dispersion for RNA-seq data with DESeq2. Genome Biol 2014; 15: 550.
11. Subramanian A, Tamayo P, Mootha VK, et al. Gene set enrichment analysis: a knowledge-based approach for interpreting genome-wide expression profiles. Proc Natl Acad Sci U S A 2005; 102: 15545-50.
12. Tian Y, Morris TJ, Webster AP, et al. ChAMP: updated methylation analysis pipeline for Illumina BeadChips. Bioinformatics 2017; 33: 3982-4.
13. Gulyaeva LF, Kushlinskiy NE. Regulatory mechanisms of microRNA expression. J Transl Med 2016; 14: 143.
14. Lu T, Chen S, Qu L, Wang Y, Chen HD, He C. Identification of a five-miRNA signature predicting survival in cutaneous melanoma cancer patients. PeerJ 2019; 7: e7831.
15. Yerukala Sathipati S, Ho SY. Survival associated miRNA signature in patients with head and neck carcinomas. Heliyon 2023; 9: e17218.
16. Sun Y, Chen C, Zhang P, et al. Reduced miR-3127-5p expression promotes NSCLC proliferation/invasion and contributes to dasatinib sensitivity via the c-Abl/Ras/ERK pathway. Sci Rep 2014; 4: 6527.
17. Zhong C, Dong Y, Zhang Q, Yuan C, Duan S. Aberrant expression of miR-1301 in human cancer. Front Oncol 2021; 11: 789626.
18. Du J, Zhang S, Zhang X, et al. miR-1301-3p promotes invasion and migration and EMT progression in esophageal cancer by downregulating NBL1 expression. Thorac Cancer 2023; 14: 3032-41.
19. Luo D, Fan H, Ma X, et al. miR-1301-3p promotes cell proliferation and facilitates cell cycle progression via targeting SIRT1 in gastric cancer. Front Oncol 2021; 11: 664242.
20. Du W, Zhang X, Wan Z. miR-3691-5p promotes hepatocellular carcinoma cell migration and invasion through activating PI3K/Akt signaling by targeting PTEN. Onco Targets Ther 2019; 12: 4897-906.
21. Fan X, Zhao Z, Song J, et al. LncRNA-SNHG6 promotes the progression of hepatocellular carcinoma by targeting miR-6509-5p and HIF1A. Cancer Cell Int 2021; 21: 150.
22. Li S, Lu C, Li X, et al. LncRNA HOXA10-AS functions as an oncogene by binding miR-6509-5p to upregulate Y-box binding protein 1 in gastric cancer. Bioengineered 2022; 13: 11373-87.
23. Zhang W, Chen X, Jia J. MiR-3150b-3p inhibits the progression of colorectal cancer cells via targeting GOLPH3. J Investig Med 2020; 68: 425-9.
24. Zhang Y, Wang J, Su H. MiR-3150b inhibits hepatocellular carcinoma cell proliferation, migration and invasion by targeting GOLPH3. J Investig Med 2020; 68: 770-5.
25. Hou Y, Wang W, Zeng Z, et al. High SEMA4C expression promotes the epithelial-mesenchymal transition and predicts poor prognosis in colorectal carcinoma. Aging (Albany NY) 2020; 12: 21992-2018.
26. Liu YZ, Yang H, Cao J, et al. KIAA1522 is a novel prognostic biomarker in patients with non-small cell lung cancer. Sci Rep 2016; 6: 24786.
27. Yi X, Hu C, Zhang C, et al. KIAA1522 is a new biomarker of

https://doi.org/10.4132/jptm.2025.07.08

promoting the tumorigenesis and distant metastasis of colorectal carcinoma. Cell Signal 2022; 90: 110202.
28. Bulman MP, Kusumi K, Frayling TM, et al. Mutations in the human delta homologue, DLL3, cause axial skeletal defects in spondylocostal dysostosis. Nat Genet 2000; 24: 438-41.
29. Huang-Hobbs E, Cheng YT, Ko Y, et al. Remote neuronal activity drives glioma progression through SEMA4F. Nature 2023; 619: 844-50.
30. Won SY, Park JJ, Shin EY, Kim EG. PAK4 signaling in health and disease: defining the PAK4-CREB axis. Exp Mol Med 2019; 51: 1-9.
31. Costa TD, Stromblad S. Why is PAK4 overexpressed in cancer? Int J Biochem Cell Biol 2021; 138: 106041.
32. Bhat HF, Baba RA, Adams ME, Khanday FA. Role of SNTA1 in Rac1 activation, modulation of ROS generation, and migratory potential of human breast cancer cells. Br J Cancer 2014; 110: 706-14.
33. Hardy S, Uetani N, Wong N, et al. The protein tyrosine phosphatase PRL-2 interacts with the magnesium transporter CNNM3 to promote oncogenesis. Oncogene 2015; 34: 986-95.
34. Kim HS. Role of insulin-like growth factor binding protein-3 in glucose and lipid metabolism. Ann Pediatr Endocrinol Metab 2013; 18: 9-12.
35. Ma C, Guo Y, Zhang Y, et al. PAFAH1B2 is a HIF1a target gene and promotes metastasis in pancreatic cancer. Biochem Biophys Res Commun 2018; 501: 654-60.
36. Zhao H, Wu L, Yan G, et al. Inflammation and tumor progression: signaling pathways and targeted intervention. Signal Transduct Target Ther 2021; 6: 263.
37. Schreiber RD, Old LJ, Smyth MJ. Cancer immunoediting: integrating immunity's roles in cancer suppression and promotion. Science 2011; 331: 1565-70.

JPTM

ORIGINAL ARTICLE

pISSN 2383-7837 · eISSN 2383-7845

Journal of Pathology and Translational Medicine 2025; 59: 382-389
https://doi.org/10.4132/jptm.2025.07.10

Attitudes toward artificial intelligence in pathology: a survey-based study of pathologists in northern India

Manupriya Sharma[1], Kavita Kumari[2], Navpreet[3], Sushma Bharti[4], Rajneesh Kumari[2]

[1]Department of Pathology and Lab Medicine, All India Institute of Medical Sciences, Bilaspur, India
[2]Department of Pathology, Dr. Radhakrishnan Government Medical College, Hamirpur, Himachal Pradesh, India
[3]Department of Community and Family Medicine, All India Institute of Medical Sciences, Bilaspur, India
[4]Tata Main Hospital, Jamshedpur, Jharkhand, India

Graphical abstract

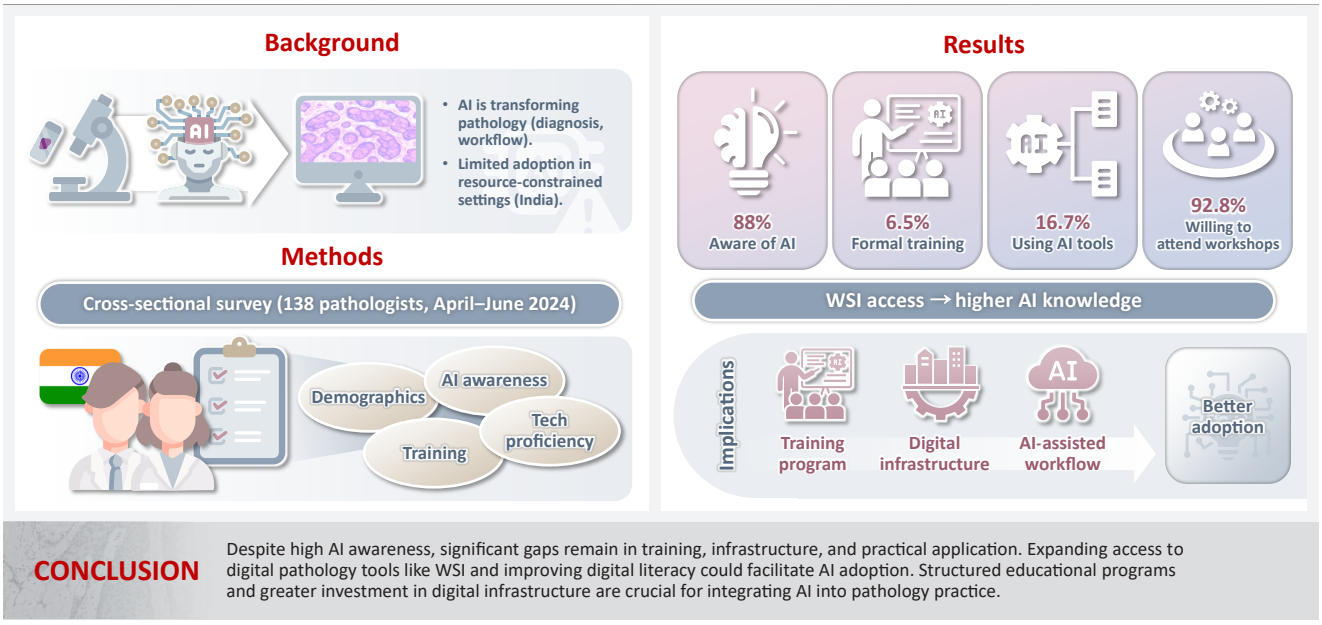

Sharma M et al. Journal of Pathology and Translational Medicine

JPTM

ORIGINAL ARTICLE

pISSN 2383-7837 · eISSN 2383-7845

Journal of Pathology and Translational Medicine 2025; 59: 382-389
https://doi.org/10.4132/jptm.2025.07.10

Attitudes toward artificial intelligence in pathology: a survey-based study of pathologists in northern India

Manupriya Sharma[1], Kavita Kumari[2], Navpreet[3], Sushma Bharti[4], Rajneesh Kumari[2]

[1]Department of Pathology and Lab Medicine, All India Institute of Medical Sciences, Bilaspur, India
[2]Department of Pathology, Dr. Radhakrishnan Government Medical College, Hamirpur, Himachal Pradesh, India
[3]Department of Community and Family Medicine, All India Institute of Medical Sciences, Bilaspur, India
[4]Tata Main Hospital, Jamshedpur, Jharkhand, India

Background: Artificial intelligence (AI) is transforming pathology by enhancing diagnostic accuracy, efficiency, and workflow standardization. Despite its growing presence, AI adoption remains limited, particularly in resource-constrained settings like India. This study assessed the knowledge, awareness, and perceptions of AI among pathologists in Northern India. **Methods:** A cross-sectional survey was conducted among 138 practicing pathologists in Northern India between April and June 2024. A structured online questionnaire was used to collect data on demographics, AI awareness, self-reported knowledge, sources of AI education, technological proficiency, and interest in AI-related training programs. Data analysis included descriptive statistics and chi-square tests, with $p < .05$ considered statistically significant. **Results:** AI awareness was high (88.4%), with significant sex differences (93.5% in females vs. 78.3% in males, $p = .008$). However, formal AI training was limited (6.5%), and only 16.7% had used AI as a diagnostic tool. Academic pathologists were more likely to engage with AI literature than their non-academic counterparts ($p = .003$). Interest in AI workshops was strong (92.8%). Access to whole slide imaging (WSI) correlated with higher AI knowledge ($p = .008$), as did self-reported technological proficiency ($p = .001$). **Conclusions:** Despite high AI awareness among pathologists, significant gaps remain in training, infrastructure, and practical application. Expanding access to digital pathology tools like WSI and improving digital literacy could facilitate AI adoption. Structured educational programs and greater investment in digital infrastructure are crucial for integrating AI into pathology practice.

Keywords: Artificial intelligence; Image interpretation; Computer assisted

INTRODUCTION

Artificial intelligence (AI), defined as the simulation of human intelligence by machines, has become a transformative force in medicine, particularly in diagnostic disciplines such as pathology [1]. Historically, pathology has relied on light microscopy and manual interpretation of glass slides, making diagnostic processes labor-intensive and subjective. However, the advent of whole slide imaging (WSI) scanners has revolutionized the field by enabling digital pathology. WSI technology allows the digitization of glass slides into high-resolution images, providing enhanced opportunities for data storage, retrieval, and computational analysis that were not possible with traditional microscopy [2,3].

The transition from analog to digital workflows has been further supported by the widespread availability of high-speed internet, cloud storage, and a growing interest in telepathology, enabling remote diagnostic practices and collaboration. These advancements have laid the foundation for the integration of AI into pathology workflows, improving the precision and efficiency of diagnosis [4-6].

Among AI technologies, automated analysis of histopathological images, applications such as tumor detection, immunostaining evaluation, pattern recognition, and diagnostic

Received: February 16, 2025 **Revised:** June 11, 2025 **Accepted:** July 10, 2025
Corresponding Author: Manupriya Sharma, MD, DNB
Department of Pathology and Lab Medicine, All India Institute of Medical Sciences, Bilaspur 174001, India
Tel: +91-8628000105, Fax: E-mail: manupriya.priyasharma@gmail.com

classification have shown promising results. Additionally, AI tools have been employed for tasks requiring precision, such as tumor margin assessment and recommending diagnostic or genetic panels [7-11]. For example, based on morphological assessment, AI systems may recommend appropriate immunohistochemical stains or molecular/genetic panels to support accurate diagnosis and guide personalized treatment planning.

Despite its potential, AI adoption in pathology remains in its infancy, especially in resource-constrained settings like India, where challenges such as limited infrastructure, insufficient training, and lack of awareness persist [7,12]. Recognizing the importance of understanding AI's role and adoption readiness, this study aims to assess pathologists' knowledge, perceptions, and interest in AI applications. By analyzing responses from professionals with diverse backgrounds, the study identifies gaps and barriers to AI adoption while offering actionable insights for effective integration into pathology practices.

MATERIALS AND METHODS

Study design, study area, study duration and sampling technique

The cross-sectional study was conducted among pathologists from April 1, 2024 to June 30, 2024 who were working in northern India after obtaining approval from the Institutional Ethics Committee of Dr. Radhakrishnan Government Medical College, Hamirpur, Himachal Pradesh (IEC No. HFW-H-Dr. RKGMC/Ethics/2023/23 dated 10/20/23). Convenience sampling was used to collect the data from participants per the inclusion and exclusion criteria.

Inclusion criteria included (1) practicing pathologists (senior residents, faculty, private practitioners); (2) affiliated with academic institutions, tertiary care centers, or private labs; (3) willing to participate and located in Northern India.

Exclusion criteria were (1) non-pathologists or non-practicing pathologists and (2) incomplete or duplicate survey responses.

Data collection tool

Data were collected from the participants with the help of a structured and anonymous questionnaire to explore the attitudes of pathologists toward AI. The questionnaire was meticulously designed to capture a broad spectrum of information, including demographics, professional background, AI awareness, technological proficiency, and practical experiences with AI in pathology.

The questionnaire was divided into three key thematic sections and comprised 15 questions as shown in Fig. 1. The first section focused on demographics and professional background (Q1–Q5). This section gathered details such as age, sex, professional designation, years of experience, and practice setting (academic, private, or institutional). The second section addressed awareness and knowledge of AI (Q6–Q12), evaluating participants' familiarity with AI concepts, sources of AI knowledge, self-assessed expertise, prior exposure to AI in pathology, and formal training. Participants rated their AI knowledge using four categories: 'no knowledge' (never heard of AI in pathology), 'basic knowledge' (general awareness without practical experience), 'good knowledge' (familiarity with concepts and some tool exposure), and 'excellent knowledge' (confidence in understanding and practical application). These were self-perceived levels, and no external validation was applied, which is an acknowledged limitation.

In the third section, technological proficiency and current practices (Q13–Q15) were assessed. This section assessed respondents' comfort with digital tools, access to WSI, and their reliance on diagnostic modalities like traditional microscopy.

Data collection method

Data were collected by administering a questionnaire online using Google Forms. The link was disseminated electronically through email and professional WhatsApp groups targeting pathologists across various institutions in Northern India. Participation was entirely voluntary, and anonymity was ensured to encourage unbiased responses. Consent was obtained from the participants through a Google Form, and confidentiality of data was ensured.

Statistical analysis

Data were entered in Microsoft Excel 2010 (Microsoft, Richmond, WA, USA) and analyzed. The categorical variables were expressed as frequency and percentage. The continuous variables were expressed as mean and standard deviation. Comparison of categorical variables was carried out using chi-square test and Fisher's exact test. All statistical analysis was done at a 5% level of significance, and a p-value < .05 was considered as significant.

Section 1: Demographics and professional background
Q1. I work as a pathologist and regularly report surgical cases.
☐ Yes ☐ No
Q2. What is your professional background?
☐ Postgraduate student ☐ Senior resident ☐ Private practicing pathologist
☐ Faculty (Less than 5 years experience). ☐ Faculty (More than 5 years experience)
Q3. What is your age?
_____ years
Q4. What is your gender?
☐ Male ☐ Female ☐ Other
Q5. In what kind of practice setting do you mainly work?
☐ Non-teaching hospital ☐ Tertiary care center
☐ State medical college ☐ Private pathology lab
Section 2: Awareness and education on AI in pathology
Q6. Are you aware of the recent interest in AI within the pathology community?
☐ Yes ☐ No
Q7. Your knowledge about artificial intelligence in pathology is based on:
☐ Social media ☐ Conferences
☐ Friends
Q8. What degree of knowledge do you have regarding AI in pathology?
☐ Excellent knowledge ☐ Good knowledge
☐ Basic knowledge ☐ No Knowledge
Q9. Have you read any medical publication regarding artificial intelligence within pathology?
☐ Yes ☐ No
Q10. Have you used artificial intelligence as a diagnostic aid in real life within pathology?
☐ Yes ☐ No
Q11. Have you undergone any formal training in AI for pathology?
☐ Yes ☐ No
Q12. Would you be interested in attending workshops or courses related to AI in pathology?
☐ Yes ☐ No
Section 3: Technological proficiency and current practices
Q13. Would you consider yourself to be tech-savvy? (i.e., knowing a lot about modern technology and how to use it)
☐ Yes ☐ No
Q14. Do you have access to whole slide imaging at work?
☐ Yes ☐ No
Q15. When I use surgical pathology, I mainly work on:
☐ Microscope and glass slides ☐ Digitally scanned slides

Fig. 1. Survey on artificial intelligence (AI) in pathology.

https://doi.org/10.4132/jptm.2025.07.10

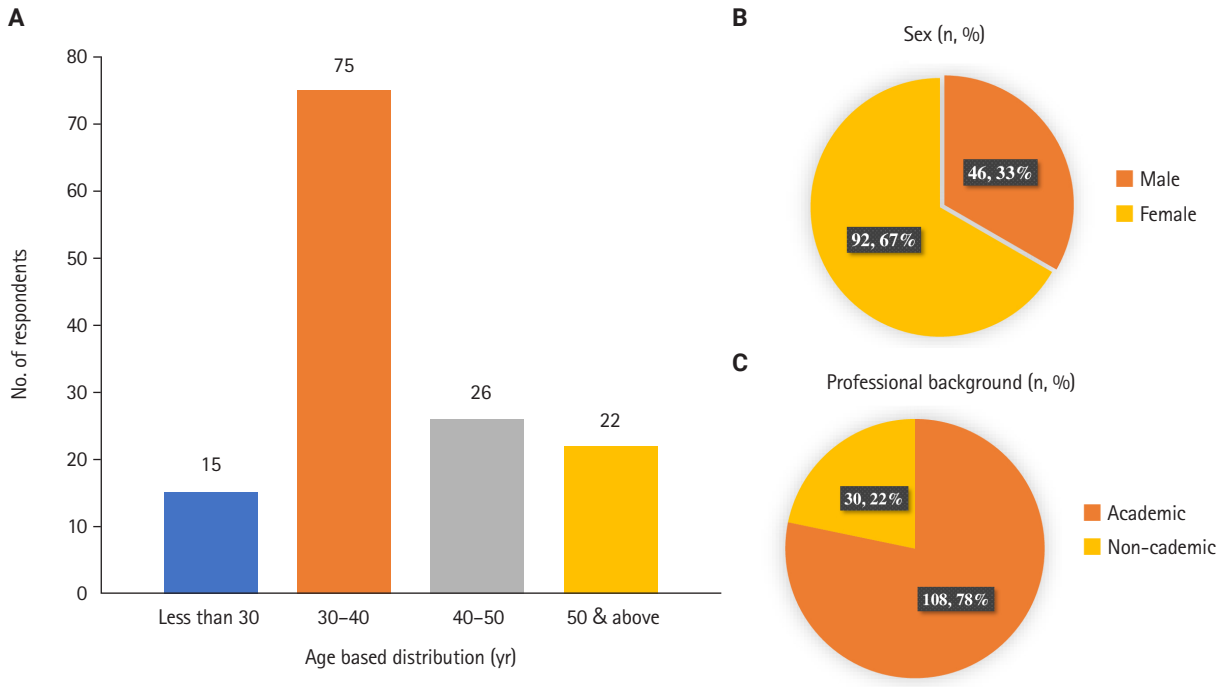

Fig. 2. Demographic details of respondents. (A) Age distribution of respondents. (B) Sex distribution of respondents. (C) Professional background of respondents.

RESULTS

Demographics and professional background

A total of 138 pathologists completed the survey. An overview of the age and sex distribution of the respondents as well as other demographic data are presented in Fig. 2. Detailed individual-level survey responses are provided in Supplementary Table S1.

The majority of respondents were female (66.7%) and aged 30–40 years (54.3%). Most participants were affiliated with academic institutions (78.3%), and faculty members with more than five years of experience constituted the largest subgroup (36.2%). The majority of participants were working in an academic environment, namely. medical colleges (37.7%) and tertiary care centers (34.8%), with 21.7% of respondents working in private practice.

Awareness and knowledge of AI

The survey revealed high levels of awareness regarding AI's role among pathologists, with 88.4% of respondents acknowledging its growing importance. Sex-based differences were found to be statistically significant, with females exhibiting greater awareness than males (93.5% vs. 78.3%, p = .008) as shown in Table 1.

Age-based differences were found to be statistically significant, with older respondents exhibiting greater awareness than younger respondents (95.8% vs. 84.4%, p = .047) as shown in Table 2.

Social media (44.2%) and conferences (41.3%) were the most frequently cited sources of AI knowledge. Formal training in AI was reported by only 6.5% of participants, underscoring a significant gap in education. When asked to self-assess their knowledge of AI in pathology, the majority reported basic knowledge (41.3%) or limited knowledge (39.1%), while only 5.8% rated their knowledge as excellent.

Academic pathologists were significantly more likely to have read medical publications about AI than their non-academic counterparts (57.4% vs. 26.7%, p = .003) as shown in Table 3. A similar trend was observed among females, with a near-significant difference in the number of publications read compared to males (p = .054), as shown in Table 1. Encouragingly, 92.8% of respondents expressed interest in attending AI-related workshops or courses, reflecting a readiness to bridge this knowledge gap.

Table 1. Sex-based awareness and AI training among pathologists

Variable	Female (n = 92)	Male (n = 46)	Total (n = 138)	p-value
Awareness of AI in pathology	86 (93.5)	36 (78.3)	122 (88.4)	.008
Read AI-related medical publications	52 (56.5)	18 (39.1)	70 (50.7)	.054
Used AI as a diagnostic aid	16 (17.4)	7 (15.2)	23 (16.7)	.747
Undergone formal AI training	7 (7.6)	2 (4.3)	9 (6.5)	.718
Interest in AI workshops/courses	89 (96.7)	39 (84.8)	128 (92.8)	.016

Values are presented as number (%).
AI, artificial intelligence.

Table 2. Age-based awareness and AI training among pathologists

Variable	Young responders (<40 yr) (n = 90)	Old responders (≥40 yr) (n = 48)	Total (n = 138)	p-value
Awareness of AI in pathology	76 (84.4)	46 (95.8)	122 (88.4)	.047
Read AI-related medical publications	41 (45.6)	29 (60.4)	70 (50.7)	.096
Used AI as a diagnostic aid	19 (21.1)	4 (8.3)	23 (16.7)	.055
Undergone formal AI training	6 (6.7)	3 (6.3)	9 (6.5)	>.99
Interest in AI workshops/courses	83 (92.2)	45 (93.8)	128 (92.8)	>.99

Values are presented as number (%).
AI, artificial intelligence.

Table 3. Academic vs. non-academic pathologist awareness and AI training

Variable	Academic (n = 108)	Non-academic (n = 30)	Total (n = 138)	p-value
Awareness of AI in pathology	97 (89.8)	25 (83.3)	122 (88.4)	.340
Read AI-related medical publications	62 (57.4)	8 (26.7)	70 (50.7)	.003
Used AI as a diagnostic aid	17 (15.7)	6 (20.0)	23 (16.7)	.580
Undergone formal AI training	6 (5.6)	3 (10.0)	9 (6.5)	.408
Interest in AI workshops/courses	101 (93.5)	27 (90.0)	128 (92.8)	.453

Values are presented as number (%).
AI, artificial intelligence.

Technological proficiency and AI application

Only 16.7% of respondents had used AI as a diagnostic tool in real-world pathology practice. Respondents with good or excellent knowledge were found to be significantly more likely to identify themselves as tech-savvy compared to those with basic or no knowledge (80.0% vs. 43.4%, p = .001), as shown in Table 4.

The respondents with good or excellent AI knowledge also reported significantly better access to WSI compared to those with limited knowledge (48.0% vs. 22.1%, p = .008).

DISCUSSION

This study provides valuable insight into the current state of AI awareness, knowledge, and adoption among pathologists in India. The high levels of awareness observed in this study align with global trends indicating growing interest in AI's transformative potential for pathology [13,14]. However, significant gaps in formal training and practical application highlight barriers that must be addressed to fully realize AI's benefits [15].

The influence of sex and professional setting on AI awareness is noteworthy. While female respondents demonstrated significantly higher awareness levels, this difference may be partially explained by professional affiliation. Notably, 82.6% (76 of 92) of female respondents worked at academic institutions, compared to 58.7% (27 of 46) of males. Given that academic environments offer greater access to AI-related resources and training, this distribution suggests a potential confounding effect, and the observed sex-based differences should be interpreted with caution. Additionally, respondents working in academic institutions exhibited greater familiarity with AI literature, like-

https://doi.org/10.4132/jptm.2025.07.10

Table 4. AI knowledge levels among pathologists based on demographics and technology access

Variable	No or basic knowledge (n = 113)	Good or excellent knowledge (n = 25)	Total	p-value
Sex				
Male	39 (34.5)	7 (28.0)	46 (33.3)	.532
Female	74 (65.5)	18 (72.0)	92 (66.7)	
Age group (yr)				
≥40	39 (34.5)	9 (36.0)	48 (34.8)	.888
<40	74 (65.5)	16 (64.0)	90 (65.2)	
Professional background				
Non-academic	23 (20.4)	7 (28.0)	30 (21.7)	.402
Academic	90 (79.6)	18 (72.0)	108 (78.3)	
Practice setting				
Private setting	26 (23.0)	9 (36.0)	35 (25.4)	.177
Academic environment	87 (77.0)	16 (64.0)	103 (74.6)	
Self-identified as tech-savvy				
Yes	49 (43.4)	20 (80.0)	69 (50.0)	.001
No	64 (56.6)	5 (20.0)	69 (50.0)	
Access to whole slide imaging at work				
Yes	25 (22.1)	12 (48.0)	37 (26.8)	.008
No	88 (77.9)	13 (52.0)	101 (73.2)	

Values are presented as number (%).
AI, artificial intelligence.

ly due to better access to academic resources and exposure to research-oriented environments.

Although awareness of AI among pathologists was high, most respondents rated their knowledge as either basic or limited, highlighting a general lack of deeper understanding. The absence of formal training in AI further reinforces the need for well-structured educational programs to equip pathologists with necessary skills. On a positive note, the majority of participants expressed a strong interest in attending AI-related workshops or courses, showing a clear willingness to close this knowledge gap. These findings emphasize the need to incorporate AI training into pathology education, especially in countries like India, where the adoption of AI in practice is still at an early stage.

Additionally, a pattern emerged suggesting that access to advanced technologies like WSI and comfort with digital tools were key contributors to higher levels of AI knowledge. The limited use of AI tools in practice underscores challenges such as inadequate infrastructure, insufficient training, and limited access to enabling technologies like WSI. These findings suggest that digital pathology infrastructure is crucial for fostering familiarity and expertise with AI-driven workflow.

Interestingly, self-identified tech-savvy respondents demonstrated a stronger association with higher levels of AI knowledge, highlighting the importance of digital literacy in adapting to emerging technologies. These findings underscore the need to prioritize technological training and infrastructure development to promote equitable AI adoption across diverse practice settings.

This study highlighted notable differences in AI exposure between academic and private practice settings, with respondents in academic environments demonstrating greater familiarity with AI literature and concepts. This disparity likely stems from variation in resource availability, institutional support, and exposure to research-oriented activities.

The challenges identified in this Indian cohort mirror those observed globally. Worldwide, the integration of AI into pathology has been met with enthusiasm but also with considerable barriers. A bibliometric analysis revealed that the United States leads the field of AI-based tumor pathology research, contributing 41.3% of publications, followed by China and the United Kingdom [16,17]. This underscores the significant investment and focus on AI in pathology within these countries. In Europe, initiatives such as the Ecosystem for Pathology Diagnostics with AI Assistance (EMPAIA) project have been instrumental in accelerating AI adoption. EMPAIA has facilitated open-

source platforms and interoperability standards, facilitating the integration of AI into clinical workflows across multiple laboratories [18]. Despite such efforts, Chua et al. [19] described system-wide challenges to AI implementation in oncology, including data bias, dynamic knowledge, and user interface design, and proposed actionable steps for overcoming these barriers through multidisciplinary collaboration. These insights affirm that the limitations seen in our study are not isolated but part of a broader global picture.

Infrastructural and technological barriers remain central to the slow uptake of AI in pathology. Specific challenges include the high cost of digital pathology systems, variable internet connectivity, limited access to computational resources, and a lack of trained personnel to manage and interpret AI outputs. Additionally, digital literacy levels vary significantly, particularly in private practice or rural settings. Data security concerns, particularly in handling sensitive patient images and records, further complicate the deployment of AI systems. Addressing these multi-layered issues will require a coordinated response involving institutional investment, government support, and public–private partnerships to create a conducive ecosystem for AI adoption.

One observation from our study is the overrepresentation of younger pathologists, with 65.2% under the age of 40. Notably, this age distribution is consistent with trends reported in both Indian and global pathology surveys [20,21]. This likely reflects greater digital engagement among younger professionals, which may introduce bias and limit the generalizability of the findings to the broader population of practicing pathologists. Future studies involving a more geographically diverse cohort of pathologists would enhance the statistical robustness of the findings and offer a more comprehensive understanding of AI awareness and adoption across different regions.

In conclusion, while awareness and interest in AI are growing among Indian pathologists, there remains a clear gap between recognition and implementation. To bridge this divide, actionable steps must include the development of standardized AI curricula for pathologists; organizing national and regional workshops; fostering collaborations between academic institutions, private sector developers, and healthcare policymakers; and expanding access to digital infrastructure and secure data-sharing platforms. By investing in education, policy, and technology together, the pathology community in India—and globally—can accelerate meaningful and equitable integration of AI into clinical practice.

Supplementary Information

The Data Supplement is available with this article at https://doi.org/10.4132/jptm.2025.07.10.

Ethics Statement

All procedures performed in the current study were approved by the Institutional Ethics Committee of Dr. Radhakrishnan Government Medical College, Hamirpur, H.P (IEC No. HFW-H-Dr. RKGMC/Ethics/2023/23 dated 20/10/23) in accordance with the 1964 Helsinki declaration and its later amendments. Participation in the survey was voluntary, and informed consent was obtained electronically from all participants at the beginning of the questionnaire.

Availability of Data and Material

All data generated or analyzed during the study are included in this published article (and its supplementary information files).

Code Availability

Not applicable.

ORCID

Manupriya Sharma https://orcid.org/0000-0002-6427-6634
Kavita Kumari https://orcid.org/0000-0002-0928-8026
Navpreet https://orcid.org/0000-0003-0927-8888
Sushma Bharti https://orcid.org/0000-0003-1045-1510
Rajneesh Kumari https://orcid.org/0000-0002-0921-9362

Author Contributions

Conceptualization: MS, KK. Data curation: MS, SB. Formal analysis: MS, RK. Investigation: MS. Methodology: MS, SB, N. Project administration: MS. Resources: MS. Supervision: MS. Validation: MS, N, KK. Visualization: MS, N, KK. Writing—original draft: MS, N. Writing—review & editing: all authors. Approval of final manuscript: all authors.

Conflicts of Interest

The authors declare that they have no potential conflicts of interest.

Funding Statement

No funding to declare.

REFERENCES

1. Tizhoosh HR, Pantanowitz L. Artificial intelligence and digital pathology: challenges and opportunities. J Pathol Inform 2018; 9: 38.
2. Bauer TW, Schoenfield L, Slaw RJ, Yerian L, Sun Z, Henricks WH. Validation of whole slide imaging for primary diagnosis in surgical pathology. Arch Pathol Lab Med 2013; 137: 518-24.
3. Fertig RM, Sangueza O, Gaudi S, Gamret AC, Cervantes J, Jukic DM. Whole slide imaging. Am J Dermatopathol 2018; 40: 938-9.
4. Evans AJ, Salama ME, Henricks WH, Pantanowitz L. Implementation of whole slide imaging for clinical purposes: issues to consider from the perspective of early adopters. Arch Pathol Lab Med 2017; 141: 944-59.
5. Hartman DJ, Pantanowitz L, McHugh JS, Piccoli AL, MJ OL, Lauro GR. Enterprise implementation of digital pathology: feasibility, challenges, and opportunities. J Digit Imaging 2017; 30: 555-60.
6. Thrall M, Pantanowitz L, Khalbuss W. Telecytology: clinical applications, current challenges, and future benefits. J Pathol Inform 2011; 2: 51.
7. Bera K, Schalper KA, Rimm DL, Velcheti V, Madabhushi A. Artificial intelligence in digital pathology: new tools for diagnosis and precision oncology. Nat Rev Clin Oncol 2019; 16: 703-15.
8. Echle A, Rindtorff NT, Brinker TJ, Luedde T, Pearson AT, Kather JN. Deep learning in cancer pathology: a new generation of clinical biomarkers. Br J Cancer 2021; 124: 686-96.
9. Couture HD, Williams LA, Geradts J, et al. Image analysis with deep learning to predict breast cancer grade, ER status, histologic subtype, and intrinsic subtype. NPJ Breast Cancer 2018; 4: 30.
10. Lu MY, Chen TY, Williamson DF, et al. AI-based pathology predicts origins for cancers of unknown primary. Nature 2021; 594: 106-10.
11. Strom P, Kartasalo K, Olsson H, et al. Artificial intelligence for diagnosis and grading of prostate cancer in biopsies: a population-based, diagnostic study. Lancet Oncol 2020; 21: 222-32.
12. Madabhushi A, Lee G. Image analysis and machine learning in digital pathology: challenges and opportunities. Med Image Anal 2016; 33: 170-5.
13. Baxi V, Edwards R, Montalto M, Saha S. Digital pathology and artificial intelligence in translational medicine and clinical practice. Mod Pathol 2022; 35: 23-32.
14. Drogt J, Milota M, Vos S, Bredenoord A, Jongsma K. Integrating artificial intelligence in pathology: a qualitative interview study of users' experiences and expectations. Mod Pathol 2022; 35: 1540-50.
15. Sajithkumar A, Thomas J, Saji AM, et al. Artificial intelligence in pathology: current applications, limitations, and future directions. Ir J Med Sci 2024; 193: 1117-21.
16. Shen Z, Hu J, Wu H, et al. Global research trends and foci of artificial intelligence-based tumor pathology: a scientometric study. J Transl Med 2022; 20: 409.
17. Hanna MG, Pantanowitz L, Dash R, et al. Future of artificial intelligence-machine learning trends in pathology and medicine. Mod Pathol 2025; 38: 100705.
18. Zerbe N, Schwen LO, Geissler C, et al. Joining forces for pathology diagnostics with AI assistance: the EMPAIA initiative. J Pathol Inform 2024; 15: 100387.
19. Chua IS, Gaziel-Yablowitz M, Korach ZT, et al. Artificial intelligence in oncology: path to implementation. Cancer Med 2021; 10: 4138-49.
20. Kanungo R, Sharma A, Pagi S, Sachar K. Exploring occupational health challenges in pathology: a cross-sectional survey of Indian pathologists. Cureus 2024; 16: e75264.
21. Sarwar S, Dent A, Faust K, et al. Physician perspectives on integration of artificial intelligence into diagnostic pathology. NPJ Digit Med 2019; 2: 28.

JPTM

ORIGINAL ARTICLE

pISSN 2383-7837 · eISSN 2383-7845

Journal of Pathology and Translational Medicine 2025; 59: 390-397
https://doi.org/10.4132/jptm.2025.07.11

Adenomatoid odontogenic tumor: clinicopathological analysis of 34 cases from Karachi, Pakistan

Summaya Zafar[1], Sehar Sulaiman[1], Madeeha Nisar[2], Poonum Khan[3], Nasir Ud Din[1]

[1]Section of Histopathology, Department of Pathology and Lab Medicine, Aga Khan University, Karachi, Pakistan
[2]Section of Histopathology, Armed Forces Institute of Pathology, Combined Military Hospital, Rawalpindi, Pakistan
[3]Department of Radiology, Aga Khan University, Karachi, Pakistan

Graphical abstract

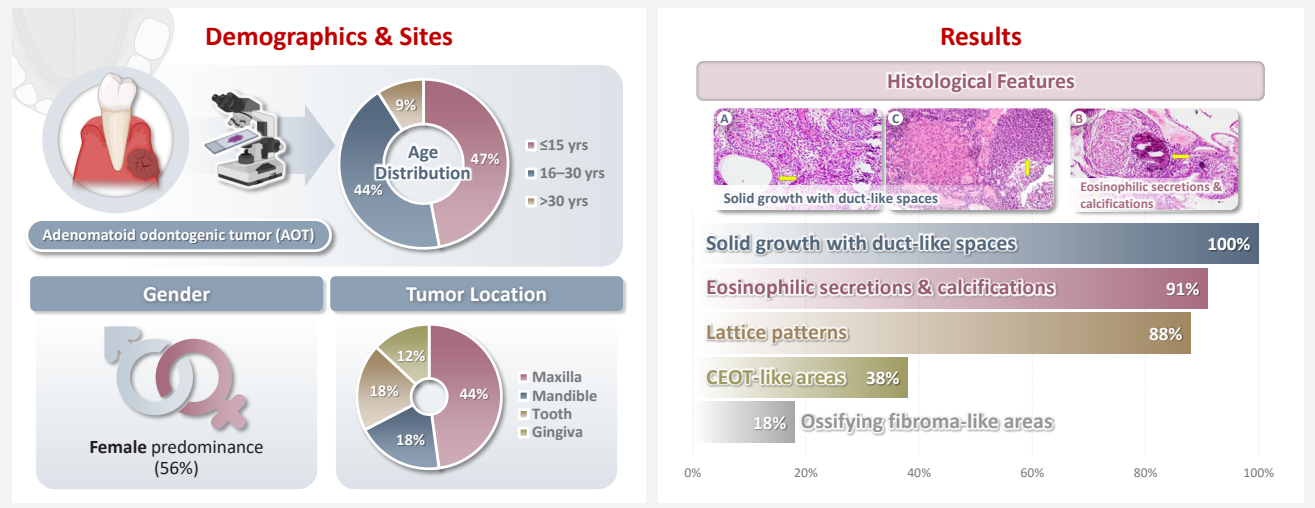

JPTM

ORIGINAL ARTICLE

pISSN 2383-7837 · eISSN 2383-7845

Journal of Pathology and Translational Medicine 2025; 59: 390-397
https://doi.org/10.4132/jptm.2025.07.11

Adenomatoid odontogenic tumor: clinicopathological analysis of 34 cases from Karachi, Pakistan

Summaya Zafar[1], Sehar Sulaiman[1], Madeeha Nisar[2], Poonum Khan[3], Nasir Ud Din[1]

[1]Section of Histopathology, Department of Pathology and Lab Medicine, Aga Khan University, Karachi, Pakistan
[2]Section of Histopathology, Armed Forces Institute of Pathology, Combined Military Hospital, Rawalpindi, Pakistan
[3]Department of Radiology, Aga Khan University, Karachi, Pakistan

Background: Adenomatoid odontogenic tumor (AOT) is a benign slow-growing neoplasm of odontogenic epithelial origin that is relatively uncommon. Only a few studies have described its histological features. Hence, we aimed to describe the clinicopathological features of AOT in a cohort of patients. **Methods:** AOT cases diagnosed between 2009 and 2024 were searched electronically. Glass slides were retrieved from archives and were reviewed by two pathologists to record the associated morphological features. Other data including patient demographics and tumor site were collected by reviewing histopathology reports. **Results:** The age of patients ranged from 9 to 44 years (mean, 17.7 years), and most were female (55.9%). The maxilla (44.1%) was the most common tumor site. Histologically, a predominantly solid growth pattern (n = 34) accompanied by ducts with a cuboidal/columnar epithelial lining (n = 31), eosinophilic secretions (n = 31), calcifications (n = 31), lattice work pattern (n = 30), and cystic areas (n = 20) were observed. Less frequent features included calcifying epithelial odontogenic tumor (CEOT)–like areas (n = 13), osteodentin (n = 6), association with impacted tooth (n = 3), mucin in tubules (n = 7), fibrocollagenous stroma (n = 6), mucin in ducts (n = 3) and ossifying fibroma-like areas (n = 6). The association of ducts with a cuboidal/columnar epithelial lining, lattice work pattern, calcifications, and eosinophilic secretions with gingival tumors was statistically significant ($p \leq .05$). Additionally, tooth tumors were significantly associated with CEOT-like areas ($p = .03$). **Conclusions:** Our study confirms the trends in the clinicopathological features of AOT in previous case reports. Our results suggest that AOTs usually exhibit a predominantly solid pattern with duct-like spaces. Only a few cases with CEOT-like and ossifying fibroma-like areas were observed, similar to infrequent cases reported in the past.

Keywords: Adenomatoid odontogenic tumor; Benign neoplasm; Histopathology

INTRODUCTION

Adenomatoid odontogenic tumor (AOT) is relatively uncommon, representing less than 3% of all odontogenic tumors [1-3]. It is a benign, slow-growing neoplasm of odontogenic epithelial origin [1-3] that originates from the remains of the dental lamina or the enamel organ [1,4-6]. The term "adenomatoid odontogenic tumor" was first coined by Philipsen et al. in 1969 and was later adopted by the World Health Organization [2-5,7,8].

The three clinical manifestations of AOT are extra-osseous (on the gingiva, often called peripheral; 5% of cases), intra-osseous extra-follicular (present between erupted teeth; 25% of cases), and intra-osseous follicular (associated with impacted teeth; 70% of cases) [1]. The most frequent sites for AOT are the mandible and the anterior maxilla, with the maxilla involved nearly twice as frequently as the mandible [3,9]. Follicular variants are more frequently linked to impacted maxillary canines, accounting for 60% of cases [1,3,10]. Although infrequently reported at sites beyond the premolars, AOT cases have also been observed in the maxilla and posterior mandible. The anterior maxilla accounts for about 53% of cases, while the maxillary premolar area accounts for 9% [11]. Approximately

Received: February 18, 2025 **Revised:** June 3, 2025 **Accepted:** July 10, 2025
Corresponding Author: Summaya Zafar, MBBS
Section of Histopathology, Department of Pathology and Lab Medicine, Aga Khan University, National Stadium Rd, Karachi City, Sindh, Pakistan
Tel: +92-3471244479, E-mail: dr.summaiyazafar@gmail.com

2% of cases involve the molar region [11]. AOT is more prevalent in females than males, with a nearly 2:1 female-male ratio [1,3,12]. About 70% of AOT cases occur between the ages of 10 and 19, with fewer cases occurring beyond 30 years of age [1]. Clinically, tumors typically have a diameter of 1–3 cm; however, larger tumor diameters have occasionally been observed [1,11].

On radiography, AOT typically presents as well-defined, corticated, unilocular, radiolucent lesions, with 10% or more exhibiting some degree of calcification [9,11,13,14]. Histologically, AOT is composed of cuboidal epithelial cells grouped in duct-like structures with or without calcifications, epithelial spheres or whorls, and strands of spindle-shaped epithelial cells [6,11,13]. The calcifications can be nonspecific or comprise cementum-like globules. Occasionally, globules of homogenous eosinophilic material representing amyloid are observed [6,15]. The thick, fibrous connective tissue capsule supporting these tumors facilitates easy lesion detachment from the tooth and surrounding bone, sometimes allowing the clinician to save the impacted tooth in cases of follicular AOT. Treatment typically involves conservative surgical excision with simple curettage or enucleation [4,9]. Recurrence is exceedingly rare, although a few cases have been reported [3,4,9,16].

Although a few cases have previously been reported from Pakistan, a comprehensive clinicopathological analysis of a series of AOT cases is lacking. Here, we present the histopathological analysis of AOT cases from a cohort of 34 patients at a single center in Pakistan.

MATERIALS AND METHODS

Study setting and design

This was a descriptive observational study conducted at the Aga Khan University, Karachi, Pakistan. Histologically proven cases of AOT reported between 2009 and 2024 were electronically retrieved along with the respective hematoxylin and eosin-stained slides. Cases were analyzed in correlation with radiological presentations, including tumor site, relationship to teeth, and other morphological features.

Data collection and case review

Data regarding patient demographics were retrieved from the institution's Integrated Laboratory Management System, including information such as age and sex. The glass slides of all cases were reviewed by two pathologists to record morphological features, including solid growth patterns, eosinophilic secretions, calcifications, lattice work patterns, calcifying epithelial odontogenic tumor (CEOT)–like areas, cystic areas, presence of dentin, ossifying fibroma-like areas, mucin in ducts and tubules, fibrocollagenous stroma, and cuboidal/columnar lining of ducts. Cases that were autolyzed or had suboptimal fixation were excluded from the study. All data were recorded on a standardized proforma.

Histopathological criteria and classification

Certain specific and/or diagnostically challenging morphological features were defined to ensure consistency in analysis, as follows: (1) CEOT-like areas were identified by the presence of polyhedral epithelial cells with nuclear pleomorphism, intercellular bridges, and eosinophilic amyloid-like material, often accompanied by concentric calcifications, but distinguished from true CEOT by the absence of infiltrative growth and coexistence with classic AOT features such as duct-like structures and whorled epithelial nests. (2) Ossifying fibroma-like areas were characterized by cellular fibrous stroma containing trabeculae of osteoid or cementum-like calcifications, interpreted as reactive metaplastic ossification rather than neoplastic fibro-osseous proliferation based on the absence of zonal maturation or osteoblastic rimming typical of ossifying fibromas. (3) For cases with overlapping features, classification prioritized predominant histology (≥50% of sampled tissue) and pathognomonic criteria. Lesions retaining encapsulation and ductal architectures despite focal CEOT-like or ossifying fibroma-like patterns were classified as AOT, whereas tumors meeting diagnostic thresholds for ossifying fibroma such as bony trabeculae with osteoblastic activity were excluded.

Statistical analysis

For statistical analysis, information from hard copies of the study proformas was entered in Microsoft Excel software (Microsoft Excel 2013 {15.0.5553.1000} 32-bit). Statistical significance for the association of tumor sites with various morphological features was determined using the chi-squared test and expressed as p-values. A p-value of ≤.05 was considered statistically significant. All chi-square tests were performed on 2 × 2 contingency tables. Fisher's exact test was substituted for expected cell frequencies <5. p-values reflect standalone comparisons and are not adjusted for multiple testing. Other descriptive data were presented as percentages, tables, and figures.

RESULTS

A total of 34 cases were diagnosed during the study period. Patient age ranged from 9 to 44 years, with a mean age of 17.7 years. Most patients were in the age group of ≤15 years (47.1%), followed by those aged 16–30 years (44.1%) and >30 years (8.8%). Most cases occurred in females (n = 19) as compared to males (n = 15), resulting in a female to male ratio of 1.3:1. Involvement of the maxilla was common (n = 15, 44.1%) as compared to the mandible (n = 6, 17.7%), tooth (n = 6, 17.7%), gingiva (n = 4, 11.8%), and buccal vestibule (n = 1, 2.9%) (Table 1).

Almost all cases exhibited typical histopathological findings of AOT: a solid growth pattern (n = 34), accompanied by ducts lined by cuboidal to low columnar epithelial cells proliferating in the form of whorls and nodules (n = 31). The ducts were filled with eosinophilic secretions in 31 cases, and interlacing strands or a lattice work pattern was seen in 30 cases. Psammomatous or dystrophic calcifications were seen in 31 cases. Other morphological findings included cystic areas (n = 20), CEOT-like areas (n = 13), ossifying fibroma-like areas (n = 6), fibrocollagenous stroma (n = 6), and associated osteodentin production (n = 6). Less frequent findings included mucin in ducts (n = 3), and in tubules (n = 7). Radiographically only six cases were associated with impacted teeth (Fig. 1A, B). The morphological features of AOT in relation to different tumor sites is presented in Table 2.

The association of ducts with a cuboidal/columnar epithelial lining, lattice work pattern, calcifications, and eosinophilic secretions with gingival tumors was found to be statistically significant ($p \leq .05$). Additionally, tooth tumors were significantly associated with CEOT-like areas ($p = .026$) (Table 2).

DISCUSSION

AOT, a benign noninvasive odontogenic tumor of epithelial origin, typically affects young people, particularly in their second decade, and is more common in women [1-3]. Our retrospective investigation revealed a predominant occurrence of AOT in the second and third decades of life, with a female predilection (55.9% vs. 44.1%), and the majority of tumors originating

Table 1. Patient characteristics and frequency of tumor sites

Characteristic	No. (%)
Age (yr)	
≤15	16 (47.1)
16–30	15 (44.1)
>30	3 (8.8)
Sex	
Female	19 (55.9)
Male	15 (44.1)
Tumor site	
Maxilla	15 (44.1)
Mandible	6 (17.7)
Gingiva	4 (11.8)
Tooth	6 (17.7)
Buccal vestibule	1 (2.9)
Not specified	2 (5.8)
Total	34 (100)

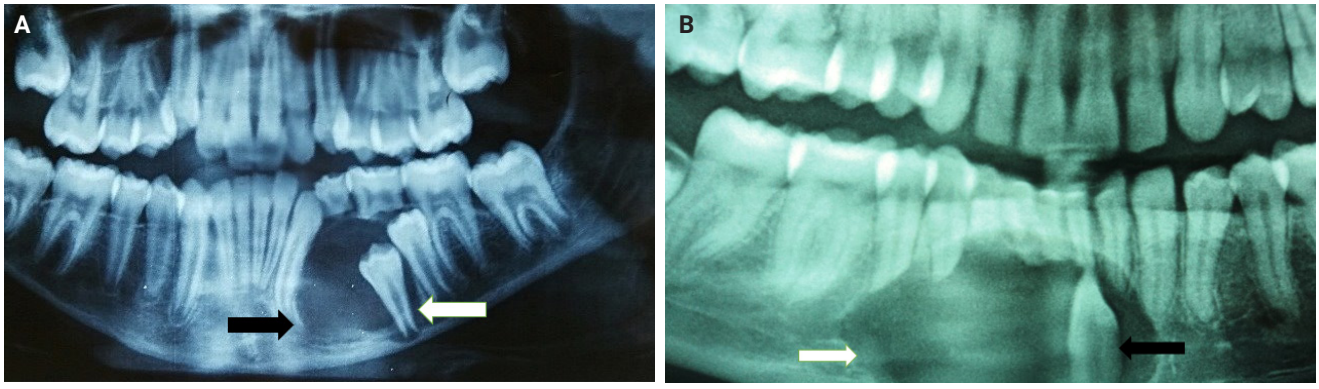

Fig. 1. Panoramic radiography demonstrating a well circumscribed unilocular lucent area in the left hemi mandible (black arrow) with thin sclerotic borders and impacted tooth on its left lateral aspect (white arrow) (A); a unilocular lucent area with thin sclerotic borders, wider than taller, occupying the symphyseal region and extending into the right parasymphyseal region (white arrow) associated with an impacted tooth in vertical orientation (black arrow) (B).

https://doi.org/10.4132/jptm.2025.07.11

Table 2. Morphological features of AOT in relation to different tumor site (total cases, n = 34)

Morphological feature	Site					
	Maxilla (n = 15)	Mandible (n = 6)	Gingiva (n = 4)	Tooth (n = 6)	Buccal vestibule (n = 1)	Not specified (n = 2)
Solid growth pattern	15 (44.1)	6 (17.6)	4 (11.8)	6 (17.6)	1 (2.9)	2 (5.9)
p-value	.922	.461	.424	.461	.185	.185
Eosinophilic secretions	14 (41.2)	6 (17.6)	2 (5.9)	6 (17.6)	1 (2.9)	2 (5.9)
p-value	.720	.720	.017	.778	.458	.778
Calcifications	15 (44.1)	6 (17.6)	2 (5.9)	5 (14.7)	1 (2.9)	2 (5.9)
p-value	.204	.720	.017	.458	.458	.778
Lattice work pattern	14 (41.2)	6 (17.6)	2 (5.9)	6 (17.6)	1 (2.9)	1 (2.9)
p-value	.424	.640	.028	.640	.667	.120
CEOT-like areas	7 (20.6)	0	0	5 (14.7)	1 (2.9)	0
p-value	.381			.026	.333	
Cystic areas	10 (29.4)	3 (8.8)	0	6 (17.6)	0	1 (2.9)
p-value	.424	.640		.085		.778
Osteodentin	2 (5.9)	1 (2.9)	1 (2.9)	1 (2.9)	0	1 (2.9)
p-value	.667	.889	.667	.889		.333
Impacted tooth	2 (5.9)	4 (11.8)	0	0	0	0
p-value	.381	.458				
Ossifying fibroma-like areas	2 (5.9)	2 (5.9)	0	2 (5.9)	0	0
p-value	.603	.333		.333		
Mucin in ducts	2 (5.9)	0	0	1 (2.9)	0	0
p-value	.381			.458		
Mucin in tubules	4 (11.8)	2 (5.9)	0	1 (2.9)	0	0
p-value	.424	.333		.778		
Fibrocollagenous stroma	4 (11.8)	0	0	2 (5.9)	0	0
p-value	.204			.333		
Ducts with cuboidal/columnar lining	14 (41.2)	6 (17.6)	2 (5.9)	6 (17.6)	1 (2.9)	2 (5.9)
p-value	.720	.720	.012[a]	.720	.458	.778

Values are presented as number (%).
AOT, adenomatoid odontogenic tumor; CEOT, calcifying epithelial odontogenic tumor.

in the maxilla (44.1%). Most of our findings are consistent with previous reports from Pakistan and internationally. The mean age of our patients was 17.7 years, close to approximate average of 16 years reported in the literature [1,15]. As reported in other studies, the maxillofacial skeleton is frequently the tumor location, with occurrences in the maxilla nearly twice as common as in the mandible (2:1) [3,9], this ratio was even more pronounced in our study, with a maxilla-to-mandible occurrence ratio of approximately 2.5:1.

The histological diagnosis of AOT requires careful differentiation from other odontogenic lesions with overlapping features. Dentigerous cysts, the most common clinical mimic, lack the duct-like epithelial structures, rosette formations, and calcification characteristics typical of AOT [1,3,17]. Unlike unicystic ameloblastoma, AOT does not exhibit invasive growth, palisading basal cells, or stellate reticulum-like stroma [13]. Calcifying odontogenic cysts may share radiopaque foci but are distinguished by ghost cell keratinization and the absence of tubular eosinophilic material [1,3]. Radiographically, AOT's association with impacted canines, unilocular radiolucency with "snowflake" calcifications, and encapsulation contrast with CEOT's diffuse calcifications and ameloblastic fibro-odontoma's mixed radiopaque-radiolucent "sunburst" appearance [1,6,17]. Immunohistochemically, AOT's strong cytokeratin (CK) 14 and CK19 expression aids in differentiation from lesions such as lateral periodontal cysts, which lack these markers [6]. These distinctions underscore the necessity of correlating histology with clinical and radiographic findings to avoid misdiagnosis.

The histological features in the present study demonstrated a predominantly solid growth pattern with interspersed duct-like structures (100%) (Fig. 2A–C). Although AOT may also exhibit a cribriform pattern to varying degrees alongside the solid growth pattern, cribriform patterns are not characteristic of AOT and have scarcely been reported in the literature [18,19]. The prevalence of duct-like spaces, a prominent finding in AOT, has been abundantly reported in previous research [20,21]. Furthermore, eosinophilic amorphous material or tumor droplets were found in 94.1% of our cases. Similarly, eosinophilic tumor droplets have been observed in almost all cases by Leon et al. [21] and Jivan et al. [22]. It has been demonstrated that tumor droplets in AOTs are immunopositive for enamel proteins, including sheathlin, enamelin, and amela-

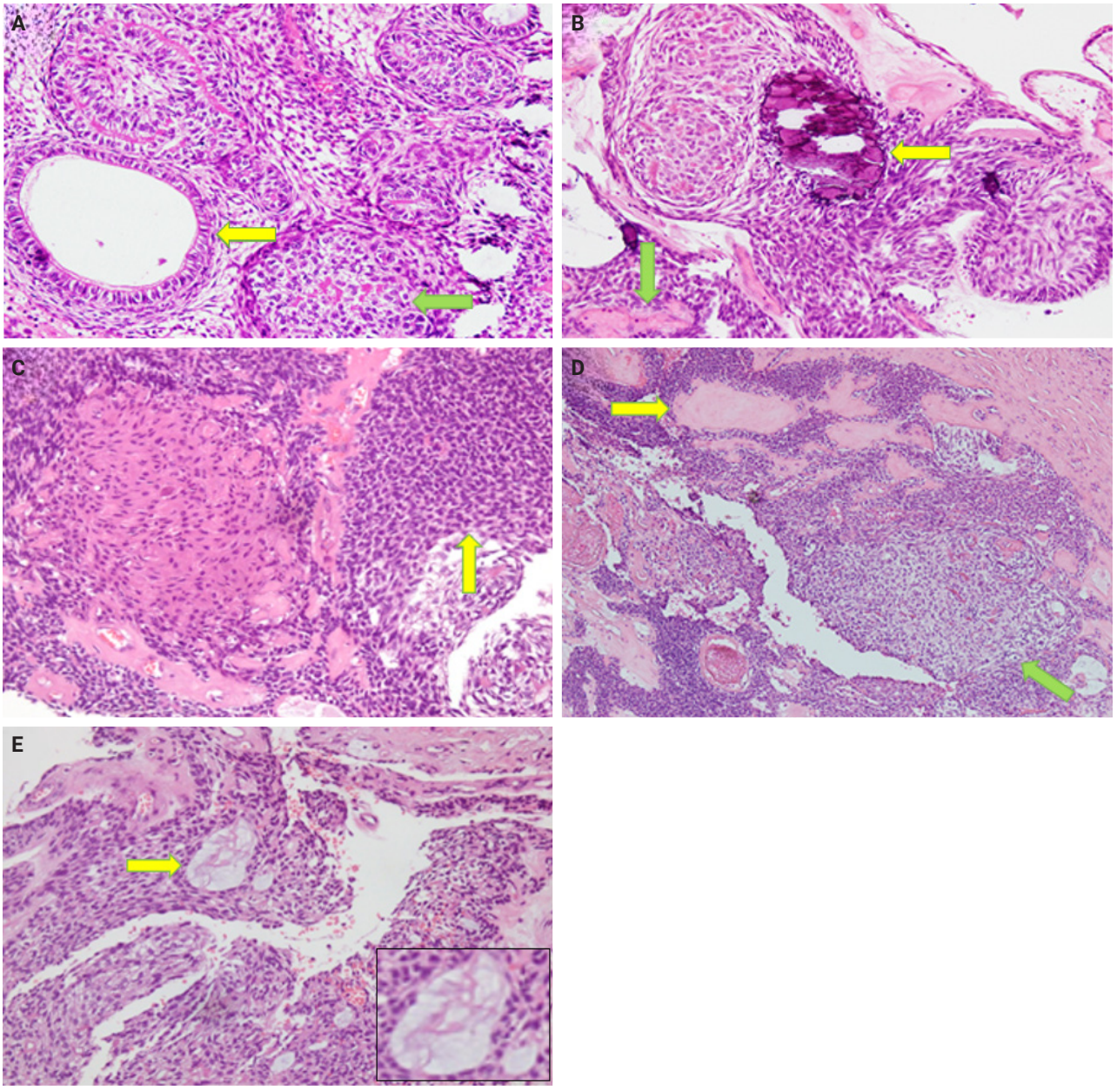

Fig. 2. Adenomatoid odontogenic tumor showing ducts with a cuboidal/columnar epithelial lining (yellow arrow) and duct-like areas (green arrow) (A); calcifications (yellow arrow) and eosinophilic secretions (green arrow) (B); a solid growth pattern (yellow arrow) (C); dentinoid material (yellow arrow) and calcifying epithelial odontogenic tumor–like areas (green arrow) (D); mucin deposition in ducts (yellow arrow and magnified in inset) (E).

https://doi.org/10.4132/jptm.2025.07.11

nogenin, suggesting that this material is most likely enamel in nature [23,24]. AOTs have also been shown to have variable quantities of calcified structures [20,21,25]; findings in the present study of psammomatous and dystrophic calcifications in 91.2% of cases support this observation. Some of the tumors exhibited osteodentin (17.6%), confirming the low frequency of this morphological feature (Fig. 2B, D). AOTs have occasionally been observed to contain hyaline, dysplastic material, or calcified osteodentin, sometimes with concurrent abortive enamel [26,27]. Since odontogenic epitomesenchyme is absent from AOTs, Philipsen and Nikai propose that these materials are most likely the product of a metaplastic process and should not be construed as an induction phenomena [25].

Areas resembling CEOT were observed in less than half of our cases (38.2%); only a few such AOT cases have been reported previously (Fig. 2D). AOT may exhibit areas that resemble CEOT, odontomas in development, and other odontogenic tumors or hamartomas [28,29]. Mosqueda-Taylor et al. [30] emphasize that, in contrast to true CEOT, CEOT-like areas in AOTs do not appear as solid, infiltrative nests. Furthermore, CEOT-like areas in AOTs do not affect the biological activity and developmental capacity of AOTs, nor do they exhibit the characteristic pleomorphism found in the epithelial component of CEOT. Therefore, areas that resemble CEOT should be regarded as normal occurrences within the histomorphological spectrum of AOT [30,31].

In the present study, cystic areas were observed in 58.8% of cases. AOTs can have cystic regions that mimic odontogenic cysts, such dentigerous cysts [21,32]. Leon et al. [21] reported cystic areas in 56.4% of AOTs. Moreover, 17.6% of our cases exhibited ossifying fibroma-like areas. This finding is unusual and has rarely been reported in the literature [33,34]. In the anterior mandible, Prakash et al. [33] documented the co-occurrence of an ossifying fibroma and a follicular variant of AOT in relation to impacted teeth, despite the two lesions existing independently. According to Li et al. [35], a 22-year-old female had AOT in her right maxilla with a fibro-osseous reaction in the surrounding tissue, as is typical of ossifying fibromas. This case showed cellular fibro-connective tissue with calcifications mimicking ossicles and cementicles, in contrast to the presence of loosely structured stroma in AOT. Instead of treating it as a collision of two distinct lesions, the authors referred to it as a secondary fibro-osseous reaction to AOT as it shared the same biological behavior and prognosis as AOT and was therefore treated conservatively in a manner similar to conventional AOT [35].

Mucin within the ducts was noted in three cases (16.8%) and within the tubules in seven cases (20.6%) (Fig. 2E). This finding is infrequent and not commonly reported in the published literature. Additionally, only three cases (8.8%) in our study were associated with an impacted tooth. Radiographically, the lesions commonly presented as unilocular radiolucent cysts.

Regarding treatment and prognosis, conservative surgical enucleation with curettage is the treatment of choice for AOT due to their benign nature and very low recurrence rates [36-38]. This approach generally allows complete bone regeneration without the need for bone grafting, as natural healing is facilitated by preservation of the periosteum [36]. Histologically, cystic variants of AOT characterized by duct-like structures and calcifications have been associated with easier surgical excision, reduced intraoperative bleeding, and faster postoperative healing [38]. For larger lesions, staged management involving fenestration decompression followed by delayed enucleation has been shown to reduce surgical morbidity while maintaining an excellent prognosis without recurrence [36-38]. Although our study did not include data regarding treatment and prognosis, these findings from the literature provide important context for interpreting the clinical significance of histopathological features and support minimally invasive, tooth-preserving treatment strategies with long-term follow-up.

Our study had a few limitations. Firstly, while this study provides comprehensive clinicopathological data, molecular characterization of *KRAS* mutations, a hallmark genetic alteration occurring in 71%–76% of AOTs globally, was not performed [39]. Emerging evidence suggests that *KRAS* mutations, particularly G12V/R at codon 12, drive mitogen-activated protein kinase/ERK pathway activation in AOTs, potentially influencing their indolent behavior [39]. In our current clinicopathological analysis, we did not include molecular profiling due to resource constraints and the retrospective nature of the study. Secondly, the study's sample size (n = 34) may limit the generalizability of our findings. Low expected frequencies in certain subgroups necessitated the use of Fisher's exact test, which is more appropriate for sparse data. Nonetheless, the risk of type II errors, wherein true associations may remain undetected, cannot be ruled out. Lastly, we did not evaluate long-term patient prognosis or document specific treatment modalities, such as surgical techniques or adjunct therapies. While the existing literature supports the effectiveness of conservative management, the absence of follow-up data precludes conclusions about recurrence rates in our cohort. To address these limitations, we aim

to conduct a future multi-center study on a broader population in Pakistan, prioritizing molecular analyses to evaluate *KRAS* mutation frequencies and to investigate potential correlations with histopathological features. We also intend to explore the efficacy of specific treatment protocols, and assess long-term patient prognosis through extended monitoring.

The clinicopathological features of AOTs observed in our investigation are consistent with those frequently reported in the literature. Our findings indicate that AOTs typically affect females, particularly in the second and third decades of life, and characteristically exhibit a solid morphological pattern with duct-like spaces and calcified material as predominant features. Furthermore, ossifying fibroma-like areas in AOTs are very rare, and CEOT-like areas may also be relatively uncommon.

Ethics Statement
This study was approved by the Institutional Review Board of the Aga Khan University (Ref # 2024-10499-31005). All patients/legally authorized guardians gave their informed consent for the publication of the respective cases.

Availability of Data and Material
All data generated or analyzed during the study are included in this published article.

Code Availability
Not applicable.

ORCID

Summaya Zafar	https://orcid.org/0009-0005-5412-4708
Sehar Sulaiman	https://orcid.org/0009-0000-6879-7114
Madeeha Nisar	https://orcid.org/0009-0004-7236-0002
Poonum Khan	https://orcid.org/0009-0005-4258-3472
Nasir Ud Din	https://orcid.org/0000-0002-1036-5121

Author Contributions
Conceptualization: NUD. Data curation: SZ, SS, MN, PK. Formal analysis: SZ. Project administration: NUD. Resources: NUD. Software: SZ, SS. Supervision: NUD. Visualization: SZ, SS, MN. Writing—original draft: SZ. Writing—review & editing: SS, MN, PK, NUD. Approval of final manuscript: all authors.

Conflicts of Interest
The authors declare that they have no potential conflicts of interest.

Funding Statement
No funding to declare.

REFERENCES

1. More CB, Das S, Gupta S, Bhavsar K. Mandibular adenomatoid odontogenic tumor: radiographic and pathologic correlation. J Nat Sci Biol Med 2013; 4: 457-62.
2. Reddy Kundoor VK, Maloth KN, Guguloth NN, Kesidi S. Extrafollicular adenomatoid odontogenic tumor: an unusual case presentation. J Dent (Shiraz) 2016; 17: 370-4.
3. Vasudevan K, Kumar S, Vigneswari S. Adenomatoid odontogenic tumor, an uncommon tumor. Contemp Clin Dent 2012; 3: 245-7.
4. Saluja R, Kaur G, Singh P. Aggressive adenomatoid odontogenic tumor of mandible showing root resorption: a histological case report. Dent Res J (Isfahan) 2013; 10: 279-82.
5. Friedrich RE, Zustin J, Scheuer HA. Adenomatoid odontogenic tumour of the mandible. Anticancer Res 2010; 30: 1787-92.
6. Seo WG, Kim CH, Park HS, Jang JW, Chung WY. Adenomatoid odontogenic tumor associated with an unerupted mandibular lateral incisor: a case report. J Korean Assoc Oral Maxillofac Surg 2015; 41: 342-5.
7. Philipsen HP, Birn H. The adenomatoid odontogenic tumour. Ameloblastic adenomatoid tumour or adeno-ameloblastoma. Acta Pathol Microbiol Scand 1969; 75: 375-98.
8. Philipsen HP, Reichart PA. The adenomatoid odontogenic tumour: ultrastructure of tumour cells and non-calcified amorphous masses. J Oral Pathol Med 1996; 25: 491-6.
9. Baskaran P, Misra S, Kumar MS, Mithra R. Adenomatoid odontogenic tumor: a report of two cases with histopathology correlation. J Clin Imaging Sci 2011; 1: 64.
10. John JB, John RR. Adenomatoid odontogenic tumor associated with dentigerous cyst in posterior maxilla: a case report and review of literature. J Oral Maxillofac Pathol 2010; 14: 59-62.
11. Kalia V, Kalra G, Kaushal N, Sharma V, Vermani M. Maxillary adenomatoid odontogenic tumor associated with a premolar. Ann Maxillofac Surg 2015; 5: 119-22.
12. Yilmaz N, Acikgoz A, Celebi N, Zengin AZ, Gunhan O. Extrafollicular adenomatoid odontogenic tumor of the mandible: report of a case. Eur J Dent 2009; 3: 71-4.
13. Lee SK, Kim YS. Current concepts and occurrence of epithelial odontogenic tumors: I. Ameloblastoma and adenomatoid odontogenic tumor. Korean J Pathol 2013; 47: 191-202.
14. Shanmuga PS, Ravikumar A, Krishnarathnam K, Rajendiran S. Intraosseous calcifying epithelial odontogenic tumor in a case

https://doi.org/10.4132/jptm.2025.07.11

with multiple myeloma. J Oral Maxillofac Pathol 2009; 13: 10-3.
15. Jivan V, Altini M, Meer S, Mahomed F. Adenomatoid odontogenic tumor (AOT) originating in a unicystic ameloblastoma: a case report. Head Neck Pathol 2007; 1: 146-9.
16. Jindwani K, Paharia YK, Kushwah AP. Surgical management of peripheral variant of adenomatoid odontogenic tumor: a rare case report with review. Contemp Clin Dent 2015; 6: 128-30.
17. Chakraborty R, Sen S, Goyal K, Pandya D. "Two third tumor": a case report and its differential diagnosis. J Family Med Prim Care 2019; 8: 2140-3.
18. Santos JN, Lima FO, Romerio P, Souza VF. Adenomatoid odontogenic tumor: an unusual case exhibiting cribriform aspect. Quintessence Int 2008; 39: 777-81.
19. de Matos FR, Nonaka CF, Pinto LP, de Souza LB, de Almeida Freitas R. Adenomatoid odontogenic tumor: retrospective study of 15 cases with emphasis on histopathologic features. Head Neck Pathol 2012; 6: 430-7.
20. Philipsen HP, Reichart PA. Adenomatoid odontogenic tumour: facts and figures. Oral Oncol 1999; 35: 125-31.
21. Leon JE, Mata GM, Fregnani ER, et al. Clinicopathological and immunohistochemical study of 39 cases of adenomatoid odontogenic tumour: a multicentric study. Oral Oncol 2005; 41: 835-42.
22. Jivan V, Altini M, Meer S. Secretory cells in adenomatoid odontogenic tumour: tissue induction or metaplastic mineralisation? Oral Dis 2008; 14: 445-9.
23. Saku T, Okabe H, Shimokawa H. Immunohistochemical demonstration of enamel proteins in odontogenic tumors. J Oral Pathol Med 1992; 21: 113-9.
24. Takata T, Zhao M, Uchida T, Kudo Y, Sato S, Nikai H. Immunohistochemical demonstration of an enamel sheath protein, sheathlin, in odontogenic tumors. Virchows Arch 2000; 436: 324-9.
25. Philipsen HP, Nikai H. Adenomatoid odontogenic tumour. In: Barnes L, Eveson JW, Reichart P, Sidransky D, eds. Pathology and genetics of head and neck tumours. Lyon: IARC Press, 2005; 304-5.
26. Tajima Y, Sakamoto E, Yamamoto Y. Odontogenic cyst giving rise to an adenomatoid odontogenic tumor: report of a case with peculiar features. J Oral Maxillofac Surg 1992; 50: 190-3.
27. Takeda Y. Induction of osteodentin and abortive enamel in adenomatoid odontogenic tumor. Ann Dent 1995; 54: 61-3.
28. Zeitoun IM, Dhanrajani PJ, Mosadomi HA. Adenomatoid odontogenic tumor arising in a calcifying odontogenic cyst. J Oral Maxillofac Surg 1996; 54: 634-7.
29. Dunlap CL, Fritzlen TJ. Cystic odontoma with concomitant adenoameloblastoma (adenoameloblastic odontoma). Oral Surg Oral Med Oral Pathol 1972; 34: 450-6.
30. Mosqueda-Taylor A, Carlos-Bregni R, Ledesma-Montes C, Fillipi RZ, de Almeida OP, Vargas PA. Calcifying epithelial odontogenic tumor-like areas are common findings in adenomatoid odontogenic tumors and not a specific entity. Oral Oncol 2005; 41: 214-5.
31. Montes Ledesma C, Mosqueda Taylor A, Romero de Leon E, de la Piedra Garza M, Goldberg Jaukin P, Portilla Robertson J. Adenomatoid odontogenic tumour with features of calcifying epithelial odontogenic tumour. (The so-called combined epithelial odontogenic tumour.) Clinico-pathological report of 12 cases. Eur J Cancer B Oral Oncol 1993; 29B: 221-4.
32. Gadewar DR, Srikant N. Adenomatoid odontogenic tumour: tumour or a cyst, a histopathological support for the controversy. Int J Pediatr Otorhinolaryngol 2010; 74: 333-7.
33. Prakash AR, Reddy PS, Bavle RM. Concomitant occurrence of cemento-ossifying fibroma and adenomatoid odontogenic tumor with bilateral impacted permanent canines in the mandible. Indian J Dent Res 2012; 23: 434-5.
34. Priya B, Kumar P, Augustine J, Malhotra R, Urs AB. Rare histological presentation of adenomatoid odontogenic tumor: a series of three unique cases. Oral Oncol Rep 2024; 9: 100167.
35. Li BB, Xie XY, Jia SN. Adenomatoid odontogenic tumor with fibro-osseous reaction in the surrounding tissue. J Craniofac Surg 2013; 24: e100-1.
36. Handschel JG, Depprich RA, Zimmermann AC, Braunstein S, Kubler NR. Adenomatoid odontogenic tumor of the mandible: review of the literature and report of a rare case. Head Face Med 2005; 1: 3.
37. Diaz Castillejos R, Maria Nieto Munguia A, Castillo Ham G. Adenomatoid odontogenic tumor: case report and literature review. Rev Odontol Mex 2015; 19: 183-7.
38. Espinoza V, Ortiz R. Adenomatoid odontogenic tumor: case report and literature review. Res Rep Oral Maxillofac Surg 2021; 5: 050.
39. Marin C, Niklander SE, Martinez-Flores R. Genetic profile of adenomatoid odontogenic tumor and ameloblastoma: a systematic review. Front Oral Health 2021; 2: 767474.

JPTM

ORIGINAL ARTICLE

pISSN 2383-7837 · eISSN 2383-7845

Journal of Pathology and Translational Medicine 2025; 59: 398-407
https://doi.org/10.4132/jptm.2025.07.22

Frozen section histopathology and preanalytical factors affecting nucleic acid integrity in biobanked fresh-frozen human cancer tissues

Soungeun Kim[1], Jaewon Kang[1], Boyeon Kim[1], Yoonjin Kwak[1,2], Hye Seung Lee[1,2,3]

[1]Cancer Tissue Bank, Biomedical Research Institute, Seoul National University Hospital, Seoul, Korea
[2]Department of Pathology, Seoul National University Hospital, Seoul National University College of Medicine, Seoul, Korea
[3]Cancer Research Institute, Seoul National University College of Medicine, Seoul, Korea

Graphical abstract

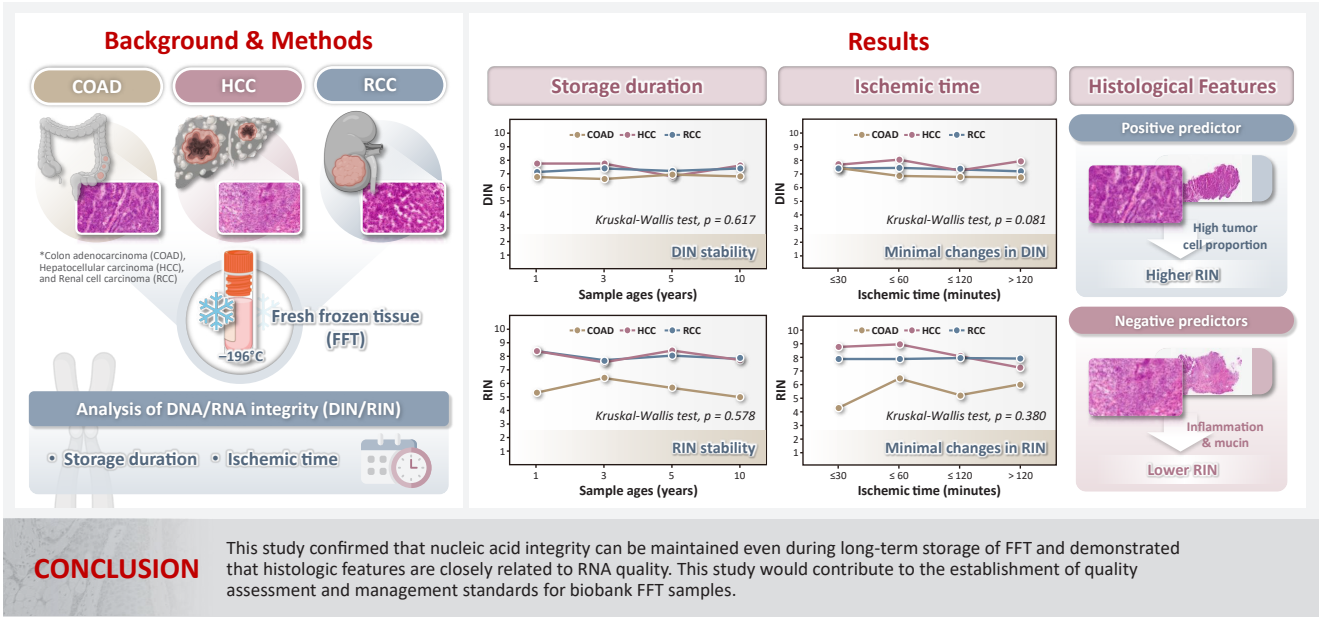

Kim S et al. Journal of Pathology and Translational Medicine

JPTM

ORIGINAL ARTICLE

pISSN 2383-7837 · eISSN 2383-7845

Journal of Pathology and Translational Medicine 2025; 59: 398-407
https://doi.org/10.4132/jptm.2025.07.22

Frozen section histopathology and preanalytical factors affecting nucleic acid integrity in biobanked fresh-frozen human cancer tissues

Soungeun Kim[1], Jaewon Kang[1], Boyeon Kim[1], Yoonjin Kwak[1,2], Hye Seung Lee[1,2,3]

[1]Cancer Tissue Bank, Biomedical Research Institute, Seoul National University Hospital, Seoul, Korea
[2]Department of Pathology, Seoul National University Hospital, Seoul National University College of Medicine, Seoul, Korea
[3]Cancer Research Institute, Seoul National University College of Medicine, Seoul, Korea

Background: In this study, we evaluated the effects of storage duration and ischemic time on nucleic acid quality of fresh-frozen tissue (FFT) from colon adenocarcinoma (COAD), hepatocellular carcinoma (HCC), and renal cell carcinoma (RCC) collected at the Cancer Tissue Bank of Seoul National University Hospital. **Methods:** A total of 102 FFT samples were analyzed to compare DNA integrity number (DIN) and RNA integrity number (RIN) according to storage duration and ischemic time. Additionally, the effects of histopathologic features—such as tumor cell proportion, inflammatory cell infiltration, and stromal fibrosis—on nucleic acid quality were evaluated. **Results:** DIN and RIN remained stable overall even though the storage duration increased, with no statistically significant differences observed. In particular, there was almost no decrease in RNA quality in HCC and RCC samples, but in COAD samples, RIN tended to decrease slightly as the storage duration increased. No significant difference was confirmed between ischemic time and nucleic acid quality, but in COAD tissue, RNA quality variability tended to increase as the ischemic time increased. Furthermore, RIN increased as the tumor cell proportion increased, whereas inflammatory cell infiltration and extracellular mucin pool were identified as independent negative predictors of RIN. **Conclusions:** This study confirmed that nucleic acid integrity can be maintained even during long-term storage of FFT and demonstrated that histologic features are closely related to RNA quality. This study would contribute to the establishment of quality assessment and management standards for biobank FFT samples.

Keywords: Biological specimen banks; Tissue preservation; RNA stability; Cryopreservation; Pathology

INTRODUCTION

Recently, rapid advancements in genome technology and precision medicine have made it increasingly crucial to secure and systematically utilize high-quality biological resources. In particular, the quality of biological samples provided by biobanks determines the reliability and reproducibility of research results, so strict management is required throughout the entire process from sample collection to storage and quality assessment [1-3]. Fresh-frozen tissue (FFT) is preferred for various genomic and transcriptomic studies due to its superior ability to preserve nucleic acid (RNA and DNA) integrity compared to formalin-fixed paraffin-embedded tissue [4,5]. Micke et al. [4] demonstrated that RNA integrity is well preserved in FFT collected as non-fixed surgical specimens, supporting its use in genomic and transcriptomic research [4]. However, the nu-

Received: June 5, 2025 **Revised:** July 21, 2025 **Accepted:** July 22, 2025

Corresponding Author:
Yoonjin Kwak, MD, PhD
Department of Pathology, Seoul National University Hospital, Seoul National University College of Medicine, 103 Daehak-ro, Jongno-gu, Seoul 03080, Korea
Tel: Fax: , E-mail: yoon131@snu.ac.kr

Hye Seung Lee, MD, PhD
Department of Pathology, Seoul National University Hospital, Seoul National University College of Medicine, 103 Daehak-ro, Jongno-gu, Seoul 03080, Korea
Tel: Fax: , E-mail: hye2@snu.ac.kr

cleic acid quality of FFT can be sensitively affected by ischemic time, storage duration, and histopathologic features—including tumor cell proportion, combined normal tissue, inflammatory cell infiltration, stromal fibrosis, necrosis, and extracellular mucin pool. Thus, to maximize the utility of FFT, it is essential to specifically and systematically evaluate the effects of these factors on nucleic acid integrity.

Previous studies have been conducted primarily based on samples collected from Western biobanks, and analyses on how ischemic time affects nucleic acid quality across different tissue types have been limited. Except for a study focusing on the effects of fixation and storage conditions on tissue sample quality [6], research on nucleic acid preservation in biobank samples has been rarely conducted in Korea [6]. The studies of Fan et al. [7] and Song et al. [5] reported that RNA quality remains stable in most cancer tissues when ischemic time is within 1 hour, but further research is still needed on the nucleic acid quality change and differences among tissue types according to the ischemic times exceeding 1 hour. In addition, Zhang et al. [8] reported that RNA quality was maintained well even after gastric cancer tissues were stored for up to 13 years, but Neuber et al. [9] reported that RNA quality began to decline after 4.5 years of storage, while DNA quality deteriorated after more than 8 years of storage in tumor tissues derived from the prostate, limbs and trunk, and gastrointerstinal tract. This suggests that the effect of storage duration on nucleic acid quality may vary depending on the tissue type.

To complement the limitations of these previous studies, this study analyzed the effects of sample age (1–10 years) and ischemic time (≤30 minutes, ≤60 minutes, ≤120 minutes, and >120 minutes) on DNA integrity number (DIN) and RNA integrity number (RIN) of FFT from colon adenocarcinoma (COAD), hepatocellular carcinoma (HCC) and renal cell carcinoma (RCC) collected at the Cancer Tissue Bank of Seoul National University Hospital. In addition, the correlations between histopathologic features and nucleic acid quality were analyzed to provide a foundation for establishing quality management and maintenance strategies for FFT in Korean biobanks in the future.

MATERIALS AND METHODS

Collection and storage of FFT

Tissue samples were transported to the laboratory for frozen sections in the operating room immediately after resection and stored at 4°C until collected by the Cancer Tissue Bank. At the bank, the samples were cut into 0.5 × 0.5 × 0.5 cm^3 fragments within a range that did not affect diagnosis and placed into 1.8 mL cryovials with anonymous labels. The vials were filled with isopentane (2-methylbutane, >99.0%, Samchun) to fully submerge the tissue, and then immediately stored in a liquid nitrogen tank at –196°C. The liquid nitrogen tank was equipped with a real-time temperature monitoring system, and no thawing occurred for the samples throughout the entire storage duration. However, due to the relocation of the Cancer Tissue Bank laboratory and adjustments in pathology department tasks, some variations existed in long-term and annual tissue collection protocols (Table 1).

This study included a total of 105 FFT samples originating from COAD, HCC, and RCC. The distribution of samples by sample age was 1 year (n = 27), 3 years (n = 25), 5 years (n = 26), and 10 years (n = 27). The distribution of samples by ischemic time was ≤30 minutes (n = 17), ≤60 minutes (n = 18), ≤120 minutes (n = 37), and >120 minutes (n = 33). Samples were selected to ensure a balanced composition of ischemic time and storage duration across tumor types. However, three samples subjected to analysis were excluded from the subsequent analysis since they did not contain any tumor cells as confirmed by hematoxylin and eosin (H&E) staining with

Table 1. Changes in tissue collection and handling protocols by organ and storage duration

Tumor type	Storage duration	Specimen handling protocol
COAD	Until Feb 2021	Collected post-gross examination; mucosal surface washed with tap water
	Feb 2021–May 2022	Collected pre-gross examination; no washing performed
	Since Jun 2022	Immediately collected upon resection, prior to pathology processing
HCC	Throughout	Sample taken in the operating room by a surgeon and delivered to the bank
RCC (partial nephrectomy)	Throughout	Specimen sent to the bank before the end of the operation for direct banking
RCC (radical nephrectomy)	Until Jun 2019	Specimen collected during gross examination at the pathology department
	Since Jul 2019	Specimen collected before gross examination at the pathology department

COAD, colon adenocarcinoma; HCC, hepatocellular carcinoma; RCC, renal cell carcinoma.

frozen sections. Histopathologic features and tapestation-based nucleic acid quality indices for these excluded samples are separately presented in Supplementary Table S1.

Extraction of nucleic acids

Each tissue sample was removed from the liquid nitrogen tank and processed by dividing it into two parts on a sterilized tray. Half of the tissue was stored back in the liquid nitrogen tank (–196°C) for the preparation of frozen sections and H&E staining. The other half was immediately used for nucleic acid extraction.

RNA was extracted using the PureLink RNA Mini Kit (Invitrogen, Thermo Fisher Scientific, Carlsbad, CA, USA). The sample was cut into a size of up to 30 mg using a single-edge blade and placed in a 1.5 mL tube of a BioMasher II Grinder (Biofact, Daejeon, Korea). Then, 100 μL of lysis buffer was dispensed and the tissue was homogenized using a pestle. The homogenized tissue was transferred to a new tube, and 900 μL of lysis buffer and 20 μL of 2 M dithiothreitol (DTT) were added, followed by vortexing. RNA was then extracted according to the manufacturer's protocol. The 2 M DTT solution was prepared by dissolving 0.3085 g of DTT (DTT molecular weight: 154.25) in 1 mL of diethyl pyrocarbonate solution. DNA was extracted using QIAamp DSP DNA Mini Kit (Qiagen, Hilden, Germany) according to the manufacturer's manual.

RIN was measured using Genomic RNA ScreenTape Kit, RNA ScreenTape Sample Buffer, Ladder of Agilent Tapestation 4200, and Analysis-Software version 5.1 (Agilent Technologies, Santa Clara, CA, USA) [10]. DIN was assessed using Genomic DNA ScreenTape Kit with the same Agilent Tapestation 4200 [10,11].

RIN and DIN of all 105 samples were measured the day after extraction, and the extracted RNA and DNA were stored in a –80°C deep freezer.

Histopathological examination

FFT samples were prepared as frozen section slides. The tissue was placed on the mold of a Cryocut microtome (CM1850UV, Leica Biosystems, Nussloch, Germany), and a small amount of optimal cutting temperature compound was applied before freezing and mounting onto the holder. The sample was trimmed to expose the front surface and then cut into 4 μm-thick sections, which were attached to slides stored at room temperature for fixation.

H&E staining was performed using the quick manual method in the laboratory for frozen sections. After staining with Harris hematoxylin for 1 minute and 30 seconds, the slides were rinsed under running tap water for 10 seconds and dipped 1–2 times in 1% HCl, followed by another rinse under running tap water for 20 seconds until they turned blue. Afterwards, staining was performed with 1% Eosin by dipping them 5–10 times, adjusting the dipping frequency to prevent excessive redness. After staining, they were rinsed under running tap water for 3 seconds, dehydrated by dipping 5–10 times in 95% and 100% alcohol, and finally dipped 10 times in xylene to complete the clearing process.

The stained slides were mounted using synthetic mountant, a non-aqueous mounting medium, with an Automatic Coverslipper (CV5030, Leica Biosystems) to prevent tissue damage and staining degradation.

H&E-stained slides of all frozen tissue samples were reviewed by a pathologist (Y.K.), and the suitability of tissue samples was assessed according to the items and criteria established based on ISBER Best Practices (5th edition) [1] and NCI Best Practices for Biospecimen Resources (2016) [2]. Based on the microscopic findings of H&E, various parameters, including tumor cell proportion, combined normal tissue, inflammatory cell infiltration, stromal fibrosis, necrosis, and extracellular mucin pool, were evaluated using a semi-quantitative grading system (Table 2).

Statistical analysis

Statistical analyses were performed using R version 4.4.2 (R Foundation for Statistical Computing, Vienna, Austria). Pearson correlation coefficient and Kendall's tau (τ) correlation analysis were performed to analyze the correlation between continuous variables. One-way ANOVA and Kruskal-Wallis test were used to compare categorical variables, and nonparametric statistical methods were applied considering the charac-

Table 2. Semi-quantitative grading criteria for histopathologic features of fresh-frozen tissue samples

Parameter	0	1	2	3
Tumor cell proportion (%)	0	1–30	31–60	>60
Combined normal tissue presence	No	Yes	-	-
Inflammatory cell infiltration	No	Scanty	Moderate	Marked
Stromal fibrosis	No	Scanty	Moderate	Marked
Necrosis (%)	Absent	<10	10–50	>50
Extracellular mucin pool (%)	Absent	<10	10–50	>50

https://doi.org/10.4132/jptm.2025.07.22

teristics of the data. For all statistical analyses, two-sided tests were applied, and cases where the p-value was less than 0.05 were considered statistically significant.

RESULTS

Nucleic acid integrity

In this study, nucleic acid integrity was assessed for 102 FFT samples, excluding three samples that did not contain tumor cells. DIN and RIN were measured using the Agilent 4200 TapeStation system.

As a result of the analysis, the mean DIN was 7.20 ± 0.71 with the median of 7.20 (interquartile range [IQR], 6.70 to 7.60), and the mean RIN was 7.03 ± 1.56 with the median of 7.50 (IQR, 6.30 to 8.30). As a result of the quality assessment, the proportion of samples with a DIN of 7.0 or higher was 61.76% (63 out of 102), and the proportion of samples with a RIN of 7.0 or higher was 58.82% (60 out of 102).

Effect of sample age on DNA and RNA integrity

The changes in DIN and RIN according to sample age (1, 3, 5, and 10 years) were compared and analyzed. The DIN showed no statistically significant difference across sample ages (Kruskal-Wallis test, p = .617) (Fig. 1A) and tended to remain stable in all tissues. The median and IQR by tumor type are presented in Table 3. COAD maintained a median DIN level of 6.6 (IQR, 6.15 to 6.85) to 6.94 (IQR, 6.50 to 7.60) despite the increase in sample age, and the variation in DIN according to sample age was not large as well in HCC and RCC, with median DINs of 6.8 (IQR, 6.40 to 7.20) to 7.75 (IQR, 7.47 to 8.12) for HCC and 7.15 (IQR, 7.05 to 7.40) to 7.4 (IQR, 7.30 to 7.60) for RCC, respectively, confirming that DNA integrity remained relatively stable even during long-term storage.

Similarly, the RIN showed no statistically significant difference across sample ages (Kruskal-Wallis test, p = .578) (Fig. 1B). However, the change in RIN showed some differences depending on the tumor type. HCC and RCC stably maintained high levels of RIN even as sample age increased, whereas COAD showed a slight decrease from a median of 5.3 (IQR, 4.4 to 6.4) in samples with a sample age of 1 year to a median of 5.0 (IQR, 4.2 to 5.9) in samples with a sample age of 10 years. However, the decrease was minor and did not appear to have a significant experimental meaning due to long-term storage (Table 3).

Effect of ischemic time on DNA and RNA integrity

To evaluate the effect of ischemic time on DIN and RIN, samples were divided into four groups for analysis: ≤30 minutes, ≤60 minutes, ≤120 minutes, and >120 minutes. DIN remained relatively constant despite the increase in ischemic time, and no statistically significant differences were observed between the ischemic time groups (Kruskal-Wallis test, p = .081) (Fig. 2A). Similarly, RIN did not show a clear decreasing trend with increasing ischemic time, and the differences between groups were not statistically significant (Kruskal-Wallis test, p = .380)

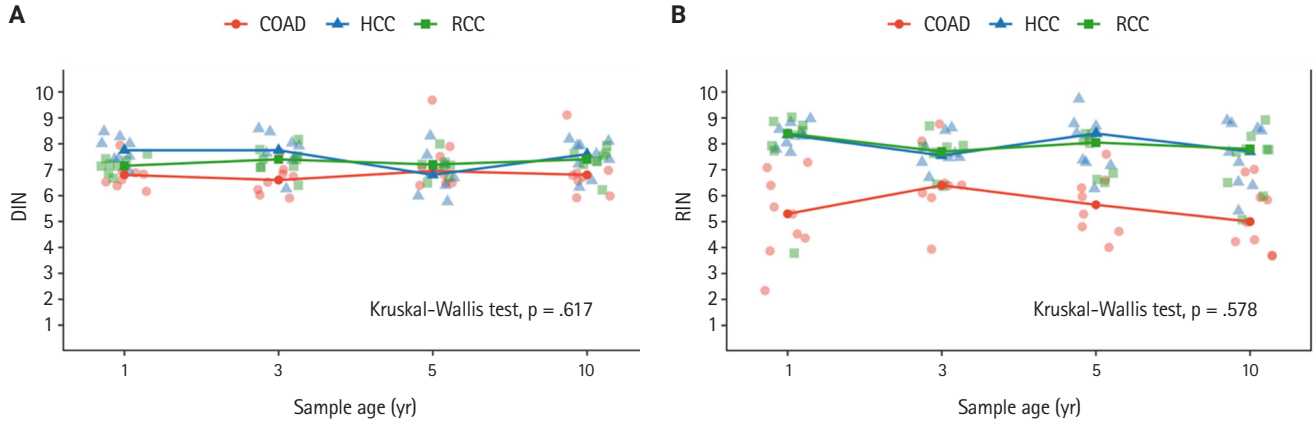

Fig. 1. Effect of sample age on DNA and RNA integrity. Each point represents an individual sample. Red circles, blue triangles, and green squares denote samples derived from colon adenocarcinoma (COAD), hepatocellular carcinoma (HCC), and renal cell carcinoma (RCC), respectively. Solid lines connect the median values of each tumor group across the indicated storage durations. (A) Relationship between DNA integrity number (DIN) and sample age. No statistically significant difference was observed among the groups (Kruskal-Wallis test, p = .617). (B) Relationship between RNA integrity number (RIN) and sample age. A similar trend was noted, with no significant difference across storage time (Kruskal-Wallis test, p = 0.578).

Table 3. Median and IQR of DIN and RIN by sample age and tumor type

Sample age group	DIN (IQR)	RIN (IQR)	COAD		HCC		RCC	
			DIN	RIN	DIN	RIN	DIN	RIN
1-yr	7.1 (6.9–7.5)	7.8 (5.6–8.5)	6.8 (6.5–6.9)	5.3 (4.4–6.4)	7.75 (7.4–8.07)	8.35 (7.95–8.65)	7.15 (7.05–7.4)	8.4 (7.85–8.75)
3-yr	7.4 (6.7–7.7)	7.6 (6.4–7.9)	6.6 (6.15–6.85)	6.4 (6.05–6.9)	7.75 (7.47–8.12)	7.55 (7.45–8.05)	7.4 (7.1–7.5)	7.7 (7.6–7.9)
5-yr	7.0 (6.5–7.3)	7.3 (6.3–8.4)	6.94 (6.5–7.6)	5.65 (4.75–6.37)	6.8 (6.4–7.2)	8.4 (7.3–8.7)	7.2 (6.92–7.22)	8.05 (6.83–8.25)
10-yr	7.3 (6.75–7.6)	6.9 (5.6–7.8)	6.8 (6.6–7.0)	5.0 (4.2–5.9)	7.6 (7.2–7.9)	7.7 (6.5–8.6)	7.4 (7.3–7.6)	7.8 (6.5–7.8)

IQR, interquartile range; DIN, DNA integrity number; RIN, RNA integrity number; COAD, colon adenocarcinoma; HCC, hepatocellular carcinoma; RCC, renal cell carcinoma.

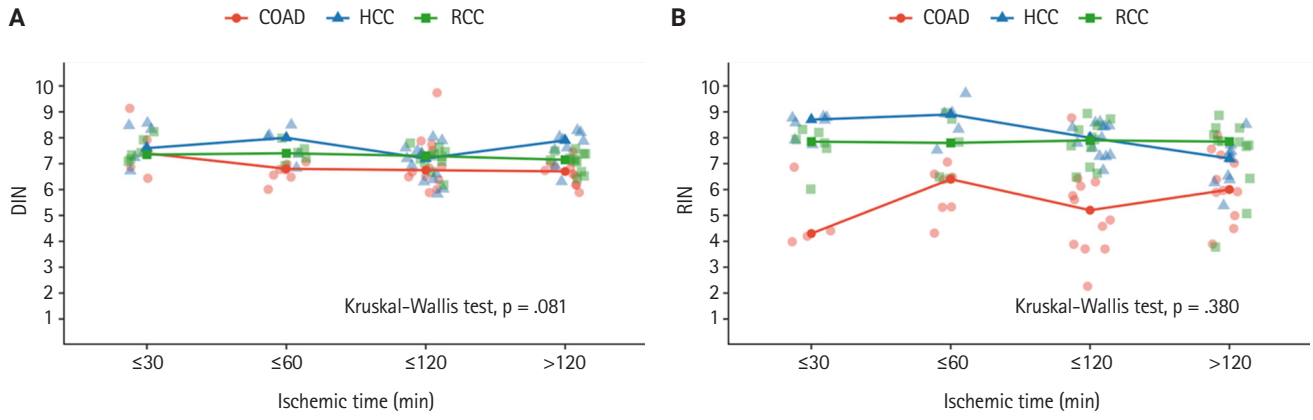

Fig. 2. Effect of ischemic time on DNA and RNA integrity across different organs. Each point represents an individual sample. Red circles, blue triangles, and green squares correspond to samples from the colon adenocarcinoma (COAD), hepatocellular carcinoma (HCC), and renal cell carcinoma (RCC), respectively. Solid lines indicate the median values for each tumor type across ischemic time intervals. (A) Association between DNA integrity number (DIN) and ischemic time (p = .081). (B) Association between RNA integrity number (RIN) and ischemic time (p = .380).

(Fig. 2B).

Additional analyses by tissue type revealed that HCC generally maintained the highest DIN and RIN levels. RCC also exhibited relatively stable DIN and RIN despite increasing ischemic time. In contrast, COAD showed a tendency for greater variability in RIN as ischemic time increased, but this tendency was not statistically significant (Table 4).

Histopathologic and preanalytic factors associated with DNA and RNA integrity

In this study, histopathologic features, including tumor cell proportion, combined normal tissue, inflammatory cell infiltration, stromal fibrosis, necrosis, and extracellular mucin pool, were evaluated using a semi-quantitative grading system, and examples of histological evaluations of representative cases observed in COAD, RCC, and HCC are presented in Fig. 3.

The correlation analysis between histopathologic and preanalytic factors and nucleic acid quality indices (DIN and RIN) is presented in Fig. 4A. No significant correlations were observed between DIN and any of the evaluated variables. In contrast, several significant correlations were identified with RIN. Tumor cell proportion showed a positive correlation with RIN ($r = 0.411$, $p < .001$). Inflammatory cell infiltration ($r = -0.473$, $p < .001$), stromal fibrosis ($r = -0.391$, $p < .001$), extracellular mucin pool ($r = -0.255$, $p = .010$), and combined normal tissue ($r = -0.223$, $p = .024$) showed significant negative correlations with RIN. Necrosis did not show a significant correlation with RIN ($r = -0.148$, $p = .138$).

To identify independent predictors of RNA integrity, multivariable regression analysis was performed including variables

https://doi.org/10.4132/jptm.2025.07.22

Table 4. Median and IQR of DIN and RIN by ischemic time and tumor type

Ischemic time group	DIN (IQR)	RIN (IQR)	COAD		HCC		RCC	
			DIN	RIN	DIN	RIN	DIN	RIN
≤30 min	7.4 (7.2–8.2)	7.9 (6.9–8.6)	7.4 (6.8–8.2)	4.3 (4.2–5.0)	7.6 (7.3–8.4)	8.7 (8.25–8.8)	7.35 (7.2–7.8)	7.85 (7.65–8.12)
≤60 min	7.1 (6.8–7.6)	7.1 (6.4–8.7)	6.8 (6.5–6.9)	6.4 (5.3–6.5)	8.0 (7.4–8.1)	8.9 (8.3–9.0)	7.4 (7.2–7.6)	7.8 (6.5–8.7)
≤120 min	7.15 (6.5–7.5)	7.45 (6.25–8.4)	6.75 (6.47–7.55)	6.2 (3.85–6.14)	7.2 (6.4–7.5)	8.0 (7.3–8.4)	7.3 (7.05–7.45)	7.9 (6.5–8.2)
>120 min	7.1 (6.67–7.5)	7.25 (5.97–7.82)	6.7 (6.35–6.95)	6.0 (5.45–7.15)	7.9 (7.5–8.0)	7.2 (6.4–7.5)	7.15 (7.0–7.4)	7.85 (7.37–8.17)

IQR, interquartile range; DIN, DNA integrity number; RIN, RNA integrity number; COAD, colon adenocarcinoma; HCC, hepatocellular carcinoma; RCC, renal cell carcinoma.

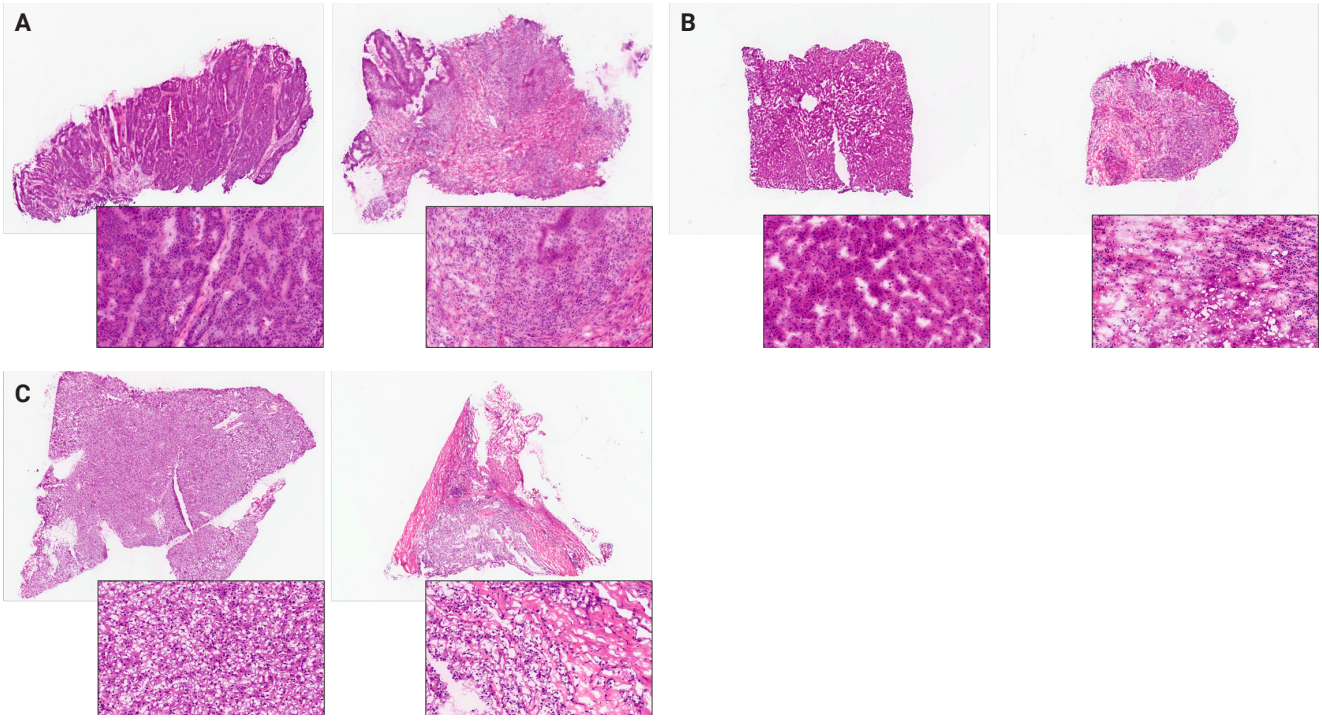

Fig. 3. Representative histopathologic features of fresh-frozen tissue samples from three different tumor types. Representative histologic features of fresh-frozen tissue samples from colon adenocarcinoma (COAD) (A), hepatocellular carcinoma (HCC) (B), and renal cell carcinoma (RCC) (C). For each tumor type, two cases (left and right) are shown, illustrating the range of histopathologic variation observed. In the COAD samples (A), the left case demonstrates high tumor cell proportion with minimal inflammatory infiltration and mild stromal fibrosis, whereas the right case shows low tumor cellularity with marked inflammatory infiltration and stromal fibrosis. The HCC (B) include a case (left) with high tumor cellularity and minimal background alteration, and a case (right) with lower tumor content and marked inflammatory infiltration and stromal fibrosis. All features were semi-quantitatively graded. The RCC samples (C) show a contrast between a predominantly tumor-rich case (left) with no notable background changes and a case (right) with moderate stromal fibrosis and mild inflammation.

that were significant in the univariable correlation analysis (inflammatory cell infiltration, stromal fibrosis, normal tissue, mucin, and tumor proportion). The results are shown in Fig. 4B. Inflammatory cell infiltration and extracellular mucin pool were identified as independent negative predictors of RNA quality (both $p < .05$).

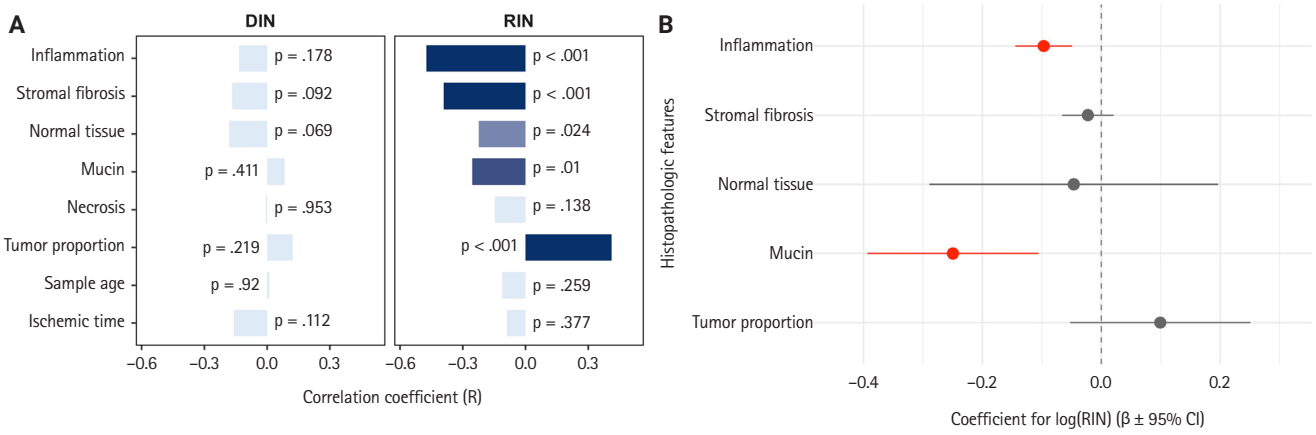

Fig. 4. Univariable and multivariable analysis of factors associated with nucleic acid integrity. (A) Pearson correlation analysis between DNA integrity number (DIN) or RNA integrity number (RIN) and histopathologic or preanalytic variables. Bars represent correlation coefficients (R), and color intensity indicates statistical significance (p-value). (B) Multivariable regression analysis including variables significant in the correlation analysis. Log-transformed RIN was used as the dependent variable. Regression coefficients (β) and 95% confidence intervals (CI) are shown.

DISCUSSION

This study comprehensively analyzed the effects of storage duration, ischemic time, and histopathologic features on DIN and RIN of FFT from COAD, HCC, and RCC collected at the Cancer Tissue Bank of Seoul National University Hospital.

The findings revealed that, despite long-term storage of up to 10 years, most tissues maintained relatively stable levels of both DIN and RIN. HCC and RCC, in particular, demonstrated excellent nucleic acid quality even after more than a decade of storage, confirming that the long-term storage of FFT does not impose practical limitations on its research use.

As a result of analyzing the effects of ex vivo ischemic time on nucleic acid quality (DIN and RIN), no statistically significant decreases in DNA and RNA integrity indices were observed even when ischemic time increased. These results may be because, at the affiliated institution where this study was conducted, surgical samples were stored under refrigerated conditions immediately after resection and until sample processing. Previous studies have also reported that refrigerated storage is effective in suppressing RNA quality deterioration. For example, Fan et al. confirmed that the RIN of COAD decreased rapidly within 8 hours when stored at room temperature, whereas the RIN remained stable for up to 48 hours in refrigerated conditions [7]. In addition, Guo et al. [12] analyzed the relationship between ex vivo ischemic time and RNA quality across various solid cancer tissues, including breast and thyroid cancers, and reported that RNA quality remained stable if ischemic time was kept within 2 hours and immediate cooling was applied, with significant RIN decline occurring only when ischemic time exceeded 4 hours.

However, in the case of COAD, the direction of change was not consistent depending on the ischemic time, and RIN tended to be lower compared to HCC and RCC. This suggests that factors other than ischemic time or sample age may have had a greater impact on RNA quality in the case of COAD, raising the need to find other factors that may have an impact on resource collection and management. In particular, Heumuller-Klug et al. [13] reported that mucosal areas of the COAD are easily exposed to bacteria, leading to rapid RNA degradation and that maintaining cooling and removing bacteria are important for preserving RNA integrity. Although this study did not directly analyze bacteria-related factors, it is highly likely that there are differences in the microbial influence on RNA degradation between the COAD, where gut microbiota normally coexist, and HCC and RCC, which are relatively sterile organs.

In this study, RINs of COAD collected before 2021 (stored for 5 or more years or 10 or more years) were generally lower compared to those collected after 2021. As noted in the methods section, specimens collected before 2021 underwent mucosal surface washing to remove fecal material. Although the direct impact of this process on nucleic acid quality has not been clearly established, previous studies have suggested that excessive exposure to certain washing conditions may affect

https://doi.org/10.4132/jptm.2025.07.22

RNA stability. For example, Ancharayothin et al. emphasized that prolonged washing of intestinal samples can reduce RNA quality and recommended minimizing washing time [14]. These findings suggest that the physical handling of COAD, including the washing step, might have contributed to the lower RINs observed in older samples. Further investigation is needed to clarify the role of such preanalytical factors. These relationships from the univariable analysis are further illustrated in Supplementary Fig. S1, which shows the correlation between histopathologic features and both RIN and DIN.

In this study, we confirmed that histopathologic findings had a greater impact on RNA quality than traditionally recognized factors such as ischemic time and storage age. In univariable analysis, most histopathologic features showed significant associations with RNA quality. Specifically, tumor cell proportion showed a moderate positive correlation with RNA quality, indicating that specimens with a higher proportion of tumor cells generally yielded better RNA integrity. Conversely, inflammatory cell infiltration, stromal fibrosis, extracellular mucin pool, and normal tissue proportion were associated with a decrease in RNA quality. According to the multivariable regression analysis conducted to identify independent predictive factors for RNA quality, inflammatory cell infiltration and extracellular mucin pool were identified as independent negative predictors of RNA quality.

Similar findings have been reported in previous studies. Galissier et al. reported that increased mucin and stromal content led to lower RNA quality in colorectal adenocarcinoma [15]. Several studies have also suggested that severe inflammation can impair RNA preservation. Inflammatory or ulcerated tissues often show increased nuclease activity and disrupted RNA homeostasis. These effects may be mediated by RNase dysregulation [16], tissue acidification [17], or RNase-driven degradation pathways [18]. Giraldo Parra et al. [19] also reported poor RNA recovery from necrotic and inflamed skin lesions. Our findings are consistent with these results. Histopathologic features such as inflammation and mucin content may serve as practical indicators of RNA quality. Incorporating microscopic evaluation may help improve sample selection for transcriptomic studies.

Meanwhile, in the additional examination on the three samples excluded from the analysis in this study as the tumor cell fraction was confirmed to be 0% (Supplementary Table S1), these samples exhibited relatively high DINs despite lacking tumor cells and consisting only of fibrotic tissues or fibrin. Since DIN analysis via Tapestation relies on assessing the fragmentation of high-molecular-weight DNA through electrophoresis, a high DIN may be shown if the DNA is preserved in the nucleus to a certain level or higher. Additionally, DNA can remain relatively stable even within necrotic or fibrotic tissues, potentially leading to misinterpretation of DNA quality. Therefore, using Tapestation-based DINs as the sole criterion for sample suitability may allow the inclusion of tissues that are actually inappropriate for analysis. Accordingly, it is desirable to conduct a histological evaluation of the frozen section through HE staining in parallel with nucleic acid analysis using FFT.

This study has several limitations. First, the tissue samples used for the analysis were limited to samples collected from a single institution, the Cancer Tissue Bank of Seoul National University Hospital, and the total number of samples (n) was relatively small, which may limit statistical interpretation. Second, this study included only three types of cancer tissues (COAD, HCC, and RCC), without including other cancer types or non-neoplastic tissues, which may limit the generalizability of the findings across broader sample types. If large-scale, multi-institutional retrospective studies are conducted in the future—including various tumor and non-tumor tissues collected under diverse conditions—the generalizability and reproducibility of the findings could be further enhanced.

In conclusion, this study confirmed that the storage duration and ischemic time of FFT had generally limited effects on DNA and RNA quality. In particular, COAD showed a tendency for RNA quality to deteriorate relatively easily, suggesting that more stringent preprocessing and quality control are necessary for the tissue. Additionally, inflammatory cell infiltration and extracellular mucin pool were identified as independent predictors of RNA degradation, highlighting the importance of considering histopathologic information as a key factor in the quality assessment of biobank samples. This study is significant in that it comprehensively analyzed the preprocessing conditions and histological factors affecting nucleic acid quality in various cancer tissues collected from a real clinical setting. In the future, the findings may serve as a practical and foundational resource for improving biobank quality management guidelines and establishing a high-quality molecular research infrastructure. Furthermore, our findings are consistent with the recent recommendation by Kim et al. [20], which emphasizes the urgent need for systematic education and training programs aligned with the ISO 20387 international standard. In particular, the identification of inflammatory cell infiltration and extracellular

mucin pool as independent predictors of RNA degradation highlights the importance of strengthening biobank personnel training to ensure that high-quality biospecimens can be selected and managed based on histological quality criteria. Such an approach may help enhance the overall quality control of biobank operations and contribute to the establishment and advancement of ISO 20387-compliant biobanking systems.

Supplementary Information
The Data Supplement is available with this article at https://doi.org/10.4132/jptm.2025.07.22.

Ethics Statement
Tissue samples used in this study were COAD, HCC, and RCC samples collected at the Cancer Tissue Bank of Seoul National University Hospital from January 2014 to December 2023. The Cancer Tissue Bank of Seoul National University Hospital collects and stores human-derived biological samples with the approval of the Institutional Review Board (IRB) of the affiliated institution, and all tissue samples were collected after obtaining voluntary written consent from the donor or legal representative in accordance with the Declaration of Helsinki. This study was conducted as part of the quality assurance process regularly performed by the biobank, and the purpose and method of the study met the review exemption criteria, so approval for review exemption was obtained from the IRB of Seoul National University Hospital (IRB No. E-2503-168-1625).

Availability of Data and Material
The datasets generated or analyzed during the study are available from the corresponding author on reasonable request.

Code Availability
Not applicable.

ORCID
Soungeun Kim https://orcid.org/0009-0006-6778-6871
Jaewon Kang https://orcid.org/0009-0004-8242-4858
Boyeon Kim https://orcid.org/0009-0006-0108-0753
Yoonjin Kwak https://orcid.org/0000-0001-5314-2465
Hye Seung Lee https://orcid.org/0000-0002-1667-7986

Author Contributions
Conceptualization: YK, HSL. Data curation: SK, JK. Formal analysis: SK, BK. Investigation: SK, BK, JK. Funding acquisition: HSL. Methodology: YK, HSL. Project administration: HSL. Resources: HSL. Software: SK. Supervision: YK, HSL. Visualization: SK. Writing—original draft: SK. Writing—review & editing: BK, YK, HSL. Approval of final manuscript: all authors.

Conflicts of Interest
The authors declare that they have no potential conflicts of interest.

Funding Statement
This research was supported by the National Research Foundation of Korea (NRF) grant funded by the Korean government (Ministry of Science and ICT) (No. RS-2024-00337984)

REFERENCES
1. International Society for Biological and Environmental Repositories. Best practices: recommendations for repositories. 5th ed. Vancouver: International Society for Biological and Environmental Repositories, 2023.
2. National Cancer Institute. Best practices for biospecimen resources. Bethesda: Natioanl Cancer Institute, 2016.
3. Linsen L, T'Joen V, Van Der Straeten C, et al. Biobank quality management in the BBMRI.be Network. Front Med (Lausanne) 2019; 6: 141.
4. Micke P, Ohshima M, Tahmasebpoor S, et al. Biobanking of fresh frozen tissue: RNA is stable in nonfixed surgical specimens. Lab Invest 2006; 86: 202-11.
5. Song SY, Jun J, Park M, et al. Biobanking of fresh-frozen cancer tissue: RNA is stable independent of tissue type with less than 1 hour of cold ischemia. Biopreserv Biobank 2018; 16: 28-35.
6. Nam SK, Im J, Kwak Y, et al. Effects of fixation and storage of human tissue samples on nucleic acid preservation. Korean J Pathol 2014; 48: 36-42.
7. Fan XJ, Huang Y, Wu PH, et al. Impact of cold ischemic time and freeze-thaw cycles on RNA, DNA and protein quality in colorectal cancer tissues biobanking. J Cancer 2019; 10: 4978-88.
8. Zhang X, Han QY, Zhao ZS, Zhang JG, Zhou WJ, Lin A. Biobanking of fresh-frozen gastric cancer tissues: impact of long-term storage and clinicopathological variables on RNA quality. Biopreserv Biobank 2019; 17: 58-63.
9. Neuber AC, Komoto TT, da Silva EC, Duval VD, Scapulatempo-Neto C, Marques MM. Quality assessment of cryopreserved human biological samples from the biobank of Barretos Cancer Hospital. Biopreserv Biobank 2023; 21: 74-80.

10. Zeugner S, Mayr T, Zietz C, Aust DE, Baretton GB. RNA quality in fresh-frozen gastrointestinal tumor specimens-experiences from the tumor and healthy tissue bank TU Dresden. Recent Results Cancer Res 2015; 199: 85-93.
11. Kap M, Oomen M, Arshad S, de Jong B, Riegman P. Fit for purpose frozen tissue collections by RNA integrity number-based quality control assurance at the Erasmus MC tissue bank. Biopreserv Biobank 2014; 12: 81-90.
12. Guo D, Wang A, Xie T, Zhang S, Cao D, Sun J. Effects of ex vivo ischemia time and delayed processing on quality of specimens in tissue biobank. Mol Med Rep 2020; 22: 4278-88.
13. Heumuller-Klug S, Sticht C, Kaiser K, et al. Degradation of intestinal mRNA: a matter of treatment. World J Gastroenterol 2015; 21: 3499-508.
14. Acharayothin O, Thiengtrong B, Juengwiwattanakitti P, et al. Impact of washing processes on RNA quantity and quality in patient-derived colorectal cancer tissues. Biopreserv Biobank 2023; 21: 31-7.
15. Galissier T, Schneider C, Nasri S, et al. Biobanking of fresh-frozen human adenocarcinomatous and normal colon tissues: which parameters influence RNA quality? PLoS One 2016; 11: e0154326.
16. Bedenbender K, Scheller N, Fischer S, et al. Inflammation-mediated deacetylation of the ribonuclease 1 promoter via histone deacetylase 2 in endothelial cells. FASEB J 2019; 33: 9017-29.
17. Miyahara K, Hino M, Yu Z, et al. The influence of tissue pH and RNA integrity number on gene expression of human postmortem brain. Front Psychiatry 2023; 14: 1156524.
18. Lasch M, Kumaraswami K, Nasiscionyte S, et al. RNase A treatment interferes with leukocyte recruitment, neutrophil extracellular trap formation, and angiogenesis in ischemic muscle tissue. Front Physiol 2020; 11: 576736.
19. Giraldo-Parra L, Ramirez LG, Navas A, Gomez MA. Quality parameters for RNA preparations from biopsies of ulcerated human skin. Wellcome Open Res 2022; 7: 249.
20. Kim JO, Kim C, Song S, et al. Professional biobanking education in Korea based on ISO 20387. J Pathol Transl Med 2025; 59: 11-25.

JPTM

ORIGINAL ARTICLE

pISSN 2383-7837 · eISSN 2383-7845

Journal of Pathology and Translational Medicine 2025; 59: 408-420
https://doi.org/10.4132/jptm.2025.08.27

E-cadherin expression and tumor-stroma ratio as prognostic biomarkers of peritoneal recurrence in advanced gastric cancer: a digital image analysis-based stratification study

Somang Lee[1], Binnari Kim[2]

[1]Department of Pathology, Ulsan University Hospital, Ulsan, Korea
[2]Department of Pathology, Ulsan University Hospital, University of Ulsan College of Medicine, Ulsan, Korea

Graphical abstract

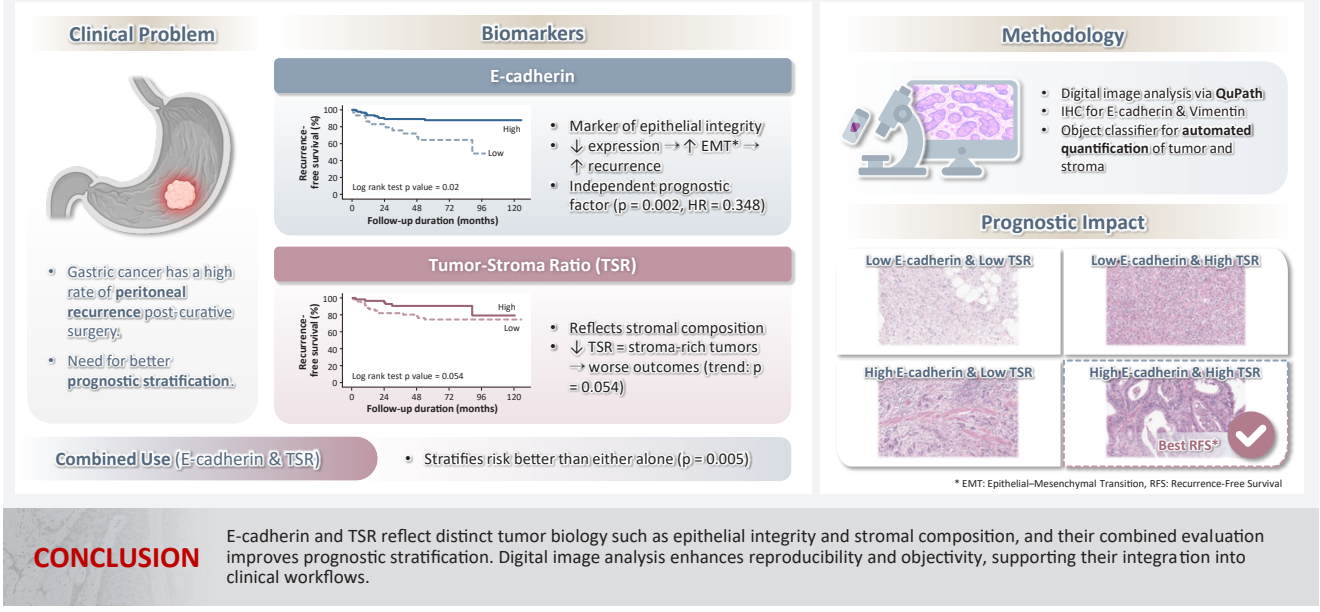

CONCLUSION E-cadherin and TSR reflect distinct tumor biology such as epithelial integrity and stromal composition, and their combined evaluation improves prognostic stratification. Digital image analysis enhances reproducibility and objectivity, supporting their integration into clinical workflows.

Lee S et al. Journal of Pathology and Translational Medicine

JPTM

ORIGINAL ARTICLE

pISSN 2383-7837 · eISSN 2383-7845

Journal of Pathology and Translational Medicine 2025; 59: 408-420
https://doi.org/10.4132/jptm.2025.08.27

E-cadherin expression and tumor-stroma ratio as prognostic biomarkers of peritoneal recurrence in advanced gastric cancer: a digital image analysis-based stratification study

Somang Lee[1], Binnari Kim[2]

[1]Department of Pathology, Ulsan University Hospital, Ulsan, Korea
[2]Department of Pathology, Ulsan University Hospital, University of Ulsan College of Medicine, Ulsan, Korea

Background: Gastric cancer remains a significant global health burden, with a high peritoneal recurrence rates after curative surgery. E-cadherin and the tumor-stroma ratio (TSR) have been proposed as prognostic indicators, but their combined prognostic utility remains unclear. **Methods:** This retrospective study included 130 patients with T3/T4a gastric cancer who underwent curative gastrectomy at Ulsan University Hospital between 2014 and 2019. Immunohistochemistry for E-cadherin and Vimentin was performed. Digital image analysis using QuPath's object classifier quantified E-cadherin expression and TSR. **Results:** Low E-cadherin expression was associated with diffuse-type histology and advanced T stage. Low TSR was linked to younger age, female sex, and XELOX treatment. In Kaplan-Meier analysis, low TSR showed a non-significant trend toward higher peritoneal recurrence (p = .054), while low E-cadherin expression was significantly associated with increased peritoneal recurrence (p = .002). Combined biomarker analysis also revealed a significant difference in recurrence-free survival (RFS) among the four groups (p = .005); patients with both high TSR and high E-cadherin expression experienced the most favorable RFS. In multivariable analysis, E-cadherin expression remained the only independent predictor of peritoneal recurrence (high vs. low; hazard ratio, 0.348; 95% confidence interval, 0.149 to 0.816; p = .015). **Conclusions:** E-cadherin and TSR reflect distinct tumor biology such as epithelial integrity and stromal composition, and their combined evaluation improves prognostic stratification. Digital image analysis enhances reproducibility and objectivity, supporting their integration into clinical workflows.

Keywords: Stomach neoplasms; CDH1 protein, human; Neoplasm stroma; Pathology, digital; Peritoneal neoplasms

INTRODUCTION

Gastric cancer ranks among the most commonly diagnosed malignancies worldwide, representing the fifth most frequent cancer and the fifth leading cause of cancer-related mortality, accounting for approximately 6.8% of all cancer deaths globally [1]. Despite significant advances in surgical techniques and systemic therapies, gastric cancer remains characterized by a high rate of postoperative recurrence, which contributes substantially to its poor overall prognosis [2]. Peritoneal recurrence, in particular, represents a major clinical challenge, occurring in approximately 29% to 38% of patients after curative resection and associated with a median survival of only four months [3,4].

E-cadherin is a calcium-dependent transmembrane glycoprotein encoded by the *CDH1* gene located on chromosome 16q22.1. It plays a pivotal role in maintaining epithelial architecture by mediating intercellular adhesion, and its dysregulation contributes to tumor initiation, progression, invasion, and metastasis [5]. Loss of E-cadherin function is a hallmark of epithelial-mesenchymal transition (EMT), a biological process in which epithelial cells acquire mesenchymal features, enhancing migratory and invasive potential [4]. Aban et al. [4] reported that diminished membranous E-cadherin expression facilitates EMT via activation of key transcription factors, including Snail,

Received: June 27, 2025 **Revised:** August 21, 2025 **Accepted:** August 27, 2025
Corresponding Author: Binnari Kim, MD, PhD
Department of Pathology, Ulsan University Hospital, University of Ulsan College of Medicine, 25 Daehakbyeongwon-ro, Dong-gu, Ulsan 44033, Korea
Tel: +82-52-250-8953, Fax: +82-52-250-8059, E-mail: 0734593@uuh.ulsan.kr

Slug, Twist, and ZEB-1. Multiple studies have demonstrated that aberrant E-cadherin expression is significantly associated with higher tumor stage, greater depth of invasion, lymph node metastasis, and unfavorable histologic features, thereby underscoring its value as a marker of tumor aggressiveness in gastric cancer [6,7].

The tumor-stroma ratio (TSR), defined as the proportion of tumor cells relative to stromal tissue, has emerged as a novel prognostic marker across various malignancies, including colorectal, prostate, breast, ovarian, cervical, nasopharyngeal, hepatocellular, esophageal, and lung cancers [2,8]. In the context of gastric cancer, stroma-poor tumors have been associated with improved overall survival and disease-free survival [2]. Tian et al. [9] reported that a high proportion of stromal area was significantly associated with aggressive tumor phenotypes and reduced cancer-specific survival, supporting the prognostic relevance of TSR in gastric cancer. TSR can be readily assessed on hematoxylin and eosin (H&E)–stained slides using conventional light microscopy, making it a practical biomarker for routine pathologic evaluation [2,10].

Despite growing interest in both E-cadherin and TSR as prognostic markers, limited research has investigated their interrelationship or joint predictive utility in gastric cancer. Several studies have directly evaluated the association between E-cadherin expression and peritoneal dissemination [11-16], including meta-analyses confirming a significant correlation [17]. Conversely, studies exploring TSR in relation to peritoneal recurrence are scarce [8], and, to our knowledge, no study has concurrently assessed both E-cadherin and TSR in predicting peritoneal recurrence.

The present study aimed to evaluate the prognostic relevance of E-cadherin expression and TSR, investigate their correlation, and determine whether their combined assessment enhances risk stratification for peritoneal recurrence in patients with advanced gastric cancer. To ensure robust and reproducible measurement, digital image analysis was employed for the quantitative evaluation of both markers, thereby minimizing interobserver variability and enhancing analytical precision.

MATERIALS AND METHODS

Study population and data collection

This retrospective study included 130 patients diagnosed with T3 or T4a advanced gastric cancer who underwent curative gastrectomy at Ulsan University Hospital between January 2014 and December 2019. Among an initial cohort of 292 patients, cases were excluded based on the following criteria: (1) presence of other primary malignancies, (2) positive intraoperative peritoneal lavage cytology, (3) M1 category at the time of diagnosis, or (4) involvement of the resection margin. Clinical and pathological data were retrieved from electronic medical records and included patient age, sex, tumor size, gross morphology, histologic type, TNM stage, lymphovascular invasion, perineural invasion, resection margin status, and results of abdominal washing cytology. TNM staging was based on the 8th edition of the American Joint Committee on Cancer (AJCC) classification system [18]. Tumor gross type was categorized according to the Borrmann classification [19], and histological subtype was classified based on the Lauren classification [20].

Slide selection

Representative formalin-fixed, paraffin-embedded (FFPE) tissue blocks were selected for each case. All H&E-stained slides were reviewed to identify the slide demonstrating the deepest tumor invasion. In cases where visual assessment was inconclusive, 2–3 candidate slides were scanned, and the depth of invasion was digitally measured to confirm selection.

Immunohistochemistry

Immunohistochemical staining for E-cadherin and Vimentin was performed on FFPE sections using an automated immunostainer (Bond-PRIME, Leica Biosystems, Buttalo Grove, IL, USA). The primary antibodies used were anti-E-cadherin (1:100 dilution, clone NCH-38, DAKO, Glostrup, Denmark) and anti-Vimentin (1:1000 dilution, clone V9, Invitrogen, Carlsbad, CA, USA). Antigen retrieval was conducted using Bond-PRIME Epitope Retrieval Solution 2 (EDTA-based buffer, pH 9.0) for E-cadherin, and Bond-PRIME Epitope Retrieval Solution 1 (citrate-based buffer, pH 6.0) for Vimentin, both at 104°C for 20 minutes. Endogenous peroxidase activity was blocked using a peroxide block for 3 minutes. Sections were then incubated with the primary antibodies for 15 minutes, followed by post-primary reagent incubation for 8 minutes. Detection was performed using a polymer-based detection system (Bond Polymer Refine Detection Kit, Leica Biosystems) for 8 minutes. Visualization was achieved using 3,3'-diaminobenzidine (DAB) chromogen for 10 minutes. Finally, the slides were counterstained with hematoxylin for 4 minutes, rinsed with distilled water, and mounted after dehydration.

Digital image acquisition

Whole-slide images of H&E-stained sections and immunohistochemically stained slides for E-cadherin and Vimentin were acquired at 40× objective magnification using an Aperio GT450 DX scanner (Leica Biosystems). Digital image analysis was performed using QuPath software ver. 0.5.1.

E-cadherin expression analysis

E-cadherin expression was evaluated in three representative tumor regions located at the deepest point of the tumor-invasive front, selected by a pathologist (B.K.). Regions were required to show well-preserved viable tumor cells, while areas with extensive necrosis, ulceration, or artifacts were excluded. All regions were analyzed at 400× magnification, and fields in normal gastric mucosa (when available) were selected at the same magnification for comparison. Cell detection was performed using QuPath's built-in algorithm, followed by manual verification by a pathologist (B.K.). An object classifier was trained to differentiate tumor from stromal cells based on cell-level features including intensity, morphology, and spatial parameters. For each region, the mean DAB optical density (OD) of positively stained tumor cells was calculated. For normal mucosa, the mean DAB OD of all positive epithelial cells was measured. The tumor-to-normal ratio was then computed to normalize for staining variability across slides. When adjacent normal mucosa was absent, a cohort-derived reference value, calculated as the mean DAB OD from all normal mucosa annotations, was used. The procedure is visually summarized in Fig. 1A and B.

TSR analysis

TSR was quantified through a sequential image analysis workflow. First, three representative tumor areas located at the

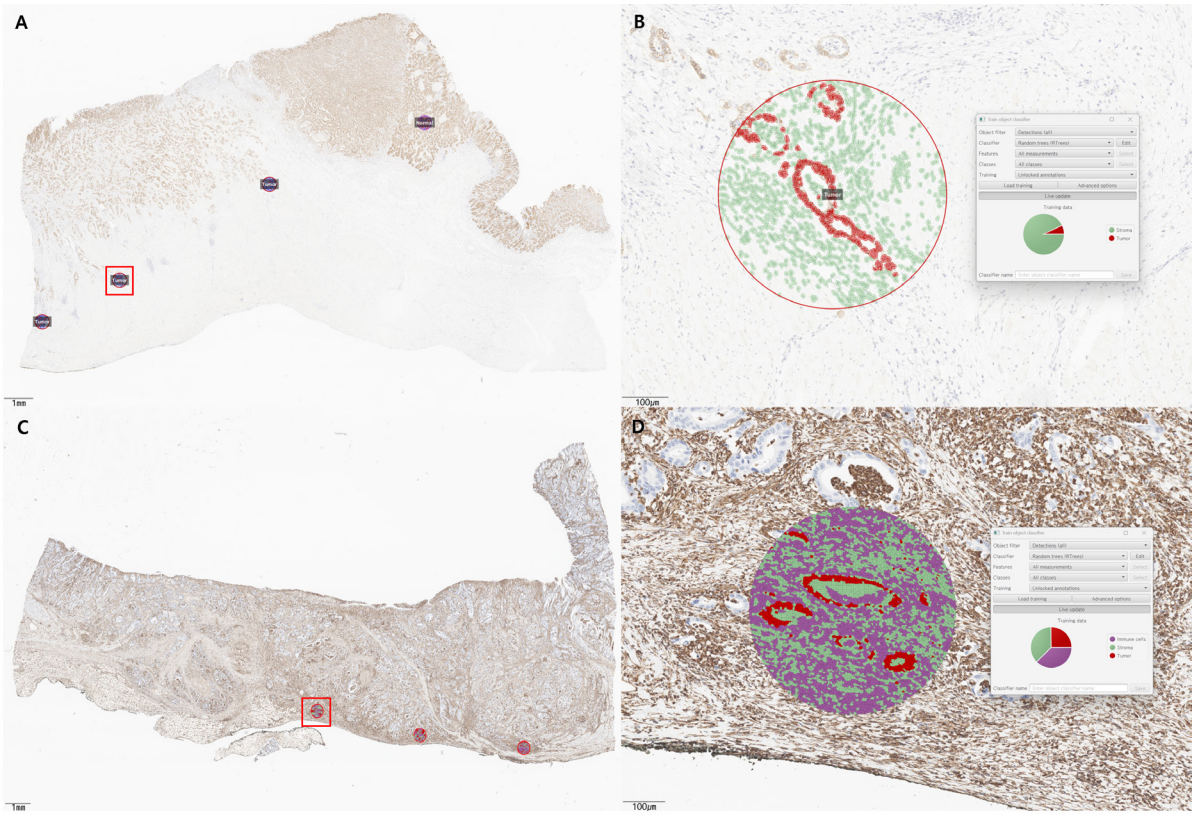

Fig. 1. Digital image analysis of E-cadherin expression and tumor-stroma ratio (TSR). (A) Three representative tumor regions at the invasive front and one area of normal gastric mucosa were selected on whole-slide images. Inset boxes indicate the areas magnified in panel B. (B) High-magnification view showing cell detection and classification of tumor cells (red) and stromal cells (green) using a trained object classifier. (C) For TSR evaluation, three representative tumor areas at the invasive front were selected. Inset boxed indicate the areas magnified in panel D. (D) High-magnification view showing superpixel segmentation and classification of tumor (red) and stroma (green). Immune cells (purple) were also annotated to enhance analytical precision in this case.

https://doi.org/10.4132/jptm.2025.08.27

deepest point of the tumor-invasive front, selected by a pathologist (B.K.). Regions were required to show abundant stromal components and well-preserved viable tumor cells, while areas with extensive necrosis, ulceration, or artifacts were excluded. Each selected region was reviewed on both H&E and vimentin-stained slides to confirm accurate tumor localization and to exclude necrotic or artifact-prone areas. For computational analysis, vimentin immunohistochemistry was used to distinguish stromal components from tumor epithelium, as vimentin is strongly expressed in fibroblasts and mesenchymal stromal cells. Digital image analysis was performed at 400× magnification, corresponding to the optical microscope view. In each region, superpixel segmentation was conducted using simple linear iterative clustering (SLIC) algorithm implemented in Qupath ver. 0.5.1. Following segmentation, superpixels were manually annotated as either tumor or stoma. An object classifier was trained using superpixel-level features such as intensity, texture, and shape to differentiate tumor from stroma. Depending on the case, additional components such as immune cells or adipocytes were included alongside tumor and stroma to improve classification performance. The trained classifier was then applied to all selected regions for automated classification. TSR was calculated as the ratio of the tumor area to the total area of encompassing both tumor and non-tumoral components. All classification results were visually reviewed to ensure consistency and accuracy. The procedure is visually summarized in Fig. 1C and D.

Statistical analysis

Categorical variables were compared using chi-square tests or Fisher's exact tests, as appropriate. Continuous variables were analyzed using independent t-tests or Mann-Whitney U tests, depending on the distribution of the data. Recurrence-free survival (RFS) was analyzed according to the combined E-cadherin and TSR groups. The curves were compared using the log-rank test, with pairwise comparisons performed between groups. Cox regression analysis was conducted to compare prognostic models for predicting peritoneal recurrence. Multivariable Cox proportional hazards regression analysis was performed to identify clinicopathologic factors associated with peritoneal recurrence. All p-values were two-sided, and values less than .05 were considered statistically significant. Data processing and statistical analyses were performed using IBM SPSS Statistics for Windows ver. 28.0 (IBM Corp., Armonk, NY, USA) and R software ver. 4.2.2 (R Foundation for Statistical Computing, Vienna, Austria).

RESULTS

Patients characteristics

The clinicopathologic characteristics of the 130 patients included in the study are summarized in Table 1. The cohort

Table 1. Baseline clinicopathologic characteristics of the study cohort

	Value
Age (yr)	57.02±11.48
Sex	
Male	106 (81.5)
Female	24 (18.5)
Tumor size (cm)	5.86±3.02
Gross type	
2	5 (3.8)
3	108 (83.1)
4	7 (13.1)
Histologic type	
Diffuse	100 (76.9)
Intestinal	30 (23.1)
T category	
T3	50 (38.5)
T4a	80 (61.5)
N category	
N0	35 (26.9)
N1	25 (19.2)
N2	29 (22.3)
N3	41 (31.5)
Lymphovascular invasion	
Negative	51 (39.2)
Positive	79 (60.8)
Perineural invasion	
Negative	21 (16.2)
Positive	109 (83.8)
Chemotherapy	
XELOX	86 (66.2)
TS-1	39 (30.0)
Others[a]	5 (3.8)
Follow-up duration (mo)	53.59±30.12
Time to recurrence (mo)	50.90±30.48

Values are presented as mean±standard deviation or number (%).
[a]FOLFOX (folinic acid, fluorouracil, and oxaliplatin), HXP (hydroxycamptothecin, capecitabine, and cisplatin), and TS-1 (tegafur, gimeracil, and oteracil potassium), switched to XELOX (capecitabine and oxaliplatin) were included.

comprised 81.5% males (n = 106) and 18.5% females (n = 24), with a mean age of 57.02 ± 11.48 years. The mean tumor size was 5.86 ± 3.02 cm. According to the Borrmann classification, type 3 was the most common gross type (83.1%, n = 108), and based on the Lauren classification, the diffuse type predominated (76.9%, n = 100). T category was classified as T3 in 38.5% (n = 50) and T4a in 61.5% (n = 80). Lymph node status was N0 in 27.1% (n = 35), N1 in 19.2% (n = 25), N2 in 22.5% (n = 29), and N3 in 31.5% (n = 41). Lymphovascular invasion and perineural invasion were present in 60.8% (n = 79) and 83.8% (n = 109) of cases, respectively. As for adjuvant chemotherapy, 66.2% (n = 86) received XELOX, 30.0% (n = 39) received TS-1, and 3.8% (n = 5) received other regimens. The mean follow-up duration was 53.59 ± 30.12 months, and peritoneal recurrence occurred after a mean interval of 50.90 ± 30.48 months.

Association between E-cadherin expression and TSR with clinicopathologic factors

To evaluate the associations of E-cadherin expression and TSR with various clinicopathologic factors, receiver operating characteristic (ROC) curve analysis was used to determine the respective cut-off values of 0.315 for E-cadherin and 9.664 for TSR. For E-cadherin, low expression was statistically significantly associated with diffuse-type histology (90.3% vs. 72.7%, p = .042) and deeper tumor invasion (T4a: 77.4% vs. 56.6%, p = .037). There were no statistically significant differences in age, sex, tumor size, gross type, N category, lymphovascular invasion, perineural invasion, chemotherapy regimen, follow-up duration, or time to recurrence between the low and high expression groups. For TSR, low group was statistically significantly associated with younger age (53.61 vs. 61.0 years, p < .001) and female patients (27.1% vs. 8.3%, p = .006). Chemotherapy regimens also differed statistically significantly between the low and high TSR groups (p = .008). No statistically significant differences were observed between these two groups in tumor size, gross type, histologic type, T category, N category, lymphovascular invasion, perineural invasion, follow-up duration, or time to recurrence. The analysis of chemotherapy regimens was not intended to assess the predictive value of these biomarkers for treatment selection, but rather to evaluate whether treatment heterogeneity might confound the observed associations between each biomarker and peritoneal recurrence. Detailed results are presented in Tables 2 and 3.

Correlation between TSR and E-cadherin expression

Correlation analysis revealed a weak positive relationship between TSR and E-cadherin expression when assessed using the mean ratio (r = 0.139, p = .114) (Fig. 2). Consistent with this, subgroup comparisons showed no significant difference in TSR values between low and high E-cadherin expression groups (p = .652; data not shown), nor in E-cadherin expression levels

Table 2. Clinicopathologic comparison based on E-cadherin expression

	Low (n=31)	High (n=99)	p-value
Age (yr)	58.48±10.35	56.57±11.82	.419
Sex			.227
Male	23 (74.2)	83 (83.8)	
Female	8 (25.8)	16 (16.2)	
Tumor size (cm)	6.10±2.69	5.78±3.13	.609
Gross type			.199
2	1 (3.2)	4 (4.0)	
3	23 (74.2)	85 (85.9)	
4	7 (22.6)	10 (10.1)	
Histologic type			.042
Diffuse	28 (90.3)	72 (72.7)	
Intestinal	3 (9.7)	27 (27.3)	
T category			.037
T3	7 (22.6)	43 (43.4)	
T4a	24 (77.4)	56 (56.6)	
N category			.526
N0	8 (25.8)	27 (27.3)	
N1	8 (25.8)	17 (17.2)	
N2	8 (25.8)	21 (21.2)	
N3	7 (22.6)	34 (34.3)	
Lymphovascular invasion			.624
Negative	11 (35.5)	40 (40.4)	
Positive	20 (64.5)	59 (59.6)	
Perineural invasion			.573
Negative	4 (12.9)	17 (17.2)	
Positive	27 (87.1)	82 (82.8)	
Chemotherapy			.742
XELOX	20 (64.5)	66 (66.7)	
TS-1	9 (29.0)	30 (30.3)	
Others[a]	2 (6.5)	3 (3.0)	
Follow-up duration (mo)	50.55±29.45	54.55±30.41	.521
Time to recurrence (mo)	48.26±30.07	53.04±30.67	.448

Values are presented as mean±standard deviation or number (%).
[a]FOLFOX (folinic acid, fluorouracil, and oxaliplatin), HXP (hydroxycamptothecin, capecitabine, and cisplatin), and TS-1 (tegafur, gimeracil, and oteracil potassium), switched to XELOX (capecitabine and oxaliplatin) were included.

https://doi.org/10.4132/jptm.2025.08.27

Table 3. Clinicopathologic comparison based on tumor-stromal ratio

	Low (n=70)	High (n=60)	p-value
Age (yr)	53.61±11.38	61.00±10.32	<.001
Sex			.006
Male	51 (72.9)	55 (91.7)	
Female	19 (27.1)	5 (8.3)	
Tumor size (cm)	5.90±3.48	5.81±2.42	.860
Gross type			.267
2	2 (2.9)	3 (5.0)	
3	56 (80.0)	52 (86.7)	
4	12 (17.1)	5 (8.3)	
Histologic type			.083
Diffuse	58 (82.9)	42 (70.0)	
Intestinal	12 (17.1)	18 (30.0)	
T category			.487
T3	25 (35.7)	25 (41.7)	
T4a	45 (64.3)	35 (58.3)	
N category			.788
N0	21 (30.0)	14 (23.3)	
N1	14 (20.0)	11 (18.3)	
N2	14 (20.0)	15 (25.0)	
N3	21 (30.0)	20 (33.3)	
Lymphovascular invasion			.102
Negative	32 (45.7)	19 (31.7)	
Positive	38 (54.3)	41 (68.3)	
Perineural invasion			.532
Negative	10 (14.3)	11 (18.3)	
Positive	60 (85.7)	49 (81.7)	
Chemotherapy			.008
XELOX	54 (77.1)	32 (53.3)	
TS-1	15 (21.4)	24 (40.0)	
Others[a]	1 (1.4)	4 (6.7)	
Follow-up duration (mo)	52.47±31.74	54.90±28.33	.649
Time to recurrence (mo)	51.17±32.51	52.75±28.16	.770

Values are presented as mean±standard deviation or number (%).
[a]FOLFOX (folinic acid, fluorouracil, and oxaliplatin), HXP (hydroxycamptothecin, capecitabine, and cisplatin), and TS-1 (tegafur, gimeracil, and oteracil potassium), switched to XELOX (capecitabine and oxaliplatin) were included.

between low and high TSR groups (p = .242; data not shown).

Prognostic impact of E-cadherin expression and TSR on RFS

Kaplan–Meier curves were generated to evaluate the prognostic value of E-cadherin expression and TSR on RFS. Patients with low E-cadherin expression had significantly shorter RFS compared to those with high expression (log-rank p = .002) (Fig. 3). When stratified by histologic subtype, low E-cadherin expression was significantly associated with shorter RFS in both diffuse type (log-rank p = .029) and intestinal type (log-rank p = .008) (data not shown). In contrast, patients in the low TSR group demonstrated a trend toward shorter RFS, but the difference was not statistically significant (log-rank p = .054) (Fig. 3).

We analyzed RFS using Kaplan–Meier curves based on a combined stratification of E-cadherin expression and TSR. According to the cut-off values determined by ROC curve analysis, patients were classified into four groups: group 1 (low E-cadherin & low TSR), group 2 (low E-cadherin & high TSR), group 3 (high E-cadherin & low TSR), and group 4 (high E-cadherin & high TSR). There were statistically significant differences in RFS among the four groups (p = .005), and Group 4 exhibited the most favorable outcome (Fig. 4). Pairwise log-rank comparisons revealed statistically significant differences between group 1 and group 4 (p < .001), as well as between group 2 and group 4 (p = .011), and between group 3 and group 4 (p = .040). However, there were no statistically significant differences between group 1 and group 2, group 2 and group 3, or group 1 and group 3. Detailed results are presented in Table 4.

Multivariable analysis of clinicopathologic factors associated with peritoneal recurrence

To identify clinicopathologic variables independently associated with peritoneal recurrence in advanced gastric cancer, a multivariable Cox proportional hazards regression analysis was conducted (Table 5). Variables included in the model were age, sex, tumor size, gross type, histologic subtype, T category, N category, lymphovascular invasion, perineural invasion, TSR, E-cadherin expression, and adjuvant chemotherapy regimen. In univariate analysis, tumor size (hazard ratio [HR], 1.161; 95% confidence interval [CI], 1.043 to 1.291; p = .006), T category (T4a vs. T3; HR, 7.828; 95% CI, 1.826 to 33.549; p = .006), N category (N0 vs. N1 + N2 + N3; HR, 4.571; 95% CI, 1.077 to 19.396; p = .039), E-cadherin (high vs. low; HR, 0.293; 95% CI, 0.127 to 0.676; p = 0.004), and chemotherapy regimen (others vs. XELOX; HR, 4.467; 95% CI, 1.281 to 15.579; p = .019) were statistically significantly associated with increased risk of peritoneal recurrence. However, in the multivariable model, only E-cadherin expression remained statistically significant (high vs. low; HR, 0.348; 95% CI, 0.149 to 0.816; p =.015), indicating that high E-cadherin expression was associated with a statistically significantly lower risk of peritoneal recurrence compared

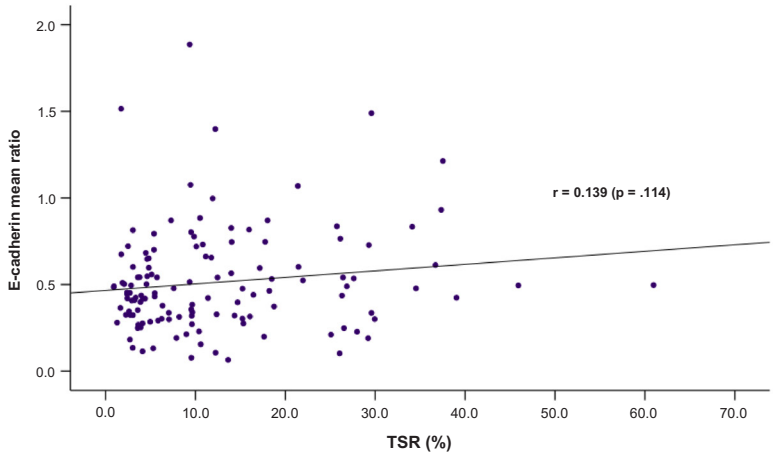

Fig. 2. Correlation between E-cadherin expression and tumor-stroma ratio (TSR). A scatter plot showing the correlation between E-cadherin expression, quantified as tumor-to-normal mean 3,3'-diaminobenzidine optical density ratios, and TSR.

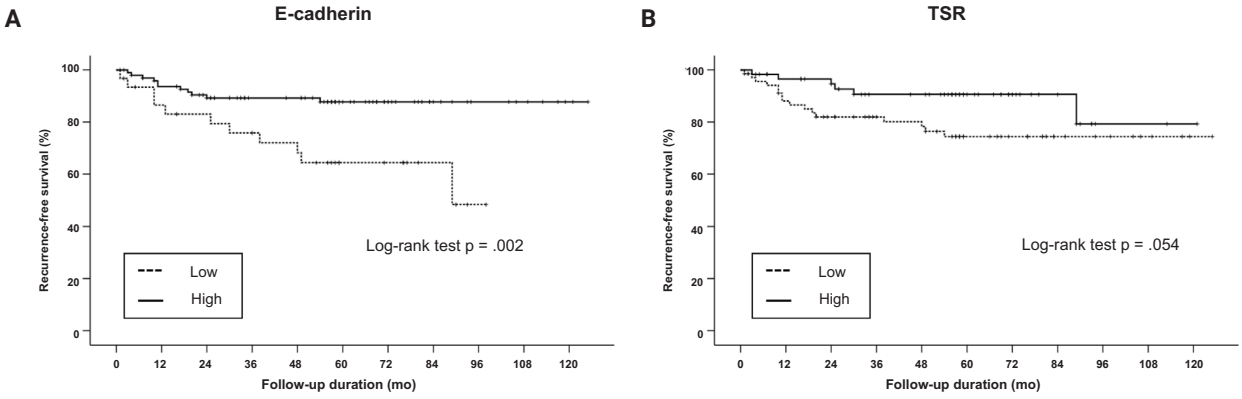

Fig. 3. Kaplan-Meier curve for peritoneal recurrence stratified by E-cadherin and tumor-stroma ratio (TSR). Kaplan–Meier analysis showing recurrence-free survival based on E-cadherin expression (p = .002) (A) and TSR (p = .054) (B).

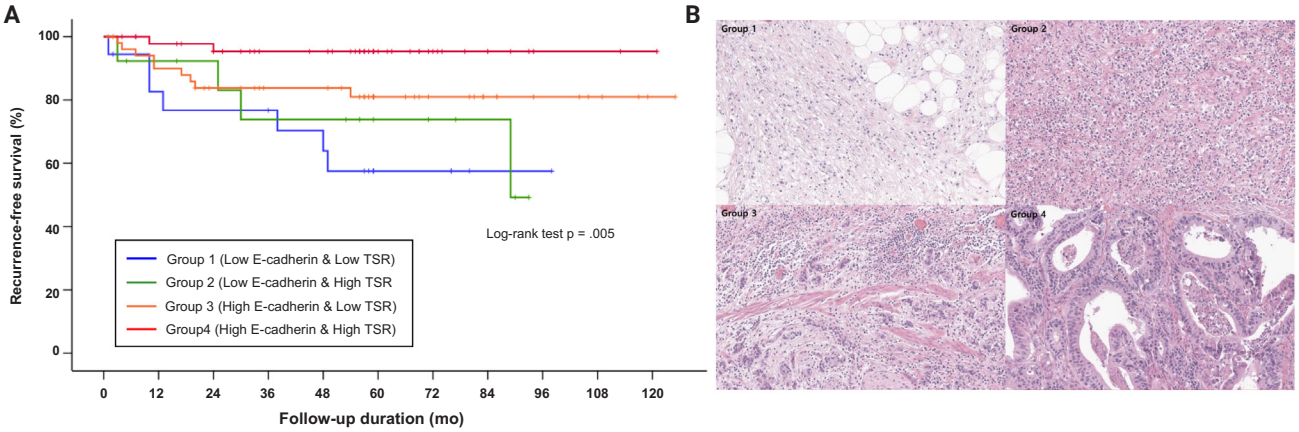

Fig. 4. Kaplan-Meier curve of recurrence-free survival (A) according to combined E-cadherin and tumor-stroma ratio (TSR) classification. Combined classification into four groups shows significant differences in recurrence-free survival (p = .005). Representative hematoxylin and eosin–stained images (B) for each group are included to aid histopathologic correlation.

https://doi.org/10.4132/jptm.2025.08.27

Table 4. Pairwise log-rank test for recurrence-free survival according to combined E-cadherin and TSR groups

	Low E-cadherin Low TSR	Low E-cadherin High TSR	High E-cadherin Low TSR	High E-cadherin High TSR
Low E-cadherin & Low TSR		.543	.071	<.001
Low E-cadherin & High TSR	.543		.348	.011
High E-cadherin & Low TSR	.071	.348		.040
High E-cadherin & High TSR	<.001	.011	.040	

TSR, tumor-stroma ratio.

Table 5. Multivariable analysis of clinicopathologic factors associated with peritoneal recurrence

	Univariable			Multivariable		
	HR	95% CI	p-value	HR	95% CI	p-value
Age	0.990	0.954–1.027	.597	-	-	-
Sex						
Male	Ref.					
Female	1.430	0.527–3.877	.482	-	-	-
Tumor size (cm)	1.161	1.043–1.291	.006	1.116	0.975–1.278	.111
Gross type						
2	Ref.					
3	3050.621	0.000–7.665E+63	.910	-	-	-
4	22421.150	0.000–5.635E+64	.888	-	-	-
Histologic type						
Diffuse	Ref.					
Intestinal	0.147	0.020–1.094	.061	-	-	-
T category						
T3	Ref.			Ref.		
T4a	7.828	1.826–33.549	.006	4.443	0.989–19.961	.052
N category						
N0	Ref.			Ref.		
N1 +N2 + N3	4.571	1.077–19.396	.039	1.338	0.378–4.736	.652
Lymphovascular invasion						
Negative	Ref.					
Positive	1.873	0.732–4.793	.190	-	-	-
Perineural invasion						
Negative	Ref.					
Positive	1.436	0.422–4.884	.563	-	-	-
TSR						
Low (<9.664)	Ref.					
High (≥9.664)	0.411	0.161–1.049	.063	-	-	-
E-cadherin						
Low (<0.315)	Ref.			Ref.		
High (≥0.315)	0.293	0.127–0.676	.004	0.348	0.149–0.816	.015
Chemotherapy						
XELOX	Ref.			Ref.		
TS-1	0.426	0.124–1.465	.176	2.558	0.715–9.148	.148
Others[a]	4.467	1.281–15.579	.019	0.501	0.144–1.744	.277

HR, hazard ratio; CI, confidence interval; TSR, tumor-stroma ratio.
[a]FOLFOX (folinic acid, fluorouracil, and oxaliplatin), HXP (hydroxycamptothecin, capecitabine, and cisplatin), and TS-1 (tegafur, gimeracil, and oteracil potassium), switched to XELOX (capecitabine and oxaliplatin) were included.

to low expression. Although T category did not reach statistical significance in the multivariable model (p = .052), its p-value was close to the threshold, suggesting a potential prognostic relevance that warrants further investigation.

Predictive value of the combined biomarker model

To identify a better predictive model for peritoneal recurrence, we compared the prognostic performance of two models: model 1, based on E-cadherin expression alone, and model 2, which incorporated both E-cadherin and TSR. The concordance index of model 1 was 0.622, with a likelihood ratio test value of 7.852 (p = .005). In model 2, the concordance index increased to 0.693, and the likelihood ratio test value was 11.318 (p = .004), indicating improved predictive performance with the addition of TSR. Detailed results are in Table 6.

DISCUSSION

This study aimed to evaluate the prognostic significance of E-cadherin expression and TSR for peritoneal recurrence in patients with advanced gastric cancer. Low E-cadherin expression was significantly associated with shorter RFS (p = .002), while low TSR also showed a trend toward shorter RFS (p = .054). When E-cadherin and TSR were combined to stratify patients into four groups, significant differences in RFS were observed among the groups (p = .005). Furthermore, predictive models for peritoneal recurrence demonstrated improved performance when TSR was incorporated into the E-cadherin–based model, compared to the model using E-cadherin alone. This study provides a novel approach by demonstrating, for the first time to our knowledge, that the combined digital evaluation of E-cadherin and TSR is a powerful predictor of peritoneal recurrence in gastric cancer. Moreover, the use of digital image analysis adds analytical precision and objectivity to the results.

Numerous studies have investigated the relationship between E-cadherin expression and clinicopathologic factors as well as prognosis in gastric cancer, and several meta-analyses have been conducted based on these findings [17,21,22]. A common conclusion across these meta-analyses is that reduced E-cadherin expression is significantly associated with diffuse-type histology, greater invasion depth, lymphovascular invasion, lymph node metastasis, distant metastasis, advanced TNM stage, and poor overall survival [17,21,22]. In our study, reduced E-cadherin expression was significantly associated with aggressive tumor features such as diffuse-type histology and deeper tumor invasion, consistent with previous reports suggesting its role as a biomarker of tumor aggressiveness [6,7,11-13,16]. However, we did not observe a statistically significant association with lymphovascular invasion or lymph node metastasis. This discrepancy may be attributed to the relatively small sample size and the single-institutional nature of our study. Moreover, as highlighted in previous meta-analyses, considerable inter-study heterogeneity exists, underscoring the need for cautious interpretation of these findings [17,21,22].

In our study, TSR showed a statistically significant association with patient age, sex, and chemotherapy regimen, but not with key clinicopathological factors, such as lymph node metastasis, lymphovascular invasion, perineural invasion or T category. Although not as extensively studied as E-cadherin, several studies have investigated the association between the TSR and clinicopathologic factors. One study reported that stroma-rich tumors were significantly associated with a greater number of metastatic lymph nodes, deeper invasion, higher TNM stage, perineural invasion, and lymphovascular invasion

Table 6. Comparison of prognostic models for peritoneal recurrence based on E-cadherin and tumor-stromal ratio

	Model 1			Model 2		
	HR	95% CI	p-value	HR	95% CI	p-value
E-cadherin						
<0.315	Ref.			Ref.		
≥0.315	0.293	0.127–0.676	.004	0.303	0.131–0.699	.005
TSR						
<9.664				Ref.		
≥9.664				0.429	0.168–1.099	.078
	Concordance = 0.622			Concordance = 0.693		
	Likelihood ratio test = 7.852, p = .005			Likelihood ratio test = 11.318, p = .004		

HR, hazard ratio; CI, confidence interval; TSR, tumor-stroma ratio.

https://doi.org/10.4132/jptm.2025.08.27

[2]. Another study found significant associations between stroma-rich tumors and tumor size ≥ 3 cm, higher T category, and higher N category [9]. These findings differ from the results of the present study, which may be attributed to differences in the methods used to measure TSR. Most previous studies used a fixed 50% cutoff to categorize TSR [2,8,9,23-25], whereas in the present study, TSR was quantified through digital image analysis, and the cutoff value was determined using ROC curve analysis to stratify tumors into low and high TSR groups. Furthermore, since the number of studies evaluating TSR in gastric cancer remains limited, additional data will be necessary to draw more definitive conclusions.

When patients were stratified into low and high E-cadherin expression groups and Kaplan–Meier curves were plotted according to peritoneal recurrence, those with low E-cadherin expression showed significantly shorter RFS (p = .002). In multivariate analysis, E-cadherin expression was also identified as an independent prognostic factor for peritoneal recurrence (high vs. low; HR, 0.348; 95% CI, 0.149 to 0.816; p = .015). These findings are consistent with previous studies reporting an association between reduced E-cadherin expression and peritoneal recurrence [11-16,21,22]. Furthermore, when stratified by histologic subtype, low E-cadherin expression remained significantly associated with shorter RFS in both diffuse type (p = .029) and intestinal type (p = .008). These findings suggest that the prognostic impact of E-cadherin expression is preserved across different histologic subtypes. However, given the relatively small number of intestinal type cases in our cohort, this association should be interpreted with caution and validated in larger datasets.

Although patients with low TSR showed a trend toward shorter RFS, the difference did not reach statistical significance (p = .054). A few studies have investigated the relationship between the TSR and peritoneal recurrence. In one study, multivariate analysis revealed that stroma-rich tumors had a significantly higher risk of developing peritoneal recurrence compared to stroma-poor tumors [8]. The authors proposed a predictive model incorporating TSR along with CA125, CA724, and Borrmann type, which demonstrated strong predictive value for peritoneal recurrence [8]. In another study, while stroma-rich tumors were significantly associated with peritoneal recurrence in univariate analysis, the association did not remain statistically significant in multivariate analysis [26]. However, the authors suggested that combining TSR with DNA ploidy and nucleotyping indices could enhance the predictive accuracy for peritoneal recurrence [26].

Correlation analysis between TSR and E-cadherin expression revealed a very weak, statistically non-significant association (r = 0.139, p = .114). E-cadherin is a transmembrane glycoprotein involved in calcium-dependent cell-cell adhesion, predominantly expressed in epithelial tissues [24]. Reduced expression weakens intercellular adhesion, facilitating tumor cell detachment, invasion, and metastasis [13,15,21], and is often regarded as a hallmark of EMT, a key mechanism in tumor progression and peritoneal dissemination [27]. In contrast, TSR represents the relative proportion of tumor cells to stromal components within the tumor [2], reflecting the composition of cancer-associated fibroblasts, immune cells, and extracellular matrix, which may influence tumor progression and therapeutic resistance [9,24,28]. A low TSR often indicates a desmoplastic, immunosuppressive microenvironment, which not only promotes EMT-related signaling via inflammatory and paracrine factors but also contributes to tumor progression through mechanical stress imposed by extracellular matrix stiffening [29,30]. These extracellular biomechanical cues can facilitate EMT and enhance malignant transformation [30]. These findings suggest that each marker reflect distinct but complementary biological characteristics: E-cadherin captures intrinsic cellular features and EMT status, while TSR reflects the structural and immunologic features of the tumor microenvironment that modulate EMT and tumor behavior. Thus, combined evaluation of E-cadherin and TSR may provide a more comprehensive assessment of tumor aggressiveness and peritoneal recurrence risk than either marker alone.

Supporting this perspective, the combined analysis of E-cadherin expression and TSR demonstrated improved predictive performance for peritoneal recurrence. Patients in group 4, with high levels of both markers, showed the most favorable outcomes, whereas group 1 and 2 showed the poorest prognoses with overlapping survival curves and no statistically significant difference between them (p = 0.543). Group 3 appeared to show intermediate outcomes on visual inspection of the survival curves; however, no statistically significant differences were observed between group 3 and either group 1 or group 2 (p = .071 and p = .348, respectively). Notably, in the subgroup with high E-cadherin expression, TSR significantly stratified prognosis (p = .040), and among patients with high TSR, E-cadherin expression also showed significant prognostic discrimination (p = .011). Although TSR did not emerge as an independent predictor in multivariable analysis, its integration with E-cad-

herin improved the model's predictive accuracy, highlighting the complementary prognostic value of the two markers in predicting peritoneal recurrence. These findings suggest that TSR may refine prognostic stratification particularly in tumors with preserved epithelial features, and that potential interactions between the two markers warrant further investigation in larger, multi-center studies.

From a therapeutic standpoint, the combined evaluation of E-cadherin expression and TSR may offer clinical utility in stratifying patients by risk of peritoneal recurrence and guiding postoperative treatment decisions. Patients in group 4, characterized by high E-cadherin expression and high TSR, demonstrated the most favorable RFS, identifying this subset as a potential low-risk group. In contrast, patients outside this favorable group—particularly those lacking one or both favorable features—may benefit from more intensive surveillance or consideration of alternative adjuvant strategies, such as intraperitoneal chemotherapy. This stratification approach could support more personalized, risk-adapted treatment planning in patients with advanced gastric cancer.

This study has several limitations. As a retrospective, single-center analysis with a relatively small sample size, its statistical power and generalizability may be limited. In addition, no external validation study was performed. Furthermore, digital image analysis was limited to three representative regions at the tumor invasive front rather than the entire tumor section. This decision was based on both biological rationale and technical feasibility: the invasive front is known to be the most active area for tumor–stroma interaction and EMT, and whole-slide analysis posed practical challenges due to variations in tissue quality and the complexity of high-resolution immunohistochemistry image processing. However, this region-restricted approach may not fully capture the extent of intratumoral heterogeneity. Future prospective studies incorporating whole-slide analysis may provide more comprehensive insights. Despite these limitations, to the best of our knowledge, this is the first study to evaluate the combined prognostic utility of the two markers, and the use of digital image analysis enhanced the objectivity and reproducibility of E-cadherin and TSR quantification.

In conclusion, our findings suggest that E-cadherin expression and TSR are complementary biomarkers that, when evaluated together, offer superior prognostic value for recurrence in patients with advanced gastric cancer. This dual-marker approach captures both tumor cell–intrinsic characteristics and tumor microenvironmental features, allowing for more refined risk stratification. Future directions should include validation of these findings in large, multi-center cohorts, as well as prospective studies to assess the predictive performance of E-cadherin and TSR in real-world clinical settings. Ultimately, incorporating these markers into routine pathology workflows may facilitate more personalized surveillance and treatment strategies for gastric cancer patients at risk of peritoneal recurrence.

Ethics Statement

This study was approved by the Ulsan University Hospital Institutional Review Board (R-BAY File No. 2024-12-037). Formal written informed consent was not required with a waiver by the appropriate Institutional Review Board.

Availability of Data and Material

The datasets generated or analyzed during the study are available from the corresponding author on reasonable request.

Code Availability

Not applicable.

ORCID

Somang Lee https://orcid.org/0009-0009-0208-0116
Binnari Kim https://orcid.org/0000-0002-0934-3056

Author Contributions

Conceptualization: Kim B. Data curation: Lee S, Kim B. Investigation: Lee S, Kim B. Methodology: Kim B. Supervision: Kim B. Validation: Kim B. Writing—original draft: Lee S. Writing—review & editing: Kim B. Approval of final manuscript: all authors.

Conflicts of Interest

The authors declare that they have no potential conflicts of interest.

Funding Statement

No funding to declare.

Acknowledgments

We would like to express our sincere gratitude to Professor Seoung Wan Chae at Samsung Kangbuk Hospital for his invaluable support and guidance in the digital image analysis conducted in this study.

https://doi.org/10.4132/jptm.2025.08.27

REFERENCES

1. Bray F, Laversanne M, Sung H, et al. Global cancer statistics 2022: GLOBOCAN estimates of incidence and mortality worldwide for 36 cancers in 185 countries. CA Cancer J Clin 2024; 74: 229-63.
2. Aurello P, Berardi G, Giulitti D, et al. Tumor-Stroma Ratio is an independent predictor for overall survival and disease free survival in gastric cancer patients. Surgeon 2017; 15: 329-35.
3. Acs M, Piso P, Glockzin G. Peritoneal metastatic gastric cancer: local treatment options and recommendations. Curr Oncol 2024; 31: 1445-59.
4. Aban CE, Lombardi A, Neiman G, et al. Downregulation of E-cadherin in pluripotent stem cells triggers partial EMT. Sci Rep 2021; 11: 2048.
5. Zhao H, Hu H, Chen B, et al. Overview on the role of E-cadherin in gastric cancer: dysregulation and clinical implications. Front Mol Biosci 2021; 8: 689139.
6. Eom BW, Won Ryu K, Man Yoon H, Kook MC. Predictive value of E-cadherin and EpCAM for detection of metastatic lymph node in early gastric cancer. Chin J Cancer Res 2020; 32: 614-20.
7. Anbiaee R, Mojir Sheibani K, Torbati P, Jaam H. Abnormal expression of e-cadherin in gastric adenocarcinoma, and its correlation with tumor histopathology and helicobacter pylori infection. Iran Red Crescent Med J 2013; 15: 218-22.
8. Zhong L, Huang H, Hou D, et al. Tumor-stroma ratio is a critical indicator of peritoneal metastasis in gastric cancer. Clin Exp Gastroenterol 2025; 18: 11-24.
9. Tian CF, Jing HY, Sinicrope FA, et al. Tumor microenvironment characteristics association with clinical outcome in patients with resected intestinal-type gastric cancer. Oncologist 2024; 29: e1280-90.
10. Hong Y, Heo YJ, Kim B, et al. Deep learning-based virtual cytokeratin staining of gastric carcinomas to measure tumor-stroma ratio. Sci Rep 2021; 11: 19255.
11. Shino Y, Watanabe A, Yamada Y, et al. Clinicopathologic evaluation of immunohistochemical E-cadherin expression in human gastric carcinomas. Cancer 1995; 76: 2193-201.
12. Yonemura Y, Nojima N, Kaji M, et al. E-cadherin and c-met expression as a prognostic factor in gastric cancer. Oncol Rep 1997; 4: 743-8.
13. Yonemura Y, Endou Y, Kimura K, et al. Inverse expression of S100A4 and E-cadherin is associated with metastatic potential in gastric cancer. Clin Cancer Res 2000; 6: 4234-42.
14. Xu Q, Wei Q, Ling J, Chen L, Ying J. RhoA/E-cadherin expression in gastric cancer patients: correlations with clinicopathological features and prognosis. Int J Clin Exp Med 2019; 12: 13757-64.
15. Chen HC, Chu RY, Hsu PN, et al. Loss of E-cadherin expression correlates with poor differentiation and invasion into adjacent organs in gastric adenocarcinomas. Cancer Lett 2003; 201: 97-106.
16. Uchikado Y, Okumura H, Ishigami S, et al. Increased Slug and decreased E-cadherin expression is related to poor prognosis in patients with gastric cancer. Gastric Cancer 2011; 14: 41-9.
17. Lu G, Cai Z, Jiang R, et al. Reduced expression of E-cadherin correlates with poor prognosis and unfavorable clinicopathological features in gastric carcinoma: a meta-analysis. Aging (Albany NY) 2024; 16: 10271-98.
18. Kumagai K, Sano T. Revised points and disputed matters in the eighth edition of the TNM staging system for gastric cancer. Jpn J Clin Oncol 2021; 51: 1024-7.
19. Japanese Gastric Cancer Association. Japanese classification of gastric carcinoma: 3rd English edition. Gastric Cancer 2011; 14: 101-12.
20. Lee JH, Chang KK, Yoon C, Tang LH, Strong VE, Yoon SS. Lauren histologic type is the most important factor associated with pattern of recurrence following resection of gastric adenocarcinoma. Ann Surg 2018; 267: 105-13.
21. Li T, Chen J, Liu QL, Huo ZH, Wang ZW. Meta-analysis: E-cadherin immunoexpression as a potential prognosis biomarker related to gastric cancer metastasis in Asian patients. Eur Rev Med Pharmacol Sci 2014; 18: 2693-703.
22. Xing X, Tang YB, Yuan G, et al. The prognostic value of E-cadherin in gastric cancer: a meta-analysis. Int J Cancer 2013; 132: 2589-96.
23. Peng C, Liu J, Yang G, Li Y. The tumor-stromal ratio as a strong prognosticator for advanced gastric cancer patients: proposal of a new TSNM staging system. J Gastroenterol 2018; 53: 606-17.
24. Kemi N, Eskuri M, Kauppila JH. Tumour-stroma ratio and 5-year mortality in gastric adenocarcinoma: a systematic review and meta-analysis. Sci Rep 2019; 9: 16018.
25. Kemi N, Eskuri M, Herva A, et al. Tumour-stroma ratio and prognosis in gastric adenocarcinoma. Br J Cancer 2018; 119: 435-9.
26. Yuan J, Jiang Y, Chen F, et al. Clinical implications of DNA ploidy, stroma, and nucleotyping in predicting peritoneal metastasis risk for gastric cancer. BMC Cancer 2025; 25: 144.
27. Thiery JP, Sleeman JP. Complex networks orchestrate epithelial-mesenchymal transitions. Nat Rev Mol Cell Biol 2006; 7: 131-42.
28. Tian W, Yang Y, Qin Q, et al. Vimentin and tumor-stroma ratio for neoadjuvant chemoradiotherapy response prediction in locally advanced rectal cancer. Cancer Sci 2023; 114: 619-29.

29. Anderson KG, Stromnes IM, Greenberg PD. Obstacles posed by the tumor microenvironment to T cell activity: a case for synergistic therapies. Cancer Cell 2017; 31: 311-25.
30. Zhang J, Hu Z, Horta CA, Yang J. Regulation of epithelial-mesenchymal transition by tumor microenvironmental signals and its implication in cancer therapeutics. Semin Cancer Biol 2023; 88: 46-66.

https://doi.org/10.4132/jptm.2025.08.27

JPTM

ORIGINAL ARTICLE

pISSN 2383-7837 · eISSN 2383-7845

Journal of Pathology and Translational Medicine 2025; 59: 421-433
https://doi.org/10.4132/jptm.2025.08.13

Spectrum of thyroiditis types: clinical, cytomorphological, and radiological findings

Anam Singh[1], Indrajeet Kundu[2]

[1]Department of Pathology, Faculty of Medicine and Health Sciences, SGT University, Gurugram, India
[2]Pratham Diagnostic and Imaging Centre, Gurugram, India

Graphical abstract

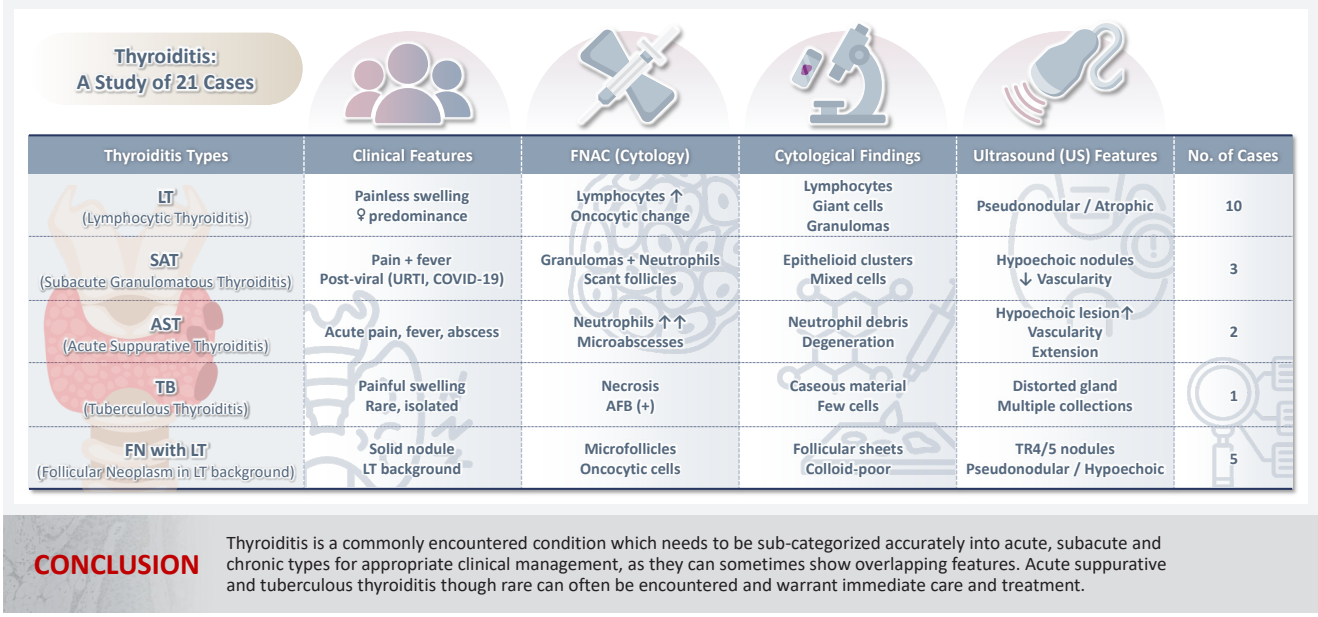

JPTM

ORIGINAL ARTICLE

pISSN 2383-7837 · eISSN 2383-7845

Journal of Pathology and Translational Medicine 2025; 59: 421-433
https://doi.org/10.4132/jptm.2025.08.13

Spectrum of thyroiditis types: clinical, cytomorphological, and radiological findings

Anam Singh[1], Indrajeet Kundu[2]

[1]Department of Pathology, Faculty of Medicine and Health Sciences, SGT University, Gurugram, India
[2]Pratham Diagnostic and Imaging Centre, Gurugram, India

Background: Thyroiditis encompasses a range of inflammatory conditions affecting the thyroid gland. Lymphocytic thyroiditis (LT) is a common form of thyroiditis, with acute suppuration of the thyroid, while tuberculous thyroiditis is relatively rare. Fine-needle aspiration cytology (FNAC) remains a safe and cost-effective tool for diagnosing thyroid-related diseases, especially when paired with ultrasound (US) and clinical examination. **Methods:** This is a cross-sectional study including 21 cases. The cases were reported as thyroiditis on US and FNAC, and the findings were correlated with patient clinical history, symptoms during presentation, and serological profiles. **Results:** The cases of thyroiditis encompassed the more common forms, LT and subacute granulomatous thyroiditis (SAT), as well as relatively rare forms like tuberculous thyroiditis and thyroid abscess. Cases of follicular neoplasms (FN) arising in the context of LT also are included in this study. The case of tuberculous thyroiditis presented as a bulky thyroid gland that appeared heterogeneous on US with extensive necrosis on FNAC. The cases of thyroid abscess and SAT presented with painful neck swellings, with granulomas in the latter cases. US features of LT showed an array of appearances ranging from pseudonodular to an atrophic thyroid gland. All cases of FN showed a lymphocytic background. **Conclusions:** Thyroiditis is a commonly encountered condition that needs to be sub-categorized accurately into acute, subacute, and chronic types for appropriate clinical management, as they can sometimes show overlapping features. Though rare, acute suppurative and tuberculous thyroiditis are often encountered and warrant immediate care and treatment.

Keywords: Abscess; Acute suppurative thyroiditis; Fine needle aspiration cytology; Follicular neoplasm; Lymphocytic thyroiditis; Subacute granulomatous thyroiditis; Thyroiditis; Tuberculous

INTRODUCTION

Thyroid fine-needle aspiration cytology (FNAC) remains an easy, safe, and cost-effective diagnostic tool for thyroid-related lesions with a high sensitivity and positive predictive value. It has led to a reduction in the number of surgeries for benign conditions and a subsequent increase in resection of malignancies [1]. Ultrasound (US) of the thyroid gland, compared to other radiological modalities, is more useful and effective in detecting thyroid pathologies [2].

Thyroiditis is most commonly caused by autoimmune conditions, which include lymphocytic thyroiditis (LT), Graves' disease, postpartum thyroiditis, and painless sporadic thyroiditis [3]. LT is more common in women, causing painless enlargement of the thyroid gland, with most of the patients presenting in a euthyroid state. However, in some patients, hypothyroidism is observed with an initial transient phase of hyperthyroidism. It is associated with elevated levels of serum antithyroid antibodies, which include anti-thyroglobulin, anti–thyroid peroxidase (TPO), and anti–thyroid-stimulating hormone (TSH) receptor antibodies (Fig. 1) [4]. The ultrasonographic features can vary from a diffusely enlarged thyroid gland to an atrophic gland in chronic stages. Presence of multiple ill-defined hypoechoic nodules with surrounding echogenic areas of thyroid parenchyma, giving it a pseudonodular appearance, is also common [5].

Subacute granulomatous thyroiditis (SAT), also known as de

Received: June 30, 2025 **Revised:** July 27, 2025 **Accepted:** August 13, 2025
Corresponding Author: Anam Singh, MD
Department of Pathology, Faculty of Medicine and Health Sciences, SGT University, Gurugram, Haryana 122505, India
Tel: +91-9560625039, E-mail: dewdropanam@gmail.com

Quervain's thyroiditis, is an inflammatory condition of the thyroid that is often self-limiting in nature. It usually occurs a few weeks following viral infections such as coxsackie, echovirus, mumps, measles, and hepatitis B and C [6,7]. Newer studies have also shown the association of SAT with coronavirus disease 2019 infection [8]. Patients usually present with a painful thyroid swelling, low-grade fever, and fatigue (Fig. 1), and US shows heterogeneously hypoechoic areas in the affected thyroid regions [9]. Most of the lesions subside within a few weeks to months following only anti-inflammatory treatment [10,11]. The presence of both epithelioid cell granulomas with admixed neutrophils and lymphocytes is a characteristic finding differentiating the condition from acute suppurative thyroiditis (AST) and LT [12].

Being an encapsulated and highly vascular organ with extensive lymphatic drainage, the thyroid gland is seldom associated with acute suppuration. When present, it is most commonly associated with bacterial infection by gram-positive bacteria like streptococcus or staphylococcus spreading through a hematogenous route [13]. It is commonly seen in malnourished individuals and immune-compromised conditions and sometimes is associated with history of trauma (Fig. 1). Clinically these patients present with painful neck swelling, fever, dysphagia, odynophagia, and raised levels of C-reactive protein [14]. On US, acute suppurative lesions are known to show hypoechoic lesions with destruction of the lobe and extension beyond the affected thyroid lobe [15].

Tuberculosis (TB) of the thyroid gland is an extremely rare condition with only a few cases reported in the literature. It is observed that tissues like thyroid, heart, pancreas, and striated muscle are much less susceptible to TB infection [16]. The low incidence of tuberculous thyroiditis can be explained by various mechanisms, including the bactericidal properties of colloids, high iodine content, and the high vascularity of the organ [17]. The spread of the *Mycobacterium* into the thyroid can occur by the hematogenous, lymphatic, or direct route. The clinical presentation can vary from mild to severe presenting with abscess or thyroiditis [16].

MATERIALS AND METHODS

This cross-sectional study presents 21 cases of patients diag-

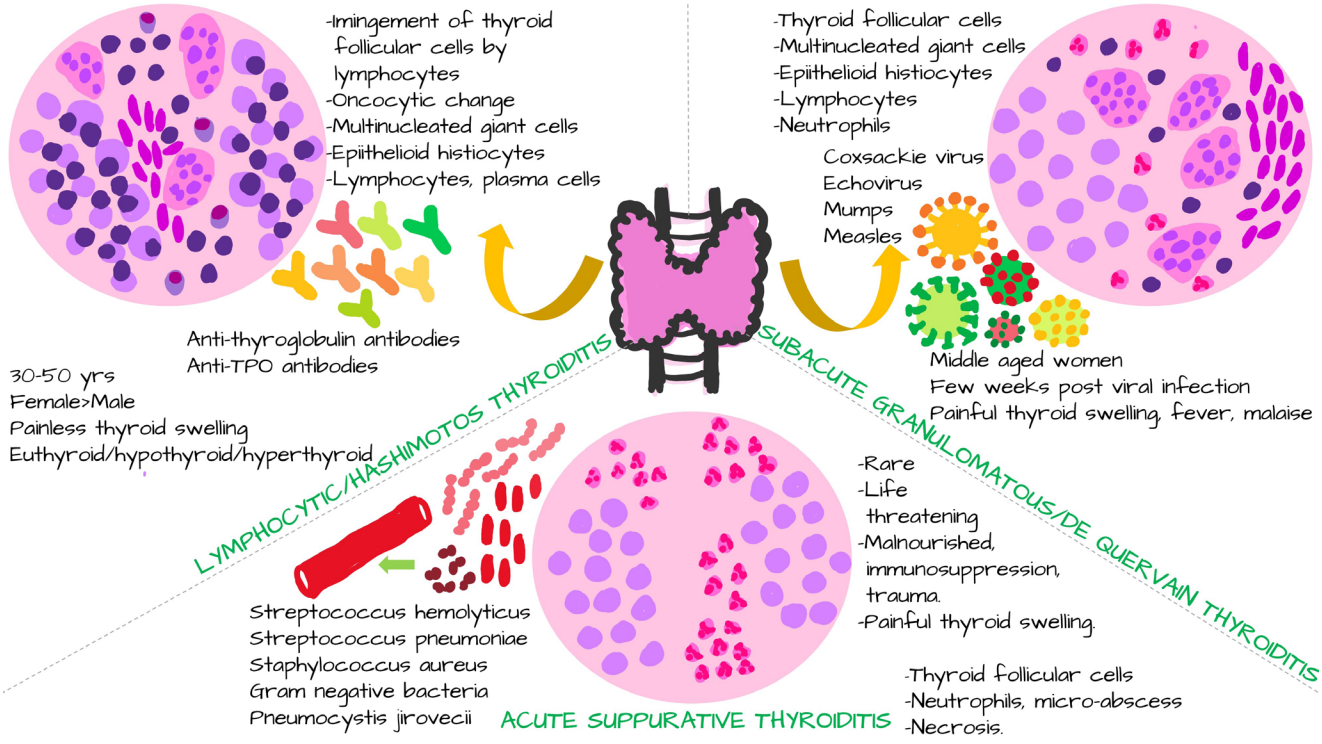

Fig. 1. Etio-pathogenesis of thyroiditis highlighting the clinical and cytomorphological features of acute suppurative thyroiditis, subacute granulomatous thyroiditis, and lymphocytic thyroiditis.

https://doi.org/10.4132/jptm.2025.08.13

nosed with different types of thyroiditis. The cases were evaluated based on clinical history, US imaging, and FNAC findings (Table 1) and included one case (n = 1) of tuberculous thyroiditis, two cases (n = 2) of AST/thyroid abscess, three cases (n = 3) of SAT, 10 cases (n = 10) of LT, and five cases (n = 5) of follicular neoplasm (FN) in the context of LT.

Each patient's clinical symptoms were documented, US findings were recorded, and US-guided FNAC was performed to analyze cytomorphological features. Patient laboratory investigations pertaining to their thyroid function tests and serological testing of antithyroid antibodies were also recorded and interpreted with their clinical, radiological, and cytomorphological findings. US was performed using a high-frequency linear transducer with a 2–14 MHz frequency operated by a trained radiologist. The cytological smears prepared following fine-needle aspiration (FNA) were stained with Giemsa, Papanicolaou stain, and special stains wherever needed. The slides were examined by a trained pathologist, the findings were recorded, and the diagnosis was further classified using the Bethesda system for reporting thyroid cytopathology. The cases of LT were further graded into 0, 1+, 2+, or 3+ according to the Bhatia et al. [18] grading system for cytology. Grade 1+ showed few lymphoid cells infiltrating the follicles. Grade 2+ showed moderate lymphocytic infiltration or mild lymphocytic infiltration with oncocytic cell change/giant cells/anisonucleosis. Grade 3+ showed florid lymphocytic inflammation with a germinal center and very few follicular cells remaining. The clinicians were immediately informed of the cases of tuberculous thyroiditis and AST/thyroid abscess owing to the emergent nature of these cases. Histopathological findings could be obtained in all five of the cases of follicular neoplasms following subtotal thyroidectomy.

RESULTS

A total of 21 cases were included in the study, with ages ranging from 28 to 45 years. The cases included one case of tuberculous thyroiditis (n = 1), two of thyroid abscess (n = 2), three cases of SAT (n = 3), 10 cases of LT (n = 10) and five cases of FN in the context of LT (n = 5).

Tuberculous thyroiditis

A 33-year-old male presented with chief complaints of a painful anterior neck swelling with odynophagia for the previous five days and low-grade fever for the previous month with no other complaints. On examination, the swelling was tender and moved with deglutition. No cervical or axillary lymph nodes were palpable. Neck US revealed a bulky, heterogeneous-appearing thyroid gland with multiple ill-defined hypoechoic areas involving both lobes of the thyroid and the isthmus. It also showed diffusely increased vascularity in the entire thyroid parenchyma, suggestive of acute inflammation of the thyroid gland. No significant cervical lymphadenopathy was noted. The patient was advised to undergo FNAC, and the treating surgeon was informed; however, the patient subsequently was lost to follow up. The patient revisited two months later for a review scan. Clinically, the swelling had increased in size with severe pain, redness, and tenderness. This time, the US showed a distorted thyroid morphology with poorly appreciable thyroid outline. Multiple hypoechoic collections were noted within the thyroid with moving internal echoes. Extra-thyroidal extension was also noted. The visualized thyroid parenchyma showed increased vascularity (Fig. 2A). An US-guided FNA from one of the collections in the isthmus yielded 1.5 mL of whitish-caseous material (Fig. 2B), and smears prepared from it revealed neutrophils with few lymphocytes, cystic macrophages and degenerated cells, against a dirty necrotic background suggestive of necrotizing thyroiditis (Fig. 2D). No giant cells or epithelioid cell granulomas were noted. Ziehl-Neelson (ZN) staining for acid fast bacilli (AFB; 20% H_2SO_4) was performed on the smear owing to the necrotic background, which showed positive *Mycobacterium tubercular* bacilli (Fig. 2C). No thyroid follicular cells were noted. The diagnosis was tuberculous thyroiditis, Bethesda category II. The remaining aspirate was also sent for cartridge-based nucleic acid amplification testing (CB-NAAT), and the result was positive. However, the patient's chest X-ray was normal, and abdominal US showed no free fluid and no lymphadenopathy or bowel wall thickening, indicating no pulmonary or abdominal tuberculous infection. The patient responded well to anti-tubercular therapy (ATT), and a repeat follow-up US scan revealed atrophic, heterogeneous-appearing thyroid morphology with resolution of the inflammation.

Thyroid abscess/AST

A 45-year-old male presented with a painful tender anterior neck swelling that moved with deglutition, with high-grade fever for the preceding three days. US findings revealed an ill-defined heterogeneously hypoechoic focal lesion within the left lobe of the thyroid, with increased vascularity. Extrathyroidal extension was noted. Aspiration of the lesion under US guidance yielded blood-mixed aspirate. The smears prepared revealed occasional

Table 1. Epidemiological details and clinical, radiological, and cytomorphological features of 21 cases diagnosed as thyroiditis

Case No.	Age (yr)/ Sex	Clinical features	Thyroid profile/Anti-thyroid antibodies/Ancillary tests	Radiological features	Cytomorphological features/Grade	Final diagnosis
1	33/M	Painful anterior neck swelling Odynophagia for 5 days Low grade fever for 1 mo	Euthyroid ZN stain for AFB-positive CB-NAAT: positive	Distorted thyroid morphology Poorly appreciable thyroid outline Multiple hypoechoic collections with moving internal echoes	Neutrophils Few lymphocytes Cystic macrophages Degenerated cells Necrotic background	Tuberculous thyroiditis Bethesda category II
2	45/M	Painful anterior neck swelling Fever for 3 days	Euthyroid/–[a]	Ill-defined heterogeneously hypoechoic focal lesion within left lobe Increased vascularity TR4	Numerous collections of neutrophils: micro-abscesses Few macrophages Occasional thyroid follicular cells	Thyroid abscess Bethesda category II
3	32/F	Painful anterior neck swelling Odynophagia Fever for 2 days	Euthyroid/–[a] Pus culture: Positive for *Staphylococcus aureus*	Large heterogeneously hypoechoic avascular collection Moving internal echoes in right lobe	Neutrophils Occasional scattered macrophages Degenerating follicular epithelial cells	Thyroid abscess Bethesda category II
4	37/F	Painful anterior neck swelling for 3 wk H/o recent URTI	Euthyroid/–[a]	Ill-defined Wider than taller Solid hypoechoic nodule in right lobe measuring 20 × 9 × 10 mm Reduced vascularity TR4	Ill-formed granulomatous aggregates of epithelioid cells Scattered lymphocytes, neutrophils Degenerating follicular cells	Subacute granulomatous thyroiditis Bethesda category II
5	35/M	Painful anterior neck swelling for 1 wk H/o recent URTI	Euthyroid/–[a]	Ill-defined Wider than taller Solid hypoechoic nodule in left lobe measuring 17 × 12 × 11 mm Reduced vascularity TR4	Few epithelioid cell granulomas Occasional neutrophils and lymphocytes	Subacute granulomatous thyroiditis Bethesda category II
6	38/M	Odynophagia for 5 days H/o recent URTI	Euthyroid/–[a]	Heterogeneous echotexture ill-defined variable sized heterogeneously hypoechoic nodular areas Reduced vascularity TR4	Few epithelioid cell granulomas Occasional neutrophils and lymphocytes	Subacute granulomatous thyroiditis Bethesda category II
7	40/F	Painless anterior neck swelling	Hyperthyroid Anti-TPO Ab: elevated Anti-TSH Ab: elevated Anti-thyroglobulin Ab: elevated	Diffusely enlarged thyroid gland Heterogeneous echotexture Increased vascularity	Impingement of thyroid follicular cells by lymphocytes Oncocytic change Lymphocytic background Grade 2+	Lymphocytic thyroiditis Bethesda category II
8	42/F	Painless anterior neck swelling	Hyperthyroid–[a]	Diffusely enlarged thyroid gland Heterogeneous echotexture Increased vascularity	Impingement of thyroid follicular cells by lymphocytes Oncocytic change Lymphocytic background Grade 2+	Lymphocytic thyroiditis Bethesda category II

(Continued to next page)

https://doi.org/10.4132/jptm.2025.08.13

https://doi.org/10.4132/jptm.2025.08.13

Table 1. Continued

Case No.	Age (yr)/ Sex	Clinical features	Thyroid profile/Anti-thyroid antibodies/Ancillary tests	Radiological features	Cytomorphological features/Grade	Final diagnosis
9	39/F	Painless anterior neck swelling	Euthyroid/–[a]	Multiple hypoechoic ill-defined nodular areas Surrounding iso- hyperechoic thyroid parenchyma: pseudonodular appearance	Impingement of thyroid follicular cells by lymphocytes Oncocytic change lymphocytic background Grade 2+	Lymphocytic thyroiditis Bethesda category II
10	41/F	Painless anterior neck swelling	Euthyroid/–[a]	Multiple hypoechoic ill-defined nodular areas Surrounding iso to hyperechoic thyroid parenchyma: pseudonodular appearance	Impingement of thyroid follicular cells by lymphocytes Oncocytic change Histiocytic giant cells Epithelioid cell granulomas Lymphocytic background Grade 2+	Lymphocytic thyroiditis Bethesda category II
11	38/F	Painless anterior neck swelling	Euthyroid/–[a]	Bulky thyroid gland Diffusely reduced echogenicity Multiple thin echogenic septations	Impingement of thyroid follicular cells by lymphocytes Oncocytic change Histiocytic giant cells Epithelioid cell granulomas Lymphocytic background Grade 2+	Lymphocytic thyroiditis Bethesda category II
12	34/F	Painless anterior neck swelling	Hypothyroid/–[a]	Multiple hyperechoic ill-defined nodular areas Surrounding hypoechoic thyroid parenchyma: pseudonodular appearance	Impingement of thyroid follicular cells by lymphocytes Oncocytic change Histiocytic giant cells Epithelioid cell granulomas Lymphocytic background Grade 2+	Lymphocytic thyroiditis Bethesda category II
13	35/F	Painless anterior neck swelling	Hypothyroid/–[a]	Bulky heterogenous appearing thyroid gland Diffusely reduced echogenicity Multiple thin echogenic septations	Impingement of thyroid follicular cells by lymphocytes Oncocytic change Histiocytic giant cells Epithelioid cell granulomas Lymphocytic background Grade 2+	Lymphocytic thyroiditis Bethesda category II
14	38/F	Painless anterior neck swelling	Hypothyroid/–[a]	Bulky heterogenous appearing thyroid gland Diffusely reduced echogenicity Multiple thin echogenic septations	Impingement of thyroid follicular cells by lymphocytes Oncocytic change Histiocytic giant cells Epithelioid cell granulomas Lymphocytic background Grade 2+	Lymphocytic thyroiditis Bethesda category II
15	42/F	Painless anterior neck swelling.	Hypothyroid/–[a]	Atrophic thyroid gland	Impingement of thyroid follicular cells by lymphocytes Oncocytic change Histiocytic giant cells Epithelioid cell granulomas Lymphocytic background Grade 2+	Lymphocytic thyroiditis Bethesda category II

(Continued to next page)

Table 1. Continued

Case No.	Age (yr)/ Sex	Clinical features	Thyroid profile/Anti-thyroid antibodies/Ancillary tests	Radiological features	Cytomorphological features/Grade	Final diagnosis
16	45/F	Painless anterior neck swelling	Hypothyroid/–[a]	Atrophic thyroid gland	Impingement of thyroid follicular cells by lymphocytes Oncocytic change Histiocytic giant cells, epithelioid cell granulomas Polymorphous population of lymphoid cells in background Grade 3+	Lymphocytic thyroiditis Bethesda category II
17	27/F	Painless anterior neck swelling	Hypothyroid Anti-TPO antibody: elevated	Well-defined large solid nodule Varying isoechoic-hypoechoic echotexture Rest of the thyroid showing a pseudonodular appearance TR3	Sheets of thyroid follicular cells with repetitive micro-follicular pattern Colloid free hemorrhagic background Scattered lymphocytes and lymphocytic impingement in occasional clusters Grade 1+	Suspicious for follicular neoplasm Bethesda category IV
18	30/M	Painless anterior neck swelling	Hypothyroid/–[a]	Well-defined solid nodule in right lobe Hypoechoic echotexture Rest of thyroid showing pseudonodular appearance TR4	Sheets of thyroid follicular cells with repetitive micro-follicular pattern Colloid free hemorrhagic background Scattered lymphocytes	Follicular neoplasm Bethesda category IV
19	35/F	Painless anterior neck swelling	Hypothyroid/–[a]	Well-defined solid nodule in left lobe Varying isoechoic-hypoechoic echotexture Rest of thyroid showing pseudonodular appearance TR4	Sheets of thyroid follicular cells with repetitive micro-follicular pattern Colloid free hemorrhagic background Scattered lymphocytes	Suspicious for follicular neoplasm Bethesda category IV
20	40/F	Painless anterior neck swelling	Hypothyroid/–[a]	Well-defined solid nodule in left lobe Hypoechoic echotexture, diffusely reduced thyroid parenchymal echogenicity Multiple echogenic septations TR4	Sheets of thyroid follicular cells with repetitive micro-follicular pattern Colloid free hemorrhagic background Scattered lymphocytes.	Suspicious for follicular neoplasm Bethesda category IV
21	33/F	Painless anterior neck swelling	Hypothyroid/–[a]	Well-defined iso to hypoechoic solid nodule in right lobe Punctate microcalcification Background of diffusely reduced thyroid parenchymal echogenicity Multiple echogenic septations TR5	Sheets and clusters of polygonal oncocytic cells Abundant granular cytoplasm Colloid free hemorrhagic background Few clusters showing lymphocytic impingement Grade 1+	Suspicious for follicular neoplasm, oncocytic type with lymphocytic thyroiditis Bethesda category IV

ZN, Ziehl-Neelson; AFB, acid fast bacilli; CB-NAAT, cartridge based nucleic acid amplification test; TR, Thyroid Imaging Reporting and Data System; H/o, history of; URTI, upper respiratory tract infection; TPO, thyroid peroxidase; TSH, thyroid-stimulating hormone.
[a]Serological antibodies status/Anti-thyroid antibodies not known.

https://doi.org/10.4132/jptm.2025.08.13

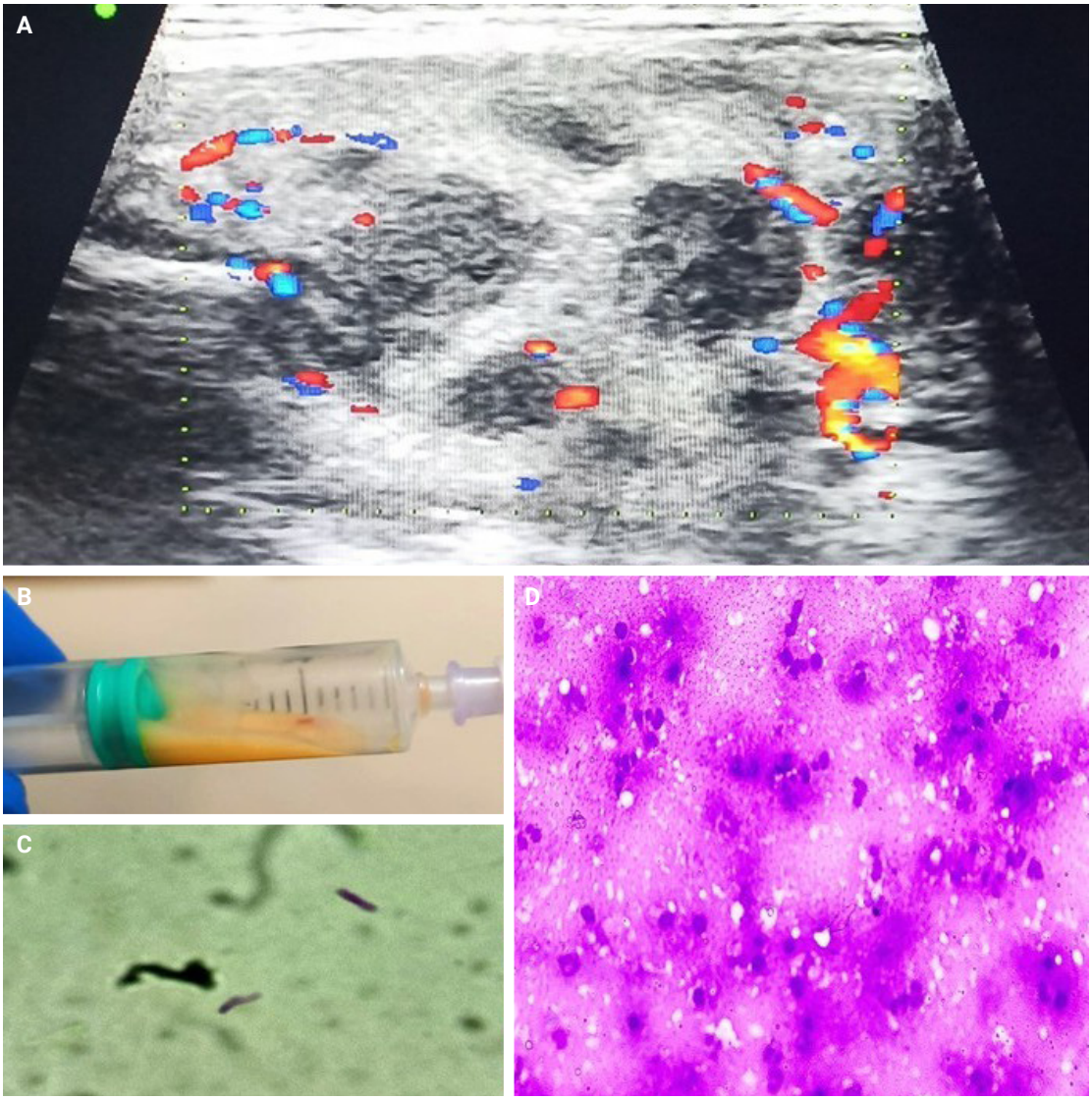

Fig. 2. Tuberculous thyroiditis. (A) Ultrasonography showing multiple hypoechoic collections with moving internal echoes and distorted thyroid morphology. (B) A total of 1.5 mL of caseous material aspirated from the thyroid lesion. (C) Ziehl-Neelson stain showing two red-stained acid fast bacilli. (D) Giemsa-stained smear revealing occasional neutrophils and degenerated cells against a necrotic background.

thyroid follicular cells with numerous collections of neutrophils forming micro-abscesses along with few histiocytes, supporting the diagnosis of AST/thyroid abscess, Bethesda category II. No pus culture could be performed due to the scant nature of the aspirate. However, the patient responded well to broad spectrum intravenous antibiotics, signifying a possible bacterial etiology. Similarly, the second case was a 32-year-old pregnant female in her 3rd trimester who reported a history of root canal treatment three months prior and no other relevant past medical history. She presented with painful anterior neck swelling, odynophagia, and fever for the preceding two days. US showed a large, heterogeneously hypoechoic avascular collection with moving internal echoes in the right lobe of the thyroid (Fig. 3A). FNA yielded frank pus, and cytology revealed numerous neutrophils with occasional scattered histiocytes and degenerating follicular epithelial cells (Fig. 3B). Subsequent pus culture was positive for Staphylococcus aureus. Due to the risk of fatality associated with these cases, the surgeon was informed of the diagnosis to confer immediate treatment to the patient.

Subacute granulomatous thyroiditis

A 37-year-old female presented with pain and swelling in the

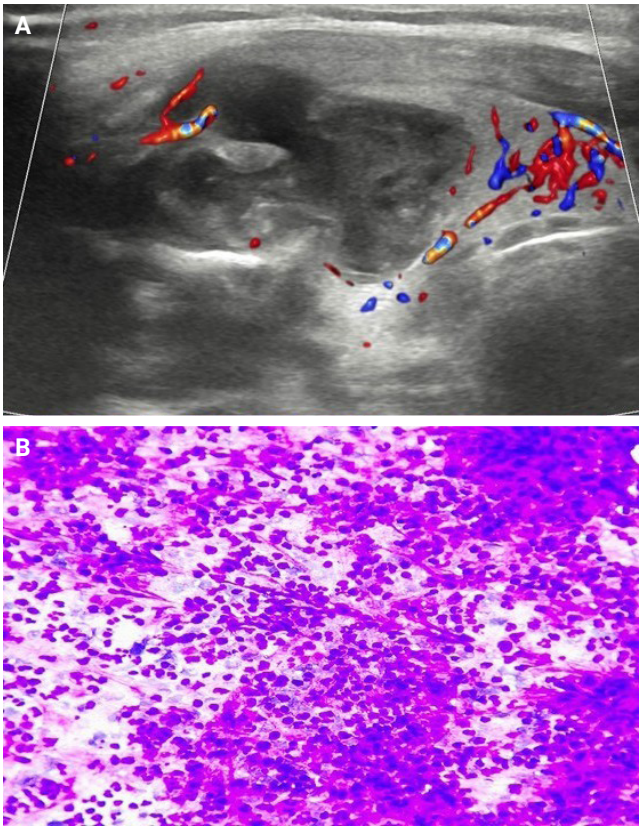

Fig. 3. Thyroid abscess. (A) Ultrasonography showing a large heterogeneously hypoechoic avascular collection with moving internal echoes in the right lobe of the thyroid. (B) Giemsa-stained smear showing an abscess with numerous neutrophils and occasional lymphocytes and degenerated cells.

anterior neck for the previous three weeks. She also relayed a history of severe upper respiratory tract infection (URTI) one and a half months earlier. US revealed a normal-sized thyroid with an ill-defined, wider-than-tall solid hypoechoic nodule in the right lobe of the thyroid measuring 20 × 9 × 10 mm and showing reduced vascularity (Fig. 4A). A few benign colloid nodules were also noted in bilateral lobes of the thyroid. An US-guided FNAC of the lesion yielded scant blood-mixed aspirate revealing a paucicellular smear with occasional ill-formed granulomatous aggregates of epithelioid cells (Fig. 4C). Also seen was a collection of neutrophils with scattered lymphocytes and degenerating follicular cells (Fig. 4D). No lymphocytic impingement of thyroid follicular cells was seen. Based on the clinical, radiological, and cytological findings, the possibility of SAT, Bethesda category II was suggested. The second case was a 35-year-old male who also presented with painful anterior neck swelling following an episode of URTI. US revealed an ill-defined wider-than-tall solid hypoechoic nodule in the left lobe of the thyroid measuring 17 × 12 × 11 mm with reduced vascularity. The third case was a 38-year-old male who had developed odynophagia five days prior. On US, the thyroid gland showed heterogeneous echotexture with ill-defined, variably sized heterogeneously hypoechoic nodular areas with reduced vascularity (Fig. 4B). US-guided FNAC showed similar findings to the previous case, showing focal aggregates of epithelioid cells with scattered neutrophils and lymphocytes.

Lymphocytic thyroiditis

All the cases (n = 10) of LT presented with clinical features of a painless thyroid swelling, and five cases (n = 5) had elevated levels of TSH, with low T3 and T4 serum thyroid hormones. Two (n = 2) of the patients presented with symptoms of hyperthyroidism, which can be seen sometimes during the initial phases of the disease, and the rest of the cases (n = 3) were euthyroid. One (n = 1) of the hyperthyroid cases subsequently underwent testing for anti-thyroid antibodies and was found to have elevated levels of anti-thyroglobulin, anti-TPO, and anti-TSH receptor antibodies. In the remaining nine cases (n = 9), serological antibody testing was advised, but the patients were lost to follow-up. US features of the two cases (n = 2) who presented with symptoms of hyperthyroidism showed a diffusely enlarged thyroid gland with a heterogeneous echotexture and increased vascularity (Fig. 5A). Two of the euthyroid cases (n = 2) showed multiple hypoechoic ill-defined nodular areas varying from 1–6 mm in size on US with surrounding iso to hyperechoic thyroid parenchyma giving a pseudonodular appearance (Fig. 5B). One (n = 1) of the euthyroid cases showed a bulky thyroid gland with diffusely reduced echogenicity and multiple thin echogenic septations. The US finding of one (n = 1) of the hypothyroid cases showed multiple hyperechoic ill-defined nodular areas varying from 1–7 mm with surrounding hypoechoic thyroid parenchyma also giving a pseudonodular appearance. Two (n = 2) of the hypothyroid cases revealed a bulky heterogenous appearing thyroid gland with diffusely reduced echogenicity and multiple thin echogenic septations. The remaining two (n = 2) of the hypothyroid cases revealed atrophic thyroid gland (Fig. 5C).

The cytomorphological findings in all 10 cases revealed benign cohesive sheets of thyroid follicular cells showing impingement by variable numbers of lymphocytes with numerous lymphoid cells in the background. Oncocytic changes were noted in all cases (n = 10) (Fig. 5D). Histiocytic giant cells and well-formed epithelioid cell granulomas were seen in seven (n = 7) of

https://doi.org/10.4132/jptm.2025.08.13

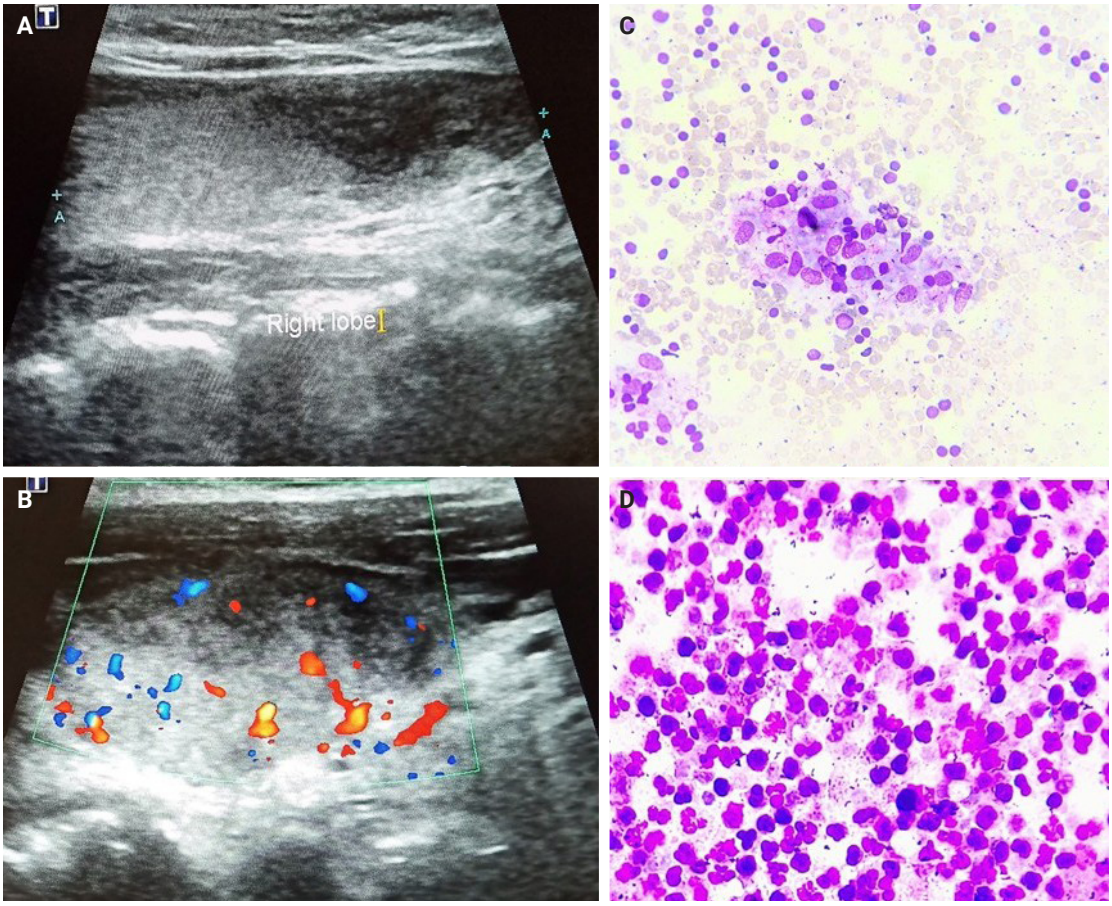

Fig. 4. Subacute granulomatous thyroiditis. (A) Ultrasonography (US) showing an ill-defined, wider-than-tall solid hypoechoic nodule in the right lobe of the thyroid. (B) Giemsa-stained smear revealing ill-formed clusters of epithelioid cells with scattered lymphocytes. (C) US showing heterogeneous echotexture of the thyroid gland with ill-defined variably sized heterogeneously hypoechoic nodular areas. (D) Giemsa-stained smear revealing areas of collection of neutrophils with admixed lymphocytes.

the 10 cases, in all the hypothyroid cases (n = 5) and two of the euthyroid cases (n = 2) (Fig. 5E, G). The degree of lymphocytic infiltration was graded from 0 to 3+ according to the Bhatia *et al*. grading system on cytology. Nine of the cases (n = 9) were graded as 2+, and only one case (n = 1) was graded as grade 3+, which showed a florid population of reactive polymorphous lymphoid cells in the background (Fig. 5F). The grade 3+ morphology was noted in the hypothyroid case with atrophic thyroid gland.

Follicular neoplasm in LT

Five (n = 5) of the cases presented with clinical features of painless thyroid swelling. One (n = 1) of the cases was known LT with elevated anti-TPO antibodies. All cases (n = 5) were hypothyroid. US in four of the cases (n = 4) showed a well-defined, wider-than-tall iso- to hypoechoic solid nodule, with the rest of the thyroid showing either a pseudonodular appearance (Fig. 6B) or diffusely reduced thyroid parenchymal echogenicity with multiple echogenic septations suggestive of chronic thyroiditis. The fifth case showed a well-defined iso- to hypoechoic solid nodule in the right lobe with punctate microcalcification against a background of diffusely reduced thyroid parenchymal echogenicity with multiple echogenic septations (Fig. 6A). US-guided FNAC of the first four cases (n = 4) revealed moderate to highly cellular smears showing thyroid follicular cells arranged in sheets and in repetitive micro-follicular patterns against a hemorrhagic background with scant or no colloids (Fig. 6D) and scattered lymphocytes, and one of the cases (n = 1) with elevated anti-TPO levels also showed grade 1+ lymphocytic impingement in a few sheets of follicular cells. The cases were diagnosed as follicular neoplasm/ suspicious for follicular neoplasm; Bethesda category IV and histopathological correlation was

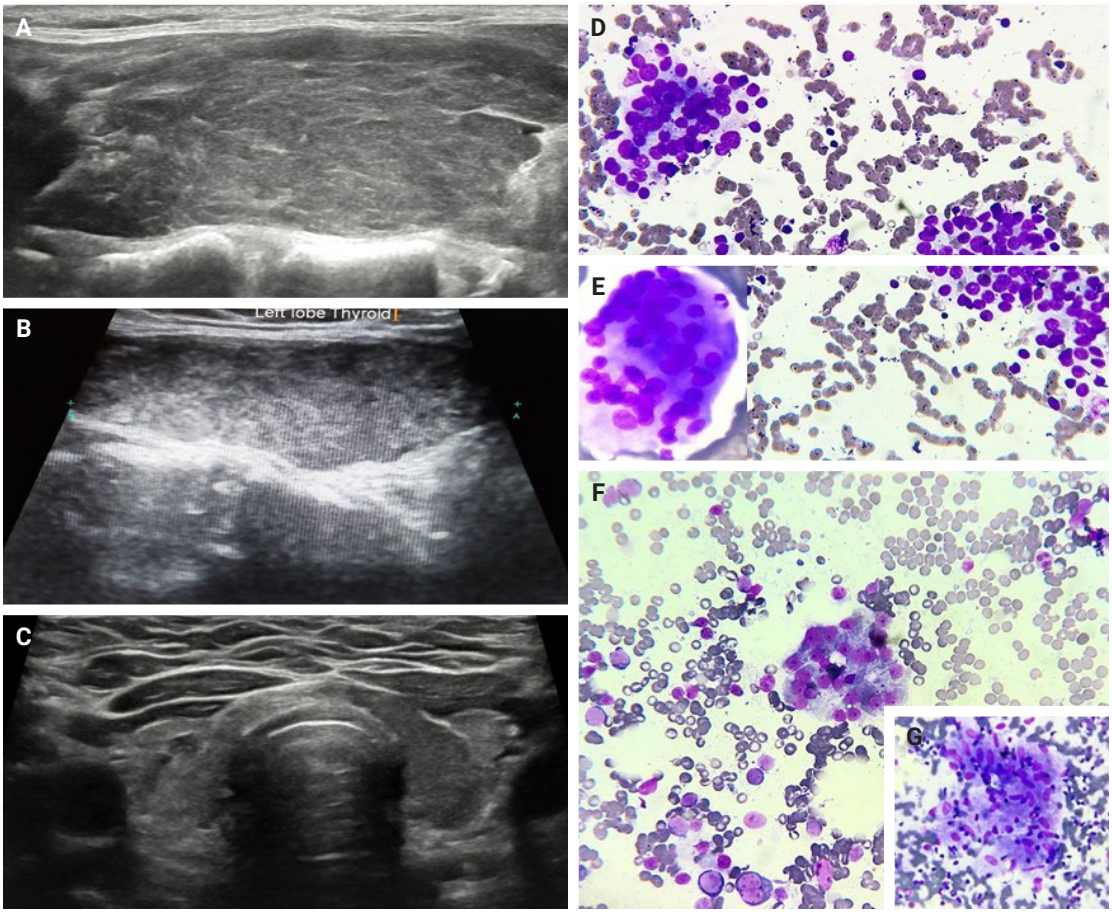

Fig. 5. Lymphocytic thyroiditis. (A) Ultrasonography (US) showing a diffusely enlarged thyroid gland with a heterogeneous echotexture. (B) US showing multiple hypoechoic ill-defined nodular areas with surrounding iso-hyperechoic thyroid parenchyma giving a pseudonodular appearance. (C) US showing an atrophic thyroid gland. (D) Giemsa-stained smear showing sheets of follicular epithelial with impinging lymphocytes (grade 2+) and a lymphocytic background. (E) Giemsa-stained smear showing a histiocytic giant cell. (F) Giemsa-stained smear sheets of follicular epithelia with impinging lymphocytes and oncocytic cell change against a polymorphous maturing population of lymphocytes (grade 3+). (G) Giemsa-stained smear showing a well-formed epithelioid cell granuloma.

advised, which showed follicular adenomas in all cases. The last case (n = 1) showed high cellularity with sheets and clusters of thyroid follicular cells, with most of the cells revealing oncocytic changes (Fig. 6C) against a hemorrhagic background with scant colloid, few scattered lymphocytes, and occasional follicular clusters showing lymphocytic impingement (grade 1+). The case was diagnosed as follicular neoplasm, oncocytic type, Bethesda category IV, and was diagnosed as oncocytic adenoma on histopathology.

DISCUSSION

The age distribution varied between 27-45 years. A notable finding was the female predominance in LT (10/10 cases) and in FN arising in the context of LT (4/5 cases). SAT is more commonly described in females than in males; however, two of the three of our cases (2/3) were males. The one case (1/1) of tuberculous thyroiditis and one case (1/2) of thyroid abscess were also males.

All the cases of AST/thyroid abscess and SAT presented with painful thyroid swellings as expected, while all the LT cases and cases of follicular neoplasm in the context of LT had painless thyroid enlargements. All the cases diagnosed with SAT reported a recent history of severe URTI, which correlates with the etio-pathogenesis of the disease. Both cases of AST/thyroid abscess were previously healthy individuals and reported no history of immunocompromise, human immunodeficiency virus, or trauma. However, one of the cases was a pregnant female with recent past history of root canal treatment. The development of

https://doi.org/10.4132/jptm.2025.08.13

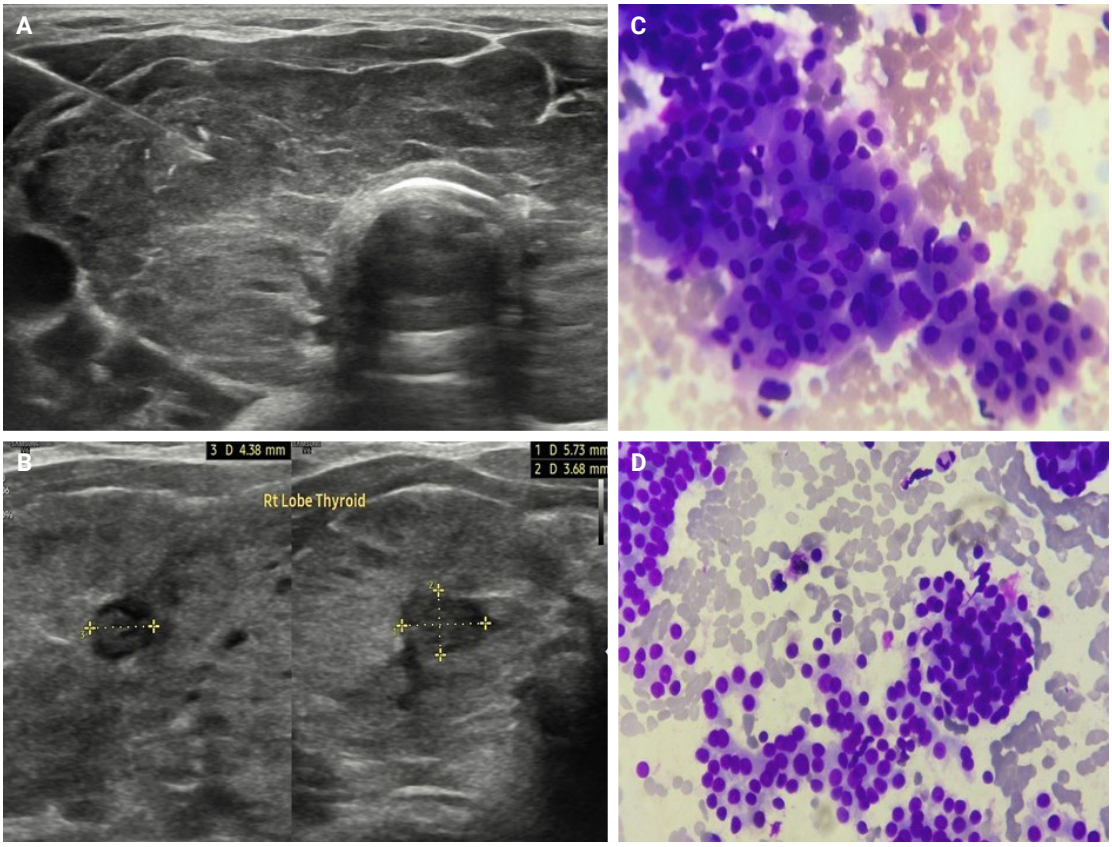

Fig. 6. Follicular neoplasm in the context of lymphocytic thyroiditis. (A) Ultrasonography (US) showing a well-defined iso to hypoechoic solid nodule in the right lobe with punctate microcalcifications against a background of diffusely reduced thyroid parenchymal echogenicity with multiple echogenic septations. (B) Giemsa-stained smear revealing sheets and a repetitive micro-follicular pattern of thyroid cells against a hemorrhagic background. (C) US showing a well-defined hypoechoic solid nodule with surrounding thyroid parenchyma showing a pseudonodular appearance. (D) Giemsa-stained smear showing sheets of thyroid follicular cells with oncocytic change.

acute suppuration could be attributable to hypertrophy and hyperplasia of the thyroid gland owing to increased levels of circulating human chorionic gonadotropin that tend to cross bind to TSH receptors [19]. The literature regarding association of both pregnancy and root canal treatment with acute suppuration of thyroid gland is, however, scant. On subsequent follow-up, the case with tuberculous thyroiditis also tested positive for CB-NAAT and responded well to ATT. The tuberculous infection was likely confined to the thyroid gland, as the chest X-ray and abdominal US showed normal findings with no cervical or axillary lymphadenopathy. This was a rare occurrence. The initial US also showed no extra-thyroidal extension, ruling out the possibility of secondary involvement of thyroid from any adjacent cervical lymph node. On subsequent US, the case of tuberculous thyroiditis showed complete effacement and distortion of the thyroid parenchyma with internal echoes; similar findings were described by Baidya et al. [20], in which they described multiple variably sized cysts in both lobes of the thyroid [20]. Tuberculous thyroiditis is rare, with scant treatment in the literature [16]. The cases of thyroid abscess showed moving internal echoes in one case and ill-defined heterogeneously hypoechoic focal lesion with extrathyroidal extension in the other. SAT on US showed ill-defined hypoechoic wider-than-tall focal nodules with normal-sized gland in two of the cases and minimally enlarged, heterogeneous-appearing thyroid gland with multiple ill-defined hypoechoic nodules in the third case. All cases showed reduced vascularity on color Doppler in the affected areas of the gland, but with absent hypervascularity in the surrounding normal thyroid parenchyma, as described in the literature in cases of SAT. This allows differentiation from AST, which shows increased vascularity in the surrounding thyroid parenchyma [21-23]. Ill-defined hypoechoic lesions can sometimes be confused

with malignant lesions, and FNAC is often advised in these cases [22]. The cases of LT showed a spectrum of US findings varying from a pseudonodular appearance, diffuse thyroid enlargement with reduced echogenicity, to an atrophic thyroid gland. In the literature, LT has also been variably described and broadly classified into nodular and diffuse forms. The diffuse forms initially can show a nodular appearance and can eventually progress to complete atrophy of the gland [23].

The cytology in AST/thyroid abscess cases typically revealed numerous neutrophils with few histiocytes, indicative of abscess formation. The case of tuberculous thyroiditis on FNA yielded caseous aspirate revealing a necrotic background with scattered neutrophils and occasional AFB on ZN staining using 20% H_2SO_4. Normally, tuberculous infection presents as giant cells and epithelioid cell granulomas, but the presence of extensive necrosis could possibly be due to long-standing and untreated illness [24]. SAT cases showed neutrophils, occasional epithelioid cell granulomas, and lymphocytes with a paucity of thyroid follicular cells and a recent history of URTI. The presence of neutrophils and neutrophilic micro-abscesses were noted in both acute and subacute cases and need to be differentiated as both can present with painful thyroid swellings. AST will show a predominance of neutrophils, with degenerating cellular debris in the absence of lymphocytes, epithelioid cell granulomas, and giant cells [12]. In addition to varying degrees of lymphocytic impingement, histiocytic giant cells and epithelioid cell granulomas were observed in a majority of the cases (7/10) of LT, whereas SAT cases showed both neutrophils and epithelioid cell granulomas with a paucity of thyroid follicular cells. Colloid was scant in all cases. Most of the cases (n = 9) of LT showed grade 2+ impingement of lymphocytes, except for one case that showed grade 3+ impingement against a reactive polymorphous population of lymphoid cells. All the cases of FN with LT showed a lymphocytic colloid-free hemorrhagic background, and grade 1+ impingement by lymphocytes was seen in two of the cases. The majority of the cases showed sheets of repetitive micro-follicles as described in the literature, with one of the cases showing a predominant oncocytic morphology. The literature describes the association of LT with thyroid lymphomas and papillary carcinoma thyroid; however, there are limited data regarding its association with FN.

In conclusion, thyroiditis is commonly encountered by clinicians, pathologists, and radiologists. Evaluation of the symptoms with the US findings and FNAC can greatly help in the diagnosis and decrease mortality rates, especially in cases with AST. SAT can present with a characteristic history of previous viral infection, painful thyroid swelling, and the presence of both neutrophils and granulomas on FNAC. LT is one of the most common types of thyroiditis, frequently associated with granulomas and epithelioid giant cells, predominantly seen in females. AST/thyroid abscess and tuberculous thyroiditis are rare entities in clinical practice. This study aims to assess the clinical, cytomorphological, and radiological findings of common and uncommon forms of thyroiditis; however, the study is limited by the small number of cases included. A larger sample size is planned for future work.

Ethics Statement

All procedures performed in the current study were approved by the IRB and/or national research ethics committee (EC-2024-1145 and 7 July 2024) in accordance with the 1964 Helsinki Declaration and its later amendments. Informed consent was obtained from all individual participants included in the study.

Availability of Data and Material

Data sharing not applicable to this article as no datasets were generated or analyzed during the study.

Code Availability

Not applicable.

ORCID

Anam Singh https://orcid.org/0000-0003-0323-354X
Indrajeet Kundu https://orcid.org/0009-0002-5299-9461

Author Contributions

Conceptualization: AN. Data curation: AN, IK. Formal analysis: AN, IK. Investigation: AN, IK. Methodology: AN, IK. Supervision: AN, IK. Validation: AN, IK. Visualization: AN, IK. Writing—original draft: AN, IK. Writing—review & editing: AN, IK. Approval of final manuscript: all authors.

Conflicts of Interest

The authors declare that they have no potential conflicts of interest.

Funding Statement

No funding to declare.

https://doi.org/10.4132/jptm.2025.08.13

REFERENCES

1. Hajmanoochehri F, Rabiee E. FNAC accuracy in diagnosis of thyroid neoplasms considering all diagnostic categories of the Bethesda reporting system: a single-institute experience. J Cytol 2015; 32: 238-43.
2. American Thyroid Association (ATA) Guidelines Taskforce on Thyroid Nodules and Differentiated Thyroid Cancer; Cooper DS, Doherty GM, et al. Revised American Thyroid Association management guidelines for patients with thyroid nodules and differentiated thyroid cancer. Thyroid 2009; 19: 1167-214.
3. Fariduddin MM, Singh G. Thyroiditis. StatPearls [Internet]. Treasure Island: StatPearls Publishing, 2024 [cited 2025 Aug 1]. Available from: https://www.ncbi.nlm.nih.gov/books/NBK555975/.
4. Klubo-Gwiezdzinska J, Wartofsky L. Hashimoto thyroiditis: an evidence-based guide to etiology, diagnosis and treatment. Pol Arch Intern Med 2022; 132: 16222.
5. Intenzo CM, Capuzzi DM, Jabbour S, Kim SM, dePapp AE. Scintigraphic features of autoimmune thyroiditis. Radiographics 2001; 21: 957-64.
6. Olah R, Hajos P, Soos Z, Winkler G. De Quervain thyroiditis. Corner points of the diagnosis. Orv Hetil 2014; 155: 676-80.
7. Vural C, Paksoy N, Gok ND, Yazal K. Subacute granulomatous (De Quervain's) thyroiditis: fine-needle aspiration cytology and ultrasonographic characteristics of 21 cases. Cytojournal 2015; 12: 9.
8. Stasiak M, Lewinski A. New aspects in the pathogenesis and management of subacute thyroiditis. Rev Endocr Metab Disord 2021; 22: 1027-39.
9. Cappelli C, Pirola I, Gandossi E, Formenti AM, Agosti B, Castellano M. Ultrasound findings of subacute thyroiditis: a single institution retrospective review. Acta Radiol 2014; 55: 429-33.
10. Volpe R. The management of subacute (DeQuervain's) thyroiditis. Thyroid 1993; 3: 253-5.
11. Ogawa E, Katsushima Y, Fujiwara I, Iinuma K. Subacute thyroiditis in children: patient report and review of the literature. J Pediatr Endocrinol Metab 2003; 16: 897-900.
12. Toschetti T, Parenti C, Ricci I, et al. Acute suppurative and subacute thyroiditis: from diagnosis to management. J Clin Med 2025; 14: 3233.
13. Falhammar H, Wallin G, Calissendorff J. Acute suppurative thyroiditis with thyroid abscess in adults: clinical presentation, treatment and outcomes. BMC Endocr Disord 2019; 19: 130.
14. She X, Zhou YN, Guo J, Yi C. Clinical analysis of acute suppurative thyroiditis in 18 children. Infect Drug Resist 2022; 15: 4471-7.
15. Masuoka H, Miyauchi A, Tomoda C, et al. Imaging studies in sixty patients with acute suppurative thyroiditis. Thyroid 2011; 21: 1075-80.
16. Bansal LK, Gupta S, Gupta AK, Chaudhary P. Thyroid tuberculosis. Indian J Tuberc 2021; 68: 272-8.
17. Ortiz-Flores A, Gioia F, Montanez-Fernandez L, et al. Incidental finding of a primary thyroid tuberculosis. Oxf Med Case Reports 2017; 2017: omx022.
18. Bhatia A, Rajwanshi A, Dash RJ, Mittal BR, Saxena AK. Lymphocytic thyroiditis: is cytological grading significant? A correlation of grades with clinical, biochemical, ultrasonographic and radionuclide parameters. Cytojournal 2007; 4: 10.
19. Ong BJ, Chua AJ, Toh ST. Suppurative thyroiditis in a pregnant patient. Otolaryngol Case Rep 2018; 8: 12-3.
20. Baidya A, Singha A, Bhattacharjee R, Dalal BS. Tuberculosis of the thyroid gland: two case reports. Oxf Med Case Reports 2015; 2015: 262-4.
21. Frates MC, Marqusee E, Benson CB, Alexander EK. Subacute granulomatous (de Quervain) thyroiditis: grayscale and color Doppler sonographic characteristics. J Ultrasound Med 2013; 32: 505-11.
22. Park SY, Kim EK, Kim MJ, et al. Ultrasonographic characteristics of subacute granulomatous thyroiditis. Korean J Radiol 2006; 7: 229-34.
23. Takahashi MS, Pedro HM, Chammas MC. Ultrasound evaluation of thyroiditis: a review. J Otolaryngol Res 2019; 2: 127.
24. Wong KW, Jacobs WR Jr. Postprimary tuberculosis and macrophage necrosis: is there a big ConNECtion? mBio 2016; 7: e01589-15.

JPTM

ORIGINAL ARTICLE

pISSN 2383-7837 · eISSN 2383-7845

Journal of Pathology and Translational Medicine 2025; 59: 434-443
https://doi.org/10.4132/jptm.2025.08.20

Modified plasma-thrombin method using patient-derived plasma for cell block preparation in endobronchial ultrasound–guided transbronchial fine-needle aspiration

Xizhe Zhang[1*], Chunli Tang[1*], Yingying Gu[1], Zeyun Lin[1,2], Shiqi Tang[1], Anzi Tan[1], Mengshi Li[1], Zhucheng Chen[1], Yuying Chen[1], Shi-yue Li[1], Juhong Jiang[1]

[1]State Key Laboratory of Respiratory Disease, National Clinical Research Center for Respiratory Disease, Guangzhou Institute of Respiratory Health, The First Affiliated Hospital of Guangzhou Medical University, Guangzhou, China
[2]Department of Clinical Laboratory, Guangzhou Development District Hospital, Guangzhou, China

Graphical abstract

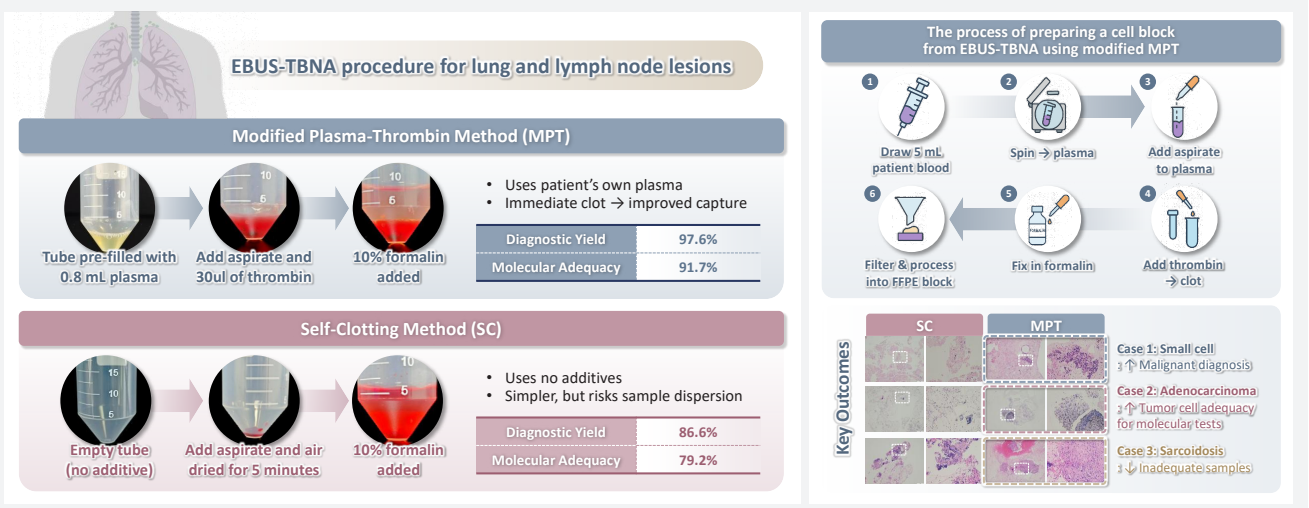

CONCLUSION The MPT method significantly improved the cellular yield of EBUS-TBNA-derived CBs. Using patient-derived fresh plasma rather than expired blood bank plasma avoids a known contamination risk. The additional step modestly prolongs the procedure and introduces minimal risks by vein puncture. This approach is generally considered cost-effective.

Zhang X et al. Journal of Pathology and Translational Medicine

JPTM

ORIGINAL ARTICLE

pISSN 2383-7837 · eISSN 2383-7845

Journal of Pathology and Translational Medicine 2025; 59: 434-443
https://doi.org/10.4132/jptm.2025.08.20

Modified plasma-thrombin method using patient-derived plasma for cell block preparation in endobronchial ultrasound–guided transbronchial fine-needle aspiration

Xizhe Zhang[1*], Chunli Tang[1*], Yingying Gu[1], Zeyun Lin[1,2], Shiqi Tang[1], Anzi Tan[1], Mengshi Li[1], Zhucheng Chen[1], Yuying Chen[1], Shi-yue Li[1], Juhong Jiang[1]

[1]State Key Laboratory of Respiratory Disease, National Clinical Research Center for Respiratory Disease, Guangzhou Institute of Respiratory Health, The First Affiliated Hospital of Guangzhou Medical University, Guangzhou, China
[2]Department of Clinical Laboratory, Guangzhou Development District Hospital, Guangzhou, China

Background: The plasma-thrombin method, which uses expired blood bank plasma as an ancillary component, has been widely used in cell block (CB) preparation. However, the application of expired blood bank plasma raises concerns about nucleic acid contamination. This study investigated the feasibility of using patient-derived plasma as a substitute for blood bank plasma in the modified plasma-thrombin (MPT) method for CB preparation in endobronchial ultrasound–guided transbronchial needle aspiration (EBUS-TBNA) samples. **Methods:** A prospective study was conducted to compare the adequacy of CB preparation between a previously used self-clotting (SC) method and the MPT method. The EBUS-TBNA specimens from each targeted lesion were divided into paired samples: one processed using the SC method and the other using the MPT method, substituting the blood bank plasma with patient-derived plasma. **Results:** A total of 82 paired EBUS-TBNA samples from 59 patients were analyzed. The diagnostic yield of the SC method and the MPT method was 86.6% and 97.6%, respectively. Among patients diagnosed with non–small cell lung cancer, the adequacy rate for molecular testing was 79.2% with the SC method and 91.7% with the MPT method. **Conclusions:** The MPT method significantly improved the cellular yield of EBUS-TBNA–derived CBs. Using patient-derived fresh plasma rather than expired blood bank plasma avoids a known contamination risk. The additional step modestly prolongs the procedure and introduces minimal risks by vein puncture. This approach is generally considered cost-effective.

Keywords: Fine needle aspiration; Cytology; Self-clotting; Plasma-thrombin; Paraffin embedding

INTRODUCTION

Cell blocks (CBs) are preparations in which cytologic material is collected and processed into a paraffin-embedded block, similar to formalin-fixed paraffin-embedded (FFPE) tissue in surgical pathology. CBs are primarily obtained from the pellet formed by cells and small solid particles in a cell suspension derived from needle rinses of aspirates, effusions, washings, or brushings [1-3]. A key advantage of CBs is that hematoxylin and eosin (H&E)–stained slides provide well-preserved cytomorphology while

Received: May 19, 2025 **Revised:** August 17, 2025 **Accepted:** August 20, 2025
Corresponding Author: Juhong Jiang, PhD
State Key Laboratory of Respiratory Disease, National Clinical Research Center for Respiratory Disease, Guangzhou Institute of Respiratory Health, The First Affiliated Hospital of Guangzhou Medical University, Guangzhou, Guangdong 510120, China
Tel: +86-20-81567845, Fax: +86-20-83395961, E-mail: juhongjiang2006@163.com

Shi-yue Li, PhD
State Key Laboratory of Respiratory Disease, National Clinical Research Center for Respiratory Disease, Guangzhou Institute of Respiratory Health, The First Affiliated Hospital of Guangzhou Medical University, Guangzhou, Guangdong 510120, China
Tel: +86-20-81566640, Fax: +86-20-83395961, E-mail: lishiyue@188.com

*Xizhe Zhang and Chunli Tang contributed equally to this work.

maintaining tissue architecture in cell clusters and tissue fragments. Moreover, the concentration of diagnostic material within a limited area facilitates rapid examination [1]. CBs also enable the preparation of multiple serial sections for ancillary studies, including special stains, immunohistochemistry, and molecular testing [4]. Furthermore, they can be archived long-term for potential future diagnostic studies or research applications.

Unlike histological tissue preparation in surgical pathology, there is no standardized method for CB preparation, with various in-house and commercially available techniques in use. A 2014 survey found that while more than 10 CB preparation methods are used, including HistoGel (27%), plasma-thrombin (PT) (33%), and the Cellient automated system (8%), up to 44% of cytopathologists are dissatisfied with CB quality, highlighting the challenges they present in routine practice [5].

Endobronchial ultrasound–guided transbronchial needle aspiration (EBUS-TBNA) is an effective technique for obtaining tissue and cytologic samples from mediastinal or hilar lymph nodes and lung parenchyma for diagnostic purposes [6,7]. Although cytomorphologic examination of cytologic slides, such as direct smears or liquid-based preparations, is an essential diagnostic tool for evaluating aspirates obtained by EBUS-TBNA, CBs allow for reproducible morphological and immunohistochemical characterization of lesions. Traditionally, CBs are prepared by rinsing the aspiration needle with normal saline or RPMI medium into a centrifuge tube. The solution is then centrifuged to form a cell pellet, which is processed into a CB. To enhance cell adhesion and clot formation, other CB preparation methods using PT, HistoGel, or sodium alginate have been employed [8-10]. However, even when all aspirated material is retrieved completely by needle rinsing and concentration, the cellular yield of CBs remains inconsistent. A primary limitation of these methods is that they focus on concentrating the cellular material after it has already been diluted during the needle rinsing, rather than preventing cell loss before processing.

The "tissue coagulum clot," also known as "self-clotting" (SC) technique, an alternative approach designed to improve cellular yield compared to the traditional needle rinse method. In the SC method described by Shi et al. (2018) [11], aspirated material for CB preparation is directly expelled onto the bottom or sidewall of a 50 mL centrifuge tube, where it subsequently forms a clot and air-dries. If the air-dried sample lacks sufficient blood or is too small in quantity, plasma and thrombin are added to form an artificial clot. The final needle rinse and collection medium, composed of RPMI, is then combined with the clot and air-dried sample. CBs are then prepared in the histology laboratory using the conventional PT method. While CB preparation—including PT-enhanced SC and the traditional PT method—can be complex, the SC technique prevents cellular material that does not form a tissue coagulum from dispersing into the collection medium. This significantly minimizes cellular loss during subsequent processing.

In the modified plasma-thrombin (MPT) method, as described by Aisagbonhi et al. (2018) [9], the fine-needle aspiration (FNA) sample is directly rinsed into previously aliquoted pooled fresh plasma. Two drops of thrombin are then added and gently mixed, leading to immediate clot formation. The clot is immediately transferred to a tissue bag and cassette, fixed in formalin, and processed using standard histological methods. The MPT method eliminates the need for centrifugation to concentrate the sample, thereby reducing processing time and avoiding tissue deformation caused by centrifugation. Moreover, immediate formalin fixation improves the preservation of both single-cell cytomorphology and the architecture of tissue fragments.

The traditional PT method, including needle rinsing and sample centrifugation, has been widely adopted as an inexpensive and simple approach despite the lack of rigorous comparisons with alternative CB techniques or validation against the gold standard of FFPE histology tissue [12]. However, using expired blood bank plasma or pooled fresh plasma as an ancillary component in the traditional PT method and MPT method raises several concerns. First, expired plasma exhibits variability in clotting ability, leading to inconsistencies in clot formation time and clot size, which can result in an uneven cell distribution through the cutting levels of the CB. Furthermore, the use of discarded human plasma introduces a theoretical risk of nucleic acid contamination or the presence of biological factors that may interfere with sensitive downstream molecular testing. This concern is increasingly relevant as cytology specimens are frequently used for molecular analysis. A study by Sung et al. [13] demonstrated that all tested expired fresh frozen donor plasma contained high-quality amplifiable DNA. Their findings, along with those of other researchers, caution against using pooled blood bank plasma for CB preparation due to potential genomic DNA interference, particularly in specimens with low cellularity [14].

Beginning in February 2022, a modified SC method based on the technique described by Shi et al. [11] was implemented for the CB processing of EBUS-TBNA samples in the authors' institute. Unlike the original method, this approach eliminates the ancillary PT step to mitigate concerns regarding nucleic acid

contamination. In this method, EBUS-TBNA samples designated for CB preparation are expelled directly into a centrifuge tube, allowing clot formation. A 10% formalin solution is then added. In the histology laboratory, a disposable paint filter with 100-μm fine nylon mesh is placed over a beaker, and a piece of embedding paper is positioned inside the filter. The sample from the centrifuge tube is poured into this device, where tissue clots and dispersed cellular material are captured by the embedding paper. The paper is then wrapped and processed as a routine histology sample [15].

The current study aimed to investigate the feasibility of using the MPT method described by Aisagbonhi et al. [9] while substituting patient-derived plasma for pooled blood bank plasma in CB preparation. By obtaining 5 mL of whole blood from the patient before the procedure, an adapted MPT method was developed and compared with the previous SC method. A prospective study was conducted to evaluate the adequacy of CB preparation between these two methods.

MATERIALS AND METHODS

Study design and participants

This single-center, prospective study was conducted to compare the SC and MPT methods for CB preparation in the pulmonary clinic of the First Affiliated Hospital of Guangzhou Medical University from January to December 2024. Adults aged 18 years or older with undiagnosed mediastinal lymphadenopathy or mediastinal masses, as well as patients with lung cancer undergoing staging, were included.

Thrombin and plasma preparation

Thrombin from bovine plasma (Absin, Shanghai, China) was used. The product was supplied as a lyophilized powder with an activity of 2,000 units/mg protein. It was reconstituted in normal saline containing 0.1% bovine serum albumin to a final concentration of 100 units/mL. The solution was aliquoted into polymerase chain reaction (PCR) tubes (100 μL per tube) and stored at −20°C. Only the required number of aliquots was thawed before use.

A mini centrifuge and other necessary materials were set up in the bronchoscopy unit (Fig. 1). Before the EBUS-TBNA procedure, 5 mL of venous blood was drawn from the patient by a nurse in the bronchoscopy unit using sodium citrate as an anticoagulant. The blood sample was centrifuged at 3,000 rpm for 5 minutes, and the supernatant (plasma) was transferred to a 2-mL Eppendorf tube for further use. The details of these processes are illustrated in Fig. 1.

Sample acquisition

Two 50-mL centrifuge tubes labeled tube A and tube B were

Fig. 1. Patient plasma preparation. (A) A 5-mL blood sample was collected from the patient before the endobronchial ultrasound–guided transbronchial needle aspiration procedure. (B) The blood sample was centrifuged at 3,000 rpm for 5 minutes using a mini-centrifuge. (C) Blood components after centrifugation. (D) The supernatant plasma was transferred to 2-mL Eppendorf tubes.

https://doi.org/10.4132/jptm.2025.08.20

prepared for each targeted lesion. Tube A was pre-filled with 0.8 mL of plasma for the MPT method, while tube B contained no additives for the SC method. Each EBUS-TBNA procedure was performed by a physician in the bronchoscopy unit of the pulmonary diseases clinic. Aspiration material was obtained from a targeted lymph node (LN) or lesion in the lung, trachea, or mediastinum using a 21-gauge or 22-gauge cytology needle. The material inside the cytology needle was gently expelled using the wire stylet provided with the needle kit, depositing the aspirate into the bottom of the respective centrifuge tube. Four passes were obtained from each targeted LN or lesion. For cases 1–10, 21–30, and 41–50, the first and third passes were expelled into tube A (pre-filled with plasma), while the second and fourth passes were expelled into tube B (without any additives). For cases 11–20, 31–40, and 51–59, the first and third passes were expelled into tube B, while the second and fourth passes were expelled into tube A. Targeted LNs or lesions with fewer than four passes were excluded from the study.

Following sample acquisition, 30 μL of thrombin was added to tube A. The tube was gently flicked to mix the thrombin, resulting in immediate clot formation. The sample in tube B, which lacked clotting material, was air-dried for 5 minutes. A 10% formalin solution was then added to both tube A and tube B. Samples were then submitted to the pathology laboratory for processing. The details of these processes are illustrated in Fig. 2.

In the pathology laboratory, a disposable paint filter with 100-μm fine nylon mesh was positioned over a beaker, with a piece of embedding paper placed inside the filter. The sample contents from each centrifuge tube were poured into this filter, allowing both tissue clots and dispersed cellular components to be captured by the embedding paper. The embedding paper was wrapped and processed as a standard histology specimen. The setup and filtration workflow are illustrated in Fig. 3.

H&E-stained FFPE sections and immunohistochemical analysis

The FFPE samples were cut at a standard thickness of 4 μm and stained with H&E following routine protocols. Immunohistochemistry was performed on cases in which the pathologist deemed additional analysis necessary for diagnostic clarification. Immunohistochemical staining was carried out using the Ventana-Roche automated immunostainer following standard staining protocols.

Slide review

H&E-stained FFPE sections were independently reviewed by two pathologists (J.J. and Y.G.), blinded and without knowledge of the CB preparation method. Sections from each case were systematically examined and compared. According to the World Health Organization (WHO) Reporting System for Lung Cy-

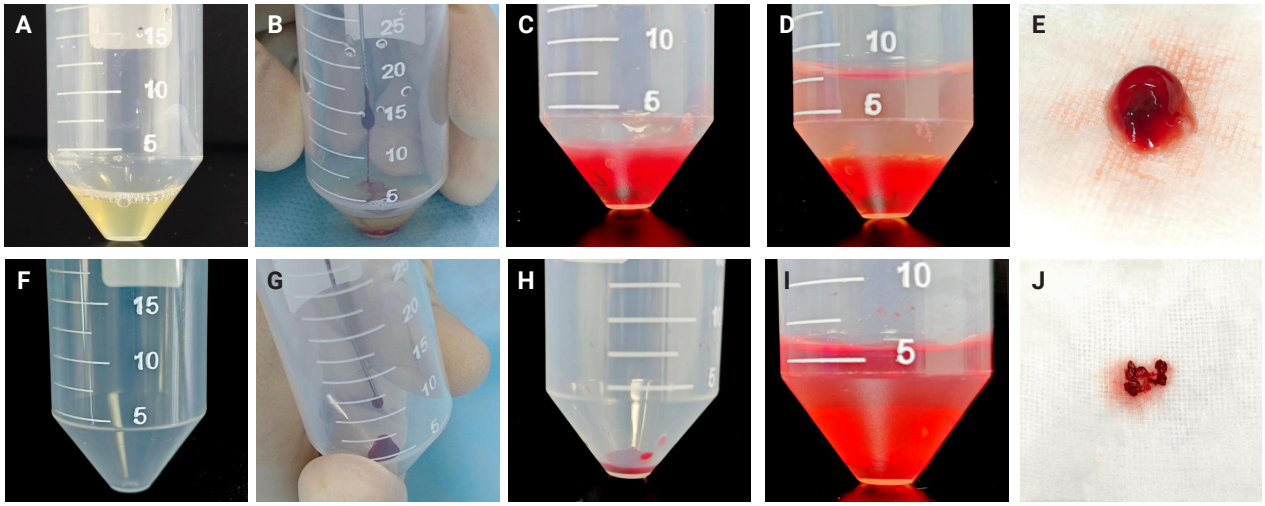

Fig. 2. Sample acquisition using the modified plasma-thrombin method (A–E) and the self-clotting method (F–J). (A) Tube A was pre-filled with 0.8 mL of plasma. (F) Tube B contained no additional components. (B, G) The aspirated specimen was expelled into the bottom of the centrifuge tube. (C) Thirty microliters of thrombin were added to the sample in tube A. (H) The sample in tube B was allowed to air dry for 5 minutes. (D, I) A 10% formalin solution was added to both tubes. (E, J) The processed samples were collected onto embedding paper in the laboratory.

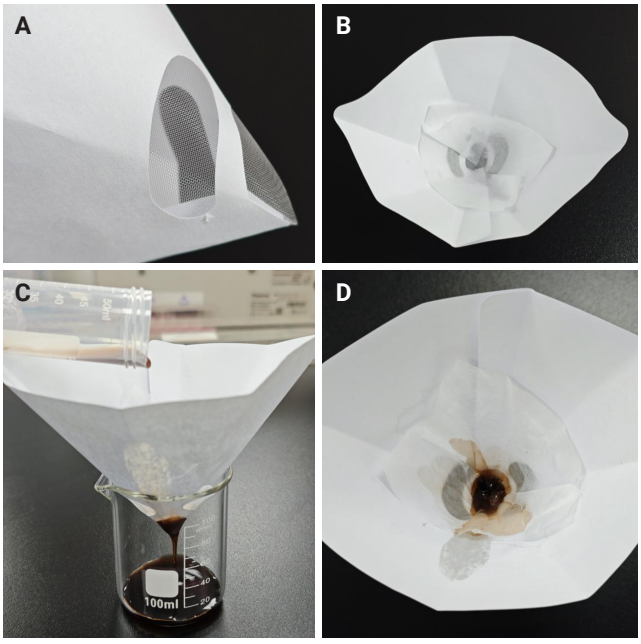

Fig. 3. Schematic illustration of the filter-based method for processing endobronchial ultrasound–guided transbronchial needle aspiration (EBUS-TBNA) specimens. (A) Side view of the commercial "100-μm paint filter." (B) Top view of the filter with the embedding paper placed inside. (C) Transfer of the EBUS-TBNA specimen from the centrifuge tube into the filter. (D) Tissue specimens captured by the embedding paper.

topathology and established criteria for evaluating inadequate EBUS-derived specimens [16-18], samples from both preparation methods were categorized into five diagnostic groups: "insufficient/inadequate/nondiagnostic," "benign," "atypical," "suspicious for malignancy," and "malignant." The "insufficient/inadequate/nondiagnostic" category was applied to cases with limited material resulting from low cellularity, suboptimal preparation, poor fixation or staining, or obscuring artifacts such as blood, inflammation, or necrosis that preclude reliable interpretation. Samples displaying cells or structures consistent with non-malignant conditions were classified as "benign," whereas those displaying clear malignant cytologic features were categorized as "malignant." Specimens categorized as "atypical" demonstrated findings predominantly characteristic of benign lesions and minor atypical features that raised the possibility of malignancy, though insufficient in quantity or quality for a definitive diagnosis. The "suspicious for malignancy" category was used when cytologic features strongly suggested malignancy but the cellular material was limited in quantity or quality, rendering a definitive diagnosis impossible despite overall specimen adequacy. For malignant cases, tumor cell quantity and fraction were systematically assessed. Tumor cellularity was estimated at three levels: low, moderate, and high. Low cellularity was defined as having 0–200 tumor cells or a tumor cell fraction <10%, which was considered insufficient for molecular testing. Moderate cellularity was defined as having 200–1,000 tumor cells and a tumor cell fraction of ≥10%, which was deemed suitable for molecular testing. High cellularity was defined as having more than 1,000 tumor cells and a tumor cell fraction of ≥10%, which was considered optimal for molecular testing.

Statistical analysis

McNemar's test was used to compare the diagnostic yield and molecular test adequacy rate between the SC and MPT methods in paired samples. A p-value of <.05 was considered statistically significant. All statistical analyses were performed using SPSS software ver. 25.0 (IBM Corp., Armonk, NY, USA).

RESULTS

Patient characteristics

A total of 82 paired EBUS-TBNA samples were collected from 59 patients. Each case had four successful passes from the target LN or lesion, which were divided into paired samples. One sample was processed using the SC method, while the other was processed using the MPT method. Patient demographics, pathological data, and the distribution of sampling stations are summarized in Table 1.

Diagnostic performance

Cellular morphology, including architectural and nuclear preservation, was comparable between the two CB preparation methods. In the SC method samples, tissue fragments were observed either wrapped in blood clots or dispersed on CB sections. On the other hand, samples processed with the MPT method showed tissue fragments and cellular material enmeshed in blood clots or pale pink eosinophilic artifacts.

The SC method demonstrated an overall diagnostic yield of 86.6% (71/82), with 49 malignant and 22 benign cases, while 13.4% (11/82) of the samples were deemed inadequate. On the other hand, the MPT method achieved a diagnostic yield of 97.6% (80/82), with 55 malignant and 25 benign cases, and only 2.4% (2/82) of samples classified as inadequate. McNemar's test revealed a statistically significant difference in diagnostic yield

https://doi.org/10.4132/jptm.2025.08.20

between the SC and MPT methods (p = .016). The diagnostic performance of both methods is summarized in Table 2. Fig. 4 presents representative microscopic images of EBUS-TBNA samples deemed inadequate by the SC method but adequate by the MPT method.

Table 1. Clinicopathological details of the 82 lesions in 59 cases

Characteristic	Value
Age (yr), median (range)	65 (21-79)
Sex, n (%)	
Male	41 (69.5)
Female	18 (30.5)
Lung lesion	16 lesions
Hilum of right lung	1
Right upper lobe	2
Right lower lobe	6
Right middle lobe	2
Left upper lobe	2
Left lower lobe	3
Lymph node	66 lesions
4L	2
4R	10
7#	28
10L	2
10R	2
11L	5
11R	7
12R	10
Malignancy	39 cases
Adenocarcinoma	24.0
Squamous cell carcinoma	4.0
Lymphoepithelial carcinoma	2.0
Small cell lung carcinoma	3.0
Large cell neuroendocrine carcinoma	1.0
NSCLC NOS	5.0
Nonmalignant diagnosis	18 cases
Benign reactive lymph node	12.0
Tuberculosis	4.0
Sarcoidosis	2.0
Inadequate specimen	2 cases

NSCLC, non–small cell lung cancer; NOS, not otherwise specified.

Tumor cellularity assessment in non–small cell lung cancer cases

Tumor cellularity was evaluated in CB sections of 48 paired samples diagnosed with non–small cell lung cancer, as this subgroup is most commonly considered for targeted therapy. Adequacy for molecular testing was defined as having more than 200 tumor cells and a tumor cell fraction ≥10%. The SC method demonstrated an adequacy rate of 79.2% (38/48), whereas the MPT method achieved an adequacy rate of 91.7% (44/48). A statistically significant difference in adequacy rates was observed between the two methods (p = .041). The tumor cellularity distribution for both methods is presented in Table 3.

Immunocytochemistry

Immunocytochemistry results for both CB preparation methods showed no difference in staining quality regarding staining intensity. However, occasional faint brown background staining was observed in MPT CBs due to trapped plasma, but this did not interfere with immunocytochemical evaluation. Representative images of cytoplasmic (cytokeratin 7) and nuclear (Ki-67) antigen staining on CB sections prepared by both methods are shown in Fig. 5.

Time consumption

The additional processing time required for the MPT method in the bronchoscopy unit, including blood sampling, plasma separation, and clot formation, was approximately 10 minutes.

DISCUSSION

The PT method is most commonly used for CB preparation due to its simplicity, low cost, and high satisfaction rate relative to other methods [12]. However, the use of expired blood bank plasma in this process is not recommended for the preparation of CBs due to nucleic acid contamination concerns. To address this issue, this study reports the development of the MPT method, which uses patient-derived plasma as a substitute for expired blood bank plasma. The findings of this study demonstrate that the MPT method using patient-derived plasma improves the

Table 2. Comparison of diagnostic yield between two specimen processing methods in 82 paired samples

Method	Insufficient/inadequate/non-diagnostic	Benign	Atypical	Suspicious for malignancy	Malignant	Diagnostic yield, n (%)	p-value
Self-clotting	10	22	0	0	49	71/82 (86.6)	.016
Modified plasma-thrombin	2	25	0	0	55	80/82 (97.6)	

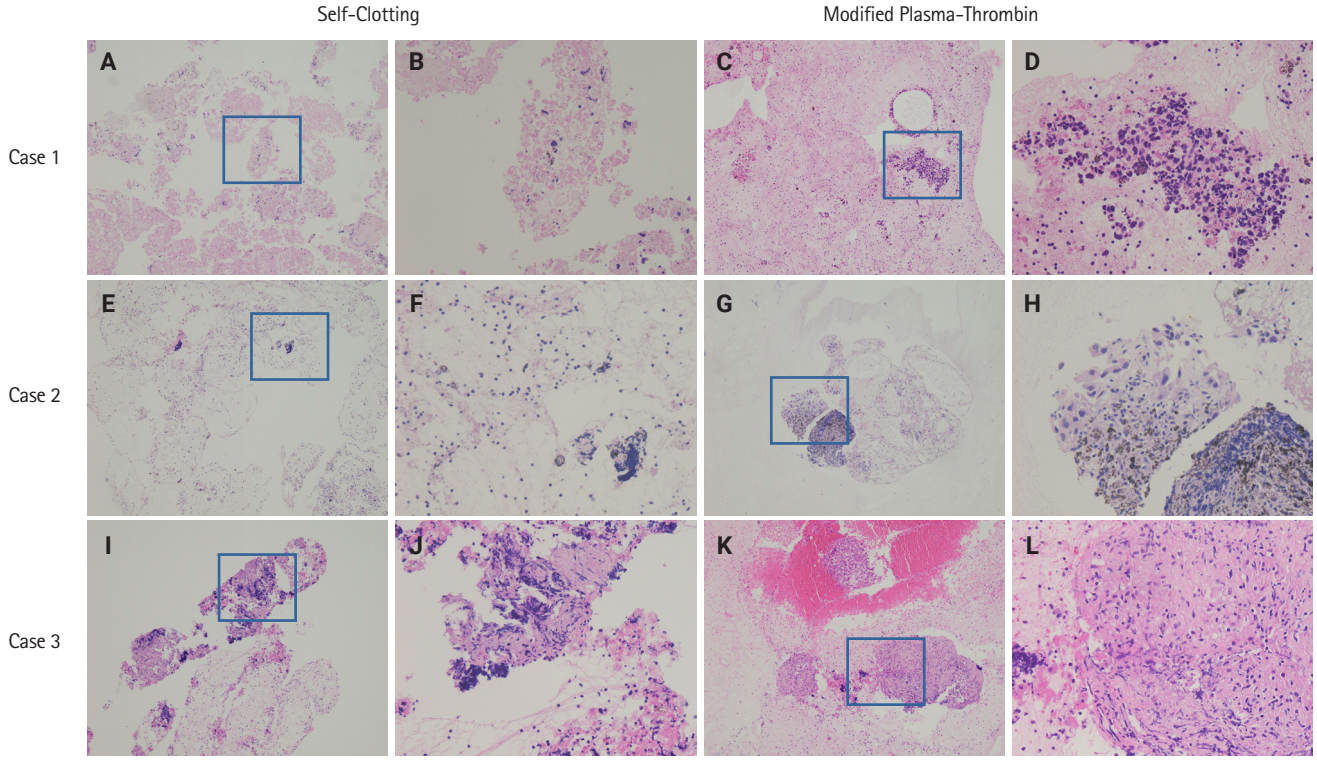

Fig. 4. Representative microscopic images of endobronchial ultrasound–guided transbronchial needle aspiration samples deemed inadequate by the self-clotting method (A, B, E, F, I, J) but adequate by the modified plasma-thrombin method (C, D, G, H, K, L) in three paired samples. Case 1: small cell lung carcinoma. Case 2: adenocarcinoma. Case 3: sarcoidosis. The self-clotting method resulted in more dispersed tissue fragments in the cell block sections, whereas the modified plasma–thrombin method led to encapsulation of tissue fragments within blood clots, improving sample adequacy.

Table 3. Tumor cellularity assessment of two specimen processing methods in 48 paired samples

Method	Tumor cellularity			Molecular test adequacy rate, n (%)	p-value
	Low	Moderate	High		
Self-clotting	10	18	22	38/48 (79.2)	.041
Modified plasma thrombin	4	24	20	44/48 (91.7)	

Low, with <200 tumor cells/section and/or a tumor cell fraction <10%, insufficient for molecular testing; Moderate, with 200–1,000 tumor cells/section and a tumor cell fraction ≥10 %, suitable for molecular testing; High, with >1,000 tumor cells/section and a tumor cell fraction ≥10%, advantageous for molecular testing.

cellularity of CB preparations from EBUS-TBNA samples. Patient-derived plasma was easily obtained and convenient for use in the procedure unit. The use of fresh patient-derived plasma in the MPT method offers several advantages over expired blood bank plasma. First, patient-derived plasma avoids a known contamination risk. Second, the stable clotting properties of fresh patient plasma ensure immediate clot formation and predictable clot size, contributing to increased cellular yield by promoting even cell concentration.

Several factors influence the cellular yield of the MPT method, including plasma volume and the plasma-to-thrombin ratio. A lower plasma volume produces CBs with more concentrated cellular material. In this study, the plasma volume used was approximately equal to that of the cellular sediment. Moreover, a small volume of thrombin (30 μL) was added, in contrast to previous reports where 3–5 drops were used. To ensure consistent clotting efficiency, the thrombin working solution was aliquoted into 100 μL portions in 0.2-mL PCR tubes and stored at −20°C. Only the required number of aliquots was thawed for use, preventing variability in clotting activity.

https://doi.org/10.4132/jptm.2025.08.20

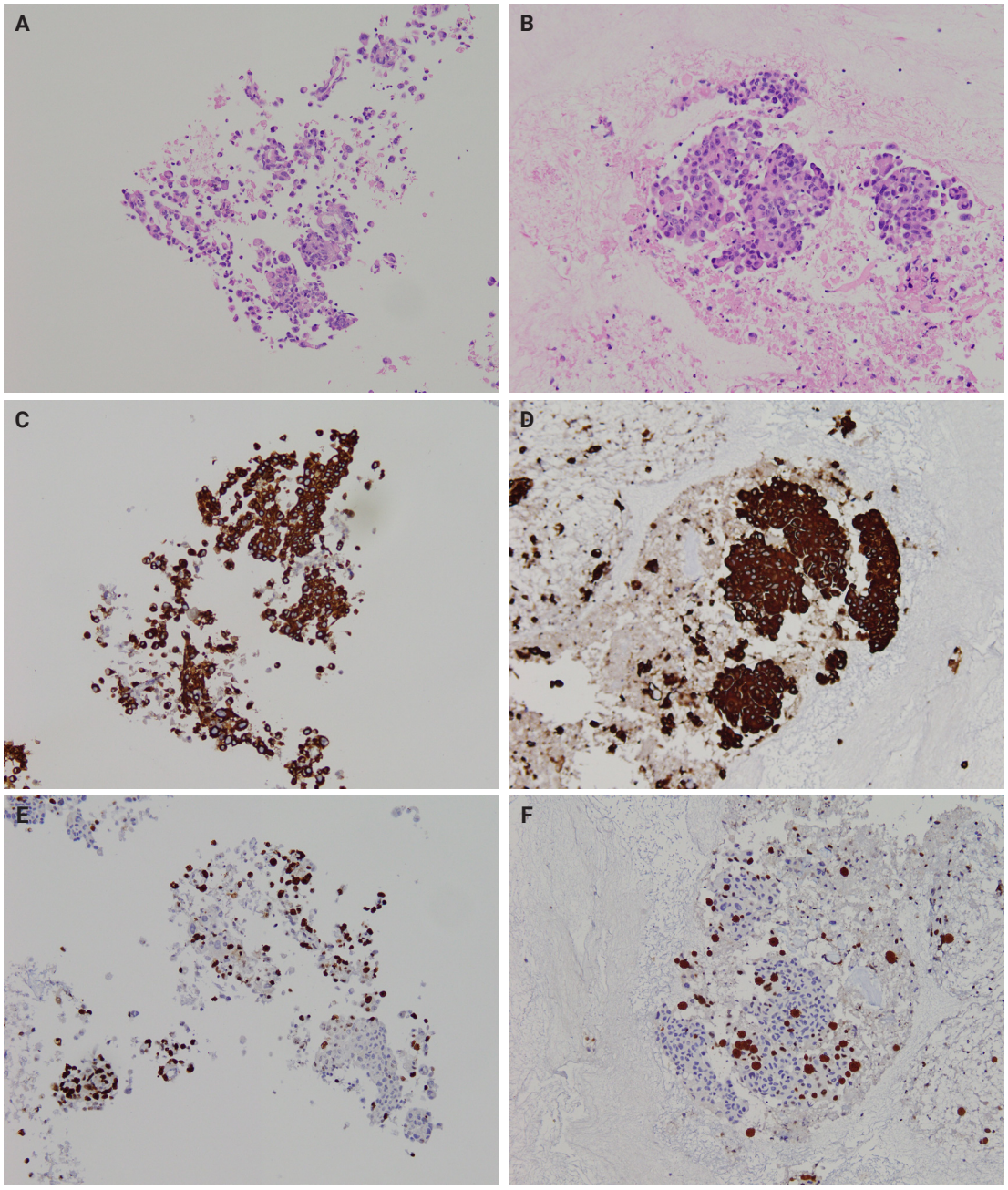

Fig. 5. Representative histologic and immunohistochemical staining showing hematoxylin and eosin–stained sections (A, B), cytoplasmic (cytokeratin 7; C, D), and nuclear (Ki-67; E, F) antigens on cell block sections prepared using the self-clotting method (A, C, E) and the modified plasma-thrombin method (B, D, F) in a paired sample.

The MPT method developed in this study offers several advantages. Compared with the previously reported normal saline needle rinsing and PT method, which involves forced spraying and dispersion of the material using a syringe filled with saline, the SC and MPT methods minimize tissue disruption by expelling the coagulum with minimal mechanical force. Moreover, immediate fixation of the clot in formalin prevents potential antigenicity loss for immunohistochemistry that may occur upon exposure to saline or water. Furthermore, the use of the filtration method in both techniques eliminates the need for centrifugation, reducing processing time and avoiding tissue deformation caused by centrifugation. This approach preserves cellular mor-

phology and prevents the loss of cell pellets during supernatant decanting.

In previously reported tissue coagulum clot methods or the SC method without the ancillary PT method, aspirated material that was not sufficiently bloody and failed to form a tissue coagulum clot became dispersed upon the addition of formalin, leading to potential sample loss during processing. The MPT method addresses this issue by allowing the aspirated material to stream directly into the tube containing plasma, followed by the addition of thrombin, which enmeshes the cellular material within a clot. This process ensures that dispersed cells or necrotic tissue are retained during subsequent processing. It not only reduces the loss of tumor cellularity but also maintains the tissue structure, which is vital for the diagnosis of cases such as lymphoma. It also helps to keep the necrotic tissue in granuloma nodules, which is important in distinguishing sarcoidosis or tuberculosis.

Incorporating routine blood sampling and plasma separation into bronchoscopy workflows at high-volume centers may lead to a considerable increase in workload. Therefore, this technique may be more efficiently applied in selected patient groups, such as those with suspected or confirmed thoracic malignancy or those with lesion sizes and locations that may be challenging to visualize or sample via EBUS-TBNA. Alternatively, an additional 5-mL blood sample could be collected during routine laboratory testing before EBUS-TBNA. In such cases, plasma separation could be performed in the laboratory, and the prepared plasma then delivered to the bronchoscopy unit.

Several limitations should be acknowledged. First, patient-derived plasma was not directly compared with expired blood bank plasma for CB preparation. Second, the MPT method was not evaluated against the traditional normal saline needle rinsing and PT method. Third, statistical validation comparing the MPT method with other CB techniques, including the collodion bag and sodium alginate methods, was not conducted to determine the optimal approach. Finally, although this study did not include image-guided FNAs from the liver, lung, pancreas, or other organs, the findings are likely applicable to these sample types as well.

In conclusion, patient-derived plasma serves as an effective alternative to expired blood bank plasma for PT-based CB preparation in routine practice. The MPT method developed in this study is a safe, cost-effective approach that poses no additional risk to patients. We encourage the adoption of this method in other image-guided FNAs.

Ethics Statement

This study was approved by the Institutional Review Board of the First Affiliated Hospital of Guangzhou Medical University (reference number: ES-2023-134-03, January 05, 2024). Procedures involving human subjects were conducted following the Declaration of Helsinki, 1975, as revised in 1983. The study was conducted following institutional ethical guidelines, and written informed consent was obtained for blood collection.

Availability of Data and Material

The datasets generated or analyzed during the study are available from the corresponding author on reasonable request.

Code Availability

Not applicable.

ORCID

Xizhe Zhang https://orcid.org/0009-0006-6109-0750
Chunli Tang https://orcid.org/0009-0001-9731-5679
Yingying Gu https://orcid.org/0000-0002-6566-3281
Zeyun Lin https://orcid.org/0009-0007-4433-0342
Shiqi Tang https://orcid.org/0009-0000-8800-0942
Anzi Tan https://orcid.org/0009-0009-7003-9182
Mengshi Li https://orcid.org/0000-0002-6891-3135
Zhucheng Chen https://orcid.org/0009-0008-0237-2963
Yuying Chen https://orcid.org/0009-0004-9376-1657
Shi-yue Li https://orcid.org/0000-0001-9622-5623
Juhong Jiang https://orcid.org/0000-0002-1609-7500

Author Contributions

Conceptualization: JJ. Data curation: XZ. Investigation: XZ, AT. Funding acquisition: JJ. Methodology: ML, ZC, YC. Project administration: SL. Resources: CT. Supervision: YG. Validation: ZL, ST. Writing—original draft: JJ. Writing—review & editing: SL. Approval of final manuscript: all authors.

Conflicts of Interest

The authors declare that they have no potential conflicts of interest.

Funding Statement

This work was supported by the National Natural Science Foundation of China [grant number 81772814] and the Open Project of the State Key Laboratory of Respiratory Disease [grant number SKLRD-OP-202205]. The funding sources had no role in

https://doi.org/10.4132/jptm.2025.08.20

study design; in the collection, analysis, or interpretation of data; in the writing of the report; or in the decision to submit the article for publication.

REFERENCES

1. Karnauchow PN, Bonin RE. "Cell-block" technique for fine needle aspiration biopsy. J Clin Pathol 1982; 35: 688.
2. Burt AD, Smillie D, Cowan MD, Adams FG. Fine needle aspiration cytology: experience with a cell block technique. J Clin Pathol 1986; 39: 114-5.
3. Olson NJ, Gogel HK, Williams WL, Mettler FA. Processing of aspiration cytology samples: an alternative method. Acta Cytol 1986; 30: 409-12.
4. da Cunha Santos G, Saieg MA, Troncone G, Zeppa P. Cytological preparations for molecular analysis: a review of technical procedures, advantages and limitations for referring samples for testing. Cytopathology 2018; 29: 125-32.
5. Crapanzano JP, Heymann JJ, Monaco S, Nassar A, Saqi A. The state of cell block variation and satisfaction in the era of molecular diagnostics and personalized medicine. Cytojournal 2014; 11: 7.
6. Tyan CC, Machuca T, Czarnecka K, et al. Performance of endobronchial ultrasound-guided transbronchial needle aspiration for the diagnosis of isolated mediastinal and hilar lymphadenopathy. Respiration 2017; 94: 457-64.
7. Rahman KK, Mohapatra PR, Panigrahi MK, Purkait S, Bhuniya S. Comparison of endobronchial ultrasound-guided transbronchial needle aspiration cytology versus cell blocks in adults with undiagnosed mediastinal lymphadenopathy. Lung India 2021; 38: 425-30.
8. Torous VF, Chen Y, VanderLaan PA. Comparison of plasma-thrombin, HistoGel, and CellGel cell block preparation methods with paired ThinPrep slides in the setting of mediastinal granulomatous disease. J Am Soc Cytopathol 2019; 8: 52-60.
9. Aisagbonhi O, Birungi A, Atwine R, et al. Modified plasma-thrombin method of cell block preparation for fine-needle aspiration biopsies in resource-limited settings. Am J Clin Pathol 2018; 150: 137-45.
10. Gupta S, Gautam U, Susheilia S, Bansal B, Uppal R, Srinivasan R. Sodium alginate versus plasma thrombin cell blocks in diagnostic cytopathology: a comparative analysis. Acta Cytol 2022; 66: 72-8.
11. Shi Y, Chiaffarano J, Yee-Chang M, et al. Self-clotting method improves cell block preparation. Cancer Cytopathol 2018; 126: 190-9.
12. Jing X, Li QK, Bedrossian U, Michael CW. Morphologic and immunocytochemical performances of effusion cell blocks prepared using 3 different methods. Am J Clin Pathol 2013; 139: 177-82.
13. Sung S, Sireci AN, Remotti HE, et al. Plasma-thrombin cell blocks: Potential source of DNA contamination. Cancer Cytopathol 2019; 127: 771-7.
14. Balassanian R, Ng DL, van Zante A. Stop using expired plasma for cell blocks. Cancer Cytopathol 2019; 127: 737-8.
15. Lin Z, Huang L, Tang S, et al. Comparison of three specimen collection techniques in tissue coagulum clot-based cell block preparation of endobronchial ultrasound-guided transbronchial needle aspiration. Pathol Res Pract 2025; 265: 155730.
16. Schmitt FC, Bubendorf L, Canberk S, et al. The World Health Organization reporting system for lung cytopathology. Acta Cytol 2023; 67: 80-91.
17. Jeffus SK, Joiner AK, Siegel ER, et al. Rapid on-site evaluation of EBUS-TBNA specimens of lymph nodes: comparative analysis and recommendations for standardization. Cancer Cytopathol 2015; 123: 362-72.
18. Vuorisalo A, Huhtala H, Paavonen T, Kholova I. Insufficient endobronchial ultrasound-guided transbronchial needle aspiration specimens. When and why? The analysis of criteria and reasons behind the insufficient specimens. Diagn Cytopathol 2024; 52: 271-87.

JPTM

ORIGINAL ARTICLE

pISSN 2383-7837 · eISSN 2383-7845

Journal of Pathology and Translational Medicine 2025; 59: 444-452
https://doi.org/10.4132/jptm.2025.10.21

Diagnostic value of cytology in detecting human papillomavirus–independent cervical malignancies: a nation-wide study in Korea

Hye-Ra Jung[1], Junyoung Shin[2], Chong Woo Yoo[2], Eun Na Kim[3], Cheol Lee[3], Kyeongmin Kim[4], Ho-chang Lee[5], Yonghee Lee[6], Ji Hye Kim[7], Soo Jin Jung[8], Yumin Chung[9], Joo Yeon Kim[10], Hye Eun Park[11], Tae Hoen Kim[12], Wonae Lee[13], Min-Sun Cho[14], Ran Hong[15], Yoon Jung Choi[16], Younghee Choi[17], Young Sub Lee[18], Sang-Ryung Lee[19], Myunghee Kang[20], Young Jin Seo[21], Seung-Sook Lee[22], Yoon-Jung Hwang[23], Hyun-Jung Kim[24]

A list of affiliations appears at the end of the paper.

Graphical abstract

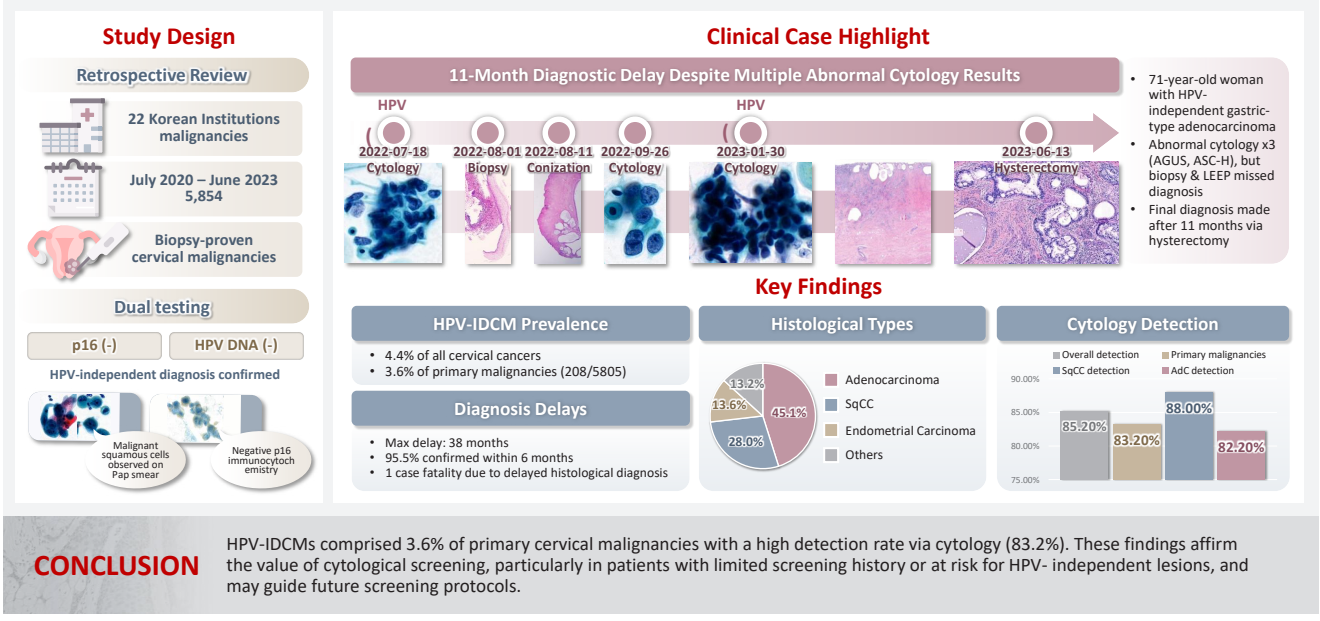

CONCLUSION HPV-IDCMs comprised 3.6% of primary cervical malignancies with a high detection rate via cytology (83.2%). These findings affirm the value of cytological screening, particularly in patients with limited screening history or at risk for HPV- independent lesions, and may guide future screening protocols.

Jung HR et al. Journal of Pathology and Translational Medicine

JPTM

ORIGINAL ARTICLE

pISSN 2383-7837 · eISSN 2383-7845

Journal of Pathology and Translational Medicine 2025; 59: 444-452
https://doi.org/10.4132/jptm.2025.10.21

Diagnostic value of cytology in detecting human papillomavirus–independent cervical malignancies: a nation-wide study in Korea

Hye-Ra Jung[1], Junyoung Shin[2], Chong Woo Yoo[2], Eun Na Kim[3], Cheol Lee[3], Kyeongmin Kim[4], Ho-chang Lee[5], Yonghee Lee[6], Ji Hye Kim[7], Soo Jin Jung[8], Yumin Chung[9], Joo Yeon Kim[10], Hye Eun Park[11], Tae Hoen Kim[12], Wonae Lee[13], Min-Sun Cho[14], Ran Hong[15], Yoon Jung Choi[16], Younghee Choi[17], Young Sub Lee[18], Sang-Ryung Lee[19], Myunghee Kang[20], Young Jin Seo[21], Seung-Sook Lee[22], Yoon-Jung Hwang[23], Hyun-Jung Kim[24]

A list of affiliations appears at the end of the paper.

Background: Human papillomavirus (HPV) independent cervical malignancies (HPV-IDCMs) have recently been classified by the World Health Organization (WHO) 5th edition. These malignancies have historically received limited attention due to their rarity and the potential for evasion of HPV-based screening. **Methods:** We retrospectively reviewed 5,854 biopsy-confirmed cervical malignancies from 22 institutions over 3 years (July 2020–June 2023). Histologic classification followed the WHO guidelines. HPV independence was confirmed by dual negativity for p16 and HPV; discordant cases (p16-positive/HPV-negative) underwent additional HPV testing using paraffin-embedded tissue. Cytological results were matched sequentially to histological confirmation. **Results:** The prevalence of HPV-IDCM was 4.4% (257/5,854) overall and was 3.6% (208/5,805 cases) among primary cervical malignancy. Patient age of HPV-IDCM was 29 to 89 years (median, 57.79). Its histologic subtypes included primary adenocarcinoma (n = 116), endometrial adenocarcinoma (n = 35), squamous cell carcinoma (n = 72), metastatic carcinoma (n = 14), carcinoma, not otherwise specified (n = 10), neuroendocrine carcinoma (n = 3), and others (n = 7). Among 155 cytology-histological matched cases, the overall and primary Pap test detection rates were 85.2% (132/155) and 83.2% (104/125), respectively. The interval between cytology and histologic confirmation extended up to 38 months. **Conclusions:** HPV-IDCMs comprised 3.6% of primary cervical malignancies with a high detection rate via cytology (83.2%). These findings affirm the value of cytological screening, particularly in patients with limited screening history or at risk for HPV-independent lesions, and may guide future screening protocols.

Keywords: Human papillomavirus viruses; Prevalence; Cytology; Uterine cervical neoplasms; Papanicolaou test

INTRODUCTION

The Papanicolaou (Pap) test has markedly contributed to the global reduction in the incidence and mortality rates of cervical cancer. In the United States, the number of new cervical cancer cases per 100,000 individuals declined from 14.81 in 1975 to 6.67 in 2018 [1-3]. In South Korea, the incidence rate decreased from 9.2 to 6.2 per 100,000, and the mortality rate fell from 3.4 to 2.5 per 100,000 population between 2001 and 2022 [4].

With increasing recognition of the role of persistent high-risk human papillomavirus (HPV) infection in cervical carcinogenesis, HPV testing has become a primary screening modality in many Western countries [5-7]. In 2014, the US Food and Drug Administration (FDA) approved the cobas HPV test (Roche Diagnostics, Basel, Switzerland) as a stand-alone screening method for women aged 25 and older [8-10].

Received: August 11, 2025 **Revised:** October 17, 2025 **Accepted:** October 20, 2025
Corresponding Author: Hyun-Jung Kim, MD
Department of Pathology, Inje University Sanggye Paik Hospital, 1342 Dongil-ro, Nowon-gu, Seoul 01757, Korea
Tel: +82-2-950-1261, Fax: +82-2-951-6964, E-mail: hjkim@paik.ac.kr

This shift has been accelerated by the widespread adoption of HPV vaccination. The efficacy of the HPV vaccines in preventing high-grade cervical lesions has been well established. A nationwide Swedish study (2006–2017) reported incidence rates of 0.51, 0.37, and 0.1 per 100,000 for unvaccinated individuals, those vaccinated between 17-30, and those vaccinated before age 17, respectively [11]. Since 2012, the Korean national immunization program has included HPV vaccination for girls under 13 years of age [12].

The 5th edition of the World Health Organization (WHO) classification of Female Genital Tumors formally recognizes HPV-independent cervical malignancies (HPV-IDCMs) and their precursor lesions in both squamous and glandular categories [13]. The 5 recognized glandular subtypes include gastric, clear cell, mesonephric, endometrioid, and not otherwise specified (NOS). According to the WHO classification, HPV-independent tumors account for approximately 5%–7% of squamous cell carcinomas (SqCCs) and up to 20% of adenocarcinomas. Emerging HPV-independent neoplasms include intraepithelial neoplasia, SqCC, and precursor lesions associated with uterine prolapse and lichen planus (LP) [14-17].

In Japan, the overall prevalence of gynecologic tumors has changed, with rising rates of endometrial and ovarian carcinomas and declining cervical carcinoma rates [18]. Similarly, Taiwan has reported a proportional increase in adenocarcinomas relative to SqCC [19]. In Korea, the most recent data (2024) show a histological distribution of 60.9% SqCC and 23.1% adenocarcinoma [20].

The primary aim of this study was to assess the prevalence rate of HPV-IDCM and to evaluate the diagnostic utility of the Pap test during this period of dynamic screening practices and histologic trends.

MATERIALS AND METHODS

Data collection

A nationwide study of biopsy–proven cervical malignancies was conducted at 22 institutions across South Korea over 3 years (July 2020 to June 2023). All contributors were actively practicing gynecologic cytopathologists. A total of 5,854 cases were collected along with clinical data including patient age, specimen type, and survival status. Histological subtypes were classified according to the WHO classification of female genital tumors, 5th edition. HPV independence was determined by negativity for both $p16^{INK4a}$ (*CDKNA2A*) immunohistochemistry and HPV testing. For p16-positive and HPV-negative cases, additional HPV real-time PCR testing (Allplex HPV Detection, Seegene, Seoul, Korea) was performed using paraffin blocks (silica-membrane technology (QIAamp), Qiagen, Hilden, Germany). Highly sensitive molecular techniques for detecting HPV DNA or mRNA were not available for this study.

Cytological-histological correlation

Cytological findings were reviewed sequentially, based on temporal relationship to the histological confirmation. Among multiple cytology reports, the report most relevant to the histologic outcome was selected. Cytological diagnoses were classified according to the Bethesda System, 3rd edition. Detection rates included diagnoses of atypical squamous cells, undetermined significance (ASC-US), and atypical glandular cells, undetermined significance (AG-US) or higher.

Interval to final diagnosis

The interval between a significant cytological diagnosis and the initial histological diagnosis was assessed. Cases with an interval longer than 6 months were classified as delayed diagnoses.

RESULTS

Sample characteristics

Overall, HPV-IDCM account for 4.4% (257/5,854) of all cases and 3.6% (208/5,805) of primary cervical malignancies (Fig. 1). Patient age of HPV-IDCM ranged from 29 to 89 years, with a median of 57.79 years. Of the 257 cases, the most common specimen type was punch biopsy (n = 158), followed by hysterectomy (n = 74), loop electrosurgical excision procedure conization (n = 18), and other excisions (n = 7). Among the 167 patients with available follow-up data, 137 were alive, 23 had died (due to disease or other causes), and seven were lost to follow-up (Table 1).

Histologic types of HPV-IDCM

Histologic subtypes were as follows; primary adenocarcinoma (n = 116), which comprised gastric (n = 41), NOS (n = 37), clear cell (n = 17), mesonephric (n = 7), adenocarcinoma in situ (AIS) (n = 14); endometrial adenocarcinoma (n = 35); SqCC (n = 72); metastatic carcinoma (n = 14); carcinoma, NOS (n = 10); neuroendocrine carcinoma (n = 3); and other histological malignancies (n = 7) (Table 2).

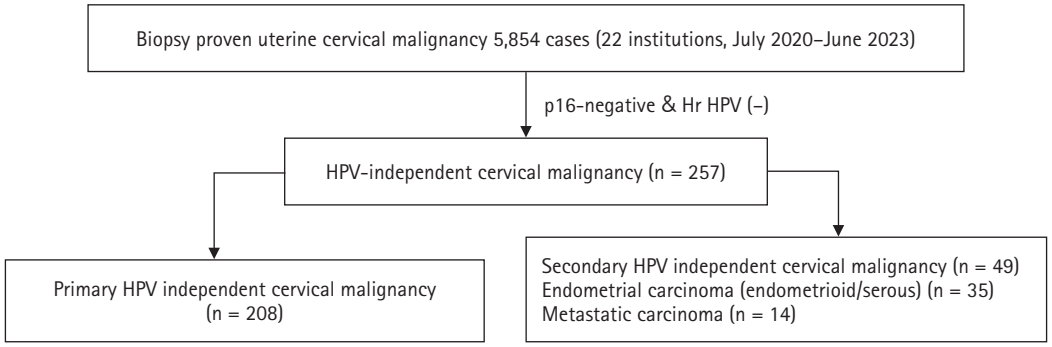

Fig. 1. Flow chart of study inclusion. Hr, high risk; HPV, human papillomavirus.

Cyto-pathologic correlation

Among 155 cytology-histological matched cases, the overall/primary Pap test detection rate were 85.2% (132/155) and 83.2% (104/125) (Table 3). A case of 86-year-old women was cytologically evident SqCC. However, two times of real-time HPV-PCR test failed to demonstrate the HPV dependency. The subsequent biopsy showed invasive squamous carcinoma (Fig. 2). Despite the fact that no HPV relationship has been supported, the cytological abnormality has been detected in 29 out of 33 SqCCs (88%). In adenocarcinoma group, the cytological detection rate was 82.2% (65/79 cases).

Interval of final histological diagnosis

Of the matched cases, 148 (95.5%) received histological confirmation within 6 months, while seven cases experienced diagnostic delays from 7 to 38 months (Table 4). In our cohort, one patient with gastric-type adenocarcinoma had three abnormal cytology reports (AG-US, favor neoplastic and 2 times of ASC-H [atypical squamous cells, cannot exclude high-grade intraepithelial lesion]) and two negative HPV tests before a definitive diagnosis was made via hysterectomy 11 months later. (Fig. 3)

Table 1. Clinicopathological characteristics of 257 patients with HPV-independent cervical malignancies

	Value
Age (yr), median (range)	57.79 (29–89)
Type of specimen (n = 257)	
Punch biopsy	158
Excisional biopsy	7
LEEP conization	18
Hysterectomy	74
Clinical follow-up (n = 167)	
Alive	137
Died of disease or other causes	23
Lost to follow-up	7

HPV, human papillomavirus; LEEP, loop electrosurgical excision procedure.

DISCUSSION

In recent years, global cervical cancer screening has increasingly shifted toward primary HPV testing [1-3]. In 2014, the US FDA approved the cobas HPV test (Roche Diagnostics) for stand-alone cervical cancer screening in women aged ≥25 years [8-10].

Despite this, a 2017 survey by the College of American Pathologists reported that nearly 60% of responding laboratories did not offer stand-alone primary HPV testing, concerns about the efficacy of cytology co-testing strategies [19,21,22].

Our study aimed to assess the role of cytology in detecting HPV-independent precursors and malignancies. Recent literature highlights the presence of HPV-negative SqCC and precursor lesions. These cases showed frequent p16 negativity, nuclear p53 overexpression, and diverse genetic alterations (including *PIK3CA*, *STK11*, *TP53*, *SMARCB2*, and *GNAS*) along with the consistent presence of the *Q472H* germline polymorphism in the *KDR* gene and chromosome 3q gain [14]. HPV-negative precursors showed TP53-mutated differentiated cervical intraepithelial neoplasia and p53 wild-type verruciform intraepithelial neoplasia based on next-generation sequencing data [15].

LP-associated HPV–independent SqCC of the vulva and vagina has also been reported [16], accounting for approximately 70% of vulvar SqCCs. The largest study to date has reported 38

https://doi.org/10.4132/jptm.2025.10.21

cases of LP-associated SqCC and vulvar intraepithelial neoplasia.

Additionally, a recent study described HPV-independent/p53-abnormal keratinizing SqCC associated with uterine prolapse. Cytological features of SqCC include prominent keratinizing, clear glycogen-rich cytoplasm, and some intracytoplasmic mucin [17].

According to the WHO, HPV-independent invasive cervical SqCC accounts for approximately 5%–7% of all cases [11]. At least 90.9% of HPV-negative lesions were flagged by abnormal cytology [23]. Although large-scale cohort studies are lacking, HPV-negative squamous lesions appear prone to delayed histologic confirmation, particularly in case with indeterminate abnormal cytological findings (ASC-US, ASC-H, low-grade squamous intraepithelial lesion). In our series, one patient with high-grade intraepithelial lesion cytology experienced a 23-month delay before histologic diagnosis and subsequently died from disease, underscoring the importance of timely cytological evaluation.

HPV-independent adenocarcinomas represent a minority of endocervical adenocarcinomas. According to the WHO 5th edition, HPV-independent adenocarcinoma of the uterine cervix include AIS, gastric type, clear cell type, mesonephric type, and NOS [11]. In our primary cohort, gastric-type adenocarcinoma was the most common subtype (41/116 cases). These tumors were associated with aggressive behavior including destructive invasion, extrauterine spread, and advanced-stage diagnosis [24,25].

Cytologically, gastric-type adenocarcinomas may appear morphologically subtle, mimicking benign cervical glands with a low nuclear to cytoplasmic ratio [26]. Gastric-type adenocarcinoma accounts for nearly 20% of all cervical adenocarcinomas in Japan. A low detection rate was observed via cytology

Table 2. Histologic classification of 257 HPV-independent cervical malignancies

	No.
Primary	208
Squamous cell carcinoma	72
Adenocarcinoma	116
Gastric type	41
NOS	37
Clear cell	17
Mesonephric	7
Adenocarcinoma in situ	14
Neuroendocrine carcinoma	3
Carcinoma, NOS	10
Others	7
Secondary	49
Endometrial carcinoma	35
Metastatic carcinoma	14

HPV, human papillomavirus; NOS, not otherwise specified.

Table 3. Cytologic-histologic correlation in matched 155 cases

	NIL	ASC-US	ASC-H	LSIL	HSIL	SqCC	AG-US	AGUS-N	AIS	AdC	Others
Primary (n = 125)	21	14	7	7	14	4	17	7	4	23	7
SqCC (n = 33)	4	6	3	7	9	2	0	0	0	0	2
AdC (n = 79)											
NOS (n = 31)	6	5	2	0	1	1	6	1	3	5	1
Gastric (n = 26)	4	1	0	0	1	0	6	4	0	10	0
AIS (n = 10)	2	0	1	0	1	1	1	2	0	2	0
Clear (n = 9)	1	0	0	0	0	0	3	0	1	4	0
Meso (n = 3)	1	0	1	0	0	0	1	0	0	0	0
Ca, NOS (n = 7)	1	2	0	0	2	0	0	0	0	1	1
SCC/NE (n = 1)	0	0	0	0	0	0	0	0	0	0	1
Others (n = 5)	2	0	0	0	0	0	0	0	0	1	2
EmC (n = 23)	1	0	1	1	2	1	7	1	4	5	0
Mets (n = 7)	1	1	1	0	0	0	0	1	0	1	2

NIL, negative for intraepithelial lesion or malignancy; ASC-US, atypical squamous cells of undetermined significance; ASC-H, atypical squamous cells cannot excluded HSIL; LSIL, low-grade squamous intraepithelial lesion; HSIL, high-grade intraepithelial lesion; SqCC, squamous cell carcinoma; AG-US, atypical glandular cells of undetermined significance; AGUS-N, atypical glandular cells of undetermined significance, favor neoplastic; AIS, adenocarcinoma in situ; AdC, adenocarcinoma; Others, Other malignant neoplasms; NOS, not otherwise specified; Ca, NOS, carcinoma, not otherwise specified; SCC/NE, small cell (neuroendocrine) carcinoma; EmC, endometrial carcinoma; Mets, metastatic malignancy.

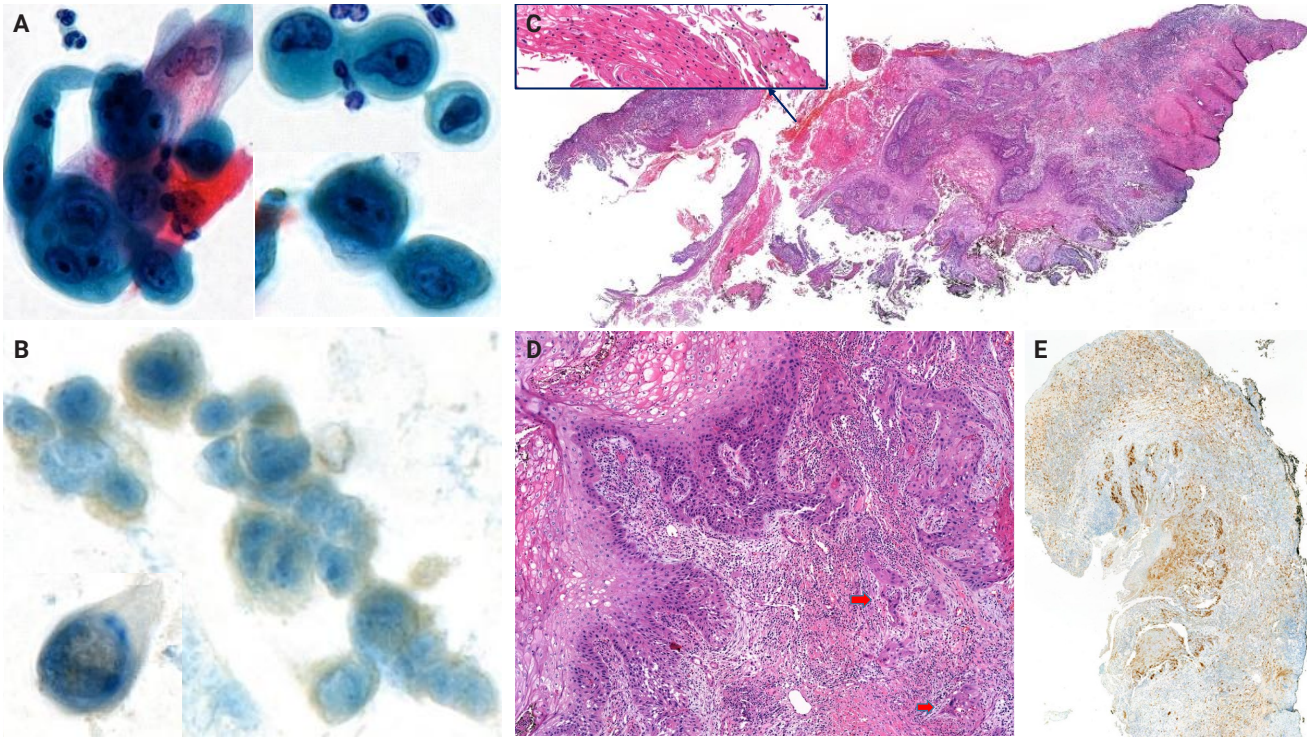

Fig. 2. A representative case of human papillomavirus–independent squamous cell carcinoma with cytohistologic and p16 immunohistochemical findings. (A) The cytological findings showed many atypical squamous cells with high nuclear to cytoplasmic ratio, hyperchromatic nuclei, irregular nuclear contour, prominent 2–3 nucleoli, and dense hyperkeratotic cytoplasms (Pap test). (B) p16 immunocytochemical staining failed to demonstrate nuclear-cytoplasmic expression. (C) The scanning view of punch biopsied tissue revealed infiltrating nests with thick keratin pearl (inset). (D) Some irregular atypical squamous nests invaded to stroma (red arrows). (E) p16 immunohistochemistry failed to demonstrate a block positivity.

Table 4. Delayed histological diagnosis in HPV-independent cervical malignancies (n = 7)

Interval (mo)	Histological diagnosis	Cytological diagnosis	Age (yr)	FU (mo)	Outcome
8	Endometrial AdC	AG-US	66	2	Lost
9	Squamous CIS	LSIL	63	2	Survived
11	AdC-HPVIPT, gastric type	AG-US	71	2	Lost
11	Invasive AdC	SqCC	77	35	Survived
18	AdC-HPVIPT, gastric type	NIL	43	11	Survived
23	SqCC	HSIL	79	7	DOD
38	Serous carcinoma	AdC	66	17	Survived

HPV, human papillomavirus; FU, follow-up; AdC, adenocarcinoma; AG-US, atypical glandular cells of undetermined significance; CIS, carcinoma in situ; LSIL, low-grade squamous intraepithelial lesion; HPVIPT, human papillomavirus independent; SqCC, squamous cell carcinoma; NIL, negative for intraepithelial lesion or malignancy; HSIL, high-grade intraepithelial lesion; DOD, patient died as a result of the malignancy.

due to the high location of lesion in endocervical canal and bland morphology [27].

Endometrial carcinomas comprise the majority of HPV-negative lesions in our matched cohort. Karaaslan et al. [23] reported that 78.8% of HPV-negative cervical malignancies were endometrial in origin. In our cohort, 22 of 23 endometrial carcinomas were detected cytologically, although the precise diagnostic role of cytology remains unclear due to high stage/grade and concurrent endometrial sampling.

Seven cases in our study experienced histologic diagnostic

https://doi.org/10.4132/jptm.2025.10.21

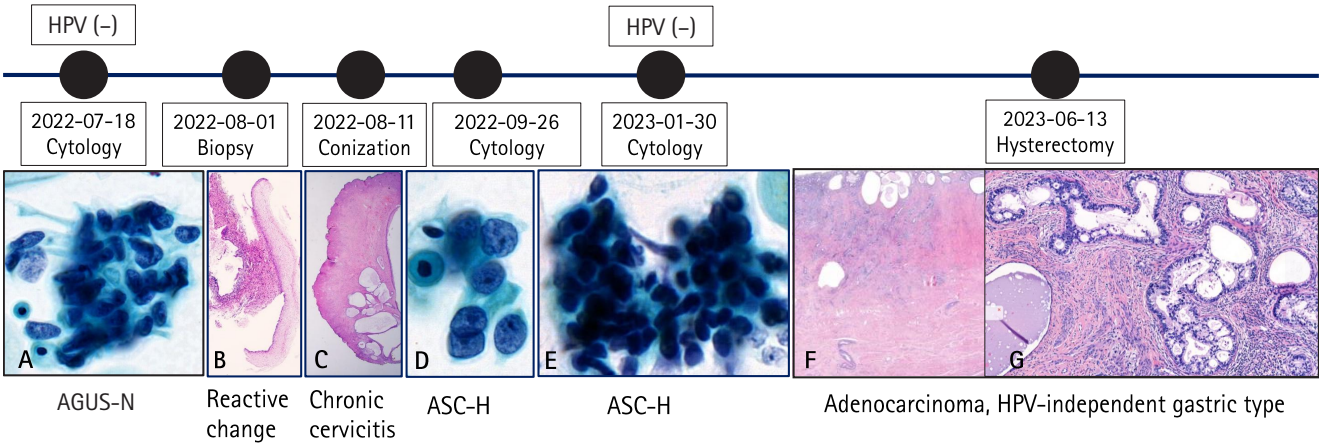

Fig. 3. A chronological sequence of delayed (11 months) diagnosis in a 71-year-old woman with human papillomavirus (HPV) independent cervical malignancies. (A) Three-dimensional cluster of atypical hyperchromatic nuclei are seen, suggestive of atypical glandular cells, undetermined significance favor neoplastic (AGUS-N) (2022-07-18). (B) No definite abnormality is identified in punch biopsied tissue (2022-08-01). (C) No glandular/squamous epithelial dysplasia was identified in loop electrosurgical excision procedure conization (2022-08-11). (D) A cluster of atypical epithelial cells with abundant dense cytoplasm are seen, atypical squamous cells cannot excluded high-grade intraepithelial lesion (ASC-H) (2022-09-26). (E) Overlapping clusters of atypical epithelial cells with hyperchromatic nuclei and dense cytoplasm were seen, ASC-H (2023-01-30). (F, G) The hysterectomy specimen showed a deeply invading atypical glands through the full thickness of the uterine cervical wall. The tumor is composed of gastric type–glands (2023-06-13).

delays exceeding 6 months, including two cases each of gastric-type adenocarcinomas, squamous (or in situ) carcinomas, and endometrial or serous carcinoma, as well as 1 adenocarcinoma, NOS. This study is limited for a statistically significant difference between HPV dependent vs. independent tumor groups for a diagnostic delay due to no control data.

HPV-negative lesions represent a blind spot in primary HPV-based screening systems, because these cases may escape detection. The impact of high-risk–HPV DNA–based screening on HPV-independent malignancies remains questionable [28]. Missed cases were overlooked due to their small subset. In our cohort, 3.6% of primary cervical cancers were HPV negative proportion that may increase with the rising incidence of adenocarcinoma and the impact of HPV vaccination. In Japan, HPV-negative CIN2+ or adenocarcinoma has not been considered a major barrier to the implementation of HPV-based screening; however, a new nationwide management algorithm has recently been proposed [29].

This study has a limitation that HPV-IDCM cannot exclude an undetectable subtype, which are not included in HPV genotypes as well as no supportive RNA works. The incidence of HPV typing-negative cervical cancer has been reported as 5%–30% with different HPV detection methods [30]. The cytology-histologic matching case are too small volume for an overall detection rate. The clinical outcome was also limited for evidence of poorer outcomes than HPV-dependent group due to no control group.

In summary, HPV-IDCM accounted for 3.6% of primary cervical malignancies, with a cytology (Pap test) detection rate of 83.2%. These findings underscore the ongoing importance of cytological evaluation, particularly in patients with limited screening history or at risk for HPV independent lesions. This evidence may contribute to future refinements in cervical cancer screening strategies.

Author Affiliations

[1]Department of Pathology, Keimyung University School of Medicine, Daegu, Korea; [2]Department of Pathology, National Cancer Center, Goyang, Korea; [3]Department of Pathology, Seoul National University Hospital, Seoul National University College of Medicine, Seoul, Korea; [4]Department of Pathology, Soonchunhyang University Seoul Hospital, Seoul, Korea; [5]Department of Pathology, Chungbuk University Hospital, Chungbuk National University College of Medicine, Cheongju, Korea; [6]Department of Pathology, Ajou University School of Medicine, Suwon, Korea; [7]Department of Pathology, Ulsan University, Ulsan, Korea; [8]Department of Pathology, Inje University Busan Paik Hospital, Busan, Korea; [9]Department of Pathology,

Kangbuk Samsung Hospital, Sungkyunkwan University School of Medicine, Seoul, Korea; [10]Department of Pathology, Inje University Haeundae Paik Hospital, Busan, Korea; [11]Department of Pathology, Seoul Metropolitan Government Boramae Hospital, Seoul National University, Seoul, Korea; [12]Department of Pathology, Bundang Medical Center, CHA University, Seongnam, Korea; [13]Department of Pathology, Dankook University Hospital, Cheonan, Korea; [14]Department of Pathology, Ewha Women's University College of Medicine, Seoul, Korea; [15]Department of Pathology, Chosun University Hospital, Gwangju, Korea; [16]Department of Pathology, Yongin Severance Hospital, Yonsei University College of Medicine, Yongin, Korea; [17]Department of Pathology, Hallym University Dongtan Sacred Heart Hospital, Hwaseong, Korea; [18]Department of Pathology, Eunpyeong St. Mary's Hospital, College of Medicine, The Catholic University of Korea, Seoul, Korea; [19]Department of Pathology, CHA Gangnam Medical Center, CHA University, Seoul, Korea; [20]Department of Pathology, Gachon University Gil Medical Center, Incheon, Korea; [21]Department of Pathology, National Forensic Service Daegu Institute, Daegu, Korea; [22]Department of Pathology, Korea Cancer Center Hospital, Seoul, Korea; [23]Department of Pathology, Seoul National University Bundang Hospital, Seongnam, Korea; [24]Department of Pathology, Inje University Sanggye Paik Hospital, Seoul, Korea

Ethics Statement

All procedures performed in the current study were approved by the institutional review boards (IRB) of all participating institutions following the Declaration of Helsinki and its later amendments. Waiver of the informed consent can only be granted by the appropriate IRB. Formal written informed consent was not required with a waiver by the appropriate IRB or national research ethics committee. The approvals were granted by the following ethics committees: Sanggye Paik Hospital (IRB approval number: SGPAIK2024-04-011; date: April 30, 2024), Soonchunhyang University Seoul Hospital (IRB approval number: 2024-04-012-002), Chungbuk National University (IRB approval number: 2024-05-003), Busan Paik Hospital (BPIRB approval number: 2024-04-030), Kangbuk Samsung Hospital (IRB approval number: KBSMC 2024-05-028-001), Chosun University Hospital (IRB approval number: CHOSUN2024-04-012), Eunpyeong St Mary's Hospital (IRB approval number: PC24RIDI0058), and Seoul National University Bundang Hospital (IRB approval number: B-2505-973-103).

Availability of Data and Material

The datasets generated or analyzed during the study are available from the corresponding author on reasonable request.

Code Availability

Not applicable.

ORCID

Hye-Ra Jung https://orcid.org/0000-0002-1477-6606
Junyoung Shin https://orcid.org/0000-0002-4833-9738
Chong Woo Yoo https://orcid.org/0000-0002-5221-4516
Eun Na Kim https://orcid.org/0000-0003-2992-7881
Cheol Lee https://orcid.org/0000-0001-5098-8529
Kyeongmin Kim https://orcid.org/0000-0002-0454-4393
Ho-chang Lee https://orcid.org/0000-0003-4687-8348
Ji Hye Kim https://orcid.org/0000-0001-7160-8601
Soo Jin Jung https://orcid.org/0000-0002-9139-701X
Yumin Chung https://orcid.org/0000-0002-4695-1114
Joo Yeon Kim https://orcid.org/0000-0002-4259-667X
Hye Eun Park https://orcid.org/0000-0003-1048-2827
Tae Hoen Kim https://orcid.org/0000-0002-2241-6694
Wonae Lee https://orcid.org/0000-0001-9266-6640
Min-Sun Cho https://orcid.org/0000-0001-8772-9686
Ran Hong https://orcid.org/0000-0001-7011-5215
Yoon Jung Choi https://orcid.org/0000-0002-5701-8864
Younghee Choi https://orcid.org/0000-0002-3882-4000
Young Sub Lee https://orcid.org/0000-0003-0841-1122
Sang-Ryung Lee https://orcid.org/0009-0000-6223-2542
Myunghee Kang https://orcid.org/0000-0003-4083-888X
Young Jin Seo https://orcid.org/0000-0002-9048-0903
Seung-Sook Lee https://orcid.org/0000-0001-6714-5851
Yoon-Jung Hwang https://orcid.org/0000-0002-8519-7521
Hyun-Jung Kim https://orcid.org/0000-0002-6617-4578

Author Contributions

Conceptualization: HJK. Data curation: HJK. Formal analysis: HJK, HRJ, JYK, HEP, YJS, SSL. Investigation: HJK, HRJ, JYK, HEP, YJS, SSL. Funding acquisition: HJK, HRJ, JYK, HEP, YJS, SSL. Methodology: HRJ, JS, CWY, ENK, CL, KK, HL, YL, JK, SJJ, JYK, HEP, THK, WL, MSC, RH, YJC, YSL, YC, SRL, MK, YJS, YJH, HJK. Project administration: HJK, HRJ, JYK, HEP, YJS, SSL. Supervision: YJC, SSL. Validation: HJK, HRJ, JYK, HEP, YJS, SSL. Writing—original draft: HJK. Writing—review & editing: HJK, YJC, SSL. Approval of final manuscript: all authors.

https://doi.org/10.4132/jptm.2025.10.21

Conflicts of Interest
The authors declare that they have no potential conflicts of interest.

Funding Statement
This research was supported in part by The Korean Society for Cytopathology (Grant No. 23-01), Republic of Korea.

Acknowledgments
The authors gratefully acknowledge the cooperation and scholarly discussions provided by members of the Korean Society of Cytopathologists during the course of this study.

REFERENCES

1. Yang DX, Soulos PR, Davis B, Gross CP, Yu JB. Impact of widespread cervical cancer screening: number of cancers prevented and changes in race-specific incidence. Am J Clin Oncol 2018; 41: 289-94.
2. Sung H, Ferlay J, Siegel RL, et al. Global cancer statistics 2020: GLOBOCAN estimates of incidence and mortality worldwide for 36 cancers in 185 countries. CA Cancer J Clin 2021; 71: 209-49.
3. National Cancer Institute. Surveillance, Epidemiology, and End Results Program. Cancer stat facts: cervical cancer [Internet]. Bethesda: National Cancer Institute, 2025 [cited 2022 Aug 21]. Available from: http://www.seer.cancer.gov/statfacts/html/cervix.html.
4. Current status of cancer incidence and mortality [Internet]. Daejeon: Ministry of Data, 2025 [cited 2022 Aug 21]. Available from: https://www.index.go.kr/unity/potal/main/EachDtlPageDetail.do?idx_cd=2770.
5. Moscicki AB, Schiffman M, Burchell A, et al. Updating the natural history of human papillomavirus and anogenital cancers. Vaccine 2012; 30 Suppl 5: F24-33.
6. Saslow D, Solomon D, Lawson HW, et al. American Cancer Society, American Society for Colposcopy and Cervical Pathology, and American Society for Clinical Pathology screening guidelines for the prevention and early detection of cervical cancer. J Low Genit Tract Dis 2012; 16: 175-204.
7. Perkins RB, Guido RS, Castle PE, et al. Erratum: 2019 ASCCP risk-based management consensus guidelines for abnormal cervical cancer screening tests and cancer precursors. J Low Genit Tract Dis 2021; 25: 330-1.
8. Wright TC Jr, Massad LS, Dunton CJ, et al. 2006 Consensus guidelines for the management of women with abnormal cervical screening tests. J Low Genit Tract Dis 2007; 11: 201-22.
9. Nayar R, Goulart RA, Tiscornia-Wasserman PG, Davey DD. Primary human papillomavirus screening for cervical cancer in the United States-US Food and Drug Administration approval, clinical trials, and where we are today. Cancer Cytopathol 2014; 122: 720-9.
10. Huh WK, Ault KA, Chelmow D, et al. Use of primary high-risk human papillomavirus testing for cervical cancer screening: interim clinical guidance. Gynecol Oncol 2015; 136: 178-82.
11. Lei J, Ploner A, Elfstrom KM, et al. HPV vaccination and the risk of invasive cervical cancer. N Engl J Med 2020; 383: 1340-8.
12. Min KJ, Kwon SH, Kim S, et al. Preventive vaccination against cervical cancer: Korean Society of Gynecologic Oncology Guideline. J Gynecol Oncol 2016; 27: e30.
13. WHO Classification of Tumours Editorial Board. WHO classification of tumours: female genital tumours. 5th ed. Lyon: International Agency for Research on Cancer, 2020.
14. Regauer S, Reich O. The histologic and molecular spectrum of highly differentiated HPV-independent cervical intraepithelial neoplasia. Am J Surg Pathol 2023; 47: 942-9.
15. Regauer S, Reich O, Kashofer K. HPV-negative squamous cell carcinomas of the cervix with special focus on intraepithelial precursor lesions. Am J Surg Pathol 2022; 46: 147-58.
16. Day T, Otton G, Jaaback K, Weigner J, Scurry J. Is vulvovaginal lichen planus associated with squamous cell carcinoma? J Low Genit Tract Dis 2018; 22: 159-65.
17. Horn LC, Brambs CE, Aktas B, et al. Human papilloma virus-independent/p53 abnormal keratinizing squamous cell carcinoma of the uterine cervix associated with uterine prolapse. Int J Gynecol Pathol 2025; 44: 2-14.
18. Yamagami W, Nagase S, Takahashi F, et al. Clinical statistics of gynecologic cancers in Japan. J Gynecol Oncol 2017; 28: e32.
19. Chiang YC, Chen YY, Hsieh SF, et al. Screening frequency and histologic type influence the efficacy of cervical cancer screening: a nationwide cohort study. Taiwan J Obstet Gynecol 2017; 56: 442-8.
20. Ministry of Health and Welfare, National Cancer Registration and Analysis Division. National Cancer Registration Statistics (for the Year 2022) [Internet]. Seoul: Ministry of Health and Welfare, National Cancer Registration and Analysis Division, 2024 [cited 2025 Nov 4]. Available from: https://cancer.go.kr/lay1/S1T639C640/contents.do.
21. Davey DD, Souers RJ, Goodrich K, Mody DR, Tabbara SO, Booth CN. Bethesda 2014 Implementation and human papillomavirus primary screening: practices of laboratories participating in the

College of American Pathologists PAP Education Program. Arch Pathol Lab Med 2019; 143: 1196-202.
22. Kaufman HW, Alagia DP, Chen Z, Onisko A, Austin RM. Contributions of liquid-based (Papanicolaou) cytology and human papillomavirus testing in cotesting for detection of cervical cancer and precancer in the United States. Am J Clin Pathol 2020; 154: 510-6.
23. Karaaslan S, Dilcher TL, Abdelsayed M, Goyal A. Significant outcomes associated with high-risk human papillomavirus negative Papanicolaou tests. J Am Soc Cytopathol 2023; 12: 189-96.
24. Mikami Y. Gastric-type mucinous carcinoma of the cervix and its precursors: historical overview. Histopathology 2020; 76: 102-11.
25. Schwock J, Starova B, Khan ZF, et al. Cytomorphologic features of gastric-type endocervical adenocarcinoma in liquid-based preparations. Acta Cytol 2021; 65: 56-66.
26. Yeo MK, Bae GE, Kim DH, Seong IO, Suh KS. Cytopathologic features of human papillomavirus-independent, gastric-type endocervical adenocarcinoma. J Pathol Transl Med 2022; 56: 260-9.
27. Nishio H, Matsuda R, Iwata T, Yamagami W. Gastric-type adenocarcinoma of the uterine cervix: clinical features and future directions. Jpn J Clin Oncol 2024; 54: 516-20.
28. Vassilakos P, Tran PL, Sahli R, Low N, Petignat P. HPV-negative CIN3 and cervical cancer in Switzerland: any evidence of impact on screening policies? Swiss Med Wkly 2017; 147: w14559.
29. Hideshima M, Hashiguchi M, Honda A, et al. Are HPV-negative lesions concerned for the introduction of primary HPV testing for cervical cancer screening in Japan? J Obstet Gynaecol Res 2023; 49: 2860-7.
30. Xu Y, Sun Y, Chang H, et al. The expression of HPV E6/E7 mRNA in situ hybridization in HPV typing-negative cervical cancer. Int J Gynecol Pathol 2023; 42: 11-20.

https://doi.org/10.4132/jptm.2025.10.21

JPTM

CASE STUDY

pISSN 2383-7837 · eISSN 2383-7845

Journal of Pathology and Translational Medicine 2025; 59: 453-459
https://doi.org/10.4132/jptm.2025.08.04

Clinicopathological characteristics of digestive system angioleiomyomas: case report and literature review

Georgios Kalliopitsas[1], Christos Topalidis[1], Constantine Halkias[2], Theodora Gkeka[2], Konstantinos Sapalidis[2], Triantafyllia Koletsa[1]

[1]Department of Pathology, School of Medicine, Aristotle University of Thessaloniki, Thessaloniki, Greece
[2]3rd Surgical Department, Aristotle University of Thessaloniki, AHEPA University Hospital Thessaloniki, Thessaloniki, Greece

Angioleiomyomas are benign soft tissue tumors originating from the vascular wall. Although angioleiomyomas mainly occur in extremities, followed by head, neck, and trunk, they can also be found throughout the digestive system and especially in the oral cavity. Herein, the fourth case of a rectal angioleiomyoma in the English literature is reported and the clinicopathological features of digestive system angioleiomyomas were investigated. In contrast to their soft tissue counterparts, digestive system angioleiomyomas mainly affect males at a slightly younger age. Angioleiomyomas are mainly asymptomatic and only rarely elicit pain. Clinicians consider angioleiomyomas infrequently and instead include more common soft tissue or epithelial tumors in their differential diagnosis. To prevent angiomyolipoma misdiagnosis, pathologists should exercise caution when examining an angioleiomyoma composed of adipose tissue, smooth muscle, and blood vessels. Pathologists, radiologists, and surgeons should be aware that angioleiomyomas can occur in the digestive system.

Keywords: Perivascular tumor; Angiomyoma; Soft tissue tumor; Intestinal tumor; Vascular leiomyoma

INTRODUCTION

Angioleiomyomas are benign neoplasms arising from the smooth muscle layer (tunica media) of the blood vessel wall, accounting for 5% of all benign soft tissue neoplasms. Angioleiomyoma typically present as a slow-growing and painful nodule in the extremities of females in their fourth to sixth decade of life. The trunk, head, and neck region can be affected, although less frequently [1,2]. Three histological forms of angioleiomyomas have been described: solid, cavernous, and the less frequent venous form that typically affects the head and neck area, including the oral cavity [2,3].

Although uncommon, angioleiomyomas in the digestive system have been documented in an increasing number of reports. Most of the reported cases involve the oral cavity; however, any part of the alimentary tract can be affected. Herein, a rare case of an incidentally found rectal angioleiomyoma is presented and a comprehensive review of the English literature regarding angioleiomyomas in the gastrointestinal tract with respect to their epidemiological, clinical, and histopathological features provided.

CASE REPORT

A 68-year-old male was admitted to the Surgical Department for a scheduled repair of an incisional hernia resulting from a surgery for a perforated ulcer of the upper gastrointestinal tract performed two decades ago. The patient was asymptomatic, with no complaints of pain, mass effect, or gastrointestinal bleeding. Both physical examination and routine laboratory tests were unremarkable. During the preoperative computed tomography (CT) scan, a round-shaped lesion 16 mm in size was

Received: April 26, 2025 **Revised:** July 3, 2025 **Accepted:** August 4, 2025
Corresponding Author: Christos Topalidis
Department of Pathology, School of Medicine, Aristotle University of Thessaloniki, University Campus, 54124 Thessaloniki, Greece
Tel: +30-2310999224, E-mail: topalidi@auth.gr

revealed in the rectal wall, 7 cm from the anal verge (Fig. 1A). Further investigation with magnetic resonance imaging (MRI) showed a high signal intensity, lobular/polypoid lesion measuring 21 × 18 mm on the posterolateral rectal wall, projecting into the lumen, with equivocal invasion of the muscular layer (Fig. 1B). The endoscopy showed an intraluminal protrusion covered by an unremarkable mucosa. Clinicians suspected a gastrointestinal stromal tumor (GIST). An endoscopic submucosal dissection, sparing the muscularis propria, was performed and the specimen was sent to pathology.

The macroscopic examination revealed a nodular lesion measuring 20 × 13 mm covered by an unremarkable mucosa (Fig. 1C), occupying the submucosal and muscular layers (Fig. 1D). Hematoxylin and eosin–stained sections showed spindle-shaped neoplastic cells, arranged in bundles, proliferating from vascular walls (Fig. 1E, F). Neoplastic cells showed minimal atypia without any mitotic activity. A minor component of mature adipose tissue was observed intermixed with spindle-shaped cells. Immunohistochemical study showed neoplastic cells positive for smooth muscle actin (Fig. 2A), caldesmon (Fig. 2B), and desmin antigens. Immunostains for CD34 (Fig. 2C), HMB-45 (Fig. 2D), MelanA (Fig. 2E), CD117, DOG-1 (Fig. 2F), and S-100 were negative. Histologic and immunohistochemical features were consistent with angioleiomyoma of the rectum, venous type.

DISCUSSION

Angioleiomyomas of the digestive system are extremely rare, except for those located in the oral cavity. The first case of an angioleiomyoma of the digestive system in English literature was documented in 1969 [4] and included a 65-year-old female with a long-standing "blister" 5 mm in size in the hard palate. At that time, angioleiomyomas were referred to as vascular leiomyomas or angiomyomas because they were considered part of the leiomyoma spectrum. Regarding the gastrointestinal tract, the first documented case of angioleiomyoma was reported by Gadaleanu and Popescu in 1988 and involved the duodenojejunal flexure of a 31-year-old female patient [5]. In 1969, Enziger et al. classified leiomyomas into three major groups based on histological features: vascular, solid, and epithelioid [6]. In 1973, Morimoto et al. subclassified vascular leiomyomas into

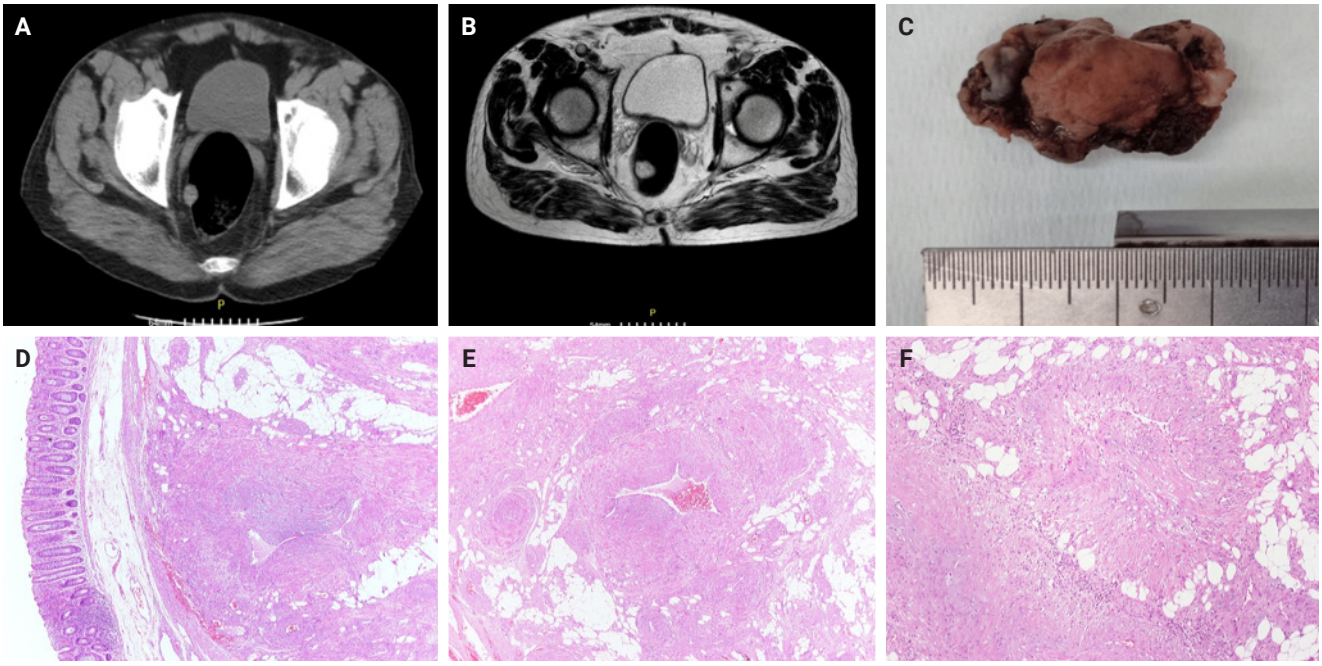

Fig. 1. Preoperative computed tomography scan (axial plane) showing an incidentally discovered round-shape lesion in the rectal wall (A) characterized by high signal, limitation in perfusion, and prominent enhancement on magnetic resonance imaging (T2-weighted magnetic resonance imaging) (B). The macroscopic examination shows a nodule measuring 20 × 13 mm located submucosally (C) confirmed based on histologic examination (D). The neoplasm is composed of thick-walled vessels, intervascular spindle cells with smooth muscle features and mature adipose tissue (E). The neoplastic cells are arranged in bundles proliferating from vascular walls (F).

https://doi.org/10.4132/jptm.2025.08.04

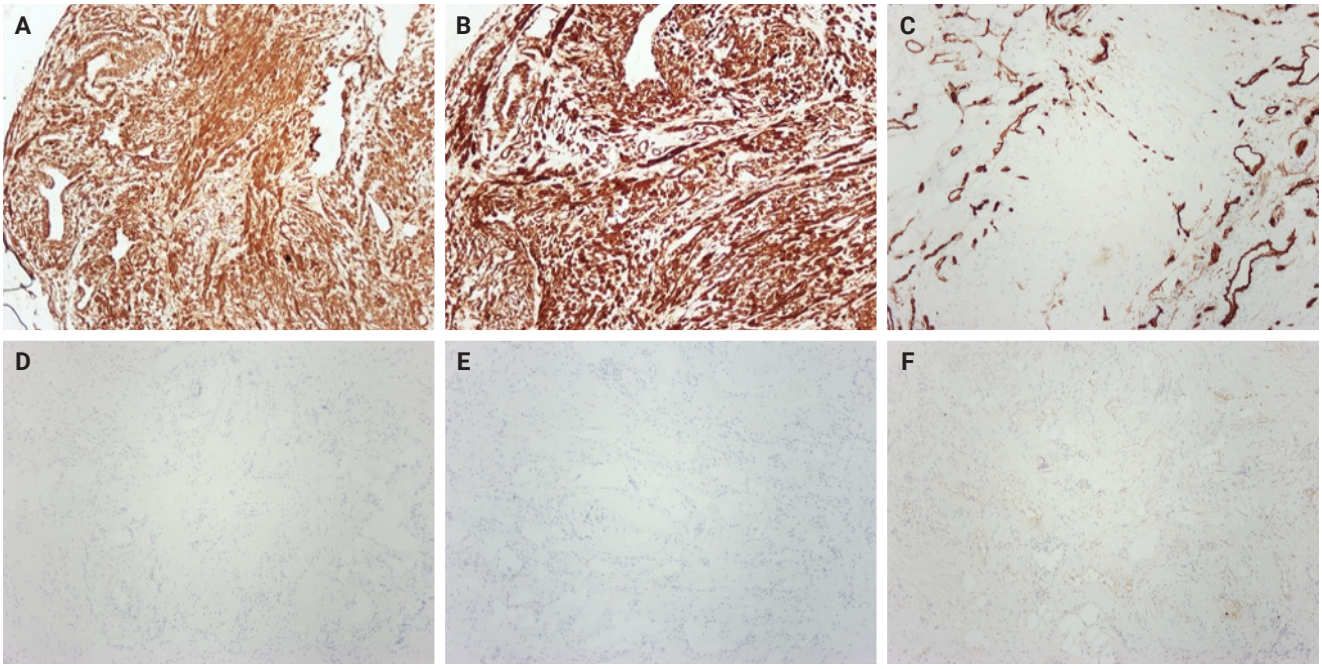

Fig. 2. Immunohistochemical findings. The neoplastic cells were positive for smooth muscle markers including smooth muscle actin (A) and caldesmon (B) and negative for CD34 (C) melanocytic markers including HMB-45 (D) and MelanA (E) as well as DOG1 (F).

solid, cavernous, and venous type [6].

In the present study, English literature from 1969 to present was searched using the terms "angioleiomyoma" and "vascular leiomyoma" in the PubMed database to identify the clinicopathological features of this entity in the digestive system. A total of 13 cases (present case included) were identified regarding the gastrointestinal canal and the main features are summarized in Table 1 [5-16].

Angioleiomyomas have been reported to affect any part of the digestive system except the esophagus, gallbladder, and pancreas. Significant sex predilection regarding these lesions does not apparently exist, which contradicts the established predominance of soft tissue angioleiomyomas in females [1,2]. Angioleiomyomas can occur at any age; the youngest patient was 21 years of age and presented with a jejunal lesion [6] and the oldest was 71 years of age with an anal lesion [14]. A clear correlation between tumor size and location in the gastrointestinal tract is not apparent.

In the present case, the patient presented with no relevant symptoms; however, angioleiomyomas of the gastrointestinal tract most often exhibit diverse symptomatology based on the size and location of the lesion. The symptoms are most frequently a result of gastrointestinal tract obstruction and disruption of its normal architecture and include hemorrhage, diarrhea, and lump/pressure sensation. In a more recent study, perforation of the ileum due to an angioleiomyoma was reported [15].

Several imaging modalities, including endoscopy, ultrasound, MRI, CT, and angiography were utilized to characterize the lesion. Ultrasound revealed a hypoechoic mass with internal vascularity and CT showed a soft tissue density mass. MRI is the modality used to identify the most helpful features in terms of differential diagnosis. Angioleiomyomas are typically T1 isointense and T2 hyperintense enhancing masses that may have a dark reticular sign and/or hypointense peripheral rim. The dark reticular sign on T2-weighted MRI has been described a characteristic feature of angioleiomyoma, usually of the cavernous and venous type [17-19]. However, the resemblance of angioleiomyoma imaging features to those of other entities renders preoperative diagnosis solely based on imaging studies highly challenging, especially when regarding digestive angioleiomyomas, which are relatively uncommon [17,18].

The clinical differential diagnosis includes more commonly occurring tumors, such as GISTs or other more aggressive malignancies [15]. Although angioleiomyomas, myopericytomas, and leiomyomas share overlapping characteristics, angioleiomyomas are distinguished based on a prominent vascular component, with smooth muscle fibers radiating from vascular

Table 1. Characteristics of the reported ALMs in the gastrointestinal tract

Study (year of publication)	Sex	Age (yr)	Tumor location	Size (cm)	Symptoms	Diagnostic modality	Surgical procedure	Immunophenotype	ALM type	Follow-up (mo)
Gadaleanu and Popescu (1988) [5]	F	31	Duodenojejunal flexure	5 × 4	Melena, dizziness, weakness, fainting	N/A	Enterectomy	N/A	N/A	No recurrence (36)
Sadat et al. (2007) [7]	F	58	Ileum	7 × 7	Melena, light-headedness	EGD, colonoscopy, angiography	Segmental resection	Smooth muscle antigens+, GIST (c-Kit) & sarcoma antigens-	N/A	N/A
Sun et al. (2009) [8]	M	57	Jejunum	0.5 × 0.5	Melena, fatigue, palpitation	EGD, angiography	Local excision	N/A	N/A	No recurrence (6)
Nakatani et al. (2010) [9]	F	45	Ileum	0.5	Melena	EGD, colonoscopy, CE	Enterectomy	SMA+, CD117–, CD34–	N/A	N/A
Stanojevic et al. (2013) [10]	F	40	Rectum	7 × 6 × 5	Pain, feelings of pressure and prolapse	N/A	Transanal excision	SMA+, Desmin+, CD117–, CD34–	N/A	No recurrence (6)
You et al. (2014) [11]	M	47	Rectum	8×5×4	Hematuria	CT, MRI	N/A	SMA+, CD117–, DOG1–, S100–	N/A	N/A
Gachabayov and Mityushin (2016) [6]	M	21	Jejunum	N/A	Melena, fatigue, bleeding	EGD, colonoscopy, CT	Enterectomy	Smooth muscle antigens+, GIST antigens–	N/A	No recurrence (3)
Liu et al. (2017) [12]	F	63	Gastric corpus	1.8 × 1.5 × 1.5	Heartburn, abdominal distension	EGD, endoscopic US, CT	EFTR	SMA+, CD34+, synaptophysin–, DOG1–, Ki67 low	N/A	No recurrence (N/A)
Shao et al. (2018) [13]	M	42	Jejunum	0.6	Melena	EGD, colonoscopy, CT, DBE	Local excision	SMA+, CD34+, CD117–, DOG1–, S100-	N/A	No recurrence (60)
Gkegkes et al. (2024) [14]	F	71	Anus	3.8 × 2.8 × 1.8	Palpable/painless lump, pressure sensation	Endoanal US, transanal US, MRI	Local excision	SMA+, desmin+, CD117–, ER–	Mainly cavernous	No recurrence, incontinence or stenosis (12)
Hou et al. (2024) [15]	M	47	Ileum	9.5 × 6.5 × 6.4	Abdominal pain, diarrhea (perforation)	CT	Enterectomy	Desmin+	Cavernous	N/A
Liu et al. (2024) [16]	F	51	Rectum	5.8 × 3.3 × 5	Perirectal mass	MRI	Local excision	SMA+, desmin+, vimentin+, CD34–/+, caldesmon–/+, TLE1–/+, CD31–, S100–, CKP–, MUC4–, Rb–, β-catenin-	N/A	No recurrence (2)
Present case	M	68	Rectum	2 × 1.3	Asymptomatic	CT, MRI, sigmoidoscopy	Endoscopic submucosal dissection	SMA+, desmin+, caldesmon+, CD34–, S100–, CD117–, DOG1–, HMB-45–, MelanA–	Venous	No recurrence (8)

ALM, angioleiomyoma; F, female; N/A, not available; EGD, esophagogastroduodenoscopy; GIST, gastrointestinal stromal tumor; M, male; CE, capsule endoscopy; SMA, smooth muscle actin; CT, computerized tomography; MRI, magnetic resonance imaging; US, ultrasonography; EFTR, endoscopic full-thickness resection; DBE, double balloon enteroscopy; ER, estrogen receptor.

https://doi.org/10.4132/jptm.2025.08.04

channels. This contrasts with the typical concentric perivascular arrangement of myopericytomas and the well-organized fascicular architecture of leiomyomas, which lack significant vascular proliferation. Notably, angioleiomyomas may also exhibit variable amounts of adipose tissue [1,2].

Differential diagnosis of angiomyolipoma is challenging for pathologists and has a potential risk of misclassification [20]. Cases of angiomyolipoma displaying the classic triphasic histology (i.e., blood vessels, smooth muscle, and adipose tissue) accompanied by an absence of melanocytic marker expression have been described in both renal and extra-renal sites [21-24]. Conversely, in several papers, the diagnosis of angiomyolipoma was clearly disregarded when melanocytic markers were negative because a perivascular epithelioid cell origin cannot be supported [25-27]. In those cases, the authors proposed the terms angioleiomyoma with fat or angiolipoleiomyoma. To improve the accuracy of the diagnosis, a broader immunohistochemical panel can be utilized, including microphthalmia transcription factor, cathepsin K, or TFE3 to support the PEComatous origin [28]. Furthermore, electron microscopy could be used for visualizing premelanosome-like granules as documented in prior studies of renal amelanotic angiomyolipomas [21]. However, the most important aspect for the diagnosis remains the morphological distinction between these entities. Specifically, in angiomyolipoma, the smooth muscle component usually displays a characteristic pale/clear and/or granular cytoplasm that is typical of PEComas and has a more mature appearance with the formation of distinct fascicles. Although rarely, angioleiomyomas may contain fat, possibly entrapped during perivascular smooth muscle proliferation corresponding to submucosal adipose tissue, as in the present case. Conversely, the hypothesis of angioleiomyomas with adipocytic metaplasia is worth consideration [2,25].

The subclassification proposed by Morimoto et al. has been seldom reported, possibly due to its limited clinical significance [6]. In the few cases when mentioned, the cavernous subtype was the most prevalent.

Treatment options exclusively encompass either excision of the tumor or partial excision of the affected area of the gastrointestinal tract. Complete excision of angioleiomyomas is considered curative [1,2] and relapse has not been reported in any documented cases.

Although rare, angioleiomyomas can be found in almost any part of the digestive system. The presence of blood vessels, smooth muscle, and adipose tissue may lead to an erroneous diagnosis of angiomyolipoma. Ancillary studies can be helpful but should be correlated and interpreted with respect to the histomorphologic features. Pathologists, radiologists, and surgeons should be aware of this rare entity and consider it in their differential diagnosis. Although angioleiomyomas of the digestive system are rare, they are clinically significantly relevant due to their potential presentation as more aggressive lesions, which can lead to serious implications for patient management. The nonspecific clinical presentation and overlapping imaging characteristics of angioleiomyomas are challenging for an accurate preoperative diagnosis. Therefore, reliable histopathological identification based on characteristic morphological and immunohistochemical features, is crucial to avoid misclassification. Future research should explore the molecular and immunohistochemical profiles of angioleiomyomas in the digestive system, their actual incidence in the population, and the prognostic and diagnostic significance of the different histopathological subtypes.

Ethics Statement

Informed consent was obtained from the patient. Institutional Review Board approval was waived due to the use of retrospective, de-identified data.

Availability of Data and Material

All data generated or analyzed during the study are included in this published article (and its supplementary information files).

Code Availability

Not applicable.

ORCID

Georgios Kalliopitsas https://orcid.org/0009-0001-9826-2054
Christos Topalidis https://orcid.org/0000-0003-0205-3117
Constantine Halkias https://orcid.org/0000-0002-6720-6754
Theodora Gkeka https://orcid.org/0009-0001-2202-2150
Konstantinos Sapalidis https://orcid.org/0000-0002-2050-8392
Triantafyllia Koletsa https://orcid.org/0000-0002-4435-3532

Author Contributions

Conceptualization: GK, TK. Data curation: GK, CT, TG, CH. Formal analysis: GK, CT, TK. Investigation: GK, CT. Methodology: GK, CT, TK. Project administration: TK. Supervision: TK. Writing—original draft: GK, CT, TK. Writing—review & editing: GK, CT, TG, CC, KS, TK. Approval of final manuscript: all

authors.

Conflicts of Interest
The authors declare that they have no potential conflicts of interest.

Funding Statement
No funding to declare.

REFERENCES

1. Goldblum JR, Weiss SW, Folpe AL. Enzinger and Weiss's soft tissue tumors. 7th ed. Philadelphia: Elsevier, 2019; 568-9.
2. Matsuyama A. Angioleiomyoma. In: WHO Classification of Tumours Editorial Board, eds. WHO Classification of Tumours. Soft tissue and bone tumours. 5th ed. Lyon: International Agency for Research on Cancer, 2020; 186-7.
3. Baek SO, Jang U, Rha EY. Angioleiomyoma of the parotid gland fed by the superficial temporal artery. J Craniofac Surg 2023; 34: e336-8.
4. Garrett JR. Angiomyoma of the palate: report of a case. Oral Surg Oral Med Oral Pathol 1969; 27: 103-5.
5. Gadaleanu V, Popescu V. Angiomyoma and vascular ectasia of the small bowel as a cause of intestinal bleeding. Pathol Res Pract 1988; 183: 519-23.
6. Gachabayov M, Mityushin P. Recurrent midgut bleeding due to jejunal angioleiomyoma. Case Rep Surg 2016; 2016: 4569781.
7. Sadat U, Theivacumar NS, Vat J, Jah A. Angioleiomyoma of the small intestine: a rare cause of gastrointestinal bleeding. World J Surg Oncol 2007; 5: 129.
8. Sun C, Sui T, Liu W, Yang R. Gastrointestinal bleeding attributable to a small intestine angioleiomyoma in a patient with haemophilia A. Haemophilia 2009; 15: 355-6.
9. Nakatani M, Fujiwara Y, Kameda N, et al. Angioleiomyoma of the small intestine detected by double-balloon enteroscopy. Gastrointest Endosc 2010; 72: 187-8.
10. Stanojevic GZ, Mihailovic DS, Nestorovic MD, et al. Case of rectal angioleiomyoma in a female patient. World J Gastroenterol 2013; 19: 2114-7.
11. You WY, Min SJ, Hwang DH, et al. A case of primary rectal angioleiomyoma: review of radiologic finding with histopathologic correlation. Acta Radiol Short Rep 2014; 3: 2047981614531755.
12. Liu G, Tan Y, Huo J. Endoscopic full-thickness resection for a gastric angioleiomyoma. Rev Esp Enferm Dig 2017; 109: 604-5.
13. Shao XD, Liang ZD, Guo XZ. A small jejunal angioleiomyoma detected by double-balloon enteroscopy: a case report. Am J Case Rep 2018; 19: 1126-8.
14. Gkegkes ID, Milionis V, Goutas N, Stamatiadis AP. Perianal angioleiomyoma: a case report and review of the literature. J Med Ultrasound 2024; 32: 179-82.
15. Hou TY, Tzeng WJ, Lee PH. Small intestine angioleiomyoma as a rare cause of perforation: a case report. World J Clin Cases 2024; 12: 2116-21.
16. Liu W, Wen X, Hu D, Ma H. Perirectal angioleiomyoma preoperatively misdiagnosed as rectal cancer: a case report. Front Oncol 2024; 14: 1476084.
17. Zhang JZ, Zhou J, Zhang ZC. Subcutaneous angioleiomyoma: clinical and sonographic features with histopathologic correlation. J Ultrasound Med 2016; 35: 1669-73.
18. Edo H, Matsunaga A, Matsukuma S, et al. Angioleiomyoma of the extremities: correlation of magnetic resonance imaging with histopathological findings in 25 cases. Skeletal Radiol 2022; 51: 837-48.
19. Chun RH, Khanna A, Glazebrook KN, Thangaiah JJ, Tiegs-Heiden CA. Angioleiomyomas of the extremities and trunk: an observational study. Acad Radiol 2025; 32: 1554-61.
20. Hachisuga T, Hashimoto H, Enjoji M. Angioleiomyoma: a clinicopathologic reappraisal of 562 cases. Cancer 1984; 54: 126-30.
21. Hohensee SE, La Rosa FG, Homer P, et al. Renal epithelioid angiomyolipoma with a negative premelanosome marker immunoprofile: a case report and review of the literature. J Med Case Rep 2013; 7: 118.
22. Sugimura N, Hirata D, Iwatate M, et al. A diminutive perivascular epithelioid cell tumor in the colon. DEN Open 2025; 5: e390.
23. Lin CY, Tsai CC, Kau HC, Yu WK, Kao SC, Liu CJ. HMB-45 negative angiomyolipoma of the orbit: a case report and review of the literature. BMC Ophthalmol 2016; 16: 8.
24. Sanchez NG, Avila Romay AA, Martinez Luna E, Padilla Rodriguez AL. Cutaneous angiomyolipoma: a distinct entity that should be separated from classic angiomyolipoma: complete review of existing cases and defining fundamental features. JMIR Dermatol 2022; 5: e40168.
25. Jones C, Shalin SC, Gardner JM. Incidence of mature adipocytic component within cutaneous smooth muscle neoplasms. J Cutan Pathol 2016; 43: 866-71.
26. Agaimy A, Michal M, Thompson LD, Michal M. Angioleiomyoma of the sinonasal tract: analysis of 16 cases and review of the literature. Head Neck Pathol 2015; 9: 463-73.
27. Garg N, Tanveer N. Angiolipoleiomyoma or HMB-45 negative angiomyolipoma of uterus: need for uniformity in terminology.

https://doi.org/10.4132/jptm.2025.08.04

Indian J Surg Oncol 2021; 12: 239-40.
28. Zavala-Pompa A, Folpe AL, Jimenez RE, et al. Immunohistochemical study of microphthalmia transcription factor and tyrosinase in angiomyolipoma of the kidney, renal cell carcinoma, and renal and retroperitoneal sarcomas: comparative evaluation with traditional diagnostic markers. Am J Surg Pathol 2001; 25: 65-70.

JPTM

CASE STUDY

pISSN 2383-7837 · eISSN 2383-7845

Journal of Pathology and Translational Medicine 2025; 59: 460-466
https://doi.org/10.4132/jptm.2025.09.18

Diagnostic challenge in Burkitt lymphoma of the mandible initially misdiagnosed as osteomyelitis: a case report

Jiwon Do[1,2], Jin-Young Choi[1,2]

[1]Department of Oral and Maxillofacial Surgery, Dental Research Institute, School of Dentistry, Seoul National University, Seoul, Korea
[2]Department of Oral and Maxillofacial Surgery, Seoul National University Dental Hospital, Seoul, Korea

Burkitt lymphoma (BL) is a highly aggressive B-cell neoplasm that rarely involves the mandible in elderly without apparent immunodeficiency. We report a case of a 72-year-old male who presented with persistent mandibular pain following extraction of tooth #46. Initial imaging findings were consistent with incipient osteomyelitis, and the patient was treated with antibiotics. Despite treatment, pain persisted, and follow-up imaging revealed swelling and diffusion restriction in the lateral pterygoid muscle without evidence of a distinct mass. Biopsy revealed BL confirmed by immunohistochemistry: CD10+, BCL6+, c-MYC+, Ki-67 >95%, and negative for BCL2, MUM-1, and Epstein-Barr virus. Although c-MYC immunopositivity was demonstrated, fluorescence in situ hybridization for *MYC* rearrangement could not be performed due to limited tissue, representing a diagnostic limitation. Notably, the patient had no trismus despite deep muscle involvement, but complained of facial paresthesia and showed remote swelling in the scapular area during hospitalization. Systemic staging with imaging, cerebrospinal fluid cytology, and imaging revealed disseminated nodal and extranodal involvement including the central nervous system, corresponding to stage IV disease by Lugano classification. This case highlights the diagnostic challenge of distinguishing lymphoma from osteomyelitis and underscores the importance of considering malignancy in cases of refractory mandibular inflammation with atypical features.

Keywords: Burkitt lymphoma; Osteomyelitis; Mandible

INTRODUCTION

Burkitt lymphoma (BL) is an aggressive B-cell non-Hodgkin lymphoma characterized by a high proliferative index and frequent MYC gene rearrangements [1-5]. While the disease most commonly involves abdominal organs such as the ileocecal region and mesentery, extramedullary involvement of the head and neck region may occur, particularly in immunocompromised individuals or in endemic forms [1,5,6]. Although up to 10%–15% of BL cases show head and neck involvement [7], sporadic BL involving the mandible in elderly patients remains exceedingly rare [8] and poses a significant diagnostic challenge. Mandibular BL is often radiographically and clinically indistinguishable from chronic osteomyelitis or odontogenic infections, particularly in the absence of overt mass formation or systemic symptoms, leading to potential diagnostic delay.

Here, we report a rare case of sporadic, Epstein-Barr virus (EBV)–negative BL involving the right mandible in a 72-year-old patient who presented with persistent mandibular pain and was initially diagnosed and treated as osteomyelitis. The disease progressed despite appropriate antimicrobial therapy, and the correct diagnosis was ultimately confirmed by biopsy and immunohistochemical analysis. This case highlights the need for heightened suspicion of malignancy when clinical and radiographic findings are atypical or refractory to conventional treatment.

CASE REPORT

A 72-year-old man presented with persistent pain in the right

Received: July 31, 2025 **Revised:** September 15, 2025 **Accepted:** September 17, 2025
Corresponding Author: Jin-Young Choi, DDS, MD
Department of Oral and Maxillofacial Surgery, School of Dentistry and Dental Research Institute, Seoul National University, 101 Daehak-ro, Jongno-gu, Seoul 03080, Korea
Tel: +82-2-6256-3129, Fax: +82-2-6256-3110, E-mail: jinychoi@snu.ac.kr

mandibular molar region. He initially underwent root canal treatment of mandibular right first molar (#46, FDI system) at a local dental clinic; however, symptoms persisted, ultimately necessitating extraction of the involved tooth. Despite this, his discomfort continued, prompting referral to our institution for further evaluation. The patient was otherwise in good general health, with no history of immunodeficiency, and had only well-controlled hypertension and hyperlipidemia.

Initial panoramic view and non-contrast computed tomography (CT) of the mandible showed thickening of the lamina dura and irregular residual alveolar crest at the #46 extraction site (Fig. 1). Based on the clinical presentation and radiologic findings, the patient was diagnosed with incipient osteomyelitis of the right mandibular body, and oral antibiotic therapy was initiated.

One month later, follow-up CT revealed cortical erosion of the right mandibular condyle, increased bone marrow attenuation, and swelling of the right lateral pterygoid muscle. Magnetic resonance imaging further showed diffuse hyperintensity of the mandibular body marrow and perimandibular soft tissues on T2-weighted images, with extension to the mandibular foramen and condyle. Marked swelling and diffusion restriction of the lateral pterygoid muscle were also noted, suggestive of progressive inflammation (Fig. 2).

Histopathologic examination of the mandibular biopsy demonstrated diffuse infiltration of medium-sized atypical lymphoid cells with round nuclei, fine chromatin, and frequent mitotic figures. Immunohistochemically, the neoplastic cells were

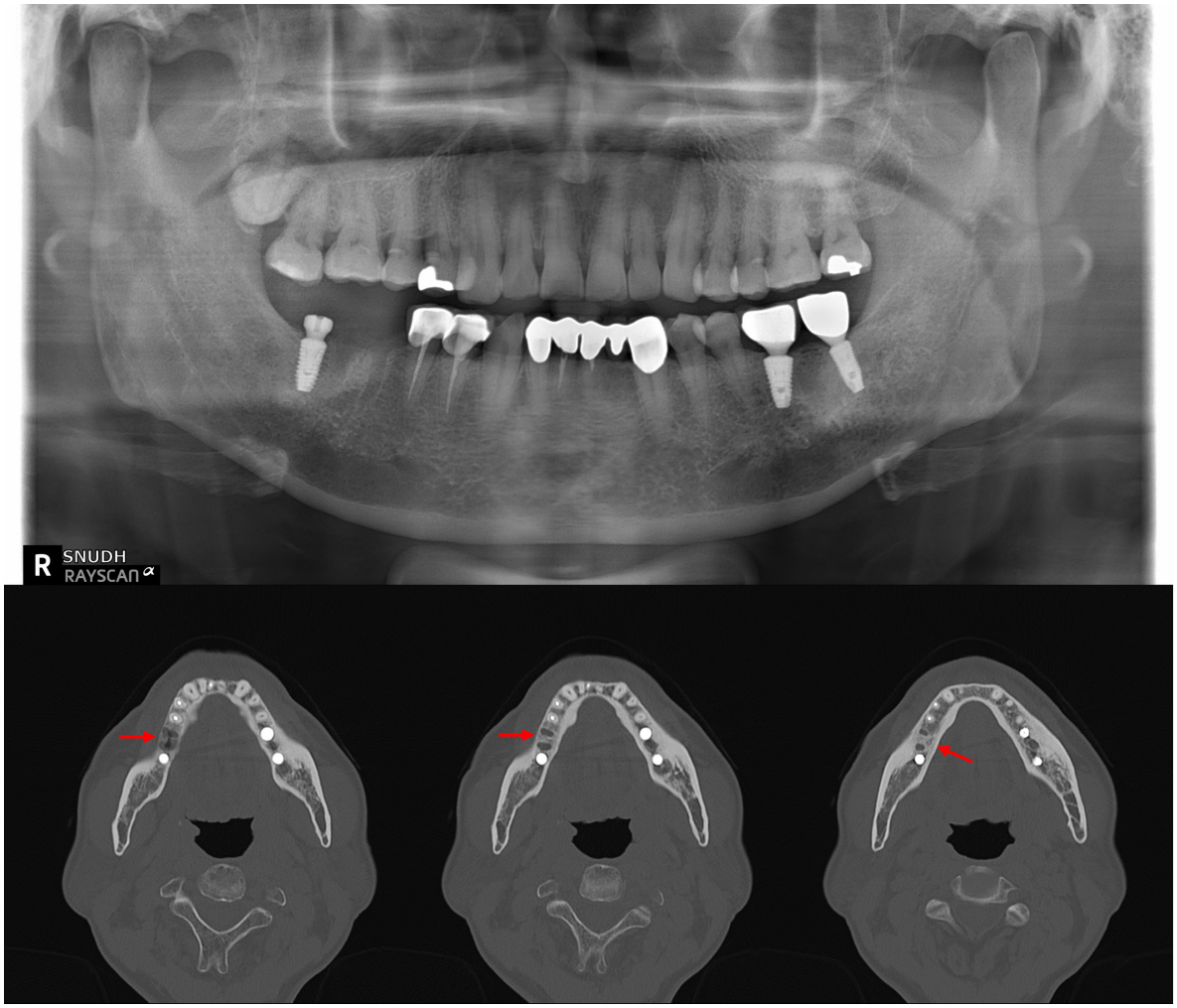

Fig. 1. Initial panoramic and computed tomography (CT) imaging findings of the mandible. Panoramic radiograph shows the extraction socket at the #46 site. Non-contrast axial CT image reveals thickening of the lamina dura and irregular residual alveolar crest at the right mandibular body (arrows), consistent with early-stage osteomyelitis.

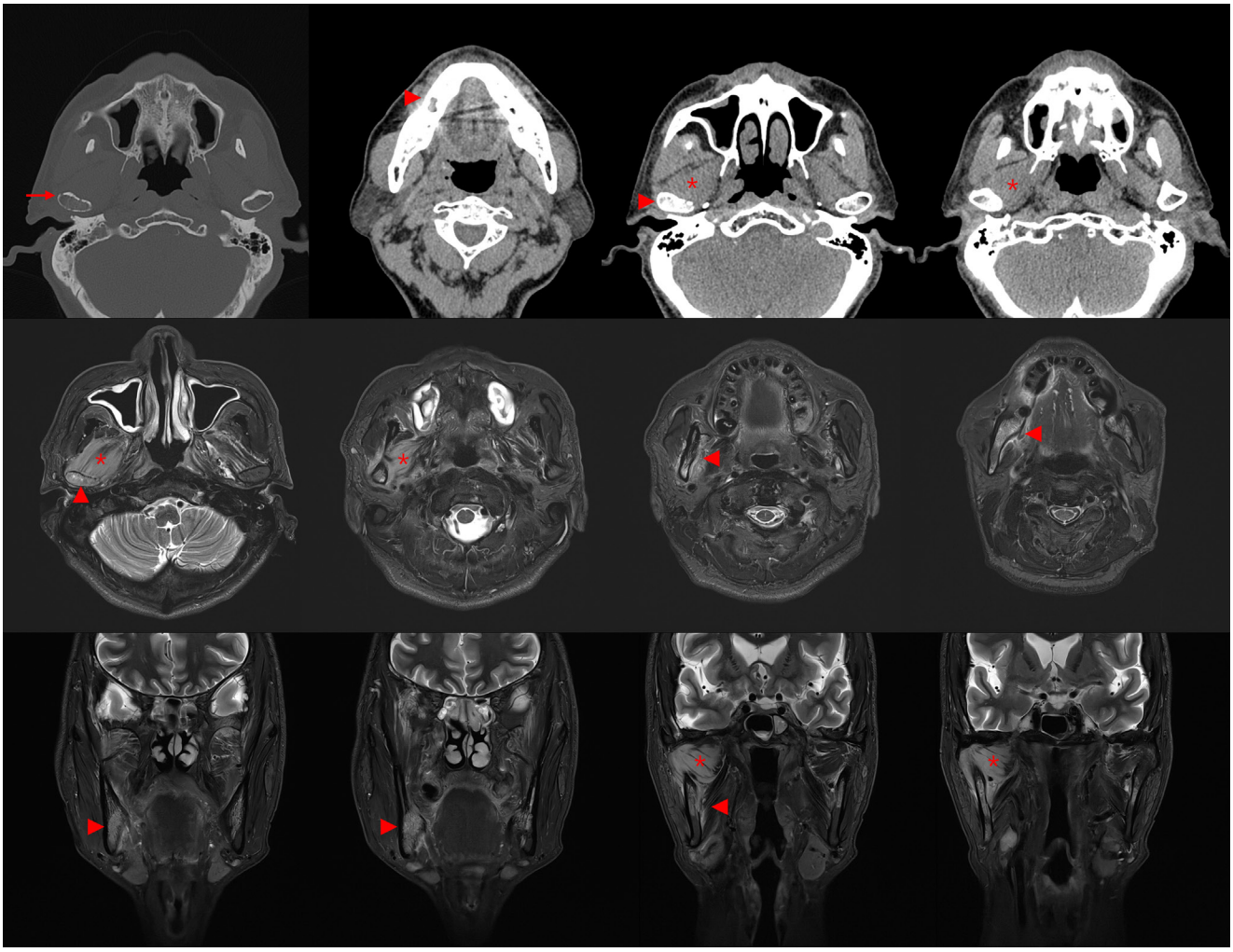

Fig. 2. Follow-up computed tomography (CT) and magnetic resonance imaging (MRI) imaging showing progressive bony and soft tissue changes. Axial CT image obtained 1 month after initial presentation shows cortical erosion of the right mandibular condyle and increased bone marrow attenuation in the right mandibular ramus. T2-weighted MRI reveals diffuse hyperintensity in the mandibular marrow and surrounding soft tissues and restricted diffusion in the right lateral pterygoid muscle. No distinct mass lesion is identified, despite these progressive changes. Arrows indicate cortical erosion, arrowheads indicate increased attenuation of bone marrow and periosteum, and asterisks indicate swelling of lateral pterygoid muscle.

diffusely positive for CD10, BCL6, and c-MYC (homogeneously >90%), with nearly 100% Ki-67 proliferation index. They were negative for BCL2, MUM-1, and EBV. Focal cytoplasmic positivity for CD3 was observed but, in the absence of other T-cell markers, was regarded as nonspecific (Fig. 3).

Subsequent systemic work-up revealed widespread disease. Fluorodeoxyglucose positron emission tomography (FDG-PET) demonstrated probable lymphoma involvement of lymph nodes above and below the diaphragm, bones, nasopharynx, tonsil, stomach, subcutaneous tissue and muscles, and lung (Fig. 4A). Cerebrospinal fluid cytospin was positive for malignant lymphoid cells, confirming central nervous system dissemination. In addition, orbit and head CT revealed a suspicious expansile soft tissue lesion in the right ethmoid sinus, together with mild bilateral maxillary sinus mucosal thickening.

Collectively, these findings were diagnostic of BL. Systemic staging with FDG-PET, cerebrospinal fluid cytology, and CT imaging revealed disseminated nodal and extranodal involvement including the central nervous system, corresponding to stage IV disease by Lugano classification. Given the widespread disease and central nervous system involvement, the therapeutic approach was palliative rather than curative. The

https://doi.org/10.4132/jptm.2025.09.18

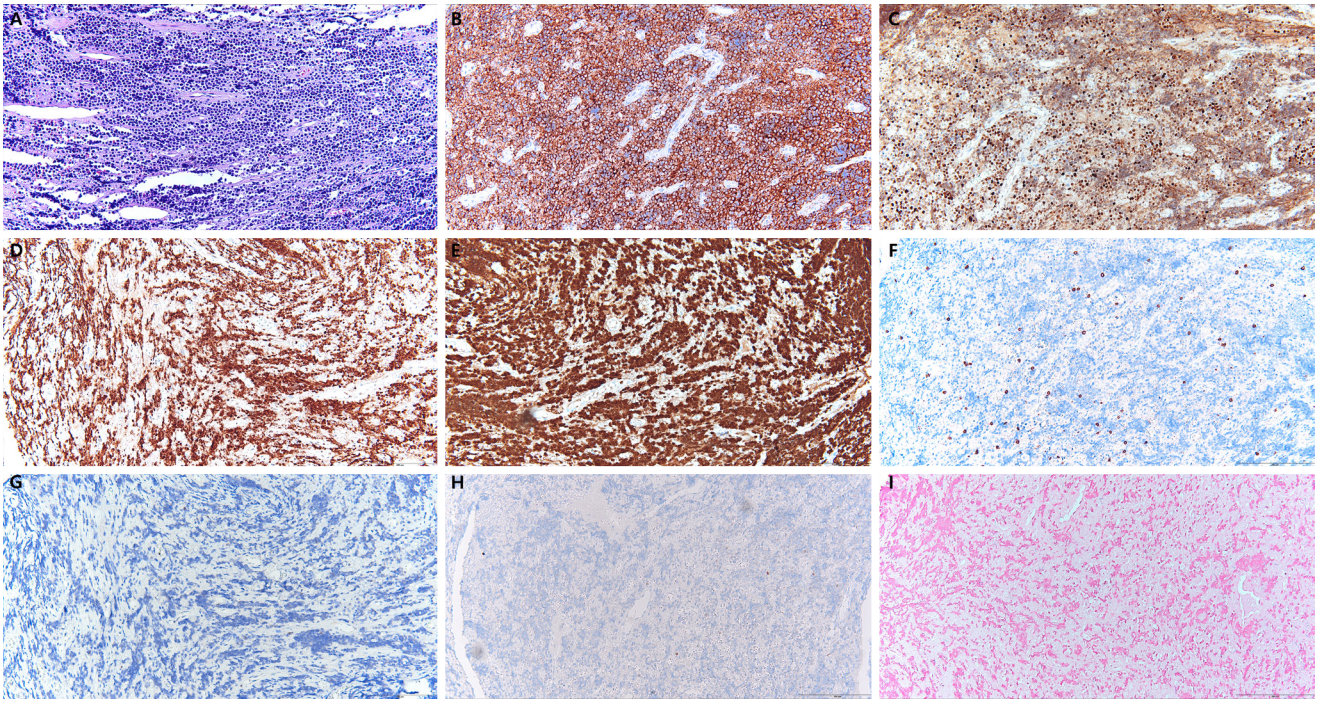

Fig. 3. Histopathologic and immunohistochemical findings of the mandibular lesion. Hematoxylin and eosin staining showing diffuse infiltration of medium-sized atypical lymphoid cells with round nuclei, fine chromatin, and numerous mitotic figures, consistent with a high-grade lymphoma (A). Immunohistochemistry for CD10 demonstrating diffuse membranous positivity (B). BCL6 showing diffuse nuclear positivity (C). c-MYC exhibiting strong nuclear expression in more than 90% of tumor cells (D). Ki-67 proliferation index approaching 100% (E). Tumor cells negative for BCL2, MUM-1, and Epstein-Barr virus (F–H). Focal cytoplasmic staining for CD3 was observed (I).

patient presented with B symptoms, including weight loss and febrile sense, and was initiated on systemic chemotherapy with R-EPOCH (rituximab, etoposide, prednisone, vincristine, cyclophosphamide, doxorubicin). Intrathecal methotrexate (IT-MTX) was administered for central nervous system prophylaxis and treatment, and he is currently undergoing the fourth cycle of R-EPOCH with IT-MTX. Thus far, the patient has tolerated therapy well without treatment-related complications, and follow-up imaging demonstrated marked improvement of the lesions (Fig. 4B).

DISCUSSION

BL is an aggressive B-cell neoplasm with distinct epidemiologic variants. Endemic BL, strongly associated with EBV, typically presents in the jaw and facial bones of children, whereas sporadic BL more commonly involves intra-abdominal organs in younger patients [1-5]. Jaw involvement in elderly individuals without apparent immunodeficiency is rare, and very few cases of sporadic, EBV-negative BL of the mandible have been reported in this age group [8-12].

In the present case, the initial clinical and radiologic findings closely resembled osteomyelitis. Osteomyelitis of the jaw is typically characterized by localized pain, sclerosis of trabecular bone, periosteal reaction, sequestrum formation, and sinus tract development [13,14]. In contrast, malignant bone lesions—including primary bone lymphomas—more often demonstrate rapidly progressive, ill-defined osteolysis, cortical destruction, and associated soft tissue masses [15]. Our patient initially showed lamina dura thickening and subtle marrow signal change, mimicking early infection, but atypical features emerged over time. These included persistent inflammatory marker elevation despite antibiotics, perineural symptoms such as facial paresthesia, and deep muscle involvement without abscess or trismus, all of which raised suspicion for malignancy.

When lymphoma involves the maxillofacial skeleton, imaging often reveals diffuse marrow replacement, cortical thinning or destruction, and soft tissue extension without abscess formation [16,17]. Reports have shown that such presentations are frequently mistaken for odontogenic infection or osteomyelitis,

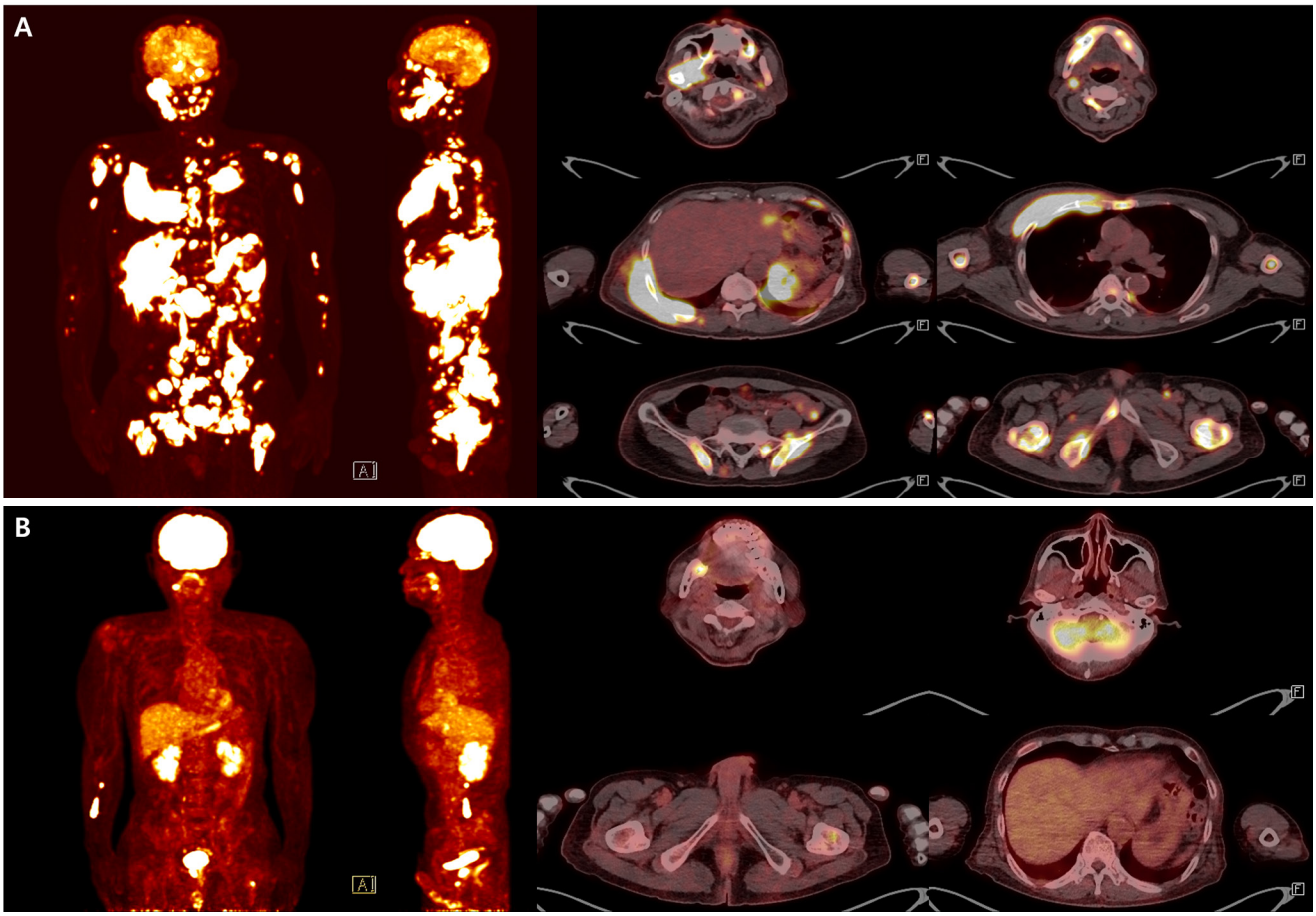

Fig. 4. Fluorodeoxyglucose positron emission tomography–computed tomography (FDG-PET/CT) images at diagnosis and after chemotherapy. Baseline FDG-PET/CT at diagnosis demonstrates disseminated hypermetabolic lesions involving multiple nodal stations (bilateral neck, axilla, mediastinum, abdomen, and pelvis) and extensive extranodal sites, including the skull, mandible, spine, long bones, clavicle, sternum, ribs, scapula, pelvis, lung, stomach, gallbladder, pancreas, nasopharynx, tonsil, and widespread subcutaneous and muscular tissues, consistent with advanced-stage Burkitt lymphoma (A). Follow-up FDG-PET/CT after the fourth cycle of chemotherapy shows a markedly improved state. Only focal residual uptake persists in the right mandible and left proximal femur (B).

leading to delayed diagnosis [11,18,19]. This case underscores the diagnostic dilemma posed by primary bone lymphomas mimicking inflammatory disease and emphasizes the importance of early biopsy when conventional treatment fails.

In the present case, the differential diagnosis included diffuse large B-cell lymphoma (DLBCL), high-grade B-cell lymphoma (HGBCL), and BL. DLBCL was considered less likely because the tumor cells in our case were morphologically monotonous and of medium size, lacking the pleomorphism typically seen in DLBCL. Moreover, the proliferation index approached 100%, which is unusually high for DLBCL. HGBCL, particularly the double-hit or triple-hit subtype, may resemble BL; however, these entities generally harbor *MYC* rearrangements in combination with BCL2 and/or BCL6 translocations. In contrast, our case showed the classic immunophenotypic profile of BL, with diffuse CD10, and BCL6 positivity, nearly 100% Ki-67, and negativity for BCL2 and MUM-1. Although molecular confirmation of *MYC* rearrangement could not be performed due to limited tissue, the combination of morphology, immunophenotype, and clinical presentation was most consistent with BL rather than DLBCL or HGBCL [6,20-22].

This study has limitations. The biopsy specimen was obtained by curettage at the dental hospital, and the slides were subsequently referred to the medical hospital for diagnostic consultation. Because only limited tissue was available and evaluation relied on a restricted number of slides, additional molec-

https://doi.org/10.4132/jptm.2025.09.18

ular studies such as fluorescence in situ hybridization for *MYC* rearrangement could not be performed. Furthermore, as the patient has already initiated systemic chemotherapy, retrospective molecular testing is not feasible. Although the morphology and immunophenotypic profile were highly characteristic of BL, the absence of molecular confirmation represents a diagnostic limitation.

In conclusion, this case illustrates the diagnostic challenge of distinguishing BL from osteomyelitis in the mandible of an elderly patient. Subtle radiographic changes, lack of a distinct mass, and initial resemblance to infection delayed recognition of the malignancy. However, persistent symptoms, rising inflammatory markers despite antibiotics, and atypical features such as perineural involvement should prompt early biopsy to exclude lymphoma. Clinicians should maintain a broad differential diagnosis for refractory mandibular inflammatory lesions, as timely recognition of BL is essential for initiating appropriate therapy in this aggressive disease.

Ethics Statement
Formal written informed consent was not required with a waiver by the Institutional Review Board of Seoul National University Dental Hospital (IRB No. ERI25038).

Availability of Data and Material
The datasets generated or analyzed during the study are available from the corresponding author on reasonable request.

Code Availability
Not applicable.

ORCID
Jiwon Do https://orcid.org/0000-0002-0973-8410
Jin-Young Choi https://orcid.org/0000-0002-2593-6089

Author Contributions
Conceptualization: JYC. Investigation: JD. Writing—original draft: JD. Writing—review & editing: JD, JYC. Supervision: JYC. Approval of final manuscript: all authors.

Conflicts of Interest
The authors declare that they have no potential conflicts of interest.

Funding Statement
No funding to declare.

REFERENCES

1. Lopez C, Burkhardt B, Chan JK, et al. Burkitt lymphoma. Nat Rev Dis Primers 2022; 8: 78.
2. Dalla-Favera R, Bregni M, Erikson J, Patterson D, Gallo RC, Croce CM. Human c-myc onc gene is located on the region of chromosome 8 that is translocated in Burkitt lymphoma cells. Proc Natl Acad Sci U S A 1982; 79: 7824-7.
3. Boerma EG, Siebert R, Kluin PM, Baudis M. Translocations involving 8q24 in Burkitt lymphoma and other malignant lymphomas: a historical review of cytogenetics in the light of todays knowledge. Leukemia 2009; 23: 225-34.
4. Dalla-Favera R, Lombardi L, Pelicci PG, Lanfrancone L, Cesarman E, Neri A. Mechanism of activation and biological role of the c-myc oncogene in B-cell lymphomagenesis. Ann N Y Acad Sci 1987; 511: 207-18.
5. Molyneux EM, Rochford R, Griffin B, et al. Burkitt's lymphoma. Lancet 2012; 379: 1234-44.
6. Alaggio R, Amador C, Anagnostopoulos I, et al. The 5th edition of the World Health Organization classification of haematolymphoid tumours: lymphoid neoplasms. Leukemia 2022; 36: 1720-48.
7. Kuo CY, Shih CP, Cheng LH, et al. Head and neck lymphomas: review of 151 cases. J Med Sci 2020; 40: 215-23.
8. Dunleavy K, Little RF, Wilson WH. Update on Burkitt lymphoma. Hematol Oncol Clin North Am 2016; 30: 1333-43.
9. Munekata T, Asaka T, Sakata KI, et al. Challenging differentiation of oral malignant lymphoma from osteomyelitis of the jawbone: a case report. Mol Clin Oncol 2025; 22: 54.
10. Bugshan A, Kassolis J, Basile J. Primary diffuse large B-cell lymphoma of the mandible: case report and review of the literature. Case Rep Oncol 2015; 8: 451-5.
11. Adalja D, Tagliaferri A, Rezkalla A, Taha B. Diffuse B-cell lymphoma of the mandible disguised as acute osteomyelitis. Eur J Case Rep Intern Med 2024; 11: 004243.
12. Kuo YS, Wu YH, Sun A, Chiang CP. Burkitt's lymphoma of the mandible. J Dent Sci 2017; 12: 421-3.
13. Baur DA, Altay MA, Flores-Hidalgo A, Ort Y, Quereshy FA. Chronic osteomyelitis of the mandible: diagnosis and management: an institution's experience over 7 years. J Oral Maxillofac Surg 2015; 73: 655-65.
14. Schuknecht B, Valavanis A. Osteomyelitis of the mandible. Neuroimaging Clin N Am 2003; 13: 605-18.

15. Musbah T, Omami G. Ill-defined lytic mandibular lesion. J Am Dent Assoc 2020; 151: 692-5.
16. Krishnan A, Shirkhoda A, Tehranzadeh J, Armin AR, Irwin R, Les K. Primary bone lymphoma: radiographic-MR imaging correlation. Radiographics 2003; 23: 1371-83.
17. Imaizumi A, Kuribayashi A, Watanabe H, et al. Non-Hodgkin lymphoma involving the mandible: imaging findings. Oral Surg Oral Med Oral Pathol Oral Radiol 2012; 113: e33-9.
18. Catania R, Belloni E, Preda L, Bortolotto C, Scagnelli P, Calliada F. Odontogenic-like pain in partial edentulism: an unusual presentation of diffuse large B-cell lymphoma of the mandible. Indian J Radiol Imaging 2021; 31: 1053-6.
19. Mika J, Schleicher I, Gerlach U, Adler CP, Uhl M, Knoeller SM. Primary bone lymphomas thought to be osteomyelitis urgently demand a rapid diagnosis in bone pathology. Anticancer Res 2012; 32: 4905-12.
20. Zhao XF, Hassan A, Perry A, Ning Y, Stass SA, Dehner LP. C-MYC rearrangements are frequent in aggressive mature B-Cell lymphoma with atypical morphology. Int J Clin Exp Pathol 2008; 1: 65-74.
21. Harlendea NJ, Harlendo K. Ki-67 as a marker to differentiate Burkitt lymphoma and diffuse large B-cell lymphoma: a literature review. Cureus 2024; 16: e72190.
22. Scott DW, King RL, Staiger AM, et al. High-grade B-cell lymphoma with MYC and BCL2 and/or BCL6 rearrangements with diffuse large B-cell lymphoma morphology. Blood 2018; 131: 2060-4.

https://doi.org/10.4132/jptm.2025.09.18

JPTM

CASE STUDY

pISSN 2383-7837 · eISSN 2383-7845

Journal of Pathology and Translational Medicine 2025; 59: 467-471
https://doi.org/10.4132/jptm.2025.08.28

Primary thyroid diffuse large B-cell lymphoma: fine needle aspiration and histological correlation

Woo Sung Moon[1], Yong Tae Hong[2], Ae Ri Ahn[1]

[1]Department of Pathology, Jeonbuk National University Medical School, Research Institute of Clinical Medicine of Jeonbuk National University, Biomedical Research Institute of Jeonbuk National University Hospital, and Research Institute for Endocrine Sciences, Jeonju, Korea
[2]Department of Otolaryngology, Jeonbuk National University Medical School, Research Institute of Clinical Medicine of Jeonbuk National University, Biomedical Research Institute of Jeonbuk National University Hospital, and Research Institute for Endocrine Sciences, Jeonju, Korea

Primary thyroid lymphoma (PTL) is a rare type of cancer that arises within the thyroid gland, representing about 2%–8% of all thyroid malignancies. Fine-needle aspiration cytology is commonly used as the first-line diagnostic approach for thyroid nodules and can assist in identifying PTL when suggestive features are present. Herein, we report the case of a 59-year-old female patient who presented with a rapidly enlarging anterior neck mass over 20 days. Clinically, the case was challenging to distinguish from anaplastic thyroid carcinoma because of the sudden enlargement of the neck mass. However, pathological examination confirmed the diagnosis of primary thyroid diffuse large B-cell lymphoma. Fine-needle aspiration cytology proved valuable in avoiding unnecessary surgical resection and guiding appropriate treatment. Additionally, we provide a brief review of the clinical and cytopathological features of primary thyroid lymphomas.

Keywords: Cytology; Thyroid; Lymphoma; Immunohistochemistry

INTRODUCTION

Primary thyroid lymphoma (PTL) is defined as a lymphoma that arises solely in the thyroid gland and regional lymph nodes, without evidence of systemic involvement at the time of diagnosis. It is a rare entity, accounting for approximately 1%–2% of all extranodal lymphomas and 2%–8% of thyroid malignancies [1,2]. Diffuse large B-cell lymphoma (DLBCL) is the most common subtype of PTL. Fine-needle aspiration cytology (FNAC) is the diagnostic method of choice for the initial evaluation of thyroid nodules and can aid in the diagnosis of primary thyroid lymphomas. Herein, we report a case of primary thyroid DLBCL and describe its cytological features as observed through FNAC. Additionally, we briefly review the literature on the clinical and cytopathological characteristics of primary thyroid DLBCL.

CASE REPORT

A 59-year-old female patient presented to the otolaryngology department for evaluation of a rapidly enlarging anterior neck mass over the past 20 days. The patient had a history of diabetes and had been taking medications for 10 years. Laboratory examinations were as follows: thyroid function test showed, thyroid stimulating hormone, 2.740 μIU/mL (normal, 0.27 to 4.2 μIU/mL) and free T4, 15.40 pmol/L (normal, 12–22 pmol/L). Contrast-enhanced computed tomography demonstrated a 5×4 cm-sized mass in the left lobe of the thyroid. The mass revealed well-defined, ovoid, and solid features (Fig. 1A). Lymphadenopathy at levels 2, 3, 4, and 6 was observed in the left side of the neck.

FNAC was performed on a lesion in the left thyroid gland. The ThinPrep slide showed a hypercellular smear and intermediate-to-large cells compared to background thyroid follicular

Received: July 21, 2025 **Revised:** August 22, 2025 **Accepted:** August 28, 2025
Corresponding Author: Ae Ri Ahn, MD, PhD
Department of Pathology, Jeonbuk National University, Medical School, 567 Baekje-daero, Doekjin-gu, Jeonju 54907, Korea
Tel: +82-63-270-3070, Fax: +82-63-270-3135, E-mail: xoxoyool@naver.com

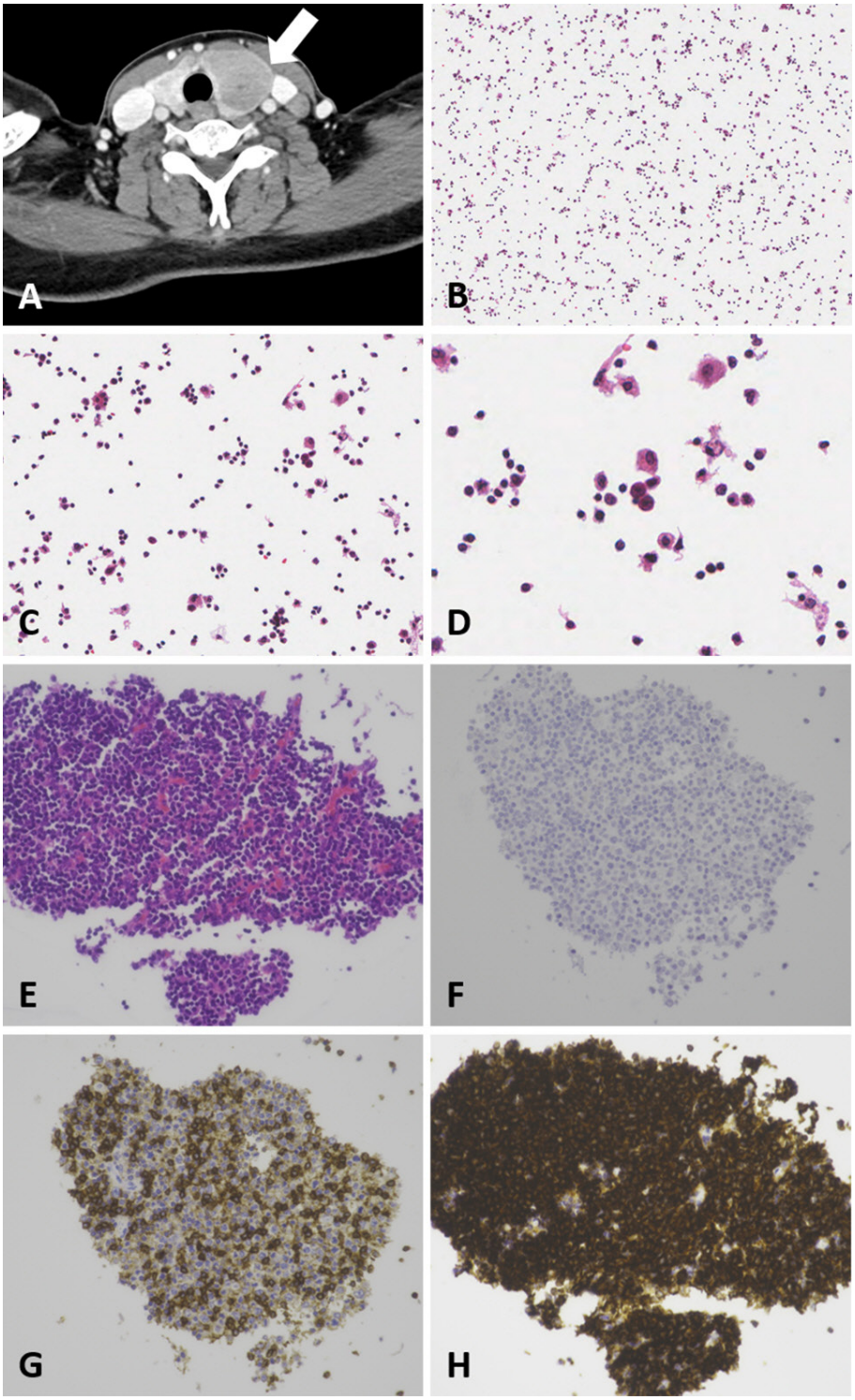

Fig. 1. Radiological findings and cytological of primary diffuse large B-cell lymphoma arising in a thyroid gland. (A) Contrast-enhanced computed tomography demonstrated a 5 × 4 cm-sized mass in left lobe of the thyroid. The mass revealed well-defined and ovoid solid feature. (B) The ThinPrep slide showed hypercellular smear. (C) Tumor cells consisted of intermediate to large cells compared to background thyroid follicular cells. (D) At higher magnification, tumor cells revealed prominent nucleoli and mitotic figures. (E) Cell block demonstrating tumor cell clusters of highly atypical large cells with prominent nucleoli. (F) Thyroid transcription factor-1 were negative. (G) CD3 show positivity on T cells. (H) CD20 shows strong cytoplasmic and membranous staining in majority of tumor cells supporting B-cell origin.

https://doi.org/10.4132/jptm.2025.08.28

cells. The tumor cells showed prominent nucleoli and mitotic figures (Fig. 1B–D). A cell block was prepared from the thyroid FNA material to clarify the tumor cell lineage. The cell block contained several tumor cell clusters of atypical large cells with prominent nucleoli. The tumor cells were immunoreactive for CD19 and CD20. Tests for CD3, pan-cytokeratin and thyroid transcription factor-1 were negative (Fig. 1E–H). Based on these findings, B-cell lymphoma was suspected.

Thyroidectomy and lymph node dissection were then performed. Gross examination of the specimen revealed a well-defined tumor measuring 3.4 × 2.5 cm. At low magnification, the thyroid parenchymal architecture was partially effaced. Infiltration of the thyroid parenchyma by a population of intermediate-to-large lymphoid cells was also observed. Pathological examination of the background thyroid gland revealed Hashimoto's thyroiditis. At a higher magnification, sheets of lymphoid cells showed irregular nuclear contours, prominent nucleoli, and mitosis (Fig. 2A, B). Immunohistochemical staining revealed strong positivity for CD20 and BCL2, and negativity for BCL6, CD3, CD10, and Epstein-Barr encoding region via in situ hy-

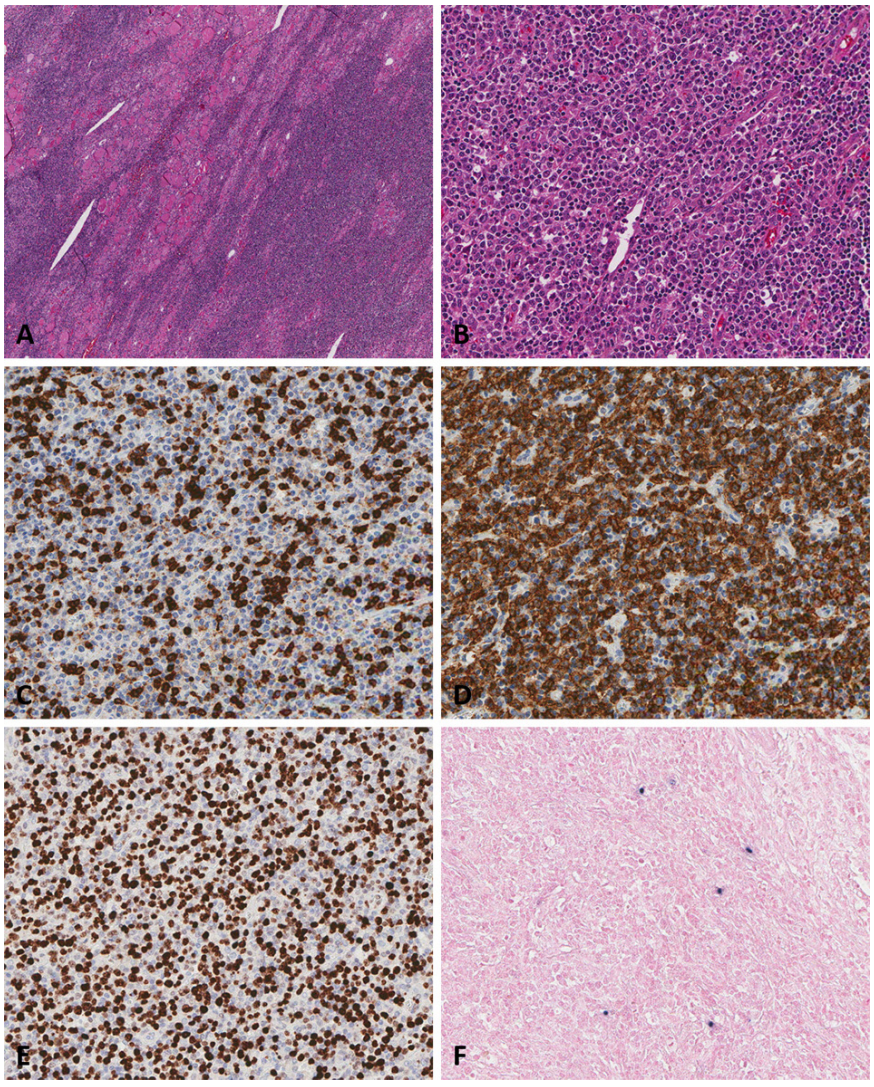

Fig. 2. Histopathological and immunohistochemical findings of primary diffuse large B-cell lymphoma arising in a thyroid gland. (A) In low magnification, thyroid parenchymal architecture was partially effaced. (B) Infiltration of the thyroid parenchyma by a population of intermediate to large lymphoid cells was noticed. (C) In the diffuse large B-cell lymphoma (DLBCL) component, CD3 staining was negative. (D) The tumor cell in DLBCL component showed diffuse and strong positivity for CD20. (E) Tumor cells showed Ki-67 index of 60%. (F) In situ hybridization was negative for Epstein-Barr encoding region.

bridization. Tumor cells showed Ki-67 index of 60% (Fig. 2C–F). The pathological diagnosis confirmed that the mass was primary thyroid DLBCL. After diagnosis, the patient was treated with the rituximab, cyclophosphamide, hydroxydaunorubicin, oncovin, prednisone, or prednisolone (R-CHOP) regimen. At the last follow-up in June 2023, the fluorodeoxyglucose-positron emission tomography/computed tomography showed decrease in the size of left cervical lymph nodes.

DISCUSSION

PTL is a rare malignancy that involves only the thyroid gland and regional lymph nodes, with no evidence of disease elsewhere at the time of diagnosis. The majority of PTLs are non-Hodgkin lymphomas, with DLBCL being the most common subtype. Other forms include mucosa-associated lymphoid tissue lymphoma, follicular lymphoma, and, less commonly, Hodgkin's lymphoma [3]. Several studies have shown that PTLs develop in the context of Hashimoto's thyroiditis [4]. It is well recognized that Hashimoto's thyroiditis serves as a precursor to PTL [5]. In the present case, the patient was diagnosed with DLBCL arising in a background of Hashimoto's thyroiditis, consistent with findings from previously reported cases.

The age of the patient with primary thyroid lymphoma typically ranges from 50 to 80 years, with a slight male predominance (male-to-female ratio, 1:0.75). Clinical presentation varies and may include systemic symptoms such as fever, weight loss, and rapidly enlarging neck mass [6]. PTLs lack specific radiological features, making it difficult to distinguish them from other thyroid neoplasms based on imaging alone. In the present case, imaging revealed a well-circumscribed, solid mass. Histopathological examination revealed aggregates of large atypical lymphoid cells. These cells formed a monomorphic population of intermediate-to-large sized lymphocytes with prominent nucleoli, irregular nuclear membranes, high nuclear/cytoplasmic ratios, and elevated mitotic activity. Immunohistochemical staining showed strong positivity for B-cell markers.

FNAC is a valuable diagnostic tool for a wide range of conditions, offering a safer and more cost-effective alternative to incisional biopsy. However, its role in the diagnosis of lymphoma remains controversial, as FNAC alone may be insufficient for definitive diagnosis and precise subtyping. In the present case, a diagnosis of primary thyroid B-cell lymphoma was established using FNAC in combination with cell block preparation and ancillary immunohistochemical studies. This case highlights the potential of FNAC, when supplemented with additional testing, to serve as a reliable alternative to conventional biopsy in the diagnosis of primary thyroid lymphoma.

Optimal treatment guidelines for PTLs have not yet been established. PTLs do not require surgical resection unless symptoms are present. In the present case, the patient underwent thyroidectomy for dysphagia caused by a rapidly enlarging mass. Targeting CD20-positive DLBCL cells has been proposed as a promising breakthrough in DLBCL treatment. Therefore, targeted therapy, including rituximab, may be a useful treatment [7]. In contrast, surgical resection is essential for the treatment of thyroid carcinomas, including papillary thyroid carcinoma, poorly differentiated thyroid carcinoma, and anaplastic thyroid carcinoma in most cases. In particular, the present case was clinically difficult to differentiate from anaplastic thyroid carcinoma in that there is a suddenly enlarging neck mass. Recognition of this entity and the utilization of FNAC are helpful in avoiding unnecessary surgical resection and establishing appropriate treatment guidelines.

Ethics Statement

This case report was approved by Jeonbuk National University Hospital Institutional Review Board (approval No. IRB 2023-02-020). Patient consent was obtained for publication. This case report was conducted in accordance with the Declaration of Helsinki (1975).

Availability of Data and Material

The datasets generated or analyzed during the study are available from the corresponding author on reasonable request.

Code Availability

Not applicable.

ORCID

Woo Sung Moon https://orcid.org/0000-0001-7951-9865
Yong Tae Hong https://orcid.org/0000-0001-7584-5823
Ae Ri Ahn https://orcid.org/0000-0002-6047-1627

Author Contributions

Conceptualization: ARA. Investigation: YTH, WSM. Supervision: ARA. Writing—original draft: WSM. Writing—review & editing: WSM, YTH, ARA. Approval of final manuscript: all authors.

https://doi.org/10.4132/jptm.2025.08.28

Conflicts of Interest
The authors declare that they have no potential conflicts of interest.

Funding Statement
No funding to declare.

REFERENCES

1. Peixoto R, Correia Pinto J, Soares V, Koch P, Taveira Gomes A. Primary thyroid lymphoma: a case report and review of the literature. Ann Med Surg (Lond) 2017; 13: 29-33.
2. Papadakis G, Tertipi A, Papazian M, Moustakas K, Pappas A. Case report: primary thyroid lymphoma presenting as a rapidly enlarging thyroid mass. Endocrinol Metab Int J 2014; 1: 4-6.
3. Chen C, Yang Y, Jin L, Dong L, Zhang X, Xiang Y. Primary thyroid T-lymphoblastic lymphoma: a case report and review of the literature. Int J Clin Exp Pathol 2014; 7: 443-50.
4. Teixeira Mendes LS, Wotherspoon A. Marginal zone lymphoma: associated autoimmunity and auto-immune disorders. Best Pract Res Clin Haematol 2017; 30: 65-76.
5. Pasieka JL. Hashimoto's disease and thyroid lymphoma: role of the surgeon. World J Surg 2000; 24: 966-70.
6. Sun H, Ma J, Chen Y, Liu M. Primary thyroid lymphoma: report of four cases and literature review. Int J Clin Exp Pathol 2023; 16: 99-107.
7. Yi J, Yi P, Wang W, et al. A multicenter retrospective study of 58 patients with primary thyroid diffuse large B cell lymphoma. Front Endocrinol (Lausanne) 2020; 11: 542.

JPTM
Journal of Pathology and Translational Medicine 2025; 59: 472-475
https://doi.org/10.4132/jptm.2025.09.24

NEWSLETTER

pISSN 2383-7837 / eISSN 2383-7845

PathologyOutlines.com

What's new in hematopathology 2025: myeloid neoplasms in the WHO 5th edition and ICC

Barina Aqil

Department of Pathology, Feinberg School of Medicine, Northwestern University, Chicago, IL, USA

Received: August 22, 2025
Accepted: September 24, 2025
Corresponding Author:
Barina Aqil, MD
Department of Pathology, Feinberg School of Medicine, Northwestern University, Chicago, IL 60611, USA
E-mail: barina.aqil@northwestern.edu

ORCID
Barina Aqil
https://orcid.org/0009-0003-9972-7655

This article has been published jointly, with consent, in both Journal of Pathology and Translational Medicine and PathologyOutlines.com.

Abstract

The previous edition of the World Health Organization (WHO) classification of hematolymphoid neoplasms was published in 2008 and later revised in 2017. A new 5th edition of the WHO classification of hematolymphoid neoplasms was released in 2022. Additionally, the Clinical Advisory Committee developed the International Consensus Classification (ICC) of hematolymphoid tumors, which differs from the WHO classification in several key defining features as outlined below.

GENERAL CHANGES IN TERMINOLOGY & TAXONOMY

- Most of the updates in this newsletter are based on the WHO 5th edition, with significant differences noted between the ICC and WHO classifications.
- Classification structure is lineage defined (based on flow cytometry and/or immunohistochemistry) with further designation under the following parameters:
  - Category, such as precursor lesions, acute and chronic neoplasms.
  - Family: myeloproliferative neoplasms (MPN), myelodysplastic neoplasm/syndrome (MDS), mastocytosis, myelodysplastic/myeloproliferative neoplasms (MDS/MPN), acute myeloid leukemia (AML), secondary myeloid neoplasms (post cytotoxic therapy [pCT], germline predisposition), myeloid/lymphoid neoplasms with eosinophilia and tyrosine kinase gene fusions (M/LN-E-TK) and acute leukemias of mixed or ambiguous lineage, including mixed phenotype acute leukemia (MPAL) and acute leukemias of ambiguous lineage (ALAL).
- Subtypes: gene fusions, rearrangements, and mutations.
- Disease entity-defining genetic abnormalities are prioritized where necessary.
- Emerging entities that are rare/new are now under the category of *other defined genetic alterations*, replacing the terminology of provisional entities.
- The Human Genome Organization (HUGO) Gene Nomenclature Classification System is used for gene symbols and names, including the new designation of gene fusions using double colon marks (::).

CLONAL HEMATOPOIESIS (CH)

- Clonal hematopoiesis of indeterminate potential (CHIP):
  - Presence of somatic mutations (Table 1) with variant allele frequency (VAF) of ≥2% (≥4% for X-linked gene mutations in male patients) in

Table 1. Driver gene mutations associated with CHIP

DNMT3A	*TET2*	*ASXL1*	*JAK2*	*TP53*
SF3B1	*PPM1D*	*SRSF2*	*IDH1*	*IDH2*
U2AF1	*KRAS*	*NRAS*	*CTCF*	*CBL*
GNB1	*BRCC3*	*PTPN11*	*GNAS*	*BCOR*
BCORL1	*BRAF*	*CALR*	*CEBPA*	*CREBBP*
CSF3R	*CUX1*	*ETV6*	*EZH2*	*GATA2*
JAK3	*KDM6A*	*KIT*	*KMT2A*	*MPL*
MYD88	*NOTCH1*	*PHF6*	*PIGA*	*PRPF40B*
SF3A1	*SMC1A*	*SMC3*	*STAG2*	*STAT3*
PTEN	*RAD21*	*RUNX1*	*SETBP1*	*SF1*
U2AF2	*WT1*	*ZRSR2*		

peripheral blood (PB) or bone marrow (BM).
  - No unexplained cytopenias.
  - No morphological features of defined myeloid neoplasms.
- Clonal cytopenia of undetermined significance (CCUS):
  - Clonal hematopoiesis in presence of unexplained persistent cytopenias (4 months or longer in duration).
  - The cytopenia thresholds used for CCUS are similar to those for MDS and MDS/MPN: hemoglobin (female <12 g/dL; male <13 g/dL), absolute neutrophil count (<1.8 × 10^9/L) and platelet count (<150 × 10^9/L).
  - Lacks morphological features of defined myeloid neoplasms.
- VEXAS syndrome, classified as a CH-related disorder, is included in the CH section and is commonly associated with cytopenias.
  - VEXAS syndrome consists of vacuoles, E1 enzyme, X-linked, autoinflammatory symptoms and somatic *UBA1* mutations.
  - Cytoplasmic vacuoles can be seen in myeloid and erythroid precursors.
  - Subset with progression is associated with MDS, typically low risk features, and limited number of mutations aside from *UBA1*.

MYELOPROLIFERATIVE NEOPLASMS

- Chronic myeloid leukemia (CML) (Fig. 1): the accelerated phase (AP) is generally considered less responsive to tyrosine kinase inhibitors (TKIs), in contrast to the chronic phase (CP) and blast phase (BP).
  - Introduction of a concept of high-risk features associated with CP progression and resistance to TKIs:
    - 10-19% blasts in BM or PB
    - ≥20% basophils in PB
    - additional chromosomal abnormalities: isochromosome 17q, trisomy 19, trisomy 21, additional Ph chromosome, monosomy 7, trisomy 8, 3q26.2 (*MECOM*) rearrangements, 11q23 rearrangements
  - Per ICC, all three phases (CP, AP and BP) in CML are retained and >5% lymphoid blasts in PB or BM represent impending lymphoid BP.
  - CML, BP according to WHO includes ≥20% myeloid blasts in PB or BM or presence of an extramedullary blast proliferation or demonstration of lymphoblasts in PB or BM (even if <10%).
- The diagnostic criteria for polycythemia vera (PV), essential thrombocythemia (ET) and primary myelofibrosis (PMF) remain the same with only minor refinements.
  - For PV, increased red cell mass with 51Cr-labeled red cells has been removed.
  - *EZH2*, *IDH1*, *IDH2*, *SRSF2*, *U2AF1* and *ASXL1* mutations in PMF are known to carry poor prognosis.
  - *TP53* mutations are associated with leukemic transformation.
- Chronic neutrophilic leukemia criteria have not changed in the new WHO.
  - ICC suggests decreasing the WBC threshold from ≥25 x 10^9/L to ≥13 x 10^9/L in cases with *CSF3R* T618I or other activating *CSF3R* mutations.
- Chronic eosinophilic leukemia has been revised with several changes.
  - "Not otherwise specified" qualifier has been removed per WHO, but ICC still retains the NOS qualifier.
  - Duration of hypereosinophilia is reduced from 6 months to 4 weeks.
  - Abnormal BM morphology (such as dysplasia) and the evidence of clonality (by cytogenetic or molecular studies) are included.
  - Exclusion of increased blasts (≥2% in PB or 5-19% in BM).
- Juvenile myelomonocytic leukemia (JMML) is now considered a childhood myeloproliferative neoplasm. Updates to diagnostic criteria include:
  - No *KMT2A* rearrangements.
  - Elimination of monosomy 7 (-7) as a cytogenetic criterion.
  - Including genetic criteria that demonstrate mutations of RAS pathway (such as somatic mutations of *NRAS*, *KRAS* or *PTPN11* as well as somatic or germline *NF1* or *CBL* mutations).

MASTOCYTOSIS

- Modification of systemic mastocytosis (SM) diagnostic criteria:
  - CD30 has been added as an aberrant expression in mast cells, like CD2 and CD25.
  - Presence of any type of *KIT* mutation is accepted as a minor criterion.
  - ICC added tryptase and *KIT* (CD117) immunostains among the major criteria for identification of mast cell aggregates.
- BM mastocytosis is a new SM subtype without skin lesions, no B-findings and basal serum tryptase <125 ng/ml.
- The nomenclature of SM with an associated hematologic neoplasm (SM-AHN) is still retained in WHO but renamed in ICC as SM with associated myeloid neoplasm (SM-AMN).
- Well-differentiated SM (WDSM) is characterized by round and well-granulated mast cells that express CD30 and are negative for CD2 and CD25. *KIT* codon 816 mutation is

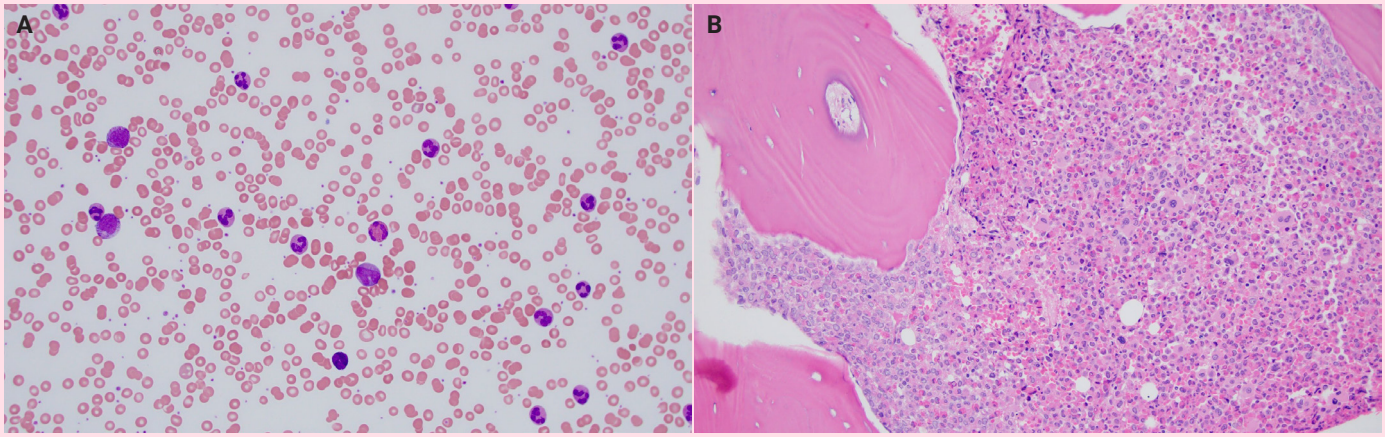

Fig. 1. Chronic myeloid leukemia. (A) Peripheral blood smear with absolute neutrophilia, basophilia and eosinophilia (Wright-Giemsa, 200x). (B) Bone core biopsy in chronic myeloid leukemia showing hypercellular marrow with increased left shifted myeloid maturation, increased eosinophils and small hypolobated megakaryocytes.

Table 2. MDS subtypes based on defining genetic abnormalities

MDS subtypes	Blasts	Cytogenetic findings	Somatic mutations
MDS with low blasts and isolated 5q deletion (MDS-5q)	<5% BM and <2% PB	5q deletion or with 1 other abnormality (exception of -7 or del7q)	
MDS with low blasts and *SF3B1* mutation (MDS-*SF3B1*)		Absence of del5q, -7 or complex karyotype	*SF3B1* (VAF >5%)
MDS with biallelic *TP53* inactivation (MDS-bi*TP53*)	<20 BM/PB	Complex karyotype	≥2 *TP53* mutations or 1 mutation with evidence of *TP53* copy number loss or copy-neutral loss of heterozygosity (cnLOH)

Table 3. MDS subtypes based on the morphology

MDS subtypes	Blasts
MDS, morphologically defined	
MDS with low blasts (MDS-LB)	<5% BM and <2% PB
MDS, hypoplastic (MDS-h) (<25% marrow cellularity)	
MDS with increased blasts (MDS-IB)	
MDS-IB1	5-9% BM or 2-4% PB
MDS-IB2	10-19% BM or 5-19% PB or Auer rods
MDS with fibrosis (MDS-f)	5-19% BM 2-19% PB

not present.

MYELODYSPLASTIC SYNDROME/ NEOPLASM

- Introduction of new terminology of "myelodysplastic neoplasm" instead of "myelodysplastic syndrome" per WHO.
- MDS is now subtyped based on defining genetic abnormalities (Table 2) and morphology (Table 3).
- Detection of ≥15% ring sideroblasts (RS) in WHO substitutes for *SF3B1* mutation and defines the entity as MDS with low blasts and ring sideroblasts. This is unlike ICC, where MDS-RS with wild type *SF3B1* is classified as MDS, NOS, irrespective of the percentage of RS.
- Due to inclusion of CCUS in the classification schemata, the verbiage of "NOS" or "unclassifiable" is not required in WHO, so MDS, unclassifiable is omitted.
- Single lineage and multilineage dysplasia in MDS have been retained according to ICC in the subclassification of MDS, NOS.
- ICC has a slight variation in the MDS subtype names: MDS with del(5q) and MDS with mutated *TP53*.
- With the introduction of the MDS/AML category in ICC, there is now only one – MDS with increased blasts (MDS-IB) – subtype. MDS/AML is characterized by cytopenia with dysplasia, 10-19% PB or BM blasts with exception of AML-defining cytogenetic abnormalities, *NPM1*, bZIP domain in *CEBPA* and *TP3* mutations.

MYELODYSPLASTIC/ MYELOPROLIFERATIVE NEOPLASMS

- ICC included cytopenia along with cytosis as the defining feature of MDS/MPN neoplasms.
- ICC introduced two new CMML precursor entities, which are not mentioned in WHO:
  - Clonal monocytosis of undetermined significance (CMUS), based on persistent monocytosis (relative monocytes ≥10% and absolute monocytes ≥0.5 x 109/L), along with the presence of myeloid neoplasm-associated mutation(s) and without BM morphologic findings of CMML.
  - If cytopenia is present in addition to above findings, the nomenclature of clonal cytopenia and monocytosis of undetermined significance (CCMUS) is suggested.
- Chronic myelomonocytic leukemia (CMML) diagnostic criteria per WHO are updated with refinement of subgrouping based on blast percentages and clinical features.
  - Absolute monocytosis is lowered from 1.0 $\times 10^9$/L to 0.5 $\times 10^9$/L in cases with presence of clonality (cytogenetic or molecular mutations).
  - PB monocyte subtypes are included as a supporting criterion. Monocytes are classified into three subsets based on CD14 and CD16 expression: classic monocytes (CD14+/CD16-), intermediate monocytes (CD14+/CD16+), and non-classic monocytes (CD14-low/CD16+).
  - CMML demonstrates an increase in the fraction of classic monocytes (>94%).
  - Further subtyping of CMML is based on white blood cell (WBC) count and blast percentage:
- Myelodysplastic (CMML-MD) with WBC <13 $\times 10^9$/L and myeloproliferative (CMML-MP) with WBC >13 $\times 10^9$/L.
- CMML-1 with <5% blasts in peripheral blood (PB) and <10% blasts in BM vs. CMML-2 with 5–19% blasts in PB and 10–19% blasts in BM. The previous CMML-0 category has been removed in the new edition.
- Atypical chronic myeloid leukemia (aCML) is renamed in WHO as MDS/MPN with neutrophilia, but ICC retained aCML terminology without *BCR::ABL1*.
- MDS/MPN with ring sideroblasts and thrombocytosis (MDS/MPN-RS-T) is redefined with incorporation of *SF3B1* mutation and rephrased as MDS/MPN with *SF3B1* mutation and thrombocytosis (MDS-*SF3B1*-T).
  - In cases with wild type *SF3B1* and ≥15% RS, the terminology of MDS/MPN-RS-T is acceptable.
- JMML is moved into MPN according to WHO and into pediatric and/or germline mutation associated disorders per ICC.
- MDS/MPN, unclassifiable is changed to MDS/MPN, NOS (not otherwise specified) per ICC.
- ICC brought forth a new provisional sub-entity in MDS/MPN, NOS category: MDS/MPN with isolated isochromosome 17q.

MYELOID/LYMPHOID NEOPLASMS WITH EOSINOPHILIA WITH TYROSINE KINASE GENE FUSIONS

- This family is renamed from prior myeloid/lymphoid neoplasm with eosinophilia (M/LN-eo) and gene rearrangement to myeloid/lymphoid neoplasms with eosinophilia and tyrosine kinase gene fusions (M/LN-E-TK).

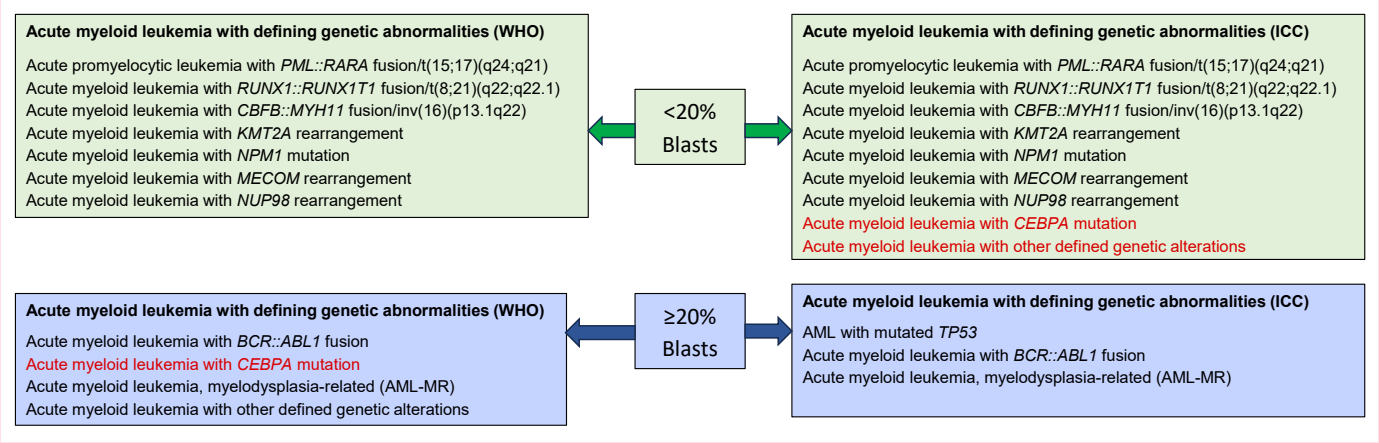

Fig. 2. Differences in blast requirement (red) for AML with defining genetic abnormalities between WHO and ICC.

- Identification of three new entities under this category:
  - Myeloid/lymphoid neoplasms with *JAK2* rearrangement
  - Myeloid/lymphoid neoplasms with *FLT3* rearrangement
  - Myeloid/lymphoid neoplasms with *ETV6*::*ABL1* fusion

MYELOID NEOPLASMS WITH MUTATED TP53

- This entity is described by ICC but not mentioned by WHO.
  - *TP53* mutation VAF has a defined lower threshold (VAF >10%).
  - This category includes separate diagnoses of MDS (0–9%), MDS/AML (10–19%), and AML with mutated *TP53* (>20%) (including AEL), based on blast percentage.
  - Irrespective of blast count, this group shows aggressive behavior and poor prognosis.

ACUTE MYELOID LEUKEMIA

- AML with defining genetic abnormalities is separated from AML defined by differentiation, so the term AML, NOS is omitted.
- Blast requirement of ≥20% is eliminated in both WHO and ICC for AML with defining genetic abnormalities, with some differences (Fig. 2). WHO has no lower threshold for blasts in cases of recurrent genetic abnormalities, while ICC requires ≥10% blasts.
- AML with *KMT2A*, *MECOM* and *NUP98* are recognized. AML with *KMT2A* rearrangement replaces the prior terminology of AML with t(9;11)(p22;q23); *KMT2A*::*MLLT3*.
- AML with *CEBPA* mutation is changed to include biallelic (bi*CEBPA*) as well as single mutations located in the basic leucine zipper (bZIP) region of the gene (smbZIP-*CEBPA*).
- AML with other defined genetic alterations is added.
- AML with myelodysplasia-related changes (AML-MRC) is changed to AML, myelodysplasia-related (AML-MR) in WHO. While the category of AML with myelodysplasia-related cytogenetic abnormalities is retained, new categories of AML with mutated *TP53* and AML with myelodysplasia-related gene mutations are added in ICC.
  - Morphology alone is taken out from diagnostic criteria of AML-MR.
  - Cytogenetic abnormalities are updated, and somatic mutations are included (Table 4).
  - AML with mutated *TP53* according to ICC requires >20% blasts and VAF of >10%.
  - MDS and MDS/MPN progression to AML is still considered under AML-MR in WHO, but ICC introduced the addition of qualifier to the diagnosis in AML progressing from MDS and MDS/MPN.
- AML with somatic *RUNX1* mutation is no longer recognized as a separate entity.
- In WHO, the diagnosis of acute erythroid leukemia (AEL) supersedes AML-MR. Because AEL is typically associated with *TP53* mutations, it is included within the category of AML with *TP53* mutations in the ICC.

ACUTE LEUKEMIAS OF MIXED OR AMBIGUOUS LINEAGE

- Two new subtypes in the defining genetic alterations are added, which are MPAL with *ZNF384* rearrangement and ALAL with *BCL11B* rearrangement.
- Lineage assignment criteria for MPAL have been refined with greater emphasis on the intensity and pattern of antigen expression on blasts as well as their association with normal hematopoietic counterparts.

SECONDARY MYELOID NEOPLASMS

- Myeloid neoplasms (MN) that arise after exposure to cytotoxic therapy (CT) or germline predisposition (GP) are included in this WHO category.
- The terminology of therapy-related is replaced with MN-pCT per WHO but retained in ICC.
- Exposure to PARP1 inhibitors is added as a qualifying criterion for MN-pCT, and methotrexate therapy has been excluded.
- The clinical manifestations of the diseases within germline predisposition are grouped into three subtypes:
  - MN with GP without a pre-existing platelet disorder or organ dysfunction
  - MN with GP and pre-existing platelet disorder
  - MN with GP and potential organ dysfunction

Meet the Authors

Dr. Barina Aqil joined the Department of Pathology at Northwestern University Feinberg School of Medicine in 2019 as an Assistant Professor, where she specializes in Hematopathology. She has been writing for PathologyOutlines.com since 2023 and joined as a Board of Reviewers for Hematopathology in 2024. Dr. Aqil's research interests include understanding genetic markers in myeloid and lymphoid neoplasms. She is also passionate about the use of newer methodologies for interactive teaching.